EVIDENCE OF THE HIGGS BOSON DECAYING INTO TWO PHOTONS

A Dissertation

Submitted to the Graduate School
of the University of Notre Dame
in Partial Fulfillment of the Requirements
for the Degree of

Doctor of Philosophy

by

Douglas R. Berry

Colin Jessop, Co-Director

Nancy Marinelli, Co-Director

Graduate Program in Physics

Notre Dame, Indiana

July 2013

EVIDENCE OF THE HIGGS BOSON DECAYING INTO TWO PHOTONS

Abstract

by

Douglas R. Berry

A search for the standard model Higgs boson decaying to two photons will be presented. The analysis will cover 5.1 fb^{-1} and 19.6 fb^{-1} of LHC proton-proton collisions collected at a center of mass energy of 7 and 8 TeV, respectively, with the CMS detector. The search reveals an excess of events near 125 GeV that is consistent with the standard model Higgs boson. The significance of the excess is 3.2σ at 125 GeV, where 4.1σ is expected. The best-fit cross-section is $0.78^{+0.28}_{-0.26}$ times the standard model, and the best-fit mass is $125.4 \pm 0.5(stat.) \pm 0.6(syst.)$ GeV. The excess is also present in a cut-based cross-check analysis with a significance of 3.9σ, where 3.5σ is expected, which corresponds to a best-fit cross-section of $1.11^{+0.32}_{-0.30}$ at 124.5 GeV. Both the measured cross-section and couplings are consistent with a standard model Higgs boson.

To my parents, Donald and Vicki, who always pushed me to follow my dreams.

CONTENTS

FIGURES

TABLES

ACKNOWLEDGMENTS

I would first like to acknowledge the support of my two advisors, Prof. Colin Jessop and Research Associate Prof. Nancy Marinelli, who provided me not only the opportunity to work at CERN but also the support and guidance needed to thrive. I would also like to thank Dr. Paolo Meridiani and Dr. Chris Seez for taking the responsibility of leading the $H \to \gamma\gamma$ analysis group through the process of discovery.

I would also like to acknowledge my fellow physicists who worked with me on the $H \to \gamma\gamma$ analysis. The work done by Chris Palmer, Matt Kenzie, Dr. Nick Wardle, Dr. Pasquale Musella, Dr. Matteo Sani, Dr. Martina Malberti, Dr. David Fuytan, Dr. Andre Holzner, Dr. Marco Pieri, and Dr. Andre David on the h2gglobe framework and the $H \to \gamma\gamma$ analysis have made this thesis possible. I would like to acknowledge the efforts of Dr. Josh Bendavid, Dr. Fabian Stoeckli, and Ming Ming Yang for providing stiff competition to the h2gglobe team and for their contributions to the $H \to \gamma\gamma$ analysis. I would like to thank Dr. Olivier Bondu, Dr. Louis Sgandurra, Prof. Susan Gascon-Shotkin, and Jiawei Fan for their contribution towards $Z \to \mu\mu\gamma$ and also Rishi Patel for his help with particle flow and single leg conversions. The contributions of all these people have made the CMS $H \to \gamma\gamma$ analysis what it is today.

I would like to thank my friends and colleagues in and associated with building 512 who have been true friends during my time at CERN. Dr. Ted Kolberg, Dr. Jamie Antonelli, Dr. Sean Lynch, Dr. Jeff Kolb, Dr. Rachel Yohay, Dr. Justin Griffiths, and Dr. Orin Harris have been excellent colleges and a great cohort. I am also indebted to Dr. Jason Slaunwhite, Dr. Sarah Boutle, and Dr. Anne-Fleur

Barfuss for their invaluable guidance in my early research career. I would also like to thank Yutaro Iiyama, Anna Woodard, Andrew Brinkerhoff, Dr. Nil Valls, Robin Luo, Nathan Kellams, Michael Planer, Charlie Mueller, Matthias Wolf, Brian Francis, Joey Goodell, and John Wood for lively office discussions and camaraderie.

Words cannot express then amount of gratitude that is owed to Dr. Ethan Uberseder and Beth Given, MLIS, and Dr. David Morse and Kat Morse, J.D., who have been the best friends a person could ask for during my time in graduate school and at CERN. And finally, I would like to thank Dr. Tessa Pearson who's love and kindness were the greatest companion as we traveled, dined, adventured, studied, and worked our way through Europe.

CHAPTER 1

INTRODUCTION

Since the Higgs boson was first theorized, there have been many searches; however, even the most promising searches at the SPS, LEP, and the Tevatron failed to find the Higgs boson. The elusiveness of the Higgs boson was the subject of a great deal of serious and jovial discussion. The standard model needs a mechanism to break electroweak symmetry, and if the Higgs boson does not exist, then more exotic theories are needed. The Large Hadron Collider (LHC) was built to answer one question, "What is the cause of electroweak symmetry breaking?". This thesis will answer that question.

First, the standard model will be introduced from a historical perspective. Starting with quantum electrodynamics and Fermi's theory of β-decay, the two sectors will be combined, and the theoretical motivation of the Higgs boson will be introduced. This will be followed by a description of the production mechanisms, backgrounds, and previous searches for the Higgs boson. Once the theory is characterized, the design of the CMS detector will be discussed. The bulk of the thesis will be devoted to an in-depth discussion of the $H \to \gamma\gamma$ analysis, covering every facet of the analysis. The final results of the search will be presented, and then evaluated in the context of other search channels.

Two versions of the $H \to \gamma\gamma$ analysis have already been published by CMS. The first version was publish in Physics Letters B in March of 2012 covering 4.8 fb^{-1} of 7 TeV data. A second result was announced on July 4^{th}, 2012 from CERN, and it was included in a result also published in Physics Letters B. The second result covered

5.1 fb^{-1} of 7 TeV data and 5.3 fb^{-1} of 8 TeV data. The results presented in this thesis will cover the full 7 and 8 TeV datasets collected by CMS.

CHAPTER 2

THEORY

This chapter will be a basic overview of the standard model of particle physics. Quantum electrodynamics and the weak nuclear interaction will be introduced from a historical perspective. The two interactions will then be unified into a single model, electroweak theory, which includes the Higgs field. The Higgs mechanism will be described in the context of GWS theory. The production mechanisms and branching ratios for the consequent Higgs boson will be discussed. Finally, the results of previous searches for the standard model Higgs boson at the Large Electron Positron collider and the Tevatron at Fermi National Accelerator Laboratory will be presented.

2.1 The Standard Model

The standard model is the most successful model in the history of particle physics. It has two sectors: the fermions, which make up all visible matter, and the bosons, which mediate interactions and give mass. The fermion sector consists of three families of spin $\frac{1}{2}$ particles. This includes six flavors of quarks and six leptons. Three of the leptons are neutral, and are called neutrinos, and the other three are charged. The boson sector consists of 12 gauge bosons, eight gluons, three weak gauge bosons, and the photon, and one Higgs boson, which gives mass to all the fermions and bosons. The fermions combined with the gauge and Higgs bosons represent all the constituents of the standard model as seen in figure 2.1. It should be noted that while the standard model is very successful at describing particle interactions, it still does not provide a complete picture of nature. The gravitational interaction is not

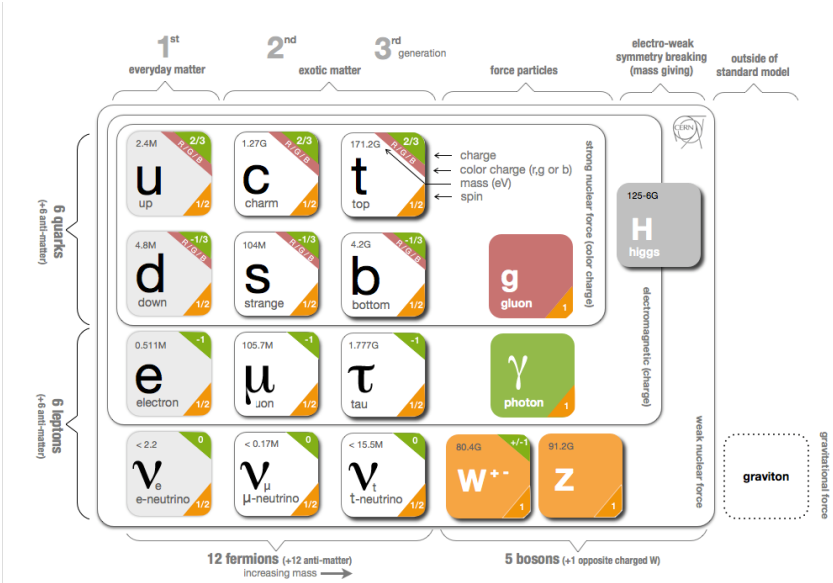

Figure 2.1. A chart of the standard model of particle physics [3].

included in the standard model, and the recent cosmological observations of dark matter [1] and dark energy [2] are also not included.

The standard model is a fully renormalizable field theory that describes, in a unified and coherent way, three of the fundamental interactions of nature: strong, weak, and hypercharge interactions. The electroweak sector is created from the weak and hypercharge interactions. Quantum electrodynamics is a relativistic quantum field theory, and the most general theory, of electrodynamics. The weak nuclear interaction is an extension of Fermi's theory of weak interactions, and the strong nuclear interaction is built upon a $SU(3)$ Yang-Mills theory. Each interaction is modeled with a Lagrangian. When the requirement of gauge invariance is imposed, a gauge boson (or bosons) is (are) created that mediate the interaction. The necessity of gauge invariance is a natural one, as it requires that the phase transformations that leave the Lagrangian invariant can be chosen independently from point to point in spacetime. However, this process only creates massless bosons, because a massive

boson makes the Lagrangian gauge dependent. The Higgs mechanism gives the gauge bosons masses without breaking the gauge invariance of the Lagrangian by adding a scalar field with a non-zero expectation value. The Higgs mechanism also produces an additional massive scalar boson and gives mass to the fermion sector through Yukawa couplings.

2.1.1 Quantum Electrodynamics and Gauge Invariance

Quantum Electrodynamics (QED) is a quantum field theory describing the interactions between photons and charged particles. QED is the result of a quantum mechanical model for electromagnetism under the constraints of special relativity. QED was the first example of a relativistic quantum field theory and was developed by Sin-Itiro Tomonaga [4], Julian Schwinger [5, 6], Richard Feynman [7–10], and Freeman Dyson [11, 12]. QED is an example of a gauge theory, a model where the observables do not change under gauge transformations. The necessity of gauge invariance demands a new term in the Lagrangian that can be interpreted as a new particle representing the gauge field. In this subsection, starting from the Dirac equation for free fermions, the Lagrangian for QED will be derived. Then it will be shown that requiring the Lagrangian to be invariant under gauge transformation creates a gauge boson, which mediates interactions between the Dirac fermions.

The QED Lagrangian can be derived starting from the Dirac equation [13, 14] for free particles,

$$i\gamma^\mu \partial_\mu \psi - m\psi = 0, \tag{2.1}$$

where γ^μ are the four Dirac matrices written below in Bjorken and Drell convention

$$\gamma^0 = \begin{pmatrix} 1 & 0 \\ 0 & 1 \end{pmatrix} \quad \text{and} \quad \gamma^i = \begin{pmatrix} 0 & \sigma^i \\ -\sigma^i & 0 \end{pmatrix}. \tag{2.2}$$

The Lagrangian for equation 2.1 is

$$\mathcal{L} = \overline{\psi}(i\gamma^{\mu}\partial_{\mu} - m)\psi. \tag{2.3}$$

Equation 2.3 is invariant under the following global transformation

$$\psi \rightarrow e^{i\theta}\psi. \tag{2.4}$$

However, equation 2.3 is not invariant under a gauge transformation

$$\psi \rightarrow e^{i\theta(x)}\psi, \tag{2.5}$$

because

$$\partial_{\mu}(e^{i\theta(x)}\psi) = i\partial_{\mu}\theta(x)e^{i\theta(x)}\psi + e^{i\theta(x)}\partial_{\mu}\psi. \tag{2.6}$$

This causes the Lagrangian in equation 2.3 to gain an extra term due to the gauge transformation,

$$\mathcal{L} = i\overline{\psi}\gamma^{\mu}\partial_{\mu}\psi - m\overline{\psi}\psi - \partial_{\mu}\theta(x)\overline{\psi}\gamma^{\mu}\psi. \tag{2.7}$$

The Lagrangian in equation 2.3 can be rewritten to cancel out this extra term,

$$\mathcal{L} = \overline{\psi}(i\gamma^{\mu}\partial_{\mu} - m)\psi - e\overline{\psi}\gamma^{\mu}\psi A_{\mu}, \tag{2.8}$$

where A_{μ} transforms as

$$A_{\mu} \rightarrow A_{\mu} - \frac{\partial_{\mu}\theta(x)}{e}. \tag{2.9}$$

The new term in equation 2.8, $e\overline{\psi}\gamma^{\mu}A_{\mu}\psi$, can be absorbed into the kinematic term replacing the ∂_{μ} operator with the gauge covariant derivative

$$\partial_{\mu} \rightarrow D_{\mu} = \partial_{\mu} - ieA_{\mu}, \tag{2.10}$$

where A_μ is the electromagnetic four-vector potential and e is the charge of the Dirac field. Thus, equation 2.3 becomes

$$\mathcal{L} = \overline{\psi}(i\gamma^\mu D_\mu - m)\psi. \tag{2.11}$$

Adding a gauge field strength tensor ($F^{\mu\nu}$) to model the kinetic properties of the photon generates the QED Lagrangian

$$\mathcal{L}_{QED} = \overline{\psi}(i\gamma^\mu D_\mu - m)\psi - \frac{1}{4}F_{\mu\nu}F^{\mu\nu}. \tag{2.12}$$

The QED Lagrangian, equation 2.12, models an abelian gauge theory under symmetry group $U(1)$. The $U(1)$ local symmetry of the Lagrangian means that the Lagrangian is invariant under a circular rotation in the complex plane, which is equivalent to the gauge transformation of $e^{i\theta(x)}$. This invariance determines the behavior of the gauge boson and necessitates the conservation of electric charge, e, via Noether's second theorem [15, 16]. Modeling QED using a gauge theory is advantageous because the Ward-Takahashi identity [17, 18] can be used to aid in the renormalization calculation to cancel out ultraviolet divergences. Without renormalization, QED, and quantized field theories in general, often give infinite amplitudes for processes that are observed to be finite in nature.

2.1.1.1 Massive Gauge Boson and Gauge Invariance

It was seen in section 2.1.1 that requiring gauge invariance of the Lagrangian creates a massless gauge field A^μ. Creating a gauge invariant theory with a massive vector boson is non-trivial. Consider a Lagrangian for Maxwell's equation with a massive photon:

$$\mathcal{L} = -\frac{1}{4}F_{\mu\nu}F^{\mu\nu} + \frac{1}{2}m^2 A_\mu A^\mu. \tag{2.13}$$

If equation 2.13 is transformed to a new gauge

$$A_\mu \rightarrow A_\mu + \partial_\mu \Lambda(x), \tag{2.14}$$

then equation 2.13 becomes

$$\mathcal{L} = -\frac{1}{4} F_{\mu\nu} F^{\mu\nu} + \frac{1}{2} m^2 (A_\mu A^\mu + \partial_\mu \Lambda(x) A^\mu + A_\mu \partial^\mu \Lambda(x) + \partial_\mu \Lambda(x) \partial^\mu \Lambda(x)). \tag{2.15}$$

In order to make equation 2.15 gauge invariant the final three terms need to sum to zero. While there many be particular gauges where this is true, it is not true for any general $\Lambda(x)$. Therefore, the Lagrangian in equation 2.13 is not gauge invariant.

2.1.2 The Weak Interaction

The weak interaction was first proposed as a model for radioactive β and μ decay. The original form was Fermi's four particle contact theory [19] as seen in figure 2.2.

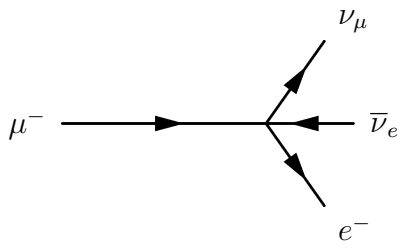

Figure 2.2. Muon Decay in Fermi Contact Theory

In this model, the four fermions meet in a single vertex. If the weak interaction is

vector like, as Fermi thought it was, then the Lagrangian for this process would be

$$\mathcal{L} = \frac{G_F}{\sqrt{2}} \overline{\psi}_{\nu_\mu} \gamma^\mu \psi_\mu \overline{\psi}_e \gamma_\mu \psi_{\overline{\nu}_e} + h.c., \tag{2.16}$$

where G_F is the Fermi coupling constant. However, experiments conducted by Wu, on suggestion from Chen Ning Yang and Tsung-Dao Lee [20], demonstrated that parity is violated in weak decays [21]. This lead to a new version of equation 2.16,

$$\mathcal{L} = \frac{G_F}{\sqrt{2}} \overline{\psi}_{\nu_\mu} \gamma^\mu (1 + \epsilon\gamma_5) \psi_\mu \overline{\psi}_e \gamma_\mu (1 + \epsilon\gamma_5) \psi_{\overline{\nu}_e} + h.c. \tag{2.17}$$

The parity violation comes from the helicity operator $(1 + \epsilon\gamma_5)$ located between the Dirac fields. It was soon clear from experiments that parity and charge conjugation is maximally violated in weak decays and $\epsilon = -1$.[1] This formulation of the weak interaction is known as V-A theory; it was first proposed by Robert Marshak and George Sudarshan [22] and made famous by Richard Feynman and Murray Gell-Mann [23]. The behavior of the helicity operator on the right and left eigenstates is:

$$\begin{aligned} h &= (1 - \gamma_5)/2, \\ h\psi_R &= 0, \quad \text{and} \\ h\psi_L &= \psi_L. \end{aligned} \tag{2.18}$$

Using this definition for the helicity operator the muon decay amplitude is

$$\mathcal{M} = \frac{G_F}{\sqrt{2}} \overline{u}_{\nu_\mu} \gamma^\mu \frac{1 - \gamma_5}{2} u_\mu \overline{u}_e \gamma_\mu \frac{1 - \gamma_5}{2} v_{\overline{\nu}_e}. \tag{2.19}$$

[1] While C and P are maximally violated in weak decays, CP is only slightly violated in certain weak processes.

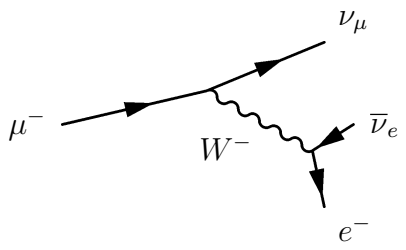

Figure 2.3. Muon Decay with W^- Propagator

The presence of these helicity terms matches what has been observed in experiments [21]. In β^- decay the electrons are left-handed accompanied by a right-handed anti-neutrino. For β^+ decay, the positrons are right-handed accompanied by a left-handed neutrino.

Fermi theory is an effective Lagrangian that can be used to model both muon and nuclear β-decay. However, the Fermi model breaks down at high energy. In particular, the calculated cross-section grows with center of mass energy. A solution to this problem is to introduce a boson propagator. This can be done by replacing the 4-point Fermi interaction vertex with a $W^\pm$ boson propagator as seen in figure 2.3. The resulting amplitude is

$$\mathcal{M} = -\left[\frac{g}{\sqrt{2}}\overline{u}_{\nu_\mu}\gamma_\mu\frac{1-\gamma_5}{2}u_\mu\right]\frac{-g^{\mu\nu}+\frac{q^\mu q^\nu}{M_W^2}}{q^2-M_W^2}\left[\frac{g}{\sqrt{2}}\overline{u}_e\gamma_\mu\frac{1-\gamma_5}{2}v_{\overline{\nu}_e}\right]. \tag{2.20}$$

The addition of the massive propagator boson introduces the $\frac{1}{q^2-M_W^2}$ term in equation 2.20. This term suppresses the cross-section. At low q^2, the coupling is effectively constant, as originally theorized by Fermi [19]. Also, the process no longer violates unitarity at high energies. There is a discontinuity when $q^2 = M_W^2$; however, this is solved by adding a finite width to the $W^\pm$ boson. In the limit $q^2 \ll M_W^2$, the

propagator becomes equivalent to the Fermi constant as seen in equation 2.21.

$$\lim_{\frac{q}{M_W}\to 0} \frac{g^2}{8(q^2 - M_W^2)} = \frac{G_F}{\sqrt{2}} \tag{2.21}$$
$$G_F = \frac{\sqrt{2}g^2}{8M_W^2}$$

The addition of the massive $W^{\pm}$ boson solves some of the problems with Fermi contact theory and provides a natural explanation why the weak nuclear interaction is so much weaker than QED [24]. The gauge group of the weak nuclear interaction is $SU(2)_{\mathrm{L}}$, where the left-handed elements are the $SU(2)$ spinors and the right-handed elements are singlets. The $SU(2)$ group has three generators that correspond to the $W^{\pm}$ and Z bosons. However, a theory with a massive vector boson is not gauge invariant, as seen in section 2.1.1.1, and it can still violate unitarity. These problems will be dealt with in section 2.1.3.

2.1.3 Unification and Spontaneous Electroweak Symmetry Breaking

The unification of the weak interaction with electromagnetism was first proposed by Julian Schwinger in 1957, where the $W^{\pm}$ bosons and photon formed an isotropic triplet of vector bosons [25] and later expanded upon by Glashow [26].[2] Though, there is the problem of the $W^{\pm}$ bosons and photon having markedly different coupling strengths, masses, and interactions. In the early 1960s, models of spontaneous symmetry breaking were presented by Goldstone, Salam, and Weinberg [27]. In these models the symmetry of the Lagrangian is spontaneously broken, which results in the generation of massless Goldstone bosons [28]. In 1964, Higgs [29], Englert and Brout [30], and Guralnik, Hagen, and Kibble [31] presented a mechanism by which the gauge bosons can acquire a mass on the electroweak scale. In 1967, Weinberg [32]

[2]Schwinger originally referred to the $W^{\pm}$ and photon as scalar particles and not vector bosons.

and Salam [33] demonstrated that the Higgs mechanism could break the electroweak symmetry as presented by Glashow. This is now referred to as Glashow-Weinberg-Salam Theory (GWS). In GWS theory, the Higgs mechanism gives mass to the $W^{\pm}$ and Z bosons, the photon remains massless, and a massive scalar field and boson remain, which are now referred to as the Higgs field and Higgs boson. The fermions in GWS theory gain their mass through the addition of a Yukawa coupling to the Higgs field. The following derivation of spontaneous electroweak symmetry breaking and the Higgs mechanism draws from *An Introduction to quantum field theory* [15].

The electroweak sector has three massive gauge bosons and one massless gauge boson. A scalar doublet field ϕ that transforms as a spinor of $SU(2)$ is needed to break the weak sector. Adding an additional $U(1)$ gauge symmetry to the group changes it to $SU(2) \times U(1)$.[3] If the scalar field is assigned a charge of $+\frac{1}{2}$ under the $U(1)$ symmetry then its complete gauge transformation is

$$\phi \rightarrow e^{i\alpha^a \tau^a} e^{\frac{i\beta}{2}} \phi, \tag{2.22}$$

where $\tau^a = \frac{\sigma^a}{2}$ and σ^a are the Pauli matrices. If the ϕ field has a non-zero vacuum expectation value of

$$\langle \phi \rangle = \frac{1}{\sqrt{2}} \begin{pmatrix} 0 \\ \nu \end{pmatrix}, \tag{2.23}$$

it breaks the $SU(2) \times U(1)$ symmetry of the vacuum. $\langle \phi \rangle$ breaks three of the four gauge symmetry generators of $SU(2) \times U(1)$ leaving only one remaining $U(1)$ sym-

[3] Georgi and Glashow [34] proposed a model of electroweak symmetry breaking using just $SU(2)$; however, this creates only massive $W^{\pm}$ bosons, a massless photon, and no Z boson, which had not been observed at the time.

metry,

$$\begin{aligned} \alpha^1 &= 0, \\ \alpha^2 &= 0, \quad \text{and} \\ \alpha^3 &= \beta, \end{aligned} \tag{2.24}$$

which is the gauge symmetry of electromagnetism or $U(1)_{\text{em}}$ [35]. The covariant derivative of ϕ can be written as

$$D_\mu \phi = (\partial_\mu - igW_\mu^a \tau^a - \frac{i}{2} g' B_\mu)\phi. \tag{2.25}$$

In equation 2.25, W_μ^a are the $SU(2)$ gauge bosons and B_μ is the $U(1)$ gauge boson. Because the $SU(2)$ and $U(1)$ gauge groups commute they have different coupling constants of g and g' respectively.

The mass of the vector gauge bosons comes from the square of equation 2.25 evaluated at the vacuum expectation value of the scaler field in equation 2.23. The term that describes the gauge bosons mass is

$$\Delta\mathcal{L} \propto \frac{1}{2} \begin{pmatrix} 0 & \nu \end{pmatrix} \left(gW_\mu^a \tau^a + \frac{1}{2} g' B_\mu \right) \left(gW^{b\mu} \tau^b + \frac{1}{2} g' B^\mu \right) \begin{pmatrix} 0 \\ \nu \end{pmatrix}. \tag{2.26}$$

By substituting $\tau^a = \frac{\sigma^a}{2}$ in equation 2.26 and performing the matrix multiplication, the Lagrangian becomes

$$\Delta\mathcal{L} \propto \frac{1}{2} \frac{\nu^2}{4} \left[g^2 (W_\mu^1)^2 + g^2 (W_\mu^2)^2 + (-gW_\mu^3 + g' B_\mu)^2 \right]. \tag{2.27}$$

From equation 2.27 it can be derived that there are three massive vector fields and

one massless vector field:

$$W_\mu^\pm = \frac{1}{\sqrt{2}}(W_\mu^1 \mp iW_\mu^2), \quad \text{where} \quad m_W = g\frac{\nu}{2}; \tag{2.28}$$
$$Z_\mu = \frac{1}{\sqrt{g^2+g'^2}}(gW_\mu^3 - g'B_\mu), \quad \text{where} \quad m_Z = \sqrt{g^2+g'^2}\frac{\nu}{2}; \text{and}$$
$$A_\mu = \frac{1}{\sqrt{g^2+g'^2}}(g'W_\mu^3 + gB_\mu), \quad \text{where} \quad m_A = 0.$$

Instead of writing the covariant derivative in terms of W_μ^a and B_μ, it is more convenient to express it in terms of the mass eigenstates. The covariant derivative in equation 2.25 can be rewritten so that it interacts with a $U(1)$ field with charge Y and a general $SU(2)$ field with the generators T^a:

$$D_\mu = \partial_\mu - igW_\mu^a T^a - ig'YB_\mu. \tag{2.29}$$

When writing equation 2.27 in terms of the mass eigenstates, the covariant derivative becomes

$$D_\mu = \partial_\mu - i\frac{g}{\sqrt{2}}(W_\mu^+T^+ + W_\mu^-T^-) - \frac{i}{\sqrt{g^2+g'^2}}Z_\mu(g^2T^3 - g'^2Y) - \frac{igg'}{\sqrt{g^2+g'^2}}A_\mu(T^3+Y), \tag{2.30}$$

where $T^\pm = (T^1 \pm iT^2)$. The normalization of $T^\pm$ can be selected such that it agrees with our earlier normalization for the spinor representation of $SU(2)$

$$T^\pm = \frac{1}{2}(\sigma^1 \pm i\sigma^2) = \sigma^\pm. \tag{2.31}$$

The final term in equation 2.30 makes it explicitly clear that the massless vector gauge boson A_μ couples to $T^3 + Y$, which is equivalent to the gauge transformation in equation 2.24. This term is actually the electromagnetic quantum number Q, and

the term preceding A_μ is the coefficient of the electromagnetic interaction:

$$e = \frac{gg'}{\sqrt{g^2 + g'^2}}. \tag{2.32}$$

Equation 2.30 can be furthered compacted by redefining it in terms of the weak mixing angle θ_w. This angle represents the $SU(2)$ rotation from the unbroken gauge fields (W^3, B) to the physical eigenstates (Z, A):

$$\begin{pmatrix} Z \\ A \end{pmatrix} = \begin{pmatrix} \cos\theta_w & -\sin\theta_w \\ \sin\theta_w & \cos\theta_w \end{pmatrix} \begin{pmatrix} W^3 \\ B \end{pmatrix}, \tag{2.33}$$

where

$$\cos\theta_w = \frac{g}{\sqrt{g^2 + g'^2}} \quad \text{and} \quad \sin\theta_w = \frac{g'}{\sqrt{g^2 + g'^2}}. \tag{2.34}$$

The Z coupling can also be rewritten in terms of Q instead of Y

$$g^2 T^3 - g'^2 Y = (g^2 + g'^2)T^3 - g'^2 Q. \tag{2.35}$$

Using the substitutions in equations 2.32 and 2.34, equation 2.30 can be rewritten as

$$D_\mu = \partial_\mu - i\frac{g}{\sqrt{2}}(W_\mu^+ T^+ + W_\mu^- T^-) - \frac{ig}{\cos\theta_w} Z_\mu (T_3 - \sin^2\theta_w Q) - ieA_\mu Q, \tag{2.36}$$

where

$$g = \frac{e}{\sin\theta_w} \tag{2.37}$$

and the mass given in equation 2.28 can be expressed as

$$m_W = m_Z \cos\theta_w. \tag{2.38}$$

By evaluating the unbroken electroweak Lagrangian at the vacuum expectation value of the Higgs field, the $SU(2) \times U(1)$ symmetry is broken and the massless vector gauge bosons of equation 2.25 gain mass terms, as seen in equation 2.27. After expressing the covariant derivative in terms of the new massive gauge bosons and some simplification of the couplings, the new mass bosons and tree level interactions can be entirely described with the quantities e, m_W, and θ_w [15].

It should be noted that the $W^{\pm}$ bosons only couple to left-handed fermions. This is done by separating the Dirac field into right and left-handed components:

$$\overline{\psi} i \not{\partial} \psi = \overline{\psi}_L i \not{\partial} \psi_L + \overline{\psi}_R i \not{\partial} \psi_R. \tag{2.39}$$

Each component of the Dirac field has its own covariant derivatives and couplings. When a Dirac field couples to a gauge boson, the ψ_L and ψ_R are assigned to different representations of that boson's gauge group. In the case of electroweak theory, the left-handed fermion fields are doublets of $SU(2)$, commonly called $SU(2)_{\mathrm{L}}$, and the right-handed fermion fields are singlets. The Y value assigned to each fermion must take into account the T^3 value of the fermion field. For right-handed fields $T^3 = 0$; therefore, $Y_{u_R} = +\frac{2}{3}$, $Y_{d_R} = -\frac{1}{3}$, and $Y_{e_R^-} = -1$. However, for the left-handed fermion fields,

$$E_L = \begin{pmatrix} \nu_e \\ e^- \end{pmatrix}_L \quad \text{and} \quad Q_L = \begin{pmatrix} u \\ d \end{pmatrix}_L \tag{2.40}$$

$T^3 = \pm\frac{1}{2}$; so, $Y = -\frac{1}{2}$ for the lepton doublet and $Y = +\frac{1}{6}$ for the quark doublet. This produces fermions with the correct electromagnetic charge and correct couplings to the weak sector.

It should be noted that masses cannot be easily added to the fermions. If the

masses are added to the Lagrangian in the simplest way,

$$\Delta\mathcal{L} \propto -m_e(\overline{e}_L e_R + \overline{e}_R e_L), \tag{2.41}$$

it breaks gauge invariance because e_L and e_R are in different $SU(2)$ groups and have different $U(1)$ charges. This means that the mass has to be added to the fermion sector in a more clever way. It is possible to couple the right-handed and left-handed fermions and quarks through the scalar Higgs doublet, ϕ. The coupling between e_L, e_R, and ϕ can be expressed as

$$\Delta\mathcal{L}_e \propto -\lambda_e \overline{E}_L \cdot \phi e_R + h.c. \tag{2.42}$$

λ_e is a coupling constant between the left-handed lepton doublet, the right-handed lepton singlet, and the Higgs field. When E_L and ϕ are contracted, ϕ is evaluated at the vacuum expectation value of the Higgs field and the Lagrangian becomes

$$\Delta\mathcal{L}_e \propto -\frac{1}{\sqrt{2}}\lambda_e \nu \overline{e}_L e_R + h.c. + \ldots. \tag{2.43}$$

The electron gains the mass term of

$$m_e = \frac{1}{\sqrt{2}}\lambda_e \nu. \tag{2.44}$$

The value of λ_e is an input to the theory and must be measured experimentally. This is unfortunately true for all fermions that gain mass via Yukawa couplings to the Higgs field. In a similar way, masses can be added to the quark sector:

$$\Delta\mathcal{L}_q \propto -\lambda_d \overline{Q}_L \cdot \phi d_R - \lambda_u \epsilon^{ab} \overline{Q}_{La} \phi_b^\dagger u_R + h.c. \tag{2.45}$$

Using the same method of contracting the fermion doublet and the Higgs field, the

up and down quarks obtain masses;

$$\Delta\mathcal{L}_q \propto -\frac{1}{\sqrt{2}}\lambda_d \nu \overline{d}_L d_R - \frac{1}{\sqrt{2}}\lambda_u \nu \overline{u}_L u_R + h.c. + \ldots. \tag{2.46}$$

The mass terms for the quarks are

$$m_d = \frac{1}{\sqrt{2}}\lambda_d \nu \quad \text{and} \quad m_u = \frac{1}{\sqrt{2}}\lambda_u \nu. \tag{2.47}$$

This is easily expanded to include three generations of quarks and equation 2.45 becomes

$$\Delta\mathcal{L}_q \propto -\lambda_d^{ij}\overline{Q}_L^i \cdot \phi d_R^j - \lambda_u^{ij}\epsilon^{ab}\overline{Q}_{La}^i \phi_b^\dagger u_R^j + h.c., \tag{2.48}$$

where

$$u_L^i = (u_L, c_L, t_L) \quad \text{and} \quad d_L^i = (d_L, s_L, b_L) \tag{2.49}$$

represent the up and down type quarks in their weak eigenstates. The quark basis can then be rotated to the mass eigenstates. This can be represented as

$$u_L'^i = U_u^{ij} u_L^j \quad \text{and} \quad d_L'^i = U_d^{ij} d_L^j. \tag{2.50}$$

Using the diagonalized quark basis, the weak current becomes

$$J_W^{\mu+} = \frac{1}{\sqrt{2}}\overline{u}_L^i \gamma^\mu d_L^i = \frac{1}{\sqrt{2}}\overline{u}_L'^i \gamma^\mu (U_u^\dagger U_d) d_L'^i, \tag{2.51}$$

which can be rewritten as

$$J_W^{\mu+} = \frac{1}{\sqrt{2}}\overline{u}_L'^i \gamma^\mu V_{ij} d_L'^i, \tag{2.52}$$

where V_{ij} is the Cabibbo-Kobayashi-Maskawa (CKM) matrix. This is a unitary matrix that describes the allowed weak transitions. The diagonal terms describe quark transitions within the same generation, and the off diagonal terms describe

quark transitions between generations. The CKM matrix is an input to the theory and must be measured experimentally [15].

2.1.4 The Higgs Boson

There is another additional observable in GWS theory. The scalar field can be reparametrized in the unitary gauge as follows:

$$\phi(x) = U(x)\sqrt{\frac{1}{2}}\begin{pmatrix} 0 \\ \nu + h(x) \end{pmatrix}. \tag{2.53}$$

The lower component of the $SU(2)$ spinor has a real value that is dependent on the vacuum expectation value of $\phi(x)$ and field $h(x)$ where $\langle h(x)\rangle = 0$. The general $SU(2)$ gauge transformation, $U(x)$, produces a complex spinor with two degrees of freedom. However, $U(x)$ can be removed with a gauge transformation leaving one remaining degree of freedom. The Lagrangian for the Higgs potential can be written as

$$\mathcal{L} = |D_\mu \phi|^2 + \mu^2 \phi^\dagger \phi - \lambda(\phi^\dagger \phi)^2. \tag{2.54}$$

The minimum of the Higgs potential can be found by evaluating equation 2.54 at the vacuum expectation value of $\langle\phi\rangle$,

$$\nu = \left(\frac{\mu^2}{\lambda}\right)^{\frac{1}{2}}. \tag{2.55}$$

The Lagrangian in equation 2.54 can be expressed with respect to the vacuum expectation value of the Lagrangian, or its unitary gauge, as

$$\begin{aligned} \mathcal{L}_V &= -\mu^2 h^2 - \lambda\nu h^3 - \frac{1}{4}\lambda h^4 \\ &= -\frac{1}{2}m_h^2 h^2 - \sqrt{\frac{\lambda}{2}}m_h h^3 - \frac{1}{4}\lambda h^4, \end{aligned} \tag{2.56}$$

where the quantum field of $h(x)$ is a scalar particle with mass

$$m_h = \sqrt{2}\mu = \sqrt{2\lambda}\nu. \tag{2.57}$$

This is the aforementioned Higgs boson. In equation 2.57, λ is the self coupling of the Higgs, as determined by measuring the Higgs mass. Expanding the kinetic term of equation 2.54 reveals the coupling of the Higgs to the massive electroweak gauge bosons, similar to what was seen in equation 2.27:

$$\mathcal{L}_K = \frac{1}{2}(\partial_\mu h)^2 + \left[m_W^2 W^{\mu+} W_\mu^- + \frac{1}{2} m_Z^2 Z^\mu Z_\mu\right] \cdot \left(1 + \frac{h}{\nu}\right)^2. \tag{2.58}$$

In equation 2.58, it can be seen that the coupling between the massive vector bosons and the Higgs is dependent on the mass of the vector bosons squared. In the fermion sector, the coupling is linearly dependent on the mass. This can be observed by shifting equation 2.43 to the unitary gauge. Doing this results in the following Lagrangian:

$$\mathcal{L} = -m_f \overline{f} f \left(1 + \frac{h}{\nu}\right), \tag{2.59}$$

where f and $\overline{f}$ are the right-handed and left-handed fermions. In conclusion, if the weak gauge bosons gain their mass via the GWS model, then there should be observable evidence from the presence of a single massive scalar boson. Additionally, it is also possible for the fermion sector to gain mass through Yukawa couplings to the same massive scalar field [15].

2.1.5 Quantum Chromodynamics

The theory of Quantum Chromodynamics (QCD) will only be covered tersely because, while it is a well developed and accurate theory describing the strong nuclear interaction, it only presents itself as a background in the $H \to \gamma\gamma$ analysis. The

first model of the strong nuclear interaction was proposed by Yukawa [36]. In 1935, Yukawa hypothesized that there is an intermediate scalar particle that is exchanged between the neutron and proton at about 200 times the mass of the electron. At the time there was no known particle that fit this description. After some confusion concerning the muon, the pion was first observed in 1947 by Lattes, Occhialini, and Powell [37, 38]. However, in the 1950s, the discovery of additional mesons (ρ, η, Kaon, and ϕ) led to the conclusion that the strong interaction was more complicated than the exchange of a single pseudoscalar. In addition to the new mesons being discovered there were baryons that had not perviously been observed. In 1961, Gell-Mann [39] and Ne'eman [40] independently proposed the Eightfold Way. The Eightfold Way organized the baryons and mesons by their quantum numbers (charge and strangeness). Then in 1964, Gell-Mann [41] and Zweig [42] independently theorized that all hadrons were composed of constituent particles called quarks, or aces, that came in three flavors. In 1965, Moo-Young Han with Yoichiro Nambu [43] and Oscar W. Greenberg [44] theorized that quarks contain an additional degree of freedom called color. Without color, baryons where all the constitute quarks have the same flavor and spin, like the Δ^{++}, Δ^{-}, and Ω^{-}, would violate the Pauli exclusion principle. Quark color is an $SU(3)$ gauge symmetry similar to the $U(1)$ symmetry of electromagnetism. The QCD Lagrangian is

$$\mathcal{L}_{QCD} = i\sum_q \overline{\psi}_q^i \gamma^\mu (D_\mu)_{ij} \psi_q^j - \sum_q m_q \overline{\psi}_q^i \psi_{qi} - \frac{1}{4} F_{\mu\nu}^a F^{\mu\nu a}, \tag{2.60}$$

where

$$D_\mu = \partial_\mu - i g_s A_\mu^\alpha \lambda_\alpha. \tag{2.61}$$

A_μ^α represent the eight gluons fields from the generators of the $SU(3)$ group and λ_α are the Gell-Mann matrices. The first term is the coupling between all the quarks and gluons, and it describes the dynamics of the quarks. The second term represents

the massive quarks. The final term describes the dynamical properties of the gluon. The gluon field tensor is

$$F^a_{\mu\nu} = \partial_\mu A^a_\nu - \partial_\nu A^a_\mu - g_s f^{abc} A^b_\mu A^c_\nu. \tag{2.62}$$

It should be noted that unlike electromagnetism, QCD is a non-abelian gauge theory. This can be seen from the final term of equation 2.62, which is the gluon self interaction [24]. The gluon self-interaction causes the strength of the strong interaction and leads directly to asymptotic freedom and confinement.

Asymptotic freedom and confinement are two very important facets of QCD, and they are two sides of the same coin. Asymptotic freedom was first theorized by Gross, Wilczek [45–47], and Politzer [48]. At low energy or large distance, the strength of the strong interaction, α_s, is larger than one. This makes the traditional perturbative approach to field theory impossible because the infinite series of Feynman diagrams does not converge. However, the coupling strength of QCD decreases at high energies such that once the energy of the interaction is above some cut off scale, Λ_{QCD}, the theory is asymptotically free and the traditional perturbation theory effectively models the strong interaction. Another effect of the strong interaction is confinement. Due to the strength of QCD, free quarks are never observed in nature. This is because the energy needed to remove a free quark from a bound state is more than the energy to create a quark anti-quark pair from the vacuum [49]. This result can be seen in lattice QCD calculations, but has yet to be described analytically [50, 51].

Evidence of quarks was first observed at the Stanford Linear Accelerator Center (SLAC) in 1969 [52, 53]. At the time, there was some debate over what was observed. Bjorken and Paschos developed a model for electron-proton deep inelastic scattering.

They predicted that the inelastic structure of the proton would vanish at high q^2.[4] [54] This phenomenon is referred to as Bjorken scaling. Feynman also produced a theory for deep inelastic scattering, where the individual components of the proton were partons [55]. At low energies, particles scattered from the valence partons and at high energy they scattered from the sea partons. The observation of the Callan-Gross relation showed that the partons within the proton were in fact fermions [56], giving credence to the quark model. The parton model is still used today to described the constituents of the proton.

The end result of QCD in a hadron collider is that many measurements are influenced by a QCD background. This is because QCD interactions, which have a cross-section $\mathcal{O}(10^6)$ times larger than electroweak interactions, create unstable mesons and baryons that quickly decay into a cascade of particles that form an object referred to as a jet. Jets and real photons from QCD interactions are the primary background for the $H \to \gamma\gamma$ analysis.

2.2 Higgs Production and Decay Modes

There have been many searches for the Higgs boson since it was first theorized in the mid-1960s. The most recent searches (excluding the LHC) are the results produced by the Large Electron-Positron Collider (LEP), which was located at CERN in the underground tunnel that today hosts the LHC, and the Tevatron located at Fermi National Accelerator Laboratory (FNAL). In the next two sections the production of the Higgs at the LHC and its detection at the Compact Muon Solenoid (CMS) will be discussed and compared to both the Tevatron and LEP results.

---

[4] At low energy, the electron scatters off the proton as if it were a point object, but at high energy the electron scatters from a individual quark. At intermediate energies the electron interacts with the complex structure of the proton producing a complicated inelastic structure before Bjorken scaling smoothes out the distribution.

2.2.1 Higgs Production Mechanisms

The higher center of mass energy of the LHC increases the total cross-section of the Higgs, as seen in figure 2.4. This is a large advantage over previous colliders that operated at lower energies. LHC can directly produce a Higgs through gluon fusion and is not dependent on associated production as LEP was.

At LEP, the center of mass energy of the electron-positron collisions was varied in order to produce many different final states. Its most famous studies resulted in the production of a large number of Z [58], WW [59], and ZZ events [59]. The primary Higgs production channel at LEP was the associated Z channel. LEP was unable to search for the Higgs directly, because of the small Yukawa coupling of the electron to the Higgs, $\lambda_e = \frac{\sqrt{2}m_e}{\nu}$. Since the final state contains both a Higgs and a Z boson, the center of mass energy of the collider needs to be equal to the mass of the Z and Higgs boson combined. The final results for the Higgs search at LEP will be presented in section 2.3.1.

At the Tevatron, protons and anti-protons were collided at a center of mass energy of 1.96 TeV. The Tevatron was capable of producing the Higgs directly and in associated production with the $W^{\pm}$ and Z boson [60]. The Tevatron had an integrated luminosity target of 15 fb^{-1} for 2008 [61]; however, by the end of its operation on September 30^{th}, 2011 only 10 fb^{-1} of data had been recorded. The primary reason for the deficiency was the inability to reach the target bunch spacing 132 ns [62], and the Tevatron only operated with a bunch spacing of 396 ns [63]. The final limits of the Higgs search at the Tevatron will be shown in section 2.3.2.

At the LHC, there are four production channels for the Higgs boson: gluon fusions, vector boson fusion, associated vector boson production, and associated top production. The primary production mechanism for the Higgs boson is gluon fusion through a fermion loop. At 7 and 8 TeV the parton distribution function (PDF) of the proton is dominated by gluons as seen in figure 2.5. Specifically, the probability

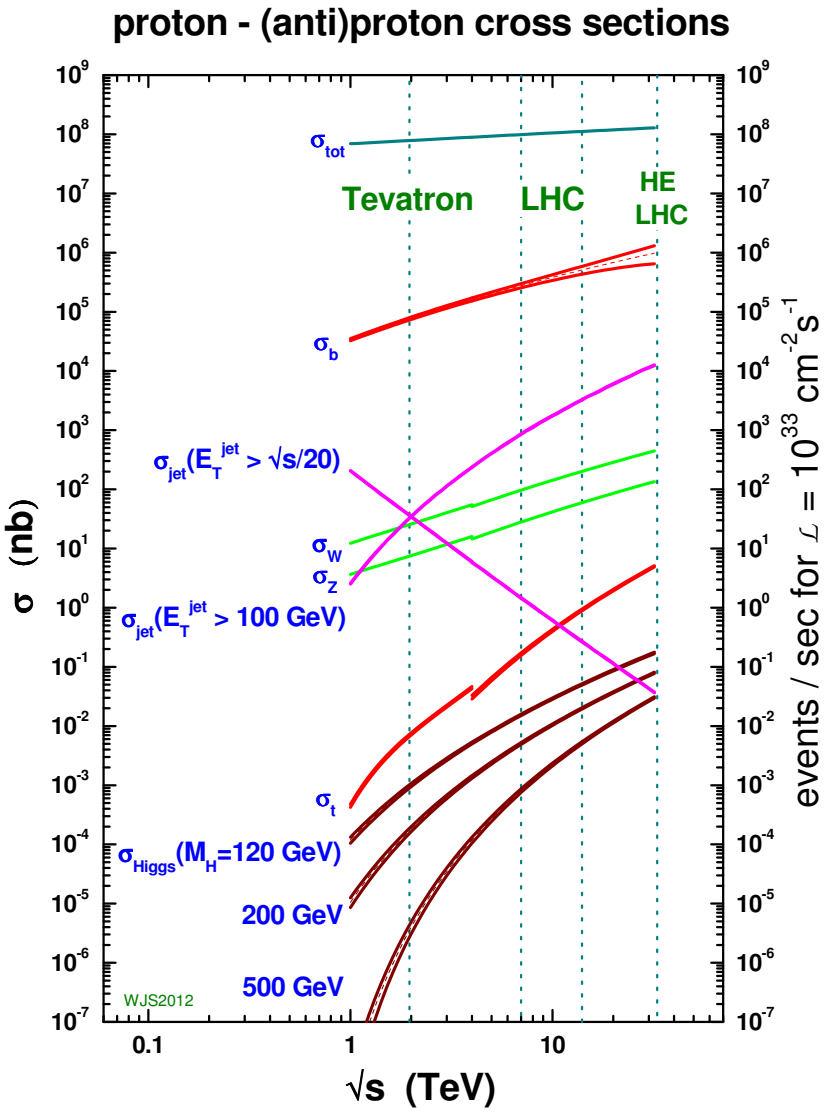

Figure 2.4. Cross-sections of high energy physics processes [57].

density of gluons is much higher than any other parton in the region where x is large enough to produce a Higgs boson [64]. The gluon-gluon fusion process has the largest Higgs production cross-section, and it produces a single Higgs boson without additional objects in the final state. Gluons are massless, and the Higgs does not possess color charge; so the gluons interact through a virtual fermion loop (mostly t quarks) that then couples to the Higgs as seen in figure 2.6a. The secondary production mechanism for the Higgs boson at the LHC is vector boson fusion (VBF). In a VBF event two incoming valance quarks emit a pair of either Z or $W^{\pm}$ bosons that fuse to a Higgs boson as seen in figure 2.6b. This process produces a Higgs boson and two far forward jets. The tertiary production mechanism is the Higgs associated with a $W^{\pm}$ or Z boson as illustrated in figure 2.6c, which was the primary production channel at LEP. The quaternary production channel is the Higgs produced in association with two top quarks. In these events, two pairs of top quarks are produced and one pair fuses to produce a Higgs as demonstrated in figure 2.6d. These four channels represent the Higgs production channels with the highest cross-sections at the LHC, which can be seen in figure 2.7 at 7 and 8 TeV [65]. Later, the analysis will take advantage of these different final states in order to maximize the sensitivity of the analysis.

2.2.2 Higgs Branching Ratios

The branching ratios and allowed decay products of the Higgs are heavily dependent on the mass of the Higgs boson. For the sake of simplicity, the mass regions can be split into two regions, below and above 160 GeV. At 160 GeV, the width of the Higgs substantially increases due to its coupling to $W^{\pm}$ bosons, as seen in figure 2.8a. Once the width of the Higgs becomes large, searching for it in the diphoton channel becomes exceedingly difficult. However, below 160 GeV, the decay products of the Higgs become more varied. In this region the Higgs still couples to off-shell $W^{\pm}$

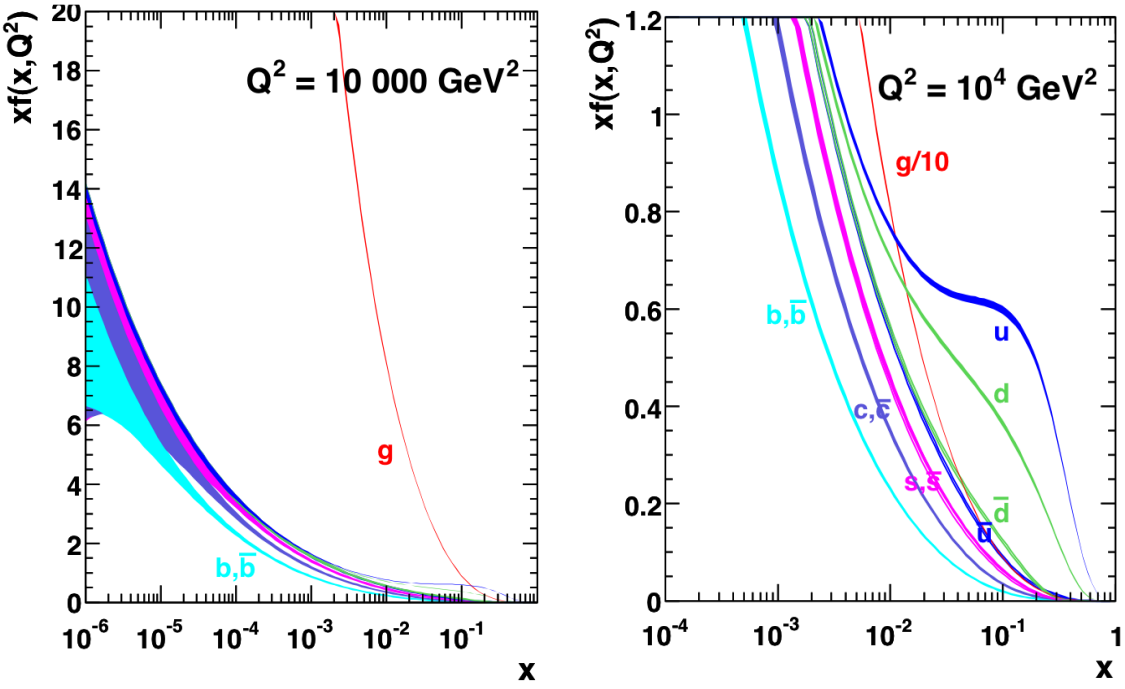

Figure 2.5. Parton distribution function of a proton at 10^4 GeV [66].

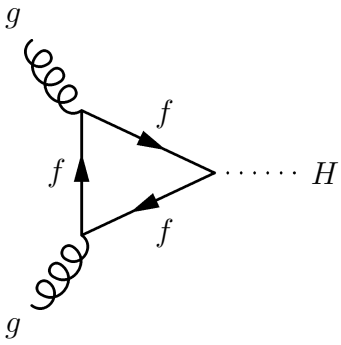

(a) Two gluons fusing to a Higgs boson via a fermion loop.

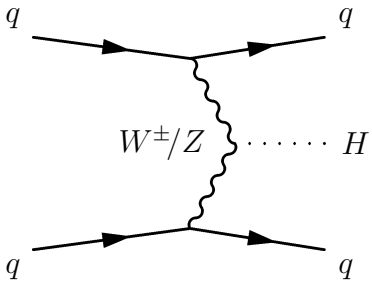

(b) Higgs boson produced through vector boson fusion.

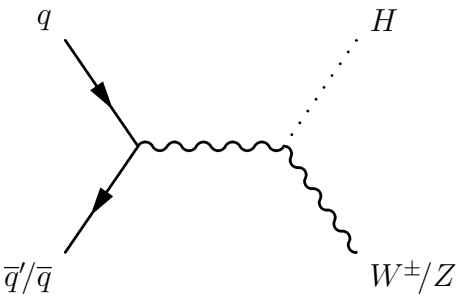

(c) A $W^{\pm}$ or Z boson emits a Higgs boson via Higgs-strahlung.

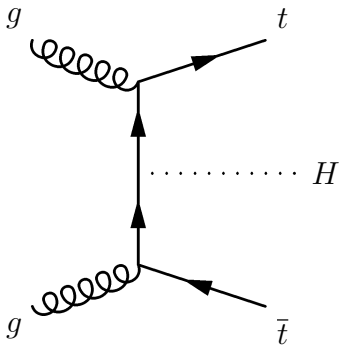

(d) A Higgs boson is produced in association with a pair of t quarks.

Figure 2.6. Primary Higgs Production Mechanisms at the LHC

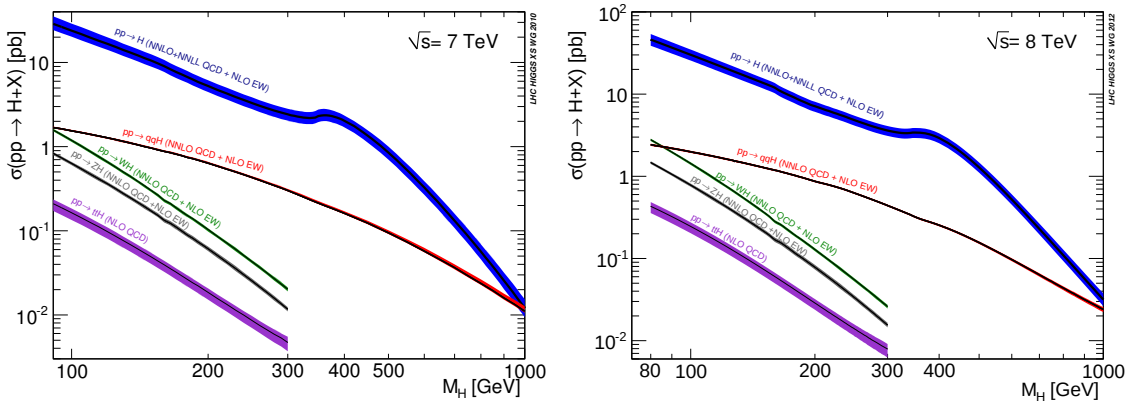

Figure 2.7. Higgs Production Cross-Sections at 7 and 8 TeV

and Z bosons; however, the total width significantly decreases. Because the Higgs coupling is dependent on mass, it preferentially decays to heavier particles as can be seen in figure 2.8b. At low mass, the Higgs decays primarily to $b\bar{b}$ pairs because the b quark is the heaviest particle that is less than half the Higgs mass. The Higgs decays to $\tau\overline{\tau}$ pairs and then to $c\bar{c}$ pairs at lower rates due to their lower masses. The Higgs also decays to gg, $\gamma\gamma$, and $Z\gamma$ through loops, which naturally suppresses their branching ratios [65]. Looking at the $H \to \gamma\gamma$ branching ratio, it does not appear to be a very powerful search channel due to its low branching ratio. However, in the mass range of 110 to 150 GeV it is a very powerful channel because of the narrow width of the Higgs before the W^+W^- turn on. The other final states; $b\bar{b}$, gg, $\tau\overline{\tau}$, $c\bar{c}$, and WW cannot take advantage of the narrow width of the Higgs. $b\bar{b}$, gg, $\tau\overline{\tau}$, and $c\bar{c}$ all form jets that have poor energy resolution that smears out the mass peak. The WW and $\tau\tau$ channels have two neutrinos, which cannot be detected by CMS, and this also results in a low resolution mass peak. So the only channels that are fully reconstructible are ZZ, $Z\gamma$, and $\gamma\gamma$. For the channels that contain Z bosons there is another caveat; in order to reconstruct the Z boson, without significant loss in energy resolution, it has to decay to muons or electrons. However, the branching ratio for $Z \to ee$ and $Z \to \mu\mu$ is 6.729% [67]. This decreases the total cross-section $\times$ branching ratio of $H \to ZZ$ and $H \to Z\gamma$ below that of $\gamma\gamma$. So, what initially seemed like an obscure and difficult channel becomes one of the most promising channels for finding the Higgs.

Since the Higgs is electromagnetically neutral and photons are massless, the Higgs does not decay directly to photons at tree level. Instead, the Higgs decays to photons through loops with particles that have mass and electromagnetic charge. The Higgs primarily decays to two photons through $W^{\pm}$ boson loops as seen in figures 2.9a and 2.9b. However, the Higgs can decay to two photons through a fermion loop as seen in figure 2.9c. This process has the opposite sign of the $W^{\pm}$ loop production,

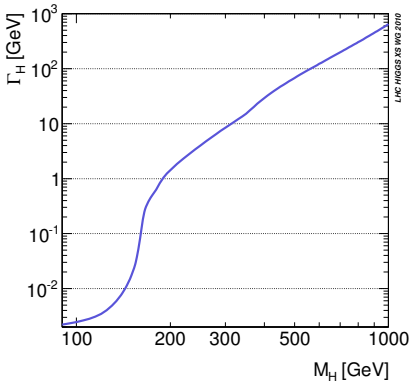

(a) Total width of the Higgs boson as a function of mass.

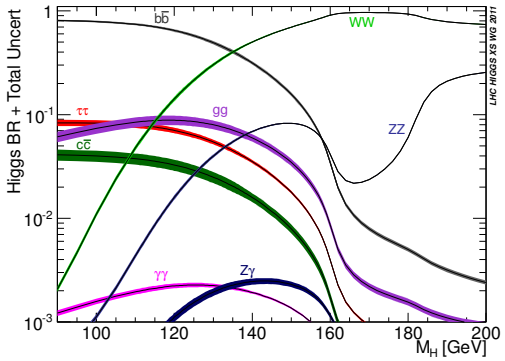

(b) Per channel branching ratio of the Higgs boson as a function of mass.

Figure 2.8. Higgs Properties

so it actually suppresses the cross-section. The end result of either of these decays is two isolated photons, which will be the primary event signature that the analysis will search for.

2.2.3 Background Processes

Since the analysis will search for events with two isolated photons, there will be a fairly large background from QCD and a smaller background from $Z/\gamma^* \to ee$ decays. QCD can produce several event topologies that look like a $H \to \gamma\gamma$ event. The most prominent background is QCD producing two real photons through the Born and Box diagrams in figures 2.10a and 2.10b, respectively. QCD can also produce one real photon and one or two jets that fake the photon signature. The $Z/\gamma^* \to ee$ events produce two real electrons that shower in the ECAL and this can fake a photon if the electron tracks are not reconstructed properly. While all of these process have production cross-sections that are much larger than the Higgs, they are all smooth, continuous backgrounds that fall off with invariant mass; whereas, a low mass Higgs will form a sharp resonance in the distribution.

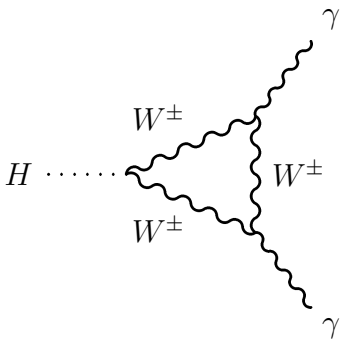

(a) Higgs decaying to two photons through a $W^{\pm}$ loop.

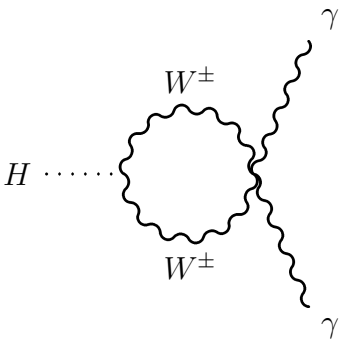

(b) Higgs decaying to two photons through a $W^{\pm}$ loop.

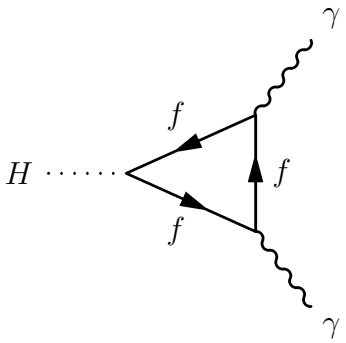

(c) Higgs decaying to two photons through a fermion loop.

Figure 2.9. $H \to \gamma\gamma$ Decay Channels

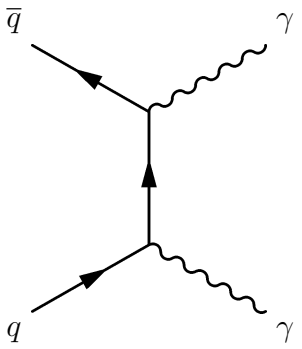

(a) Two photons produced from the Born process.

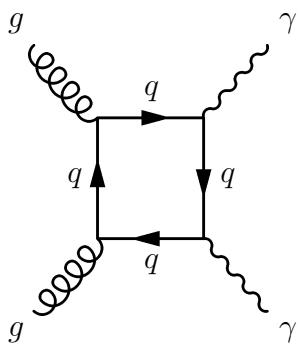

(b) Two photons produced from two gluons via a quark loop.

Figure 2.10. $H \to \gamma\gamma$ Background Channels

2.3 Previous Higgs Searches

There have been many searches for various Higgs bosons since its inception, but for purposes of brevity only the most recent searches for the standard model Higgs boson at LEP and the Tevatron will be covered. The reason for focusing on these two experiments is because they represent the frontier of Higgs searches before the results presented by the LHC.

2.3.1 The Large Electron-Positron Collider

As mentioned in section 2.2.1, LEP provided a significant contribution to the understanding and measurement of the electroweak sector. However, one thing missing from the LEP measurements was the observation of the Higgs boson. LEP searched for the standard model Higgs in association with a Z boson. Unfortunately, the maximum energy of LEP was 104.5 GeV per beam [68], which limited the search of the Higgs to 114.4 GeV/c^2. Though it is unfair to summarize the LEP experiment in one plot, the final limits of the Higgs search can be seen in figure 2.11. The yellow band is the exclusion as measured by LEP, and the black line is the best-fit Higgs

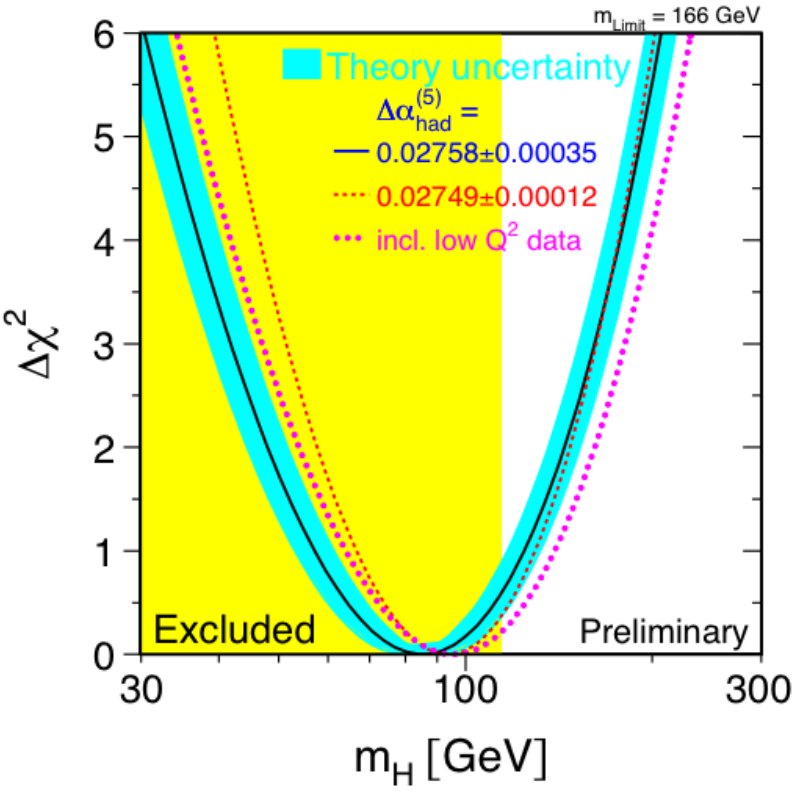

Figure 2.11. Final Limits of the Higgs Search at LEP

mass from precision electroweak measurements with the uncertainty represented by the blue band.

2.3.2 The Tevatron

The Tevatron also has a prestigious history of physics discovery. CDF and DØ first observed the top quark in 1995 [69, 70] and they also produced the most accurate measurement of the $W^{\pm}$ mass [71, 72]. Throughout its experimental lifetime, the Tevatron searched for the Higgs boson. However, the Tevatron did not produce enough data to completely exclude or verify the existence of the Higgs boson. The most stringent limits set by the Tevatron can be seen in figure 2.12 and the associated significance can be seen in figure 2.13. It is clear from figure 2.13 that the combined

significance of the excess is just below the 3σ threshold for evidence, and it is over a large mass range. The best-fit cross-section can be seen in figure 2.14; there is a broad excess that is consistent with the standard model [60].

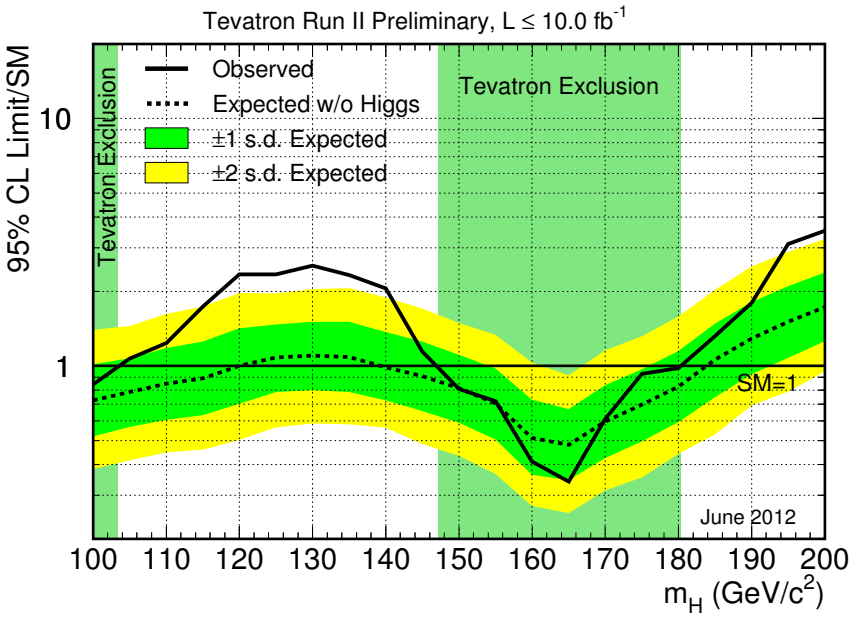

Figure 2.12. Bayesian limits from 10 fb^{-1} of $p\overline{p}$ collisions collected at $\sqrt{s} = 1.96$ TeV.

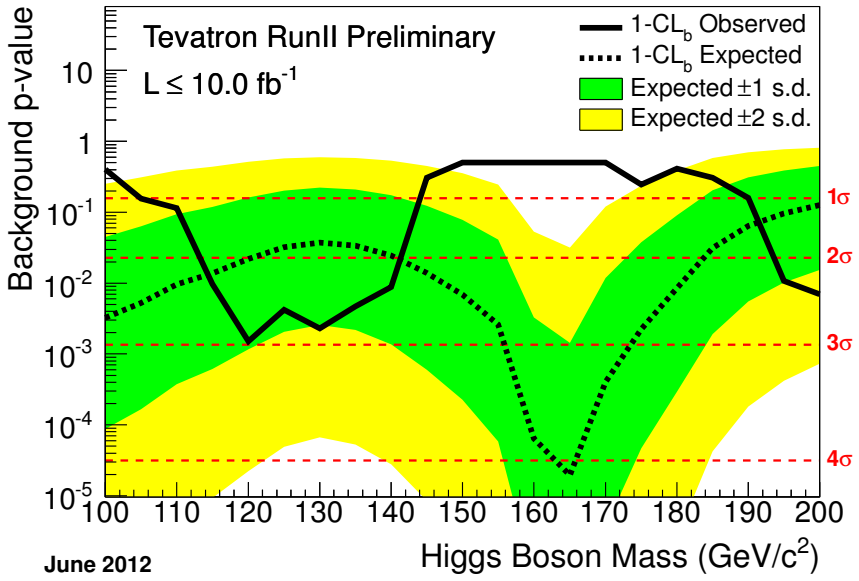

Figure 2.13. Observed p-values from 10 fb^{-1} of $p\bar{p}$ collisions collected at $\sqrt{s} = 1.96$ TeV.

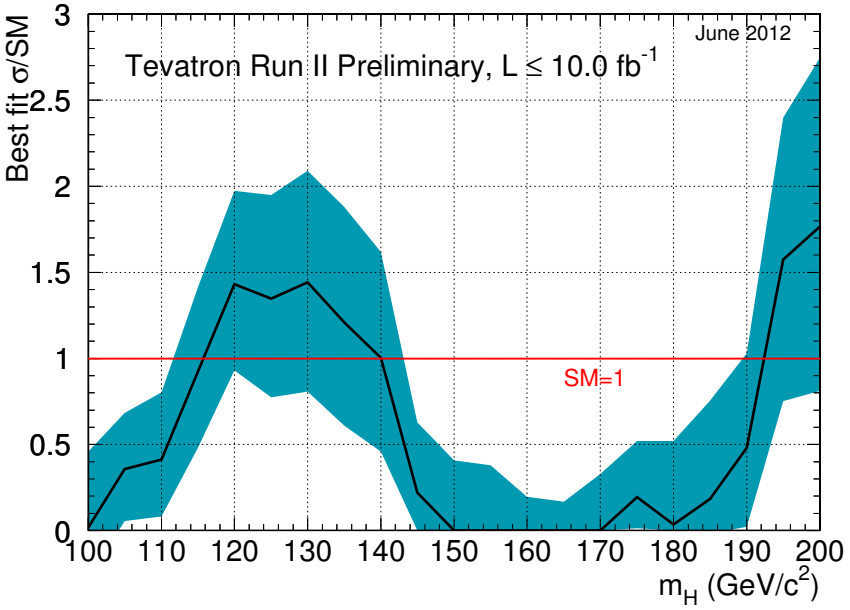

Figure 2.14. Best-fit cross-section from 10 fb^{-1} of $p\bar{p}$ collisions collected at $\sqrt{s} = 1.96$ TeV.

CHAPTER 3

THE DETECTOR AND EXPERIMENTAL APPARATUS

CERN is an international research laboratory with participation from 20 member and 7 observer states, including the United States. The LHC is located in Geneva, Switzerland and straddles the Swiss-French border. It is a significant investment from both the scientific and international community, and has a long record of discoveries in particle physics. CERN's largest experiment is the LHC, which has four primary detectors that lay along the collider ring. There are two general purpose detectors, A Toroidal LHC Apparatus (ATLAS), the larger of the two general purpose detectors, is located at P1 just outside the town of Meyrin, Switzerland. The other general purpose detector is the Compact Muon Solenoid (CMS) that is located on the other side of the ring LHC at P5, outside the town of Cessy, France. Large Hadron Collider beauty (LHCb) is a b-physics experiment located at P8 between the towns of Meyrin and Ferney-Voltaire. There is also an experiment focused on heavy ion collisions called A Large Ion Collider Experiment (ALICE) located at P2 in the town of Saint-Genis-Pouilly, France. Additionally, there are three smaller experiments that perform measurements at the LHC. Two experiments focus on far forward physics, Total Elastic and diffractive cross section Measurement (TOTEM) and the Large Hadron Collider forward (LHCf), that run in conjunction with CMS and ATLAS, respectively [73]. The final detector is dedicated to a monopole search named Monopole and Exotics Detector At the LHC (MoEDAL), which is located with LHCb [74]. These seven detectors perform all the measurements at the LHC and represent the frontier of collider based particle physics. Many of the following

sections and figures are from *The CMS experiment at the CERN LHC* [73].

3.1 The Large Hadron Collider

The Large Hadron Collider is a 26.7 km (16.6 mile) long proton-proton collider straddling the French-Swiss boarder outside of Genève, Switzerland. It was constructed in the old LEP tunnel, which is anywhere between 45 m to 170 m underground. The LHC is a double ring collider that was designed to collide particles at a center of mass energy of 14 TeV. However, due to a small problem in the splices between the superconducing magnets, it only ran at a center of mass energy of 7 TeV in 2010 and 2011 and 8 TeV in 2012. At the LHC, the colliding particles have the same charge, so two beam pipes are needed to house magnetic fields that point in opposite directions. The LHC was designed for a maximum instantaneous luminosity of 10^{34} $\text{cm}^{-2}\text{s}^{-1}$ for proton-proton collisions and 10^{27} $\text{cm}^{-2}\text{s}^{-1}$ for heavy ion collisions. It was designed to hold a total of 2,808 bunches with a spacing of 25 ns [73]. The LHC has had three major run periods so far: 2010, 2011, and 2012. The 2010 run period was a low luminosity run at 7 TeV and 44.2 pb^{-1} were delivered by the LHC. The 2011 run was a much higher luminosity run period where 6.1 fb^{-1} of luminosity was acquired. And 2012 was the most successful run period where 23.3 fb^{-1} was delivered at 8 TeV [75].

The LHC is dependent on a large accelerator complex, which first began operation in 1958. The LHC is the final storage ring after a long series of accelerators. A full schematic of the LHC accelerator complex can be seen in figure 3.1. The protons intended for the LHC originate in a tank of hydrogen gas that is ionized by a Duoplasmatron source. They are passed to a 4-vane Radio Frequency Quadruple that accelerates particles from 92 keV to 750 keV. The beam is then passed to the Alvarez Proton Linac, or Linac 2, which accelerates it to 50 MeV. Next, the protons travel to the Proton Synchrotron Booster that accelerates them to 1.4 GeV. The beam is then

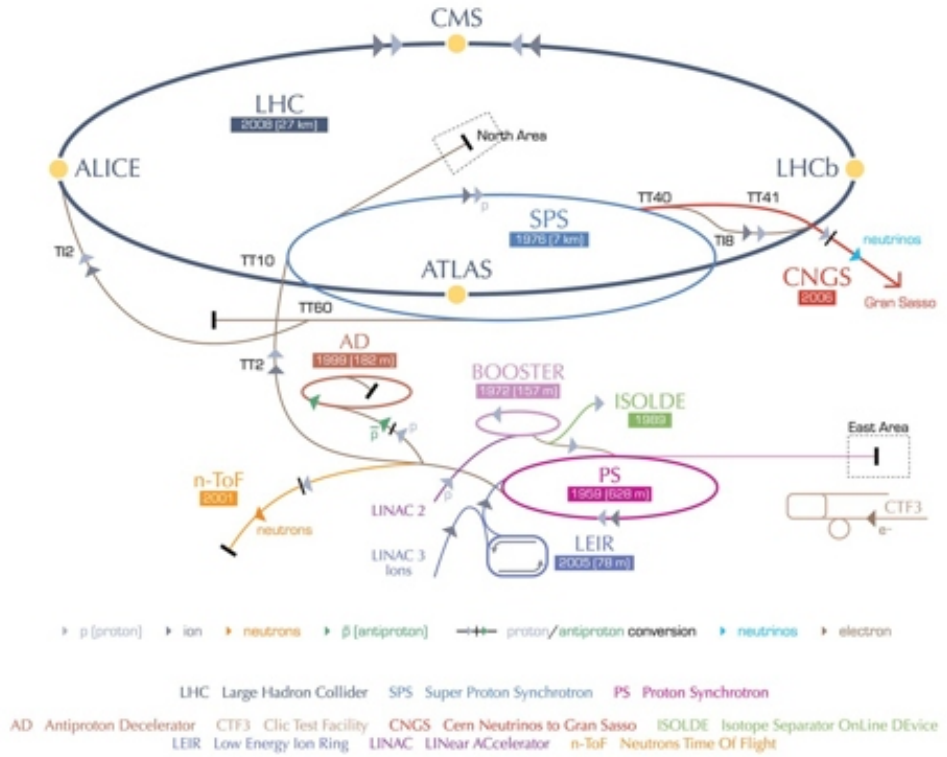

Figure 3.1. Schematic of the CERN accelerator complex [77].

fed to the Proton Synchrotron (PS), which accelerates the protons to 28 GeV and groups the protons into 81 bunches with a bunch spacing of 25 ns. The bunches from the PS are fed into the Super Proton Synchrotron that accelerates them to 450 GeV. The bunches are then finally passed to the LHC where they are accelerated to 4 TeV per beam [76]. This complicated process results in the highest energy accelerator on earth. Figure 2.4 demonstrates that high energy is needed to produce more exotic physical processes.

The LHC superconducting magnetic system is an incredibly powerful and delicate arrangement that controls the immensely powerful beams and is the quintessential ingredient for the LHC's success. The primary purpose of the LHC magnet system is

to steer and focus the beams. The magnets are made of NbTi superconducting wire cooled by superfluid helium at 1.9 K. Keeping the helium at superfluid temperatures significantly improves the temperature margins for the magnets and heat transfer within the fluid itself. The combination of superconducting cables and superfluid helium allows the magnets to operate with a nominal field of 8.33 T for a 7 TeV beam. The LHC ring has 1,232 dipole magnets used for steering and about 3,800 single aperture and 1,000 double aperture magnets used for orbital corrections. A diagram of an LHC dipole and a quadruple magnet can be seen in figures 3.2a and 3.2b, respectively. The LHC magnet system is capable of storing approximately 600 MJ of electromagnetic energy. The LHC magnets control the proton beams that contains a total energy of 135 MJ and a current of 0.584 A.

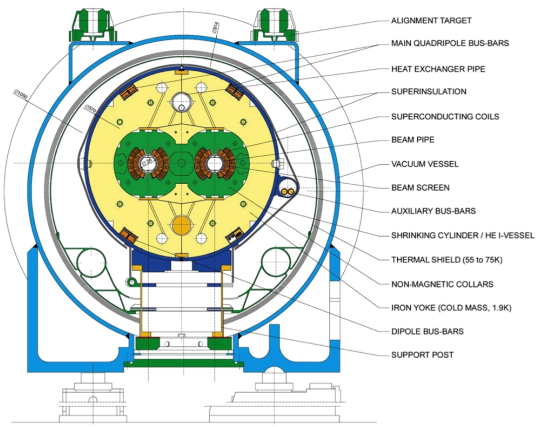

(a) Cross-section of a Dipole Magnet

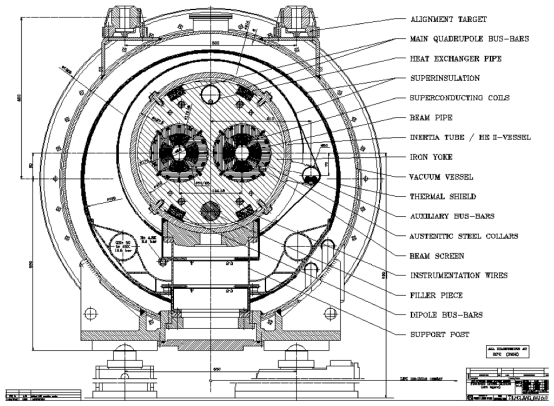

(b) Cross-Section of a Quadrupole Magnet with Cold Mass

Figure 3.2. LHC Dipole and Quadrupole Magnets

3.2 The Compact Muon Solenoid

The Compact Muon Solenoid (CMS) detector is a hermetic general purpose particle detector located at P5 just outside the village of Cessy, France. It is 21.6 m long, 14.6 m in diameter, and has a total weight of 12,500 t. CMS is actually a collection of multiple detectors that are layered, as seen in figure 3.3, in order to measure different types of particles. The innermost detector is the silicon pixel tracker, which is surrounded by the strip tracker. These two detectors measure the momentum of charged particles produced in LHC collisions. The next detectors are the electromagnetic calorimeter (ECAL) and pre-shower (ES). The ECAL measures the energy of electrons and photons. Outside of the ECAL lies the hadronic calorimeter (HCAL), which measures the energy of hadrons (mesons and baryons). All of these detectors are located inside the CMS magnet. The CMS magnet produces a very strong 3.8 T magnetic field that causes charged particles to bend, enabling the tracker to measure their momentum. Outside the magnet is the CMS muon system and iron return yoke, which is used for muon identification. The far-forward calorimeter, which measures jets at high η, is located past the muon chambers along the beam pipe. These detectors make up the CMS detector and enable it to measure nearly all the standard model particles. The only particles that are not detected are the neutrinos, which have to be reconstructed from the missing transverse energy ($\not\!\!E_T$) in the event.

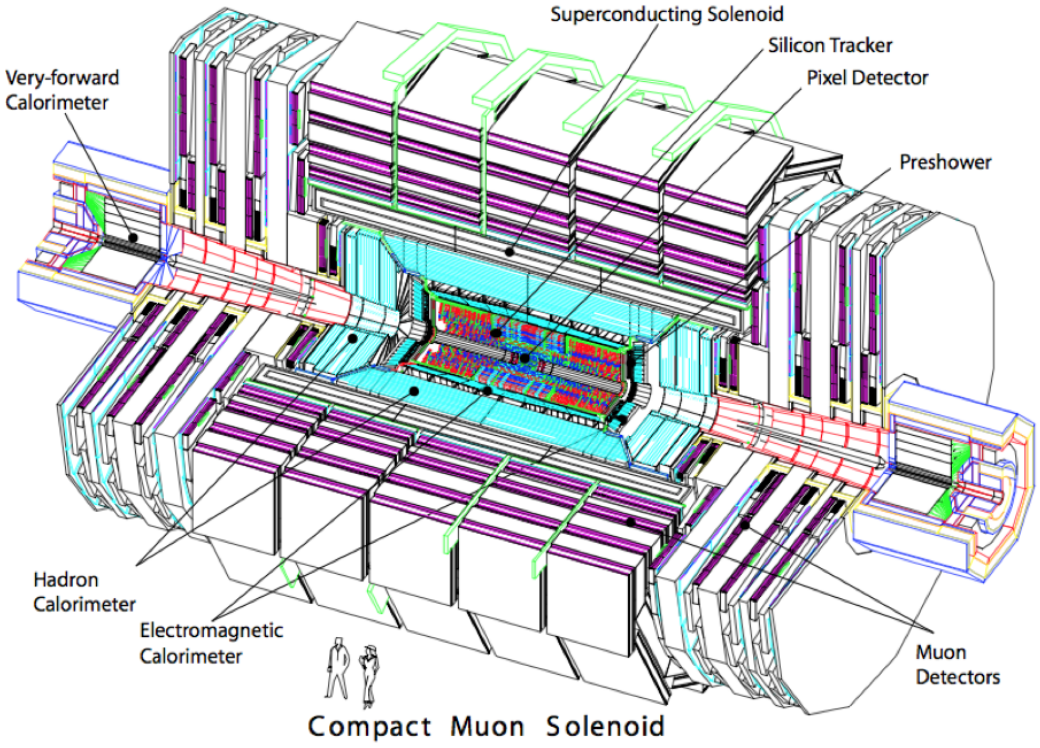

Figure 3.3. Schematic of the CMS Detector

3.2.1 Coordinate System

It is convenient to introduce a coordinate system in order to apply some orientation to CMS. Starting with a simple Cartesian coordination system, set the x-axis to point towards the center of the LHC ring, and then set the y-axis to point up towards the surface. Since a right handed coordinate is desired, the z-axis points west, in the direction of a counter-clockwise rotating beam when viewed from the surface. While this creates a complete coordinate description of CMS, it is not particularly useful. A much more useful set of coordinates are ρ, η, and ϕ. ρ (or r) is simply the radial

distance from the center of the detector,

$$\rho = \sqrt{x^2 + y^2}. \tag{3.1}$$

ϕ is the azimuthal angle in the xy-plane and ϕ is limited to a range of π to $-\pi$. Objects with a positive y value are assigned positive ϕ values. θ is the polar angle in the ρz-plane, where $\theta = 0$ points along the z-axis, $\theta = \pi$ points along the negative z-axis, and $\theta = \frac{\pi}{2}$ is in the xy-plane at the center of the detector when at the detector origin. η is defined as

$$\eta = -ln\left[tan\left(\frac{\theta}{2}\right)\right]. \tag{3.2}$$

$\eta = 0$ corresponds to the same xy-plane as $\theta = \frac{\pi}{2}$. However, in the limit that $\theta \to \pi$, $\eta \to \infty$. The η variable is convenient because the flux density of particles produced in LHC collisions are generally flat in η. The coordinates ρ, η, ϕ, and θ, will be used to describe both the CMS detector and the physical topology of LHC collisions for the rest of this thesis.

3.2.2 The Magnet

The CMS solenoid is a 220 t, 14.2 H, superconducting, NbTi magnet that is designed to create a 4 T field over a cylinder with a diameter of 6.3 m and a length of 12.5 m. At full current, 19.14 kA, the total stored energy of the magnet is 2.6 GJ, and the ratio between the stored energy and the cold mass is 11.6 KJ/kg. Due to the very high magnetic field requirements of CMS solenoid, four layers of NbTi Rutherford-type cable are used, which have an aluminum insert and additional aluminum reinforcement. The cables create the 41.7 MA-turns needed to generate the 4 T designed magnetic field. The operational temperature of the solenoid is 1.8 K, and the magnet is cooled by a liquid helium refrigeration system. Operating the magnet at 1.8 K keeps the helium at superfluid temperatures and this improves the thermal

conductive properties of the coolant. The fringe field is carried back to the magnet through a 10,000 t steel return yoke. This causes charged particles in the muon detectors to bend in the opposite direction than in the tracker. Over the 2010-2012 run period, the solenoid performed very well, though the operating current has been lowered to 18.16 kA corresponding to a magnetic field of 3.8 T.

3.2.3 The Inner Tracking System

The CMS Inner Tracking System is composed of two different detectors. The inner detector is the pixel vertex tracker and the outer one is the strip tracker. These two detectors allow CMS to reconstruct charged particle tracks with energies as low as 1 GeV. The CMS Tracker is the largest detector of its kind with over 200 m^2 of active silicon. The entire tracking system contains over 70 million channels. The high density of channels is needed to provide very fine granularity in the CMS environment, because at the designed luminosity of 10^{34} $cm^{-2}s^{-1}$, there is a charged particle flux of 1000 incident particles on the tracker per bunch crossing. At the innermost part of the tracking system, at 4 cm from the CMS origin, there is a hit density of 1 MHz/ mm^2. This hit rate falls to 3 kHz/mm^2 at the outer edge of the system, at a radius of 115 cm. Since there is such a steep drop in particle flux as a function of ρ, the tracking system uses a fine pixel pitch in the vertex tracker and coarser strips in the outer detectors varying from 10 to 20 cm in length. A schematic of the entire tracking system can be seen in figure 3.4.The tracker presents a significant engineering challenge in terms of cooling and readout. In order to minimize the noise produced from dark current in the silicon, the temperature of the tracker needs to be between -10°C and -27°C depending on the amount of radiation damage. However, the 66 million pixels produce 3.6 kW of heat. In order to keep the tracker within its operational parameters, a tetradecafluorohexane (C_6F_{14}) refrigeration system with a flow rate of 1 liter/s is needed. Reading the 66 million pixels requires extensive

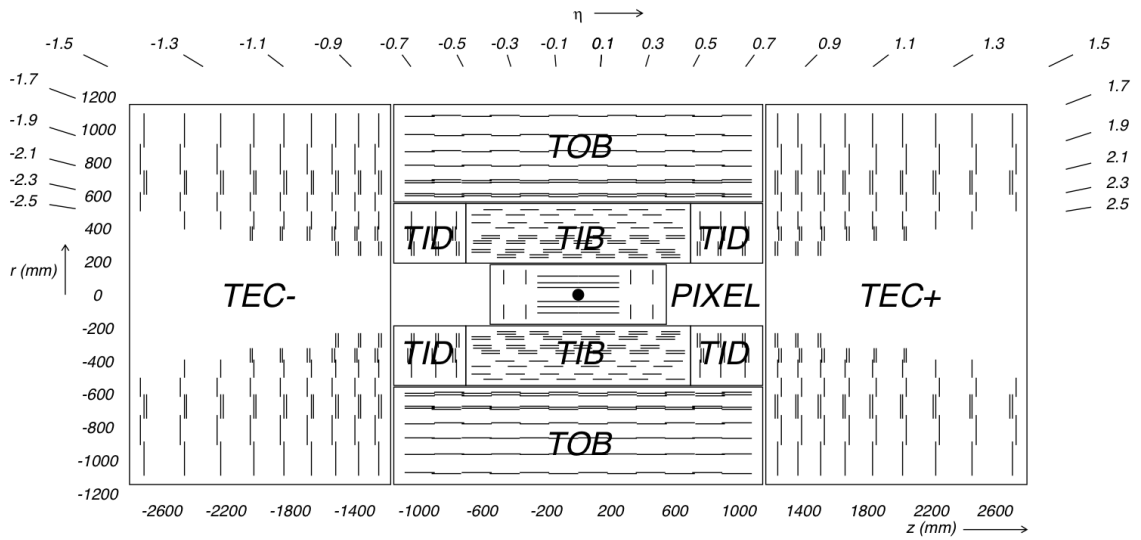

Figure 3.4. Schematic of the CMS tracker in the ρz-plane and its six different regions. Each line is a set of detector modules and the double lines represent the stereo strip layers.

electronics on the backside of the silicon and cabling. The electronic readout system in combination with the cooling system and the support structure needed to suspend the tracker represents a massive amount of material in front of the ECAL, as can be seen in figure 3.5. This material presents complications to the $H \to \gamma\gamma$ analysis, as it worsens the resolution of the ECAL.

The CMS Tracker serves several roles in the $H \to \gamma\gamma$ analysis. The first and foremost is the measurement of photon charged particle isolation. When the Higgs decays to two isolated photons, the photons, being neutral particles, do not produce a track like charged particle; however, they can interact with the tracker material causing the photon to convert to an e^+e^- pair. Hadronic showers produced by QCD interactions leave hits in the tracker volume. Electromagnetic objects that are accompanied by tracks are generally associated with jets from QCD and not real photons. A complete explanation of photon isolation will be covered in section 4.7. Another very important task of the tracker is photon conversion reconstruction. Due to the large material

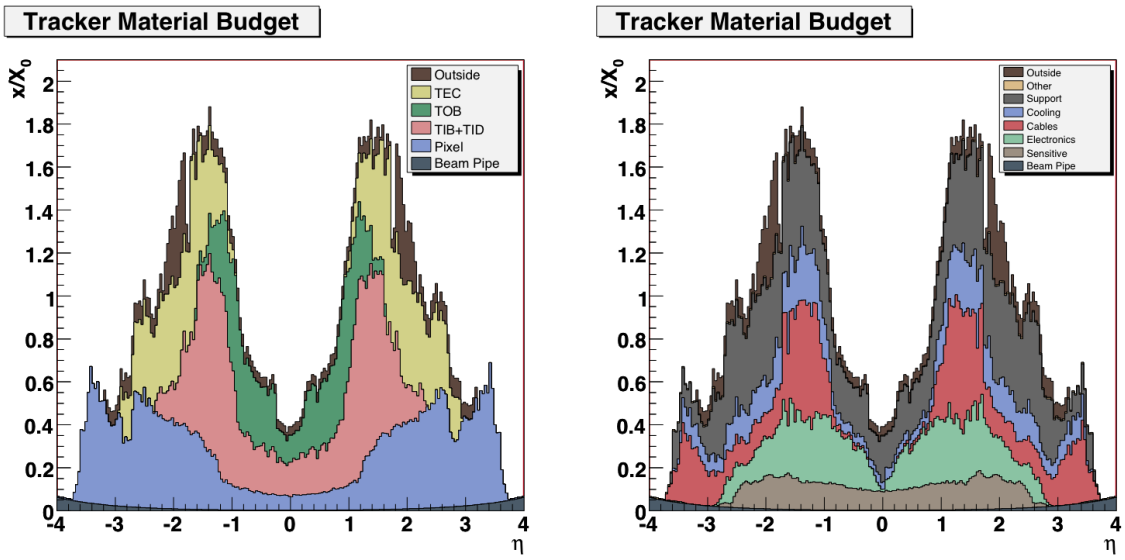

Figure 3.5. Material budget for the CMS tracking system in units of radiation lengths for photons versus η. The left is divided based on sub-detector and the right based on function.

budget of the tracker, there is up to one electromagnetic radiation length (X_0) in front of the ECAL. This material causes the photon to begin showering early and it converts to an electron-positron pair inside the tracker volume. The tracks from the photon conversions can be reconstructed, and they provide pointing information for the primary vertex in the event that would otherwise not be available. The topic of vertex selection will be covered completely in section 4.8.

3.2.3.1 The Pixel Detector

In order to have a hit occupancy below 1%, a fine grained pixel detector must be used for a radius less than 10 cm. The pixel tracker has a pitch of 100 $\times$ 150 μm^2 in ρ-ϕ and z, respectively, with a thickness of 320 μm. The pixel detector is sometimes referred to as the vertex tracker because its fine granularity is responsible for resolving multiple pileup vertices from one another and reconstructing displaced vertices with small impact parameters from b and τ decays. It covers an η range

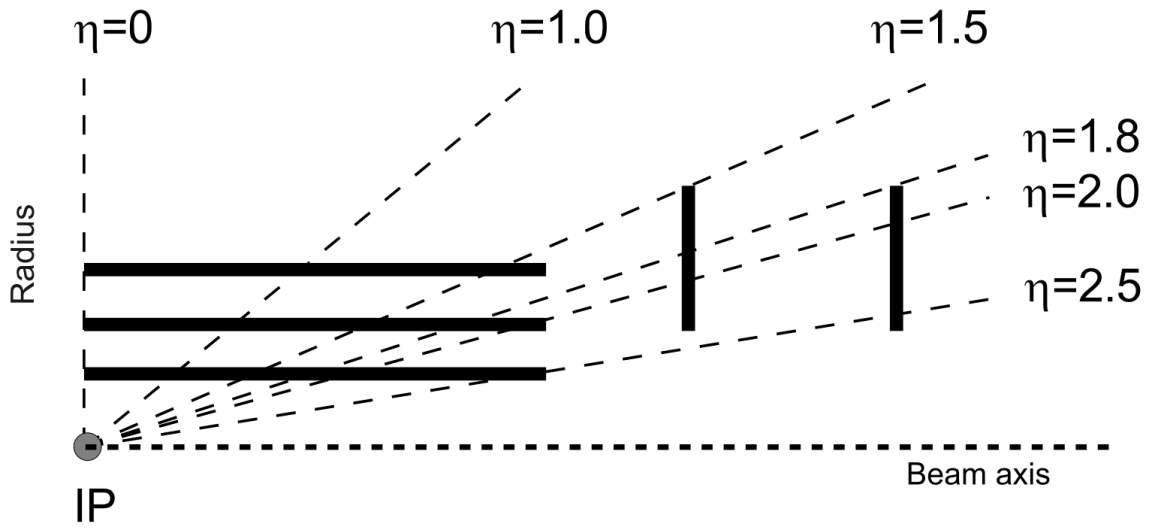

Figure 3.6. η Coverage of the Pixel Tracker

from -2.5 to 2.5 as seen in figure 3.6. The pixel tracker can be divided into two subcomponents: the Pixel Barrel and Pixel Endcap. The Pixel Barrel is composed of three layers of silicon oriented parallel with the beam line at a radii of 4.4, 7.3, and 10.2 cm, respectively. It has a total of 48 million pixels and an active area of 0.78 m^2. The Pixel Endcap has two layers of pixels positioned orthogonal to the beam line at a $|z|$ of 34.5 and 46.5 cm. The Pixel Endcap posses a total of 18 million pixels covering an area of 0.28 m^2. The positioning of the Pixel Barrel and Pixel Endcap allow for 3 point tracking for nearly all $|\eta| < 2.5$ as seen in figure 3.6.

3.2.3.2 The Strip Tracker

The CMS Strip Tracker covers a ρ from 20 cm to 116 cm and uses 9.3 million silicon strips instead of pixels. This is possible because at the higher radii it is permissible to use lower resolution (and cost) strips instead of pixels. The strip tracker is assembled from four different subcomponents: Tracker Inner Barrel (TIB), Tracker Outer Barrel (TOB), Tracker Inner Disk (TID) and Tracker Endcap (TEC). The TIB and TID

cover a radius up to 55 cm. The TIB consists of 4 layers of silicon strips oriented parallel to the beam pipe positioned at radii of 25.5, 33.9, 41.85, and 49.8 cm and covers a z from -70.0 to 70.0 cm. The inner 2 layers of strips have a pitch of 80 μm and the outer two layers have a pitch of 120 μm and a thickness of 320 μm. The TID has 3 layers of active silicon positioned perpendicular to the beam pipe between a $|z|$ of 80.0 and 90.0 cm and have a pitch that varies from 100 μm to 141 μm. The TIB and TID is surrounded by the TOB. The TOB consists of six layers at radii of 60.8, 69.2, 78.0, 86.8, 96.5, and 108.0 cm with 500 μm thick strips that have a pitch of 186 μm on the first four layers and 122 μm on the final two layers. The TOB extends to a $|z|$ distance of 118 cm. Charged particles that travel outside the TIB-TID-TOB region are measured by the TEC. The TEC covers a ρ of 22.5 cm to 113.5 cm and a z of 124 cm to 282 cm. It has 9 layers of silicone strips positioned orthogonal to the beam pipe. The inner 4 rings have a thickness of 320 μm and the outer three are 500 μm thick and the pitch varies from 97 μm to 184 μm. The first two layers of the TIB, TID, and TOB, and layers 1, 2, and 5 of the TEC, have a second strip detector that is mounted at a stereo angle of 100 mrad to the one in front of it in order to constrain the second dimension of the particle hit. This corresponds to the z position in the barrel and the ρ position in the disks.

3.2.4 The Electromagnetic Calorimeter

The Electromagnetic Calorimeter (ECAL) is the key detector in the $H \rightarrow \gamma\gamma$ search. The expected width for a Higgs boson with a mass below 160 GeV is very narrow, meaning that the Higgs boson should present itself as a narrow peak on a smoothly falling background. In order to resolve this peak, an ECAL with excellent resolution is needed. However, the very high instantaneous luminosity and narrow bunch spacing of the LHC means that the calorimeter needs to be fast and relatively radiation hard. Lead Tungstate ($PbWO_4$) was selected as the material for the ECAL

because of its fast scintillation time, 80% of its scintillation light is released in 25 ns, and its radiation hardness. $PbWO_4$ has a very high density (8.28 g/cm^3), short radiation length (0.89 cm), and small Molière radius (2.2 cm). These quantities make $PbWO_4$ an ideal scintillator for a fine granularity, compact, total absorption calorimeter.

The CMS ECAL is composed of a barrel (EB) and two endcaps (EE). The barrel contains 61,200 crystals and covers a range of $|\eta| < 1.479$. The barrel has a very fine granularity, 360 crystals in ϕ and 170 in η. The ECAL crystals are polished in order to maximize total internal reflection at the crystal edges. The crystals have a tapered design, the front face is 0.0174 $\times$ 0.0174 in η-ϕ (22$\times$22 mm^2) and the rear face is 26$\times$26 mm^2. The tapering causes a non-uniformity in light collection along the length of the crystal. This is corrected by de-polishing the rear face of the crystal. Each crystal is 23.0 cm in length that corresponds to 25.8 radiation lengths. The crystals are arranged in a quasi-projective geometry such that their axes make a 3° angle with respect to the particle trajectories from the origin. This is done so that the trajectory of particles do not align with the gaps in between the crystals. The crystals are placed such that the front face is at a ρ of 129 cm. Each crystal is contained in an aluminum layer followed by two layers of glass fibre-epoxy resin that is 0.1 mm thick. The crystals are then arranged into submodules with a gap spacing of 0.35 mm within the submodule and 0.50 mm between submodules. Two submodules are combined into modules, and then four modules are combined in η making a supermodule, which contains 1700 crystals that are separated by a 4 mm thick aluminum web. In the barrel, there are a total of 18 supermodules, 9 in -z and 9 in +z, that are narrow in ϕ and wide in η. The total weight of the ECAL barrel is 67.4 t. On the back of each crystal is a Hamamatsu S8148 reverse structure avalanche photodiode (APD). Each APD has an area of 5$\times$5 mm^2 and an optical gain of $\sim$50 when operated at a bias voltage of 340 to 430 V.

The ECAL endcap extends the coverage of the calorimeter to $1.479 < |\eta| < 3.0$. Each of the two endcaps is divided into two Dees that hold 3,662 crystals, and are placed at a $|z|$ of 315.4 cm. In the endcap, crystals are grouped into 5×5 supercrystals in a carbon fibre sheath. Each Dee contains 138 supercrystals and 18 special partial supercrystals. The crystals are arranged in a xy-grid that is focused 130.0 cm beyond the origin. Each of the endcap crystals have a front face of 28.62×28.62 mm^2 and a rear face of 30×30 mm^2 and a total length of 22.0 cm, which corresponds to 24.7 radiation lengths. The combined crystal volume of the endcaps is 2.90 m^3, which corresponds to a total weight of 24.0 t. A diagram of the ECAL barrel and endcap can be seen in figure 3.7. The ECAL endcap uses PMT188 vacuum photon triodes (VPT) instead of APDs. Photomultiplier tubes are used instead of silicon amplifiers, because they are more resistant to the higher radiation flux seen at high η. Additionally, a standard photon multiplier tube cannot operate in the 4 T magnetic field of the endcap. Each VPT has an area of 280 mm^2 and a diameter of 25 mm. The VPTs have a quantum efficiency of 22% at 430 nm compared to 75% for the APDs. Another disadvantage of VPTs is that their sensitivity is dependent on the flux of interacting particles. The VPTs are constantly pulsed by LEDs during the abort gap in order to maintain a constant gain. The endcap significantly extends the η coverage of the ECAL and improves the measurement of $\not\!\!E_T$.

In front of the ECAL endcaps is the CMS Preshower (ES). The ES consists of two layers of lead each followed by a layer of active silicon. The silicon sensor has 61×61 mm^2 of active area and has a thickness of 320 μm. The sensors are divided into 32 strips oriented in opposite directions on each plane of the preshower. The ES covers an $|\eta|$ range of 1.653 to 2.6 and has a radiation thickness of 1 X_0. It is preceded by another radiation length of tracker and support material so that by the time a photon reaches the endcap it has travelled through 2 X_0 of material. The purpose of the ES is to induce photons and electrons to shower in the lead plates.

The active silicon then performs a fine granularity measurement of electromagnetic shower shape and position.

Over the course of the LHC run period, γ and hadronic radiation damages the ECAL's $PbWO_4$ crystals. The flux of high energy particles cause the formation of color centers in the crystals that lowers their transparency. This in turn causes the number of photons collected by the APD or VPT to fall and limits the resolution of the calorimeter.

The resolution of the ECAL can be parameterized as:

$$\left(\frac{\sigma}{E}\right)^2 = \left(\frac{S}{\sqrt{E}}\right)^2 + \left(\frac{N}{E}\right)^2 + C^2, \tag{3.3}$$

where S is the stochastic term from photon statistics, N is the electronic noise, and C is a constant. As the transparency of the ECAL crystal falls the stochastic term increases as $1/\sqrt{N_\gamma}$. This means that as the LHC is running, the ECAL crystals' transparency needs to be constantly measured. For transparency corrections, a blue laser at 440 nm is used. The laser is flashed during the abort gaps and it takes 30 minutes of run time to scan the ECAL barrel. The inter-calibration between the ECAL's 75848 crystals is done with neutral $\pi^0 \to \gamma\gamma$ and $\eta \to \gamma\gamma$ events. The calibration is then validated on $Z \to ee$ events.

3.2.5 The Hadronic Calorimeter

The Hadronic Calorimeter (HCAL) is a sampling calorimeter that measures the energy of jets that form from high energy quarks and gluons. The HCAL consists of four different sub-detectors: the barrel (HB), endcap (HE), outer (HO), and forward (HF) detectors. The HCAL Barrel and Endcap is composed of brass absorber plates and organic scintillator tiles. The HCAL barrel starts at a radius of 1.77 m and ends at a radius of 2.95 m, and it covers a range of $|\eta| < 1.3$. The HCAL is assembled from

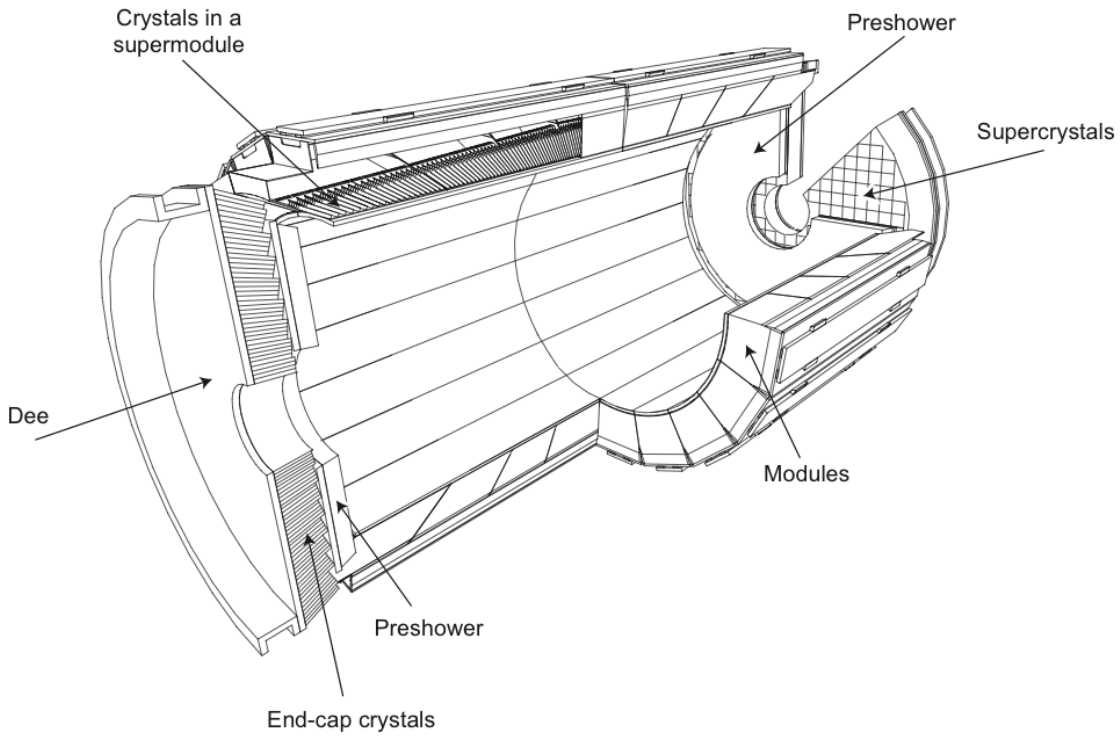

Figure 3.7. Schematic of the ECAL showing the barrel, preshower, and endcaps.

36 wedges that form the HB+ and HB-. Each half has 18 wedges that have complete ϕ coverage, and a single wedge covers an $\eta\phi$-area of 0.087 $\times$ 0.087. Each wedge has 16 absorber plates, the innermost plate is 40.0 mm of supportive steel, followed by eight 50.5 mm brass absorption plates, followed by an additional six 56.5 mm brass absorption plates, and then finally another 75 mm steel supportive plate. The effective thickness varies as a function of $\frac{1}{sin(\theta)}$. The effective thickness of the HCAL at $\eta = 0$ is 5.82 hadronic radiation lengths and the effective thickness at the end of the barrel ($|\eta| = 1.3$) is 10.6 λ_I. The presence of the ECAL adds an additional 1.1 λ_I. The HCAL has 70,000 scintillator tiles that are 3.7 mm thick Kuraray SCSN81 plastic scintillators. The light from each tile is collected by a 0.94 mm diameter, double-clad, green, wavelength-shifting fiber (Kuraray Y-11). The wave shifting fibers are then readout by a silicon hybrid photodiode (HPD).

The HCAL Endcap (HE) extends the HCAL coverage from an $|\eta|$ of 1.3 to an $|\eta|$ of 3.0. The HE has 17 layers of 79 mm brass absorber plates with 9 mm gaps for the plastic scintillator. The HE is separated into $\eta\phi$-towers of 0.087$\times$0.087 for $|\eta| < 1.6$ and 0.17$\times$0.17 for $|\eta| > 1.6$. The HO is a layer of scintillator outside the solenoid. The purpose of the HO is to catch showers that extend through the HCAL. The solenoid extends the depth of the HCAL by $1.4 \sin\theta\lambda_I$. The HO is separated into 5 η rings and into towers that approximately match the tower of HB with $\eta\phi$-towers of 0.087$\times$0.087, and is read out by the same Y11 Kuraray wavelength shifting fibers as the HB. The HCAL Forward (HF) measures the energy of jets in the far forward η region ($3.0 < |\eta| < 5.0$). This region is particularly difficult to perform calorimetry because of the high flux of charged particles. On average, 760 GeV of energy is deposited in the HF per event and there is a particle flux of 10^{11} per cm^2. In order to withstand the high particle flux, radiation hard quartz fibers are used. The HF uses Cherenkov light in order to measure the energy of incident particles. The HF is assembled from 5 mm grooved steel absorber plates with quartz fibers imbedded in

the grooves. Two different lengths of fibers are used. The first length of quartz fiber is 165 cm and runs the full length of the HF, and the second starts 22 cm after the first. The layering enables the HF to differentiate between electromagnetic and hadronic objects, because electrons and photons deposit the majority of their energy in the first 22 cm. The HF is located 11.2 m from the interaction point and is made from 36 wedges that cover 20° in ϕ each. The quartz fibers are bundled in towers the cover an $\eta\phi$-area of 0.175×0.175. The Cherenkov light is collected by 24 photomultiplier tubes that connected directly to the quartz fibers. The entire detector is encased in 40 cm of steel, 40 cm of concrete, and 5 cm of polyethylene [78].

The HCAL does not directly detect the photons in the $H \to \gamma\gamma$ analysis. However, it is used in two different ways in the analysis. The ratio between the energy in the ECAL and HCAL is used in the photon selection to exclude jets that fake photons. The HE and HF are used to detect far-forward jets in VBF Higgs production.

3.2.6 The Muon System

The CMS Muon System is designed to identify, trigger, and measure muons generated by the collisions in the LHC. The system covers an area of 25,000 m^2 and up to an $|\eta|$ of 2.4. Since the muon system covers the most volume of any sub-detector, the detectors and material need to be inexpensive. However, muons are very important for the $H \to ZZ$ analysis, so it is also important for the system to be reliable.[1] The muon system is composed of three different subsystems: drift tubes (DTs), cathode strip cambers (CSCs), and resistive plate chambers (RPCs).

[1]It is important for CMS to be able to measure the $H \to ZZ \to 4l$ channel, because it offers excellent mass resolution, similar to $H \to \gamma\gamma$, and spin information.

3.2.6.1 Drift Tubes

Four layers of Drift Tubes (DTs) surround the CMS barrel and cover an $|\eta| < 1.2$. The three innermost layers contain 60 chambers and the outermost layer contains 70. It is possible to use DTs because of the low particle density at such a high ρ and a relatively low magnetic field. Each DT is 21 mm thick, filled with a gas mixture of 85% Ar and 15% CO_2, and has a response time of 380 ns. Between each of the DT layers is a layer of steel return yoke. Each DT has 8 chambers in 2 groups. One group measures the muon position in the $\rho\phi$-plane and the other group measures the z. The final DT station does not measure the z position. Each of the DT chambers are displaced by half the cell width in order to minimize the amount of dead area. The position and orientation of the DTs was selected to maximize muon track reconstruction efficiency and limit the contamination from background.

3.2.6.2 Cathode Strip Chambers

The cathode strip chambers (CSCs) serve as the muon detection system in the endcap region. They cover a range of $0.9 < |\eta| < 2.4$ using 468 chambers that are filled with a gas mixture that consists of 50% CO_2, 40% Ar, and 10% CF_4. Each endcap has 4 CSC stations with wires that run perpendicular to the beam pipe. Each CSC chamber has 7 layers of cathode strips and 6 layers of anode wires that run approximately perpendicular to each other. The cathode wires run radially outward to measure the muon position in $\rho\phi$-plane and the anode wires measure the η position. The multiple layers allow for pattern recognition discrimination between muons and hadronic particles, which are prevalent in the high η region. Between each of the CSC stations is a layer of iron return yoke. The CSCs are arranged such that muons cross 3 to 4 stations as they leave the detector. If muons are between a range of $0.9 < |\eta| < 1.2$ they fall between the overlap region of the DTs and CSCs.

3.2.6.3 Resistive Plate Chambers

The Resistive Plate Chambers (RPCs) are high speed gaseous parallel-plate detectors that are used to match a muon to a particular bunch crossing. Due to the low speed response of the DTs and CSCs the RPCs play a crucial role in muon detection. The RPCs are double-gap chambers, which run in avalanche mode so that their response time is minimized. The RPCs are filled with a gas mixture that is composed of 96.2% R134a ($C_2H_2F_4$), 3.5% iC_4H_{10}, and 0.3% SF_6. There are six layers of RPCs in the barrel. The first two layers of DTs are sandwiched between two RPCs, and the outer two layers of DTs have an RPC placed in front of them. The double layering in the inner DTs is helpful in detecting low p_T muons that may not reach the outer layers of the detector. In the endcap there are three layers of RPCs in front of each of the CSC stations that cover a rapidity range of $|\eta| < 1.6$ [79]. Combining the barrel and endcap there are 480 RPC chambers with an active area of 2400 m^2. The RPCs are generally only used for the L1 trigger system, and then only for timing purposes, because they have modest spacial resolution, and the DTs and CSCs provide a higher resolution measure of momentum.

3.2.7 The Trigger System

The LHC produces collisions at a rate of 20 MHz, or a collision every 50 ns. Considering that the average event size is 1 MB for proton-proton events, it is impossible to store and analyze every event. The CMS trigger system is a two-tiered hardware and software system that selects which events are written to disk. These two systems are the Level-1 (L1) Trigger and the High Level Trigger (HLT). The goal of these two systems is to reduce the event rate to near 300 Hz.

3.2.7.1 The L1 Trigger

The first step in the triggering process is the Level-1 Trigger. The role of the L1 Trigger is to reduce the event rate from 20 MHz to 50-100 kHz. The L1 Trigger is assembled from field programmable gate arrays, application specific integrated circuits, and programmable memory lookup tables. The L1 Trigger looks at the detector in a very coarse manner in order to minimize the amount of time spent on each event, because the L1 Trigger only has 3.2 μs to analyze each event. The L1 can be divided into two smaller subsystems: the Global Calorimeter Trigger and the Global Muon Trigger. The Global Muon Trigger connects partial track segments from the three muon detectors and passes the four best muon tracks to the Global Trigger. The Global Calorimeter Trigger groups towers from the ECAL, HCAL, and HF together and passes the best physics objects to the Global Trigger. A schematic of the L1 Trigger can be seen in figure 3.8.

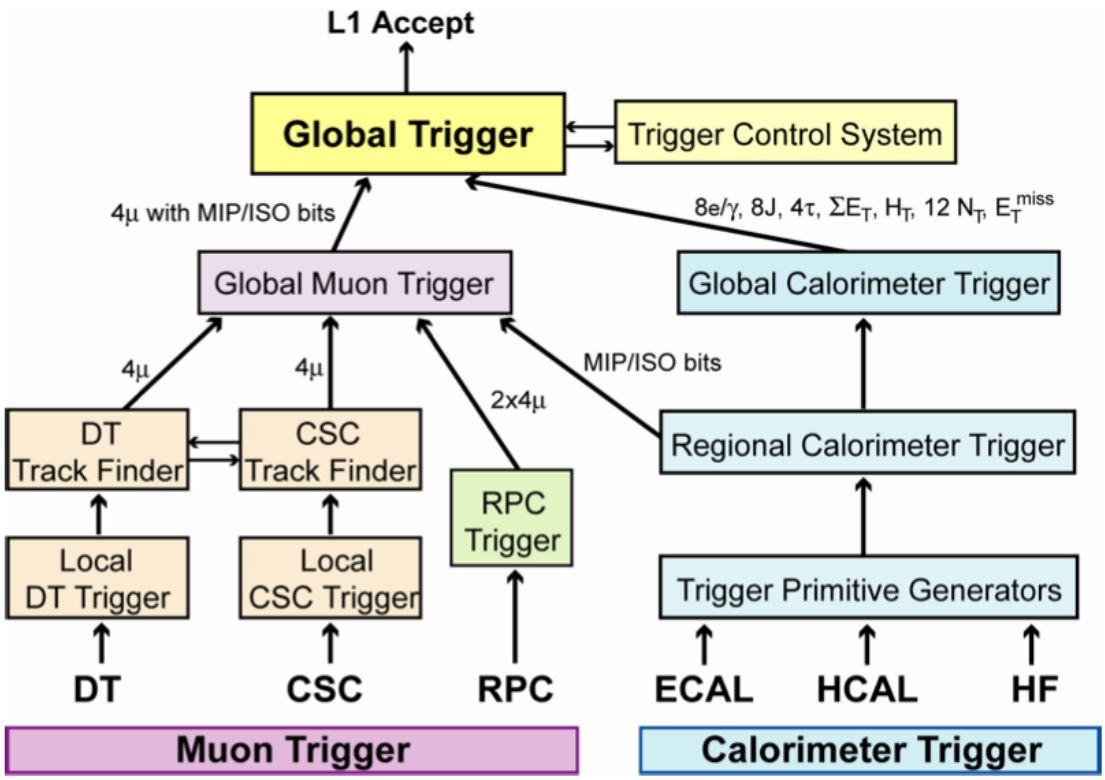

Figure 3.8. Diagram of the L1 Trigger Architecture

3.2.7.2 The High Level Trigger

The High Level Trigger (HLT) is a large array of computers that processes the events that pass the L1 Trigger in parallel. The HLT is a filter farm made from over 1000 commercially available processors. It reads from a buffer of hard disks, which are filled with events that pass the Level 1 Accept (L1A). The goal of the HLT is to reduce the event rate from 50-100 kHz to ∼300 Hz. The HLT accesses the full event information and performs a partial event reconstruction. The entire HLT software package is a collection of C++ sequences that run preliminary event reconstruction and filtration. Each individual trigger path has its own sequence of modules that are

associated with it. If an event passes through all the modules in an HLT path then it passes that HLT trigger. Once an event passes the HLT it is fully reconstructed and saved to a primary dataset.

CHAPTER 4

EVENT SELECTION AND CATEGORIZATION

The $H \to \gamma\gamma$ analysis is a mass resolution driven analysis. The analysis searches for a narrow peak on a broadly falling background. Since there are relatively few signal events over a large number of background events, it is paramount to maximize the mass resolution of every event, separate background events from signal events, and differentiate low-resolution events from high-resolution events. All of the analysis components are oriented around these tasks. The analysis searches for two isolated photons, where isolated means that there are no tracks or calorimeter deposits near the photon energy deposit in the ECAL. The invariant mass is then reconstructed from the four-vectors of the two photons. The invariant mass of the di-photon system is

$$\begin{aligned} M^2 &= (E_1 + E_2)^2 - |\mathbf{p}_1 + \mathbf{p}_2|^2 \\ &= 2E_1E_2(1 - \cos\theta_{\gamma\gamma}). \end{aligned} \tag{4.1}$$

The invariant mass is dependent on the energy of each photon and the opening angle between them ($\theta_{\gamma\gamma}$). The invariant mass resolution $\left(\frac{\Delta m_{\gamma\gamma}}{m_{\gamma\gamma}}\right)$ of the di-photon system is given by

$$\frac{\Delta m_{\gamma\gamma}}{m_{\gamma\gamma}} = \frac{1}{2}\left[\frac{\Delta E_{\gamma 1}}{E_{\gamma 1}} + \frac{\Delta E_{\gamma 2}}{E_{\gamma 2}} + \frac{\Delta\theta_{\gamma\gamma}}{\tan(\theta_{\gamma\gamma}/2)}\right]. \tag{4.2}$$

It is clear from equation 4.2 that in order to resolve the Higgs invariant mass peak, the energy of each photon and the open angle between them needs to be well measured. Naturally, the analysis will focus on optimizing the determination of these two

quantitates [80]. This chapter will overview the process of event selection and categorization, and the next chapter will focus on signal and background parameterization and final results.

There are two analyses that will be described in the next two chapters. Both analysis will use categorization to separate events with high resolution and high signal to background (S/B) ratios from events with low resolution and low S/B ratios. Using categorization creates an analysis that is more sensitive than an analysis with only one category because it separates high sensitivity events from low sensitivity events. The main analysis uses a variety of boosted decision trees (BDTs) that perform many different functions: vertex identification and probability, supercluster energy regression and resolution estimation, photon identification, and inclusive and di-jet categorization. There is also a cross-check analysis that uses a more traditional cut-based categorization and a cuts-in-categories (CiC) method for photon identification. The vertex identification and supercluster energy regression BDTs are still used in the cross-check analysis, but the vertex probability and energy resolution BDTs are not. While the main analysis is more sensitive, it also has a categorization systematic uncertainty associated with the theoretical kinematic uncertainties of the Higgs boson. The cut-based cross-check analysis does not have this uncertainty and is less dependent on the underlying model of Higgs production.

4.1 Data Samples

Two datasets will be used for the $H \to \gamma\gamma$ analysis. They are the 7 and 8 TeV datasets, which correspond to 5.1 and 19.6 fb^{-1}, respectively. A full list of the datasets used can be found in table 4.1. All of the signal and background samples are generated using a Monte Carlo simulation technique (MC). The $H \to \gamma\gamma$ signal sample for the gluon fusion and VBF production channels are generated with POWHEG at NLO, while the associated vector boson and top production is done with PYTHIA at LO.

The cross-sections and branching ratios are calculated by the LHC Cross-Section Working-Group [65]. The gluon fusion cross-section is calculated at NNLO+NNLL for perturbative QCD and NLO for electroweak. While the VBF cross-section is calculated at NNLO for perturbative QCD and NLO for electroweak. The signal samples are generated between 110-150 GeV in 5 GeV steps with finer stepping near 125 GeV. A list of the calculated cross-sections for 7 and 8 TeV can be found in tables 4.2 and 4.3 respectively. The Monte Carlo simulation background samples are generated with POWHEG at NLO plus PYTHIA, Madgraph plus PYTHIA, or just PYTHIA 6.4. The QCD and γ + jet sample are produced with a generator level electromagnetic enrichment filter that increases the number of electrons and photons in the final state. The generated backgrounds along with their cross-sections, filter efficiency, number of simulated events, and equivalent lumi can be found in table 4.4.

TABLE 4.1

DATASETS

Energy	Dataset
7 TeV	/Photon/Run2011A-16Jan2012-v1/AOD
7 TeV	/Photon/Run2011B-16Jan2012-v1/AOD
8 TeV	/Photon/Run2012A-13Jul2012-v1/AOD
8 TeV	/Photon/Run2012A-recover-06Aug2012-v1/AOD
8 TeV	/DoublePhoton/Run2012B-13Jul2012-v1/AOD
8 TeV	/DoublePhoton/Run2012C-24Aug2012-v2/AOD
8 TeV	/DoublePhoton/Run2012C-PromptReco-v2/AOD
8 TeV	/DoublePhoton/Run2012D-PromptReco-v1/AOD

TABLE 4.2

7 TEV CROSS-SECTIONS FOR $H \to \gamma\gamma$

m_H (GeV)	Gluon Fusion	Vector Boson Fusion	$W \to WH$, $Z \to ZH$	$t\bar{t} \to H$	Branching Fraction
110	19.5	1.41	0.88, 0.47	0.126	1.95×10^{-3}
115	18.1	1.34	0.75, 0.41	0.111	2.11×10^{-3}
120	16.7	1.28	0.66, 0.36	0.098	2.23×10^{-3}
125	15.3	1.22	0.57, 0.32	0.086	2.28×10^{-3}
130	14.2	1.17	0.50, 0.28	0.077	2.25×10^{-3}
135	13.1	1.12	0.44, 0.25	0.068	2.13×10^{-3}
140	12.2	1.07	0.39, 0.22	0.061	1.93×10^{-3}
145	11.3	1.02	0.34, 0.19	0.049	1.68×10^{-3}
150	10.6	0.98	0.30, 0.17	0.049	1.37×10^{-3}

TABLE 4.3

8 TEV CROSS-SECTIONS FOR $H \to \gamma\gamma$

m_H (GeV)	Gluon Fusion	Vector Boson Fusion	$W \to WH$, $Z \to ZH$	$t\bar{t} \to H$	Branching Fraction
110	25.0	1.81	1.06, 0.59	0.19	1.95×10^{-3}
115	23.0	1.73	0.92, 0.51	0.17	2.11×10^{-3}
120	21.1	1.65	0.80, 0.45	0.15	2.23×10^{-3}
125	19.5	1.58	0.70, 0.39	0.13	2.28×10^{-3}
130	18.1	1.51	0.61, 0.35	0.12	2.25×10^{-3}
135	16.8	1.45	0.54, 0.31	0.10	2.13×10^{-3}
140	15.6	1.39	0.47, 0.27	0.09	1.93×10^{-3}
145	14.6	1.33	0.42, 0.24	0.08	1.68×10^{-3}
150	13.7	1.28	0.37, 0.22	0.07	1.37×10^{-3}

TABLE 4.4

MONTE CARLO SIMULATION BACKGROUND SAMPLES

Dataset	$\widehat{p}_T$	σ (pb)	ϵ_{filter}	# events	Lumi (pb^{-1})
/DiPhotonJets_Madgraph	-	75.4	1.	1154970	15300
/DiPhotonBox_Pt-10to25_Pythia	$10 - 25GeV$	424.8	1.	500400	1180
/DiPhotonBox_Pt-25to250_Pythia	$25 - 250GeV$	15.54	1.	500352	32200
/DiPhotonBox_Pt-250toInf_Pythia	$> 250GeV$	1.18×10^{-3}	1.	500050	424000
/PhotonJet_DoubleEmenriched_Pt20to40	$20 - 40GeV$	8.19×10^{4}	1.84×10^{-3}	5907942	39200
/PhotonJet_DoubleEmenriched_Pt40	$> 40GeV$	8.84×10^{3}	5.39×10^{-2}	5956149	12500
/QCD_DoubleEmenriched_Pt30to40	$30 - 40GeV$	5.20×10^{7}	2.35×10^{-4}	6061407	500
/QCD_DoubleEmenriched_Pt40	$> 40GeV$	2.37×10^{7}	2.18×10^{-3}	9790851	189
/DYJetsToLL_TuneZ2_M-50_7TeV-madgraph-tauola	$> 50GeV$	3.53pb $\times 10^{3}$	1	30461028	10300

4.2 Trigger Selection

The $H \to \gamma\gamma$ analysis uses two different HLT triggers, which select events that have two superclusters above a certain energy threshold, where a supercluster is an ECAL deposit that is a precursor to a photon. The two primary triggers for the $H \to \gamma\gamma$ analysis are:

- HLT_Photon36_R9Id85_OR_CaloId10_Iso50_Photon22_R9Id85_OR_CaloId10_Iso50_v*
- HLT_Photon26_R9Id85_OR_CaloId10_Iso50_Photon18_R9Id85_OR_CaloId10_Iso50_Mass*

The first HLT trigger selects events where a supercluster has a $p_T > 36$ GeV and a second supercluster with a $p_T > 22$ GeV. This trigger is seeded by L1_SingleEG_22, which is an L1 trigger that looks for an e/γ object with a p_T greater than 22 GeV. The second HLT trigger requires two L1 seeds (L1_DoubleEG_13_7), the leading seed needs to have a $p_T > 13$ GeV and the sub-leading seed needs to have $p_T > 7$ GeV. Once either L1 trigger is satisfied, the HLT unpacks the ECAL information in an $\eta\phi$-tower of 0.25×0.4 around the L1 seed. The HLT then looks at three properties of the supercluster: shower shape, isolation, and H/E ratio. The shower shape in the HLT is parameterized in terms of R_9 and $\sigma_{i\eta i\eta}$. R_9 is the ratio between the energy in the center 3×3 crystals over the entire supercluster. Narrow showers have an R_9 that is near one and these photons have good resolution. Photons that begin to shower, or convert, inside the tracker material have low R_9 values. The magnetic field spreads the shower in the ϕ direction, causing a wider shower footprint and worse energy resolution. $\sigma_{i\eta i\eta}$ is an energy weighted standard deviation of the ECAL supercluster

in η,

$$\sigma^2_{i\eta i\eta} = \frac{\sum_i^{5\times5} \omega_i(\eta_i - \overline{\eta}_{5\times5})^2}{\sum_i^{5\times5} \omega_i}, \text{ where} \tag{4.3}$$

$$\overline{\eta} = \frac{\sum \omega_i \eta_i}{\sum \omega_i} \text{ and}$$

$$\omega_i = \max\left(0, 4.7 + \ln\frac{E_i}{E_{5\times5}}\right).$$

The isolation parameter is the energy that is deposited in a ΔR cone of 0.15 around the L1 seed in the tracker, ECAL, and HCAL. The isolation energy is used to separate real photons, which are isolated and only leave energy deposited in the ECAL, from fake photons from QCD jets, which are generally π^0 or η particles accompanied by charged or neutral hadrons. H/E is the ratio of energy between the HCAL and the ECAL in a ΔR cone of 0.15 around the L1 seed. Again, this is because jets from QCD are generally accompanied by hadrons that leave energy in the HCAL. Both of the HLT triggers used in $H \to \gamma\gamma$ are cross-triggers. Either the lead or sub-lead photon can pass either the isolation, as seen in table 4.5, or the R_9 requirement (R_9-R_9, iso-iso, R_9-iso, or iso-R_9), this way a single trigger functions as four. If a photon has an $R_9 > 0.85$ then that photon does not have to pass the isolation requirements for it to pass that leg of the trigger. Conversely, if the photon has an $R_9 < 0.85$, then the photon must pass the isolation requirements defined in the trigger. Both of the photons must have an $H/E < 0.1$ and a $\sigma_{i\eta i\eta} < 0.014$ for the barrel and $\sigma_{i\eta i\eta} < 0.035$ for the endcap, regardless of the photon's R_9 value. The second trigger, which requires two L1 seeds at a lower energy threshold, also has an invariant mass cut. The invariant mass cut was initially set at 60 GeV, but it was increased to 70 GeV during the run period to limit the trigger rate [81].

TABLE 4.5

TRIGGER ISOLATION THRESHOLDS

Isolation Type	Isolation Energy
ECAL Isolation	$5.0 + 0.12 \times E_T$
HCAL Isolation	$5.0 + 0.0050 \times E_T$
Tracker Isolation	$5.0 + 0.0020 \times E_T$

The L1 and HLT trigger efficiency is measured using a tag-and-probe methodology in $Z/\gamma^* \rightarrow ee$ events in data and Monte Carlo simulation. However, the shower shapes of electrons do not perfectly match that of photons, and the R_9 of the electrons in data are re-weighted to the R_9 of photons in $H \rightarrow \gamma\gamma$ Monte Carlo simulation. The trigger efficiency systematic uncertainty is estimated by performing the tag-and-probe measurement twice. It is performed with an electron+supercluster trigger and then again with a pre-scaled non-isolated di-photon trigger. The difference in the efficiency is taken as a systematic uncertainty [82]. The L1 and HLT trigger efficiency can be seen in table 4.6. It should be noted that while these two triggers represent the primary $H \rightarrow \gamma\gamma$ triggers for 2012 data taking, there are many triggers used in the $H \rightarrow \gamma\gamma$ analysis. A complete list of triggers can be seen in tables 4.7, 4.8, and 4.9 [81].

TABLE 4.6

L1 AND HLT TRIGGER EFFICIENCIES

	L1_DoubleEG_13_7	L1_SingleEG_22	L1+HLT
Main Analysis	$99.83 \pm 0.02\%$	$97.82 \pm 0.03\%$	$99.78 \pm 0.03\%$
Cut-Based Cross-Check	$99.72 \pm 0.02\%$	$97.70 \pm 0.03\%$	$99.68 \pm 0.03\%$

TABLE 4.7

7 TEV RUN 2011A TRIGGER TABLE

Trigger Path	Prescale	L1 Seed
Runs 165970–173198		
HLT_Photon26_CaloIdL_IsoVL_Photon18_CaloIdL_IsoVL_v	1	L1_SingleEG15
HLT_Photon26_CaloIdL_IsoVL_Photon18_R9Id_v	1	L1_SingleEG15
HLT_Photon26_R9Id_Photon18_CaloIdL_IsoVL_v	1	L1_SnigleEG15
HLT_Photon26_R9Id_Photon18_R9Id_v	1	L1_SingleEG15
HLT_Photon26_CaloIdL_IsoVL_Photon18_v	20–120	L1_SingleEG15
HLT_Photon26_Photon18_v	180–1100	L1_SingleEG15

TABLE 4.7

Continued

Trigger Path	Prescale	L1 Seed
HLT_Photon36_CaloIdL_IsoVL_Photon22_CaloIdL_IsoVL_v	1	L1_SingleEG20
HLT_Photon36_CaloIdL_IsoVL_Photon22_R9Id_v	1	L1_SingleEG20
HLT_Photon36_R9Id_Photon22_CaloIdL_IsoVL_v	1	L1_SingleEG20
HLT_Photon36_R9Id_Photon22_R9Id_v	1	L1_SingleEG20
HLT_Photon36_CaloIdL_IsoVL_Photon22_v	7–45	L1_SingleEG20
HLT_Photon36_IsoVL_Photon22_v	5–30	L1_SingleEG20

TABLE 4.7

Continued

Trigger Path	Prescale	L1 Seed
Runs 161216–165633		
HLT_Photon26_CaloIdL_IsoVL_Photon18_CaloIdL_IsoVL_v	1	L1_SingleEG12
HLT_Photon26_CaloIdL_IsoVL_Photon18_R9Id_v	1	L1_SingleEG12
HLT_Photon26_R9Id_Photon18_CaloIdL_IsoVL_v	1	L1_SingleEG12
HLT_Photon20_R9Id_Photon18_R9Id_v	1	L1_SingleEG12
HLT_Photon26_CaloIdL_IsoVL_Photon18_v	1	L1_SingleEG12
HLT_Photon26_Photon18_v	10–200	L1_SingleEG12
HLT_Photon20_CaloIdVL_IsoL_v	250–5000	L1_SingleEG12

TABLE 4.7

Continued

Trigger Path	Prescale	L1 Seed
Runs 160404–161176		
HLT_Photon26_CaloIdL_IsoVL_Photon18_CaloIdL_IsoVL_v	1	L1_SingleEG12
HLT_Photon26_IsoVL_Photon18_IsoVL_v	1	L1_SingleEG12
HLT_Photon26_CaloIdL_IsoVL_Photon18_v	1	L1_SingleEG12
HLT_Photon26_IsoVL_Photon18_v	1	L1_SingleEG12
HLT_Photon26_Photon18_v	1–30	L1_SingleEG12

TABLE 4.8

7 TEV RUN 2011B TRIGGER TABLE

Trigger Path	Prescale	L1 Seed
Runs 178420–180252		
HLT_Photon26_CaloIdXL_IsoXL_Photon18_CaloIdXL_IsoXL_Mass60_v	1	L1_DoubleEG_12_5
HLT_Photon26_CaloIdXL_IsoXL_Photon18_R9IdT_Mass60_v	1	L1_DoubleEG_12_5
HLT_Photon26_R9IdT_Photon18_CaloIdXL_IsoXL_Mass60_v	1	L1_DoubleEG_12_5
HLT_Photon26_R9IdT_Photon18_R9IdT_Mass60_v	1	L1_DoubleEG_12_5
HLT_Photon26_CaloIdXL_IsoXL_Photon18_v	110–190	L1_DoubleEG_12_5
HLT_Photon26_Photon18_v	340–600	L1_DoubleEG_12_5

TABLE 4.8

Continued

Trigger Path	Prescale	L1 Seed
HLT_Photon36_CaloIdL_IsoVL_Photon22_CaloIdL_IsoVL_v	1	L1_SingleEG20
HLT_Photon36_CaloIdL_IsoVL_Photon22_R9Id_v	1	L1_SingleEG20
HLT_Photon36_R9Id_Photon22_CaloIdL_IsoVL_v	1	L1_SingleEG20
HLT_Photon36_R9Id_Photon22_R9Id_v	1	L1_SingleEG20
HLT_Photon36_CaloIdL_IsoVL_Photon22_v	45–75	L1_SingleEG20
HLT_Photon36_Photon22_v	180–300	L1_SingleEG20

TABLE 4.8

Continued

Trigger Path	Prescale	L1 Seed
Runs 173236–178380		
HLT_Photon26_CaloIdXL_IsoXL_Photon18_CaloIdXL_IsoXL_v	1	L1_DoubleEG_12_5
HLT_Photon26_CaloIdXL_IsoXL_Photon18_R9Id_v	1	L1_DoubleEG_12_5
HLT_Photon26_R9Id_Photon18_CaloIdXL_IsoXL_v	1	L1_DoubleEG_12_5
HLT_Photon26_R9Id_Photon18_R9Id_v	1	L1_DoubleEG_12_5
HLT_Photon26_CaloIdXL_IsoXL_Photon18_v	20–190	L1_DoubleEG_12_5
HLT_Photon26_Photon18_v	180–1740	L1_DoubleEG_12_5

TABLE 4.8

Continued

Trigger Path	Prescale	L1 Seed
HLT_Photon36_CaloIdL_IsoVL_Photon22_CaloIdL_IsoVL_v	1	L1_SingleEG20
HLT_Photon36_CaloIdL_IsoVL_Photon22_R9Id_v	1	L1_SingleEG20
HLT_Photon36_R9Id_Photon22_CaloIdL_IsoVL_v	1	L1_SingleEG20
HLT_Photon36_R9Id_Photon22_R9Id_v	1	L1_SingleEG20
HLT_Photon36_CaloIdL_IsoVL_Photon22_v	6–65	L1_SingleEG20
HLT_Photon36_Photon22_v	75–750	L1_SingleEG20

TABLE 4.9

8 TEV RUN 2012 TRIGGER TABLE

Trigger Path	Prescale	L1 Seed
HLT_Photon26_R9Id85_OR_CaloId10_Iso50_Photon18_R9Id85_OR_CaloId10_Iso50_Mass60	1	L1_DoubleEG_13_7
HLT_Photon26_R9Id85_OR_CaloId10_Iso50_Photon18_R9Id85_OR_CaloId10_Iso50_Mass70	1	L1_DoubleEG_13_7
HLT_Photon26_CaloId10_Iso50_Photon18_CaloId10_Iso50_Mass60	1	L1_DoubleEG_13_7
HLT_Photon26_CaloId10_Iso50_Photon18_R9Id85_Mass60	1	L1_DoubleEG_13_7
HLT_Photon26_R9Id85_Photon18_CaloId10_Iso50_Mass60	1	L1_DoubleEG_13_7
HLT_Photon26_R9Id85_Photon18_R9Id85_Mass60	1	L1_DoubleEG_13_7
HLT_Photon26_Photon18	600-160	L1_DoubleEG_13_7
HLT_Photon26_R9Id85_OR_CaloId10_Iso50_Photon18	1000-1600	L1_DoubleEG_13_7

TABLE 4.9

Continued

Trigger Path	Prescale	L1 Seed
HLT_Photon36_CaloId10_Iso50_Photon22_CaloId10_Iso50	1	L1_SingleEG_22
HLT_Photon36_CaloId10_Iso50_Photon22_R9Id85	1	L1_SingleEG_22
HLT_Photon36_R9Id85_OR_CaloId10_Iso50_Photon22_R9Id85_OR_CaloId10_Iso50	1	L1_SingleEG_22
HLT_Photon36_R9Id85_Photon22_CaloId10_Iso50	1	L1_SingleEG_22
HLT_Photon36_R9Id85_Photon22_R9Id85	1	L1_SingleEG_22
HLT_Photon36_Photon22	300-800	L1_SingleEG_22
HLT_Photon36_R9Id85_OR_CaloId10_Iso50_Photon22	300-500	L1_SingleEG_22

4.3 Photon Reconstruction

Photon reconstruction is an iterative process in CMS. When a photon impacts the ECAL it produces an electromagnetic shower of electrons and photons that spreads across many of the $PbWO_4$ crystals. In order to maximize the energy resolution of the photon, each crystal near the photon shower must be included in the energy summation. This is accomplished with an iterative cluster algorithm. Due to the different geometries of the ECAL barrel and endcap, different clustering algorithms are used in each region of the detector [81].

The first step of the process is identifying basic clusters of energy from groups of individual ECAL crystals. The energy deposited in a single crystal is referred to as a rechit. Basic clusters are assembled from a descending sorted list of ECAL rechits. If the E_T of a barrel rechit is above the 1 GeV E_T seed threshold, then it is a candidate basic cluster seed. The four crystals next to the seed crystal in η are added to the basic cluster making a 1×5 crystal strip in η-ϕ. The basic cluster is then grown, in the ϕ direction, into a supercluster by including crystal strips measuring 1×5 in η-ϕ, as long as the E_T in the $\eta\phi$-strip is greater than 0.1 GeV. A supercluster can expand up to 17 crystals in the ϕ direction. Any η-strips that touch each other are merged into the same supercluster. The supercluster is then cleaned by removing 1×5 basic clusters where the maximum crystal of the basic cluster has an E_T less than 0.35 GeV [83].

Since the endcap crystals are arranged in the xy-plane, and not the $\eta\phi$-plane, the basic clustering algorithm has to be fundamentally different. The clustering algorithm in the endcap also uses a list of rechits that are sorted by E_T. If the E_T of an endcap rechit is above 0.18 GeV E_T seed threshold, then the clustering process begins. The crystal is verified to be a local maximum by checking the neighboring crystals in a swiss cross pattern. If it is a local maximum, a 5×5 basic cluster is created around the seed crystal. If crystals in this 5×5 tower are already included in other basic

clusters they are excluded from being added to a new one. The outermost 16 crystals of an endcap basic cluster are allowed to be seeds for new basic clusters. Again, any crystals that are associated with the a basic cluster cannot be included in the new basic cluster. This allows basic clusters in the endcap to be placed adjacent to one another. Basic clusters with an E_T greater than 1 GeV are seeds for a supercluster. Basic clusters that have seed crystals within 0.07 radians in η and 0.3 radians in ϕ of the supercluster seed crystal are formed into a supercluster [84]. The ES can absorb a small amount of energy associated with an electromagnetic shower. The ES covers a range of $1.6 < |\eta| < 2.6$ and any supercluster within this must be corrected. This is calculated by summing all ES strips in the region between the supercluster and the primary vertex. The ES correction is the first in a long line of supercluster corrections that will be applied [83].

4.3.1 Shower Rescaling

The shape of the electromagnetic shower shape is a powerful tool in the $H \to \gamma\gamma$ analysis, because it separates signal from background and high resolution photons from low resolution photons. Several different shower shapes are used in the $H \to \gamma\gamma$ analysis: R_9, $\sigma_{i\eta i\eta}$, $\mathrm{cov}_{i\eta i\phi}$, $E_{2\times2}/E_{5\times5}$, σ_n, σ_ϕ, and σ_{RR}. These variables will be described in section 4.9.1. However, most of these variables are slightly mis-modeled in the Monte Carlo simulation. This is mostly due to the Geant4 release 9.4 causing wider showers than observed in data. The agreement between simulated and real data is improved by rescaling the simulated shower shapes using the linear transformation ($y = mx + b$), where the coefficients are determined by matching the Monte Carlo simulation with data. A $Z/\gamma^* \to ee$ sample is used to derive the corrections as listed in table 4.10.

TABLE 4.10

ELECTROMAGNETIC SHOWER RESCALING PARAMETERS

	Barrel		Endcap	
	b	m	b	m
R_9	0.0010	1.0045	-0.0007	1.0086
$E_{2\times2}/E_{5\times5}$	-0.01034	1.01894	-0.03642	1.04969
$\sigma_{i\eta i\eta}$	0.0009133	0.891832	0.00003	0.99470
σ_η	-0.000618	1.04302	0.001346	0.903254
σ_ϕ	-0.000371	1.00002	-0.00000048	0.99992

4.3.2 Conversion Reconstruction

Due to the large amount of material in front of the ECAL, up to 70% of photons, depending on η, convert to an e^+e^- pair before they reach the ECAL [85]. Converted photons have a larger shower cross-section when they impact the ECAL. This results in a lower energy resolution measurement for the photon because the energy is lost between the gaps of the ECAL crystals. However, if the conversion is reconstructed, it can then provide information on the z-position of the primary vertex, resulting in a more precise measurement of the opening angle between the photons. Conversions are reconstructed from three different track collections: standard tracks reconstructed by the default iterative tracking algorithm, GSF electron tracks that pass a Gaussian sum filter specifically designed to recognize electrons [86], and ECAL seeded tracks, which are tracks seeded from the external layers of the Tracker and the ECAL supercluster. Tracks are pre-selected if they pass two quality cuts: nHits > 4 and $\chi^2 < 10$. In order for a pair of tracks to be reconstructed as a conversion they must have opposite

charge, a distance of minimum approach greater than 0, and a $\Delta\cot(\theta) < 0.1$. The innermost track hit must also fall within the well instrumented region of the tracker ($\rho < 120$ cm and $z < 300$ cm). If the track pair satisfies all of these conditions, then the track pair is constrained to a single vertex and the momentum of the two tracks is refitted with respect to the new vertex. The $H \to \gamma\gamma$ conversion selection criteria requires the fit to a single vertex to converge, the χ^2 probability of the fit to be greater than 10^{-6}, and the p_T of the refitted track pair to be greater than 10 GeV. Once the conversion satisfies the selection criteria, it then has to be matched to a photon supercluster. Matching is done using the ΔR from the refitted conversion pair momentum and the supercluster position, where $\Delta R = \sqrt{\Delta\eta^2 + \Delta\phi^2}$. If the $\Delta R < 0.1$, then the conversion is matched to the supercluster [81, 87].

4.4 Photon Energy Resolution

Photon energy resolution is of the utmost importance in the $H \to \gamma\gamma$ analysis. The $H \to \gamma\gamma$ signal is a narrow peak on a broadly falling background. If the photon resolution is too coarse, then the signal will be lost in the background. There are three terms that determine the photon energy resolution: the channel inter-calibrations, transparency loss corrections, and supercluster energy corrections. The first two quantities are dependent on the ECAL crystals and not on the interacting object. The final term is depended on the shower shape, which is different for photons and electrons.

4.4.1 Crystal Inter-Calibration

The channel inter-calibration refers to the uniformity and time-stability of the individual ECAL crystals. The calibrations are derived during normal data taking from the decay of π^0 and η particles. In CMS, there is a large flux of these low mass mesons that decay directly to photon pairs. Using the well known invariant mass

of these particles, the response of each individual ECAL crystal can be measured. The inter-calibration is then validated in minimum bias events by examining the ϕ-invariance of the ECAL energy deposits and by measuring the ratio of the energy to the momentum of isolated electrons. The performance of the inter-calibrations on the $Z/\gamma^* \rightarrow ee$ peak can be seen in figure 4.1a and 4.1b [88].

4.4.2 Transparency Corrections

Over the course of normal LHC operations, the ECAL $PbWO_4$ slowly becomes damaged by hadronic and electromagnetic radiation. The radiation causes the formation of color centers that lowers the transparency of the crystals, which causes lower light collection efficiency and reduced photon statistics. The effect is more severe at higher η because of the larger particle flux. Once the collisions cease, the crystals slowly recover, but not completely. The end result is that the transparency of the ECAL crystals is constantly in flux and must be corrected for. The transparency of each crystal is monitored by the laser mentioned in section 3.2.4. The laser continuously monitors the transparency of the ECAL crystals during the beam abort gaps, which are periods during normal LHC operation where there are no collisions, and the transparency corrections are applied during photon reconstruction. The transparency corrections are validated on π^0's, η's, isolated electrons, and $Z/\gamma^* \rightarrow ee$ events [88].

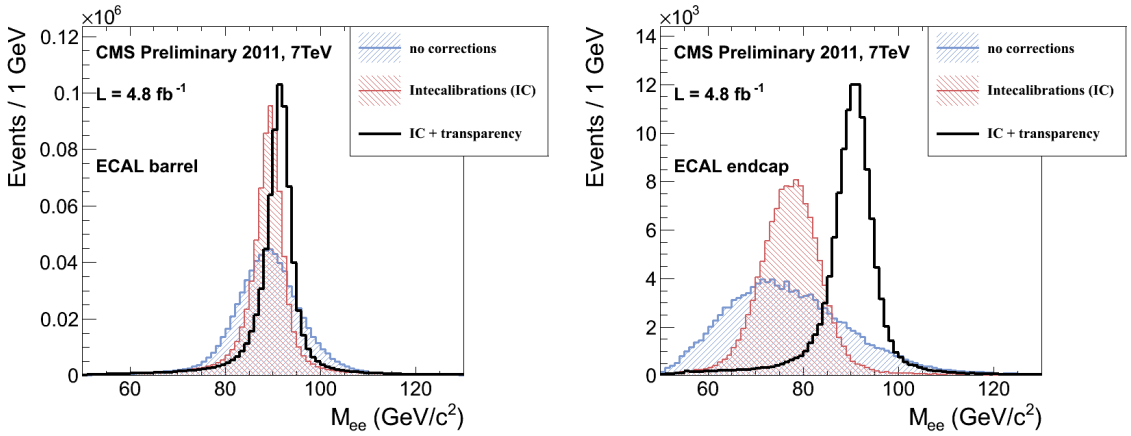

(a) ECAL Barrel (b) ECAL Endcap

Figure 4.1. The reconstructed Z peak from $Z/\gamma^* \to ee$ events in the ECAL barrel and endcap with and without inter-calibration and transparency corrections.

4.4.3 Supercluster Energy Corrections

The supercluster energy corrections adjust the photon supercluster energy for shower containment and losses for photons that begin showering in detector material before the ECAL. The corrections are calculated from a multivariate regression technique using a gradient boosted decision tree (BDT [89]). The regression is trained on the ratio of generator level photon energy to the supercluster energy for prompt photons from 3/4 of the events in a simulated $\gamma +$ jet sample. The regression input variables are the supercluster η and ϕ positions, shower shape variables, and the local cluster coordinates. A complete list can be found in table 4.11. The performance of the energy regression BDT can be seen in figure 4.2 [88].

TABLE 4.11

REGRESSION AND RESOLUTION BDT INPUTS

	2011 (7 TeV)	2012 (8 TeV)
Supercluster	Raw Energy, η, ϕ, R_9 $E_{5\times5}/E_{\mathrm{RAW}}$, η-width	Unchanged
Basic Cluster	η and ϕ of Lead, Sub-Lead, Sub-Final, and Final Crystals (EB Only)	η and ϕ of Lead Crystal Only
HCAL	CONE H/E (EB Only)	Tower H/E
ES	Raw Energy	Raw Energy and $E_{\mathrm{ps}}/E_{\mathrm{RAW}}$
Pileup	$\mathrm{N_{vtx}}$	$\mathrm{N_{vtx}}$ and ρ

An additional BDT is trained using the same input variables that provides a Gaussian uncertainty (σ_E) on the corrected energy provided by the regression BDT. The energy resolution estimation BDT is trained on the remaining quarter of the events in the γ + jet Monte Carlo simulation. Instead of the BDT being trained to return the generator energy of the photon, as the regression BDT, the energy resolution BDT is trained to return the difference between the energy regression BDT and the generator energy of the photon. The output of this BDT is then translated into a Gaussian uncertainty on the energy regression BDT. This methodology is used because the per-event mass resolution is a driving factor in the event categorization. It also ensures that the resolution estimation BDT has the same correlations as the regression BDT [88].

The methodology of the energy regression BDT and resolution estimation BDT

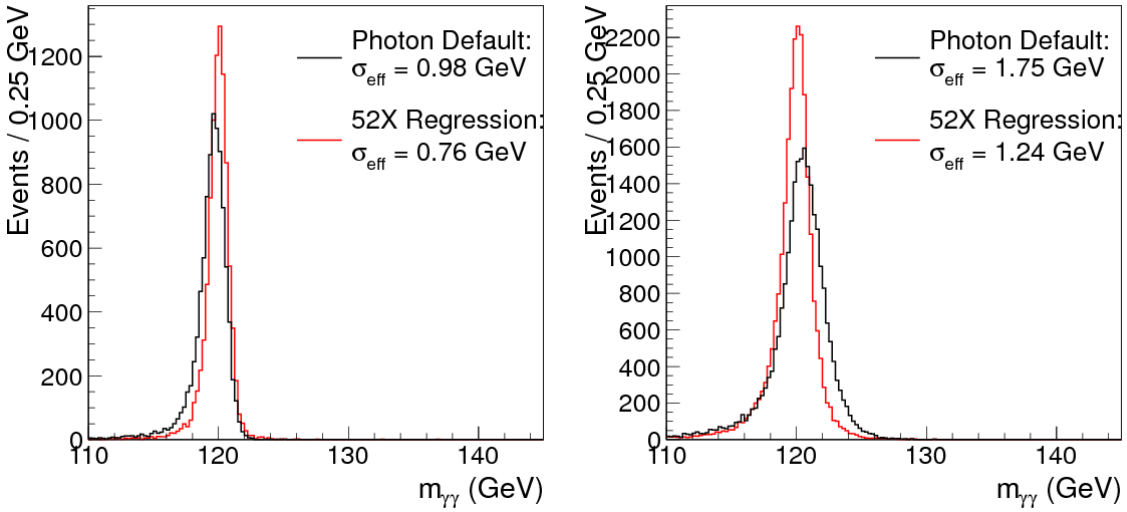

(a) Both EB, High R_9

(b) Both EB, Low R_9

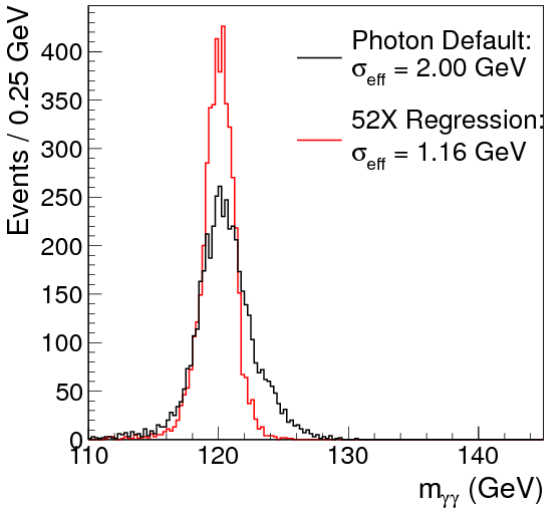

(c) One EE, High R_9

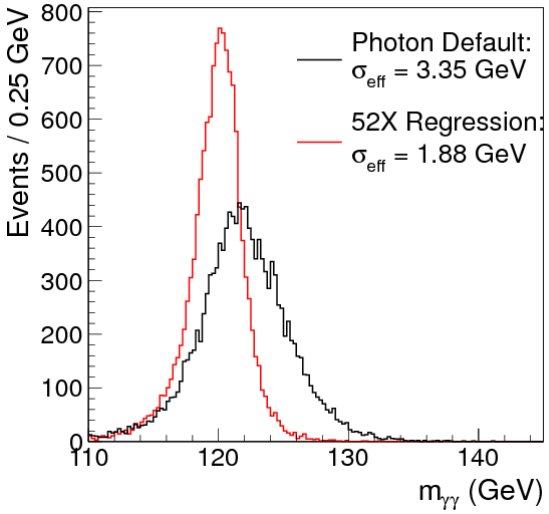

(d) One EE, Low R_9

Figure 4.2. Comparison of the invariant mass resolution for simulated $H \to \gamma\gamma$ events at 120 GeV. The resolution of the default supercluster resolution can be seen in black and the performance after the regression can be seen in red.

are validated $Z/\gamma^* \to ee$ events. It should be noted the $Z/\gamma^* \to ee$ events are different from $H \to \gamma\gamma$ events. Specifically, the p_T spectrum and the shower shape of electrons are different from that of the photons. In order to use $Z/\gamma^* \to ee$ events to validate the energy regression BDT, a separate regression is trained on electrons using the same variables as the photon regression. In figure 4.3, the measured energy resolution, from a fit to the $Z/\gamma^* \to ee$ peak, is compared to the value returned from the energy resolution estimation BDT. The resolution is shown in bins of predicted mass resolution (σ_m). σ_m is gathered from an un-binned likelihood fit of the $Z/\gamma^* \to ee$ peak using a Breit-Wigner,

$$f(x) = \left(\frac{1}{(x - M_Z)^2 + \frac{1}{4}\Gamma_Z^2} \right), \tag{4.4}$$

convoluted with a Crystal Ball function,

$$f(x) = N \cdot \begin{cases} e^{-\frac{(x-\overline{x})^2}{2\sigma^2}} & \text{for } \frac{x-\overline{x}}{\sigma} > -\alpha \\ \left(\frac{\gamma}{|\alpha|} - |\alpha| - \frac{x-\overline{x}}{\sigma} \right)^{-\gamma} \left(\frac{\gamma}{|\alpha|} \right)^{\gamma} e^{-|\alpha|^2/2} & \text{for } \frac{x-\overline{x}}{\sigma} \leq -\alpha. \end{cases} \tag{4.5}$$

The center and width of the Breit-Wigner is fixed to the PDG mass and width of the Z boson ($M_Z = 91.188$ GeV and $\Gamma_Z = 2.495$ GeV). The Gaussian width of the Crystal Ball function (σ) is taken as the smearing from the detector. Overall, the regression BDT provides a significant improvement in the energy resolution for both the ECAL barrel and endcaps for data and the Monte Carlo simulation. It can be seen in figure 4.3 that the resolution in data is worse than the Monte Carlo simulation. The difference between data and the Monte Carlo simulation is similar between both the energy regression BDT and that of the default superclusters. In order to resolve the inconsistent resolution between data and the simulation, additional smearing is applied to the Monte Carlo simulation. After the additional smearing is applied, a ± 0.10 variation in the smear correction is applied as a systematic uncertainty for the

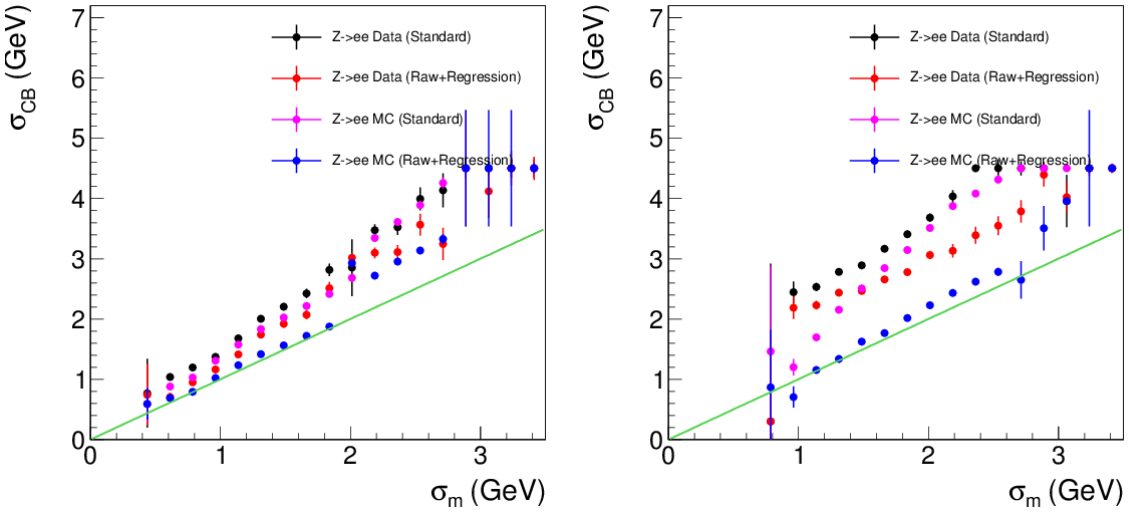

(a) EB Regression Performance

(b) EE Regression Performance

Figure 4.3. Comparison of the measured versus predicted invariant mass resolution in the ECAL barrel (left) and endcap (right).

photon resolution estimation BDT as seen in figure 4.4 [88].

4.4.4 Energy Scale Corrections

The supercluster energy scale is corrected by varying the energy scale to match that of a simulated $Z/\gamma^* \to ee$. A convolution of a Breit-Wigner and a Crystal Ball are fit to the $Z/\gamma^* \to ee$ peak from ECAL superclusters in data and Monte Carlo simulation. The difference between data and the Monte Carlo simulation is then used to extract the scale differences. The energy scale varies as a function of time and η, though it is similar in R_9. A two-step procedure is used to measure the energy scale corrections. First, the scale offset correction is extracted per run range for four η-bins (two bins in EB and two bins in EE). The second step is to compare the scale differences in data and the Monte Carlo simulation in the two different R_9 bins for each η-bin. This is done to factorize the effect of different amounts of tracker material in each of the η-bins. The final energy scale is calculated from the product of the

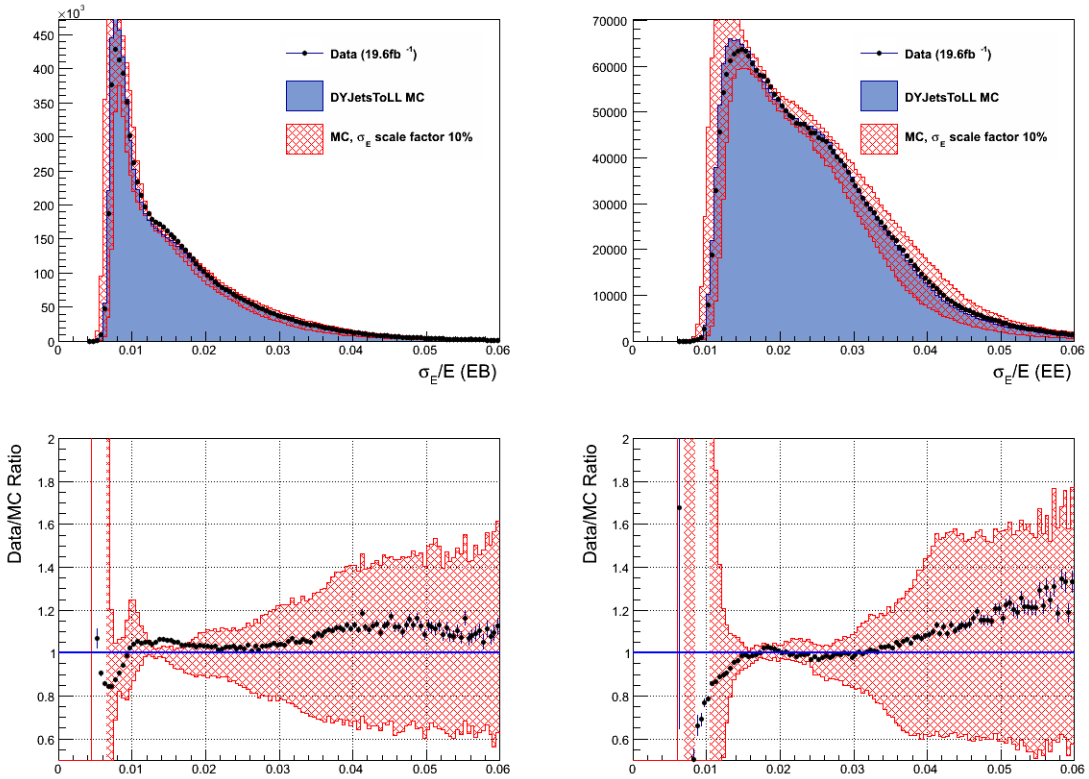

Figure 4.4. Distribution of the energy resolution from $Z/\gamma^* \to ee$ events with a ± 0.1 smearing systematic.

(run range)×(η-bin)×(R_9 categories). The scale difference is defined as

$$\Delta P = \frac{\Delta m_{\text{data}} - \Delta m_{\text{MC}}}{m_Z}. \tag{4.6}$$

The supercluster energy in data is then multiplied by $(1 - \Delta P)$ to place it at the correct scale [88].

4.4.5 Energy Smear Corrections

As seen in section 4.4.3 there is a discrepancy in the energy resolution in data compared to that of the Monte Carlo simulation. This resolution discrepancy is addressed by applying additional smearing to the Monte Carlo simulation. The energy smears are extracted from $Z/\gamma^* \to ee$ events in data. The electron supercluster energy is smeared by a Gaussian centered around the scale corrections derived in section 4.4.4 and with a resolution term $\Delta\sigma$. The electrons are split into eight η-categories. Then the $Z/\gamma^* \to ee$ invariant mass distribution is built for all the possible category combinations. This method uses the full $Z/\gamma^* \to ee$ dataset regardless of where the electrons impact the calorimeter. The smear numbers are calculated by maximizing the likelihood of the distributions of the invariant mass of the Z peak in data and Monte Carlo simulation as a function of ΔP and $\Delta\sigma$. The eight categories and their (σ_E/E) can be seen in tables 4.12 and 4.13 for 7 and 8 TeV. Examples of the $Z/\gamma^* \to ee$ mass distribution before and after smearing can be seen in figure 4.5. The $Z/\gamma^* \to ee$ invariant mass peak for electrons reconstructed as photons with the electron veto inverted can be seen in figures 4.6 [88].

TABLE 4.12

7 TEV SMEARINGS

Category	σ_E/E (%) Pho. regr. (New) No R_9 reweight
EB, $\|\eta\| < 1$, $R9 > 0.94$, NOT GAP	$0.67^{+0.10}_{-0.33} \pm 0.22$
EB, $\|\eta\| < 1$, $R9 > 0.94$, GAP	$0.77^{+0.06}_{-0.12} \pm 0.22$
EB, $\|\eta\| < 1$, $R9 < 0.94$	$0.96^{+0.05}_{-0.05} \pm 0.24$
EB, $\|\eta\| > 1$, $R9 > 0.94$	$1.41^{+0.15}_{-0.33} \pm 0.60$
EB, $\|\eta\| > 1$, $R9 < 0.94$	$1.96^{+0.06}_{-0.07} \pm 0.59$
EE, $\|\eta\| < 2$, $R9 > 0.94$	$2.68^{+0.15}_{-0.20} \pm 0.90$
EE, $\|\eta\| < 2$, $R9 < 0.94$	$2.79^{+0.09}_{-0.10} \pm 0.30$
EE, $\|\eta\| > 2$, $R9 > 0.94$	$2.93^{+0.08}_{-0.08} \pm 0.34$
EE, $\|\eta\| > 2$, $R9 < 0.94$	$3.01^{+0.11}_{-0.12} \pm 0.52$

TABLE 4.13

8 TEV SMEARINGS

Category	σ_E/E (%)
EB, $\|\eta\| < 1$, $R_9 > 0.94$	$1.11 \pm 0.07 \pm 0.22$
EB, $\|\eta\| < 1$, $R_9 < 0.94$	$1.07 \pm 0.06 \pm 0.24$
EB, $\|\eta\| > 1$, $R_9 > 0.94$	$1.55 \pm 0.40 \pm 0.60$
EB, $\|\eta\| > 1$, $R_9 < 0.94$	$1.94 \pm 0.11 \pm 0.59$
EE, $\|\eta\| < 2$, $R_9 > 0.94$	$2.95 \pm 0.25 \pm 0.90$
EE, $\|\eta\| < 2$, $R_9 < 0.94$	$2.76 \pm 0.13 \pm 0.30$
EE, $\|\eta\| > 2$, $R_9 > 0.94$	$3.70 \pm 0.11 \pm 0.34$
EE, $\|\eta\| > 2$, $R_9 < 0.94$	$3.71 \pm 0.16 \pm 0.52$

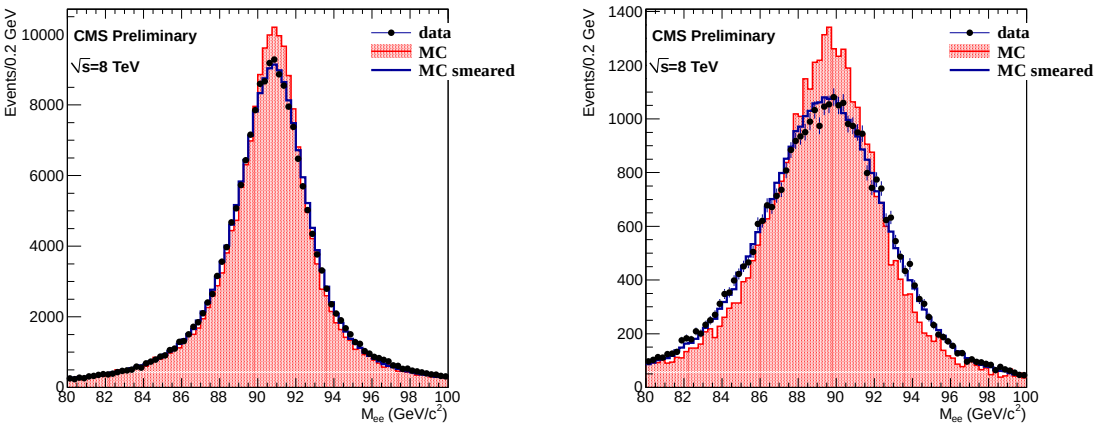

Figure 4.5. The invariant mass distribution of $Z/\gamma^* \to ee$ events in two of the smearing categories: EB, $|\eta| < 1$, $R_9 > 0.94$ (left) and EB, $|\eta| > 1$, $R_9 < 0.94$ (right).

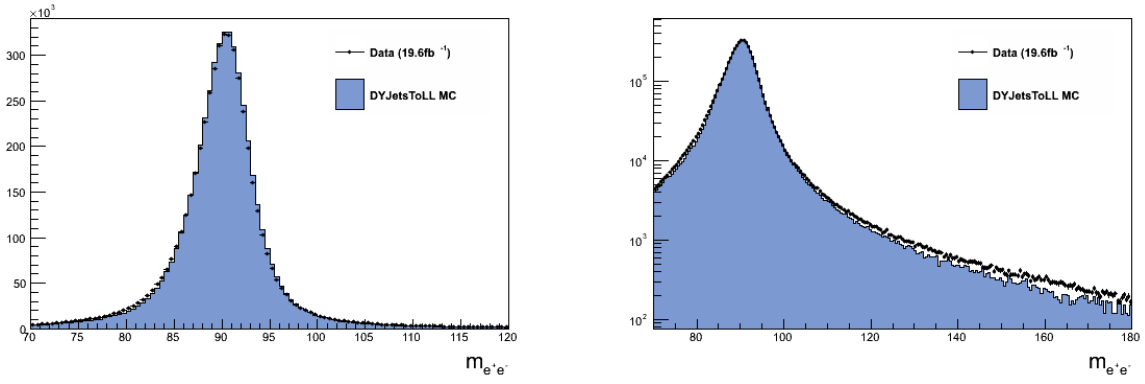

Figure 4.6. The invariant mass distribution of $Z/\gamma^* \to ee$ events where the electrons are reconstructed as photons that pass the analysis pre-selection with an inverted electron veto.

4.4.6 Energy Scale and Smear Systematics

The energy scales and smears from sections 4.4.4 and 4.4.5 introduce a systematic uncertainty because they are calculated from electrons and not photons. Figure 4.7a compares the R_9 distribution from $Z/\gamma^* \to ee$ events and $H \to \gamma\gamma$ at 90 GeV. It can be seen that the electrons have a larger R_9 due to Bremsstrahlung radiation. Figure 4.7b shows the fraction of electrons and photons with an $R_9 > 0.94$, and demonstrates the R_9 dependence on η. In order to use $Z/\gamma^* \to ee$ events to validate the $H \to \gamma\gamma$ analysis, the electrons in $Z/\gamma^* \to ee$ events are re-weighted, taking into account the difference in R_9 distribution and the R_9-η dependance.

The systematic uncertainty associated with the re-weighting is evaluated by shifting the R_9 category boundary at 0.94. The maximum change in the R_9 value from the nominal one is then used as the systematic R_9 uncertainty. The systematic uncertainty associated with the difference between electrons and photons is evaluated by comparing the difference between the photon and electron tuned regression on $Z/\gamma^* \to ee$ events. The p_T cut and electron identification cuts are also varied to estimate the systematic uncertainty. The systematic uncertainties on the energy

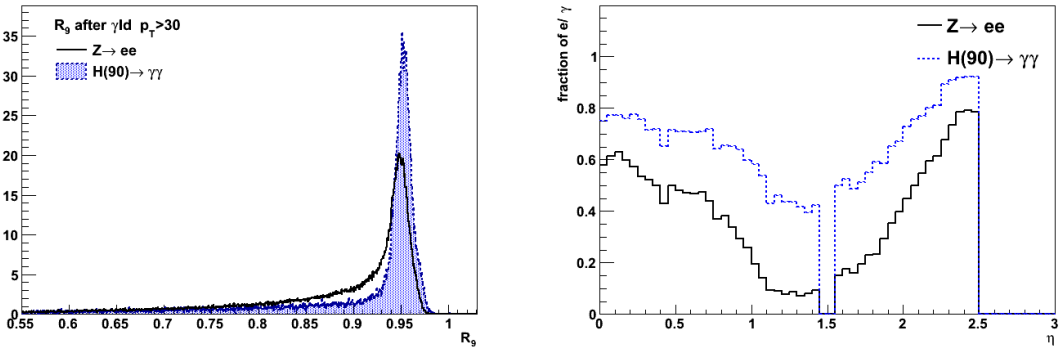

(a) R_9 distribution of photons from $H \to \gamma\gamma$ and electrons in $Z/\gamma^* \to ee$

(b) Fraction of events with an $R_9 > 0.94$ for electrons and photons.

Figure 4.7. R_9 Comparison for $H \to \gamma\gamma$ and $Z/\gamma^* \to ee$.

scale and smears can be seen in tables 4.14 and 4.15, respectively. The combined uncertainty on σ_E is

$$\sigma = \sqrt{\max(\Delta R_9)^2 + \Delta_{\text{PhoRegr}} + \max(\Delta p_T)^2 + \Delta^2_{\text{sel}}}. \tag{4.7}$$

4.5 Pileup

In order to trust the comparisons between data and Monte Carlo simulation, the distributions of the number of pileup vertices needs to match between data and the Monte Carlo simulation. However, when the Monte Carlo simulation is produced, it is with a pileup distribution that does not match data, this is because the distribution of the number of pileup vertices in data is not known a-priori. Additionally, the observed distribution of the number of reconstructed vertices can be affected by the offline event selection and triggering. In order to avoid the differences in the underlying event reconstruction in the Monte Carlo simulation and data, the number of pileup

TABLE 4.14

ENERGY SCALE SYSTEMATIC UNCERTAINTIES FOR DATA.

ECAL Region	7 TeV $\Delta E/E$ Syst (%)	8 TeV$\Delta E/E$ Syst (%)
EB, $\|\eta\| < 1$, $R_9 > 0.94$	0.19	0.20
EB, $\|\eta\| < 1$, $R_9 < 0.94$	0.13	0.20
EB, $\|\eta\| > 1$, $R_9 > 0.94$	0.71	0.71
EB, $\|\eta\| > 1$, $R_9 < 0.94$	0.51	0.51
EE, $\|\eta\| < 2$, $R_9 > 0.94$	0.88	0.88
EE, $\|\eta\| < 2$, $R_9 < 0.94$	0.18	0.18
EE, $\|\eta\| > 2$, $R_9 > 0.94$	0.19	1.2
EE, $\|\eta\| > 2$, $R_9 < 0.94$	0.28	1.2

TABLE 4.15

ENERGY SMEAR SYSTEMATIC UNCERTAINTIES

ECAL Region	7 TeV σ_E/E (Syst) (%)	8 TeV σ_E/E (Syst) (%)
EB, $\|\eta\| < 1$, $R_9 > 0.94$	0.22	0.23
EB, $\|\eta\| < 1$, $R_9 < 0.94$	0.24	0.25
EB, $\|\eta\| > 1$, $R_9 > 0.94$	0.60	0.72
EB, $\|\eta\| > 1$, $R_9 < 0.94$	0.59	0.60
EE, $\|\eta\| < 2$, $R_9 > 0.94$	0.90	0.93
EE, $\|\eta\| < 2$, $R_9 < 0.94$	0.30	0.33
EE, $\|\eta\| > 2$, $R_9 > 0.94$	0.34	0.36
EE, $\|\eta\| > 2$, $R_9 < 0.94$	0.52	0.54

interactions from the simulated truth is re-weighted to the target pileup distribution in data. The pileup distribution in data is derived from the per bunch-crossing instantaneous luminosity of each luminosity section, 2^{20} orbits or 93.2 s [90], and the total proton-proton inelastic cross-section of 69.4 mb. In order to validate the pileup re-weighting technique, the distribution of the number of vertices in $Z \to \mu\mu$ events in data is compared to re-weighted, simulated $Z/\gamma^* \to ee$ events. The comparison of the distribution of the number of primary vertices can be seen in figure 4.8.

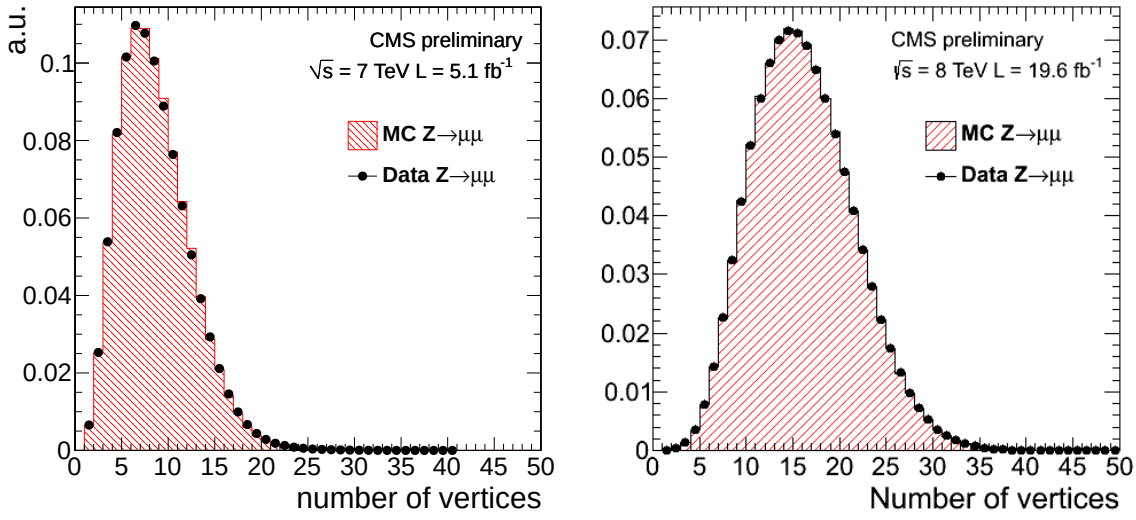

Figure 4.8. The number of reconstructed vertices in data (black) and re-weighted, simulated $Z \to \mu\mu$ events (red hash) for 7 (left) and 8 (right) TeV.

4.5.1 Beamspot

The Monte Carlo simulation samples used to model the signal have a simulated beamspot width (σ_{BS}) of 6.2 cm, where the beamspot width is the mean Gaussian

width of the z-position for all the vertices in the event. The actual σ_{BS} for 2012 data taking is approximately 5 cm. A special set of gluon fusion Monte Carlo simulation samples are produced to study the affect σ_{BS} has on $H \to \gamma\gamma$ invariant mass resolution. It is observed that a smaller beamspot resulted in a narrower Higgs boson invariant mass peak. When the width of the beamspot is smaller, the impact on the direction measurement of the two photons from selecting the incorrect primary vertex is smaller, hence the invariant mass resolution is better. In order to correct for this effect, all the Higgs signal samples have their beamspot re-weighted to 5 cm with the following procedure:

- If the selected vertex is within 0.1 cm of the generator vertex ($\Delta Z_{\text{Sel-Gen}}$) no re-weighting is needed in figure 4.9.
- If ($\Delta Z_{\text{Sel-Gen}}$) > 0.1 cm then the event is re-weighted based on the ratio of a double Gaussian fit to $\Delta Z_{\text{Sel-Gen}}$ for the 4.8 cm sample and the 6.2 cm sample, as seen in figure 4.10.

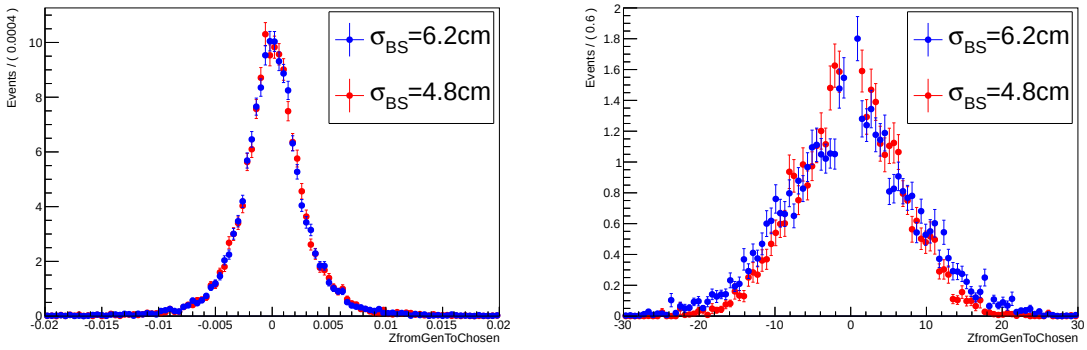

Figure 4.9. The distribution of $\Delta Z_{\text{Sel-Gen}}$ for Monte Carlo simulation samples with $\sigma_{BS} = 6.2$ cm (blue) and $\sigma_{BS} = 4.8$ cm (red) for events where $\Delta Z_{\text{Sel-Gen}} < 0.1$ cm (left) and $\Delta Z_{\text{Sel-Gen}} > 0.1$ cm (right).

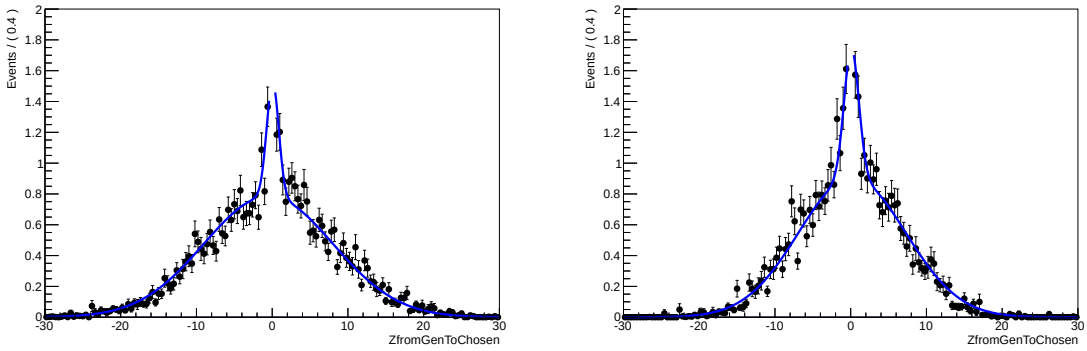

Figure 4.10. The double Gaussian fit to $\Delta Z_{\text{Sel-Gen}}$ for the old (left) and new (right) beamspot widths. The ratio of the fits is used to re-weight the Monte Carlo simulation events.

The $H \to \gamma\gamma$ signal models can be seen in 4.11b, 4.11a, and 4.11c with beamspot widths of 4.8 cm, 6.2 cm, and re-weighted to 5 cm, respectively. The re-weighting procedure is validated on $Z \to \mu\mu$ events in data and Monte Carlo simulation after removing the muon tracks to emulate a $H \to \gamma\gamma$ event. The distribution of the ΔZ between the selected and true vertex can be see in figure 4.12 for data and Monte Carlo simulation. The beamspot re-weighting is only applied to the 8 TeV Monte Carlo simulation because the beamspot width for the 7 TeV data and Monte Carlo simulation are in very good agreement.

4.6 Particle Flow

The goal of particle flow (PF) is to identify every individual particle produced in a proton-proton collision by coherently combining the information of all the sub-detectors. This is done with iterative tracking and clustering techniques, and then linking the tracks and clusters together to form physics objects. The particle flow algorithm receives most of its power from the fine granularity and resolution of the pixel and strip tracker. But the fine granularity of the ECAL also aids in particle

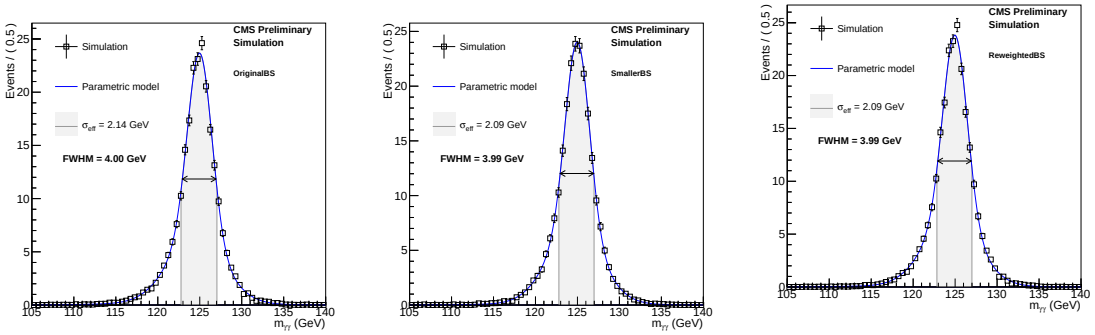

(a) $\sigma_{BS} = 6.2$ cm (b) $\sigma_{BS} = 4.8$ cm (c) $\sigma_{BS} = 5.0$ cm (re-weighted)

Figure 4.11. Comparison of the different signal models in simulated gluon fusion $H \to \gamma\gamma$ with beamspot widths of 6.2, 4.8, and re-weighted 5.0 cm in figures 4.11a, 4.11b, and 4.11c, respectively.

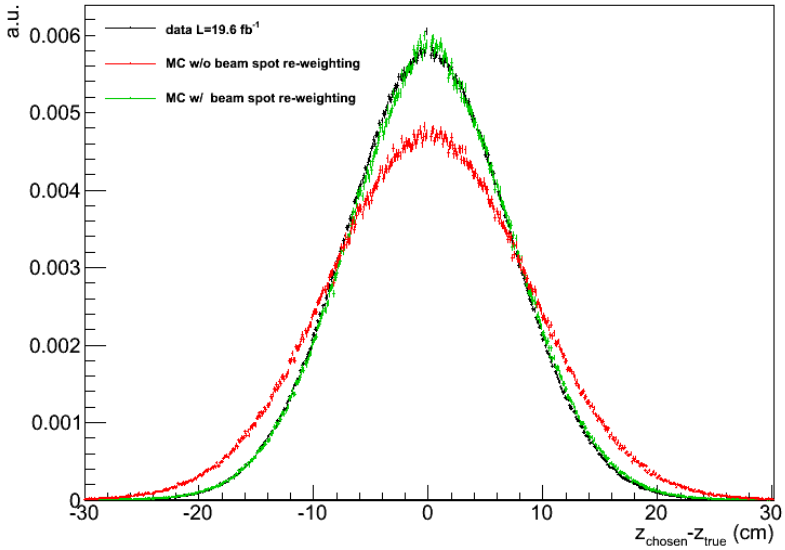

Figure 4.12. The distribution of ΔZ between the selected and true vertex for data, Monte Carlo simulation, and re-weighted Monte Carlo simulation in $Z \to \mu\mu$ events.

flow reconstruction. Particle flow reconstruction is used in $H \to \gamma\gamma$ for evaluating the photon isolation and for jet reconstruction. In both cases the particle flow techniques perform much better than the more traditional detector-based algorithms.

4.6.1 Iterative Tracking

The first step of the particle flow reconstruction process is constructing particle flow tracks. This is done with an iterative tracking algorithm. It is designed to have high efficiency and low fake rates. The first iteration of the tracking algorithm looks for tracks that are seeded and reconstructed with very tight criteria. After the first iteration, the hits in the tracker associated with the best tracks are removed. The tracking algorithm is then run again on the remaining track hit collection but with looser criteria. In the first three iterations 90% of the tracks for charged hadrons are reconstructed. The fourth and fifth iterations have even looser constraints on the origin of the tracks, which enables the reconstruction of tracks from displaced vertices such as photon conversions, nuclear interaction, and hadronic decays.

4.6.2 Calorimeter Clustering

The primary purposes of the particle flow clustering algorithm are:

1. Measure the four-momentum of un-charged particles (e.g., photons and neutral hadrons).
2. Separate the energy deposits of neutral particles from that of charged particles.
3. Correctly group Bremsstrahlung photons with their source electrons.
4. Assist in the measurement of charged hadronic particles that have either low track quality or high p_T.

The particle flow clustering algorithm is designed to have high detection efficiency for low energy particles and to separate energy deposits that are close together. First, the PF clustering algorithm locates cluster seeds, which are calorimeter energy deposits

that are the local maxima. Then clusters are grown around the seeds by adding cells that are adjacent to the seed or cells that have already been added to the cluster. Each added cell must have an energy that is above the 2σ noise level for that sub-detector (80 MeV EB, 300 MeV EE, and 800 MeV HCAL). Each cluster seed creates one particle cluster. The energy in the cells that are in multiple PF clusters can be shared between PF clusters depending on its distance to the seed [91].

4.6.3 Link Algorithm

Once the PF tracks and PF clusters are created they are linked together. This is because many physics object: muons, electrons, and charged hadrons, leave deposits in multiple sub-detectors. The link algorithm looks at any two PF objects in the event and evaluates whether or not the two objects should be grouped together. The link algorithm then blocks the elements that are linked together, typically less than three PF objects. Due to the fine granularity of the detector, complicated events have more blocks and not more objects per block. Below are examples of several different links the algorithm searches for:

- Charged tracks propagated to the cell that contains the expected longitudinal shower maximum for electrons in the ECAL.
- Charged tracks propagated to an HCAL depth corresponding to one nuclear interaction length. (In both the ECAL and HCAL case, if the expected cell position is along the boundary of a cell then the search area is expanded to include the neighboring cell or cells.)
- ECAL clusters that are positioned along the tangents of GSF tracks are linked with that track in order to recover Bremsstrahlung radiation.
- Clusters near each other but in different sub-detectors are also linked and the cluster position is assigned to the sub-detector with the greatest granularity (ES>ECAL>HCAL).
- Charged particle tracks are linked with a muon track if the χ^2 is low enough. If there are multiple tracks and multiple muon tracks only the link that has the minimum χ^2 is kept [91].

4.6.4 Particle Flow Reconstruction and Identification

Once the links are assigned, the particle flow blocks are identified. This processes involves analyzing each block and identifying PF elements within the block. Once a PF element is identified, it is removed from the block. The PF blocks are reconstructed into PF elements in the following order:

Particle Flow Muons
PF muons are reconstructed from linked tracks and muon tracks, if its combined momentum is within 3σ of the momentum measurement of the tracker.

Particle Flow Electrons
PF electrons are reconstructed from tracks that pass a Gaussian-Sum Filter (GSF). The GSF track is then propagated to the calorimeters and linked with a PF cluster and possible Bremsstrahlung photons are associated with the GSF track. The information is then passed to a BDT that distinguishes between pions and electrons. If the candidate PF electron has a BDT score greater than -0.1, it is considered a PF electron.

Particle Flow Charged Hadrons
PF charged hadrons are constructed from PF tracks that pass an additional resolution selection and PF clusters. When the PF tracks are linked the PF clusters, multiple tracks can be associated to a single cluster if that cluster energy is near to the combined energy of the charged tracks. However, multiple clusters cannot be grouped with a single track, and only the track nearest the cluster can be linked. If the PF cluster is not significantly greater than the PF track, then they are linked as a PF charged hadron. In this case the energy is measured from a combination of the tracker and calorimeter measurements. Any remaining PF tracks not associated with PF clusters have their momentum and energy directly measured by the tracker under the charged pion mass hypothesis.

Particle Flow Photon
PF photons are constructed from the remaining PF clusters inside the ECAL. PF photons can be associated with tracks as long as the PF track energy is significantly lower then the ECAL cluster energy.

Particle Flow Neutral Hadrons
PF neutral hadrons are constructed from the remaining PF clusters that are in the HCAL.

After a particle flow element is constructed it cannot belong to any other PF element in order to limit double counting of energy. Once all PF elements are assembled,

PF jets, PF taus, and PF $\not\!\!E_T$ are reconstructed from the PF elements. PF jets are assembled from PF charged particles, photons, and neutral hadrons. PF $\not\!\!E_T$ is calculated by taking the negative of the sum of all the transverse components of the final particle flow objects in the event [91]. Both PF jets and PF $\not\!\!E_T$ are later used in the $H \to \gamma\gamma$ analysis to form exclusive categories to the Higgs boson search. The jet energy and $\not\!\!E_T$ measurements from particle flow have better resolution than traditional detector based methods, because the energy between the sub-detectors is not double counted and the response of the detector is calibrated independently for all the different particle flow objects. The jet energy measurement is also less affected from pileup, because charged hadrons from pileup vertices do not alter the energy of the jet. Additionally, isolation parameters assembled from charged hadrons, neutral hadrons, and photons are used for photon identification. Particle flow isolation is used because it is less dependent on pileup than traditional detector based isolation. The matching between the charged tracks and calorimeter deposits associates energy in the calorimeter with a particular vertex. This is useful because the energy deposited by charged hadrons from other pileup vertices in the event do not spoil the isolation of the photon.

4.7 Event Preselection

All events in the $H \to \gamma\gamma$ analysis are required to have two photons that pass a basic pre-selection. The pre-selection is the same for the main analysis and the cuts-in-categories (CiC) cross-check. The initial cut is on the η of the supercluster. In order for a photon to be classified as a barrel photon it must have a supercluster $|\eta| < 1.4442$. For a photon to be within the fiducial region of the endcap, the photon must fall within the range of $1.566 < |\eta| < 2.5$. The next set of pre-selection cuts is dependent on the shower shape variable R_9. Narrow photons with high R_9 pass a set of shower shape, H/E, loose isolation requirements. Photons with a broad ECAL

TABLE 4.16

7 TEV PRE-SELECTION CUTS

Cut Variable	Region	$R_9 > 0.9$	$R_9 \leq 0.9$
H/E	Barrel	< 0.082	< 0.075
	Endcap	< 0.075	
$\sigma_{i\eta i\eta}$	Barrel	< 0.014	
	Endcap	< 0.034	
EtCorrEcalIso	Barrel and Endcap	< 50 GeV	< 4 GeV
EtCorrHcalIso	Barrel and Endcap	< 50 GeV	< 4 GeV
EtCorrTrkIso	Barrel and Endcap	< 50 GeV	< 4 GeV
PuCorrHcalEcal	Barrel and Endcap	< 3 GeV	
AbsTrkIsoCIC	Barrel and Endcap	< 2.8 GeV	
HollowConeTrkIsoDr03	Barrel and Endcap	< 4 GeV	

footprint have to pass similar cuts but with a tighter isolation selection. It should also be noted that the cut on $\sigma_{i\eta i\eta}$ is different for EB and EE due to differences in the material budget and crystal geometry. A full set of cuts can be seen in tables 4.16 and 4.17 for 7 and 8 TeV [81].

The efficiency of the photon pre-selection is measured using a tag-and-probe technique with $Z/\gamma^* \to ee$ events with the electron veto inverted. This technique is used to compute the pre-selection efficiencies in tables 4.18 and 4.19 for 7 and 8 TeV.

The efficiency of the conversion safe electron veto is measured on $Z \to \mu\mu\gamma$ events

TABLE 4.17

8 TEV PRE-SELECTION CUTS

Cut Variable	Region	$R_9 > 0.9$	$R_9 \leq 0.9$
H/E	Barrel	< 0.082	< 0.075
	Endcap	< 0.075	
$\sigma_{i\eta i\eta}$	Barrel	< 0.014	
	Endcap	< 0.034	
E_T Corrected HCAL Iso.	Barrel and Endcap	< 50 GeV	< 4 GeV
E_T Corrected Track Iso.	Barrel and Endcap	< 50 GeV	< 4 GeV
Charged Particle Flow Iso.	Barrel and Endcap	< 50 GeV	< 4 GeV

TABLE 4.18

7 TEV PRE-SELECTION EFFICIENCIES

Category	$\epsilon \pm \sigma_{\mathrm{STAT}}$ (DATA)	$\epsilon \pm \sigma_{\mathrm{STAT}}$ (MC)	Ratio$\pm\sigma_{\mathrm{STAT}}$
EB R9>0.9	0.92267±0.00123	0.93005±0.00061	0.99206±0.00148
EB R9<0.9	0.88820±0.00231	0.89051±0.00097	0.99741±0.00281
EE R9>0.9	0.94421±0.00104	0.92904±0.00003	1.01633±0.00112
EE R9<0.9	0.86387±0.00001	0.84688±0.00134	1.02007±0.00161

TABLE 4.19

8 TEV PRE-SELECTION EFFICIENCIES

Category	$\epsilon \pm \sigma_{\mathrm{STAT}} \pm \sigma_{\mathrm{SYST}}$ (DATA)	$\epsilon \pm \sigma_{\mathrm{STAT}}$ (MC)	Ratio$\pm\sigma_{\mathrm{STAT}}$
EB R_9 >0.90	0.9864±0.0002±0.0030	0.9897±0.0001	0.997±0.003
EB R_9 <0.90	0.9406±0.0007±0.0055	0.9614±0.0003	0.978±0.006
EE R_9 >0.90	0.9880±0.0003±0.0090	0.9824±0.0002	1.006±0.009
EE R_9 <0.90	0.9368±0.0012±0.0170	0.9460±0.0004	0.990±0.018

in data and Monte Carlo simulation. The γ in $Z \to \mu\mu\gamma$ events must pass the pre-selection described above, a cut-based (CiC4PF) photon identification cut, and the three-body mass must be between 70 and 110 GeV. The efficiency is measured by taking the ratio of the number of events with photons that pass the conversion safe electron veto to the total number of $Z \to \mu\mu\gamma$ events. The efficiency of the conversion safe electron veto can be seen in table 4.20.

TABLE 4.20

CONVERSION-SAFE ELECTRON VETO EFFICIENCIES

Category	$\epsilon \pm \sigma_{\mathrm{STAT}}$ (DATA)	$\epsilon \pm \sigma_{\mathrm{STAT}}$ (MC)	Ratio$\pm\sigma_{\mathrm{STAT}}$
EB R_9 >0.94	0.998±0.001	1.000±0.000	0.995±0.001
EB R_9 <0.94	0.986±0.002	0.993±0.002	0.998±0.001
EE R_9 >0.94	0.991±0.002	0.998±0.001	0.992±0.002
EE R_9 <0.94	0.962±0.004	0.972±0.005	0.990±0.007

4.7.1 Photon Pre-Selection Systematics

The pre-selection efficiency is measured in $Z/\gamma^* \to ee$ events with an inverted electron veto. The systematic uncertainties for the pre-selection efficiency are estimated by re-weighting the R_9 and E_T distribution of the electrons from $Z/\gamma^* \to ee$ to that of photons from $H \to \gamma\gamma$ at 120 GeV. Then the pre-selection efficiency is calculated again after the re-weighting and the difference is treated as a systematic uncertainty.

4.8 Vertex Selection

As seen in equation 4.2, the mass resolution is driven by two factors: the energy resolution of each of the photons and the resolution of the opening angle between the two photons ($\theta_{\gamma\gamma}$). The opening angle of the two photons is determined by two factors: supercluster position and vertex location. The supercluster position is well measured due to the fine granularity of the ECAL. So, it is important to select the correct primary vertex from all the pileup vertices. In the 8 TeV data there are 19.9 mean pileup vertices spread over 5 cm in z due to the high number of interactions per

bunch crossing.[1] This complicates the vertex selection process, because the primary method of Higgs boson production is gluon-gluon fusion, which produces only a Higgs boson and no high p_T tracks. So the primary vertex of the Higgs boson looks very similar to the numerous pileup vertices. It has been shown that a displacement of 1 cm from the true vertex has a minimal effect on the mass resolution. So if the primary vertex is within 1 cm of the true vertex, then it is considered to be the correct vertex.

In order to select the correct vertex in di-photon events, a BDT is used to assign a score to each vertex. The vertex selection BDT is trained on $H \to \gamma\gamma$ Monte Carlo simulation and takes four inputs:

$$\begin{aligned} &\sum_i |\vec{p}_T^{\,i}|^2, \\ &-\sum_i \left(\vec{p}_T^{\,i} \cdot \frac{\vec{p}_T^{\,\gamma\gamma}}{|\vec{p}_T^{\,\gamma\gamma}|} \right), \\ &\frac{\left| \sum_i \vec{p}_T^{\,i} \right| - \vec{p}_T^{\,\gamma\gamma}}{\left| \sum_i \vec{p}_T^{\,i} \right| + \vec{p}_T^{\,\gamma\gamma}}, \quad \text{and} \\ &\frac{|Z_{vertex} - Z_{\rm conv}|}{\sigma_{\rm conv}}. \end{aligned} \tag{4.8}$$

The first value is the sum p_T squared of all the tracks associated with a given vertex. The second term is the p_T balance of the vertex. The third quantity is the p_T asymmetry of the tracks associated with the vertex. The fourth term is the pull to the z-position of the primary vertex from a photon matched to a conversion. If both photons are matched to a conversion, then the resolution weighted average z-position is used. While the first variable is the default quantity used by CMS to select the primary vertex, the second and third quantities take advantage of the fact that the

[1]The smearing in the xy-plane due to pileup is negligible because the bunches are narrow in x and y. The only ambiguity is the z-position of the primary vertex due to multiple proton-proton scatterings as the bunches pass through each other.

Higgs recoils off the underlying event. Since the $H \to \gamma\gamma$ decay is trackless, unless a photon converts, the p_T balance and asymmetry are greater for Higgs vertices when compared to ordinary pileup vertices [81].

4.8.1 Conversions

In events where one or both of the photons convert to an e^+e^- pair, the pointing information of the conversion tracks is used to determine the z-position of the primary vertex. If a photon is matched to a conversion, as detailed in section 4.3.2, two methods are used to determine the primary vertex of the Higgs. The first method uses the angle α between the conversion vertex and the refitted conversion tracks. The z-position of the primary vertex is calculated as

$$Z_{PV} = Z_{\text{conv}} - R_{\text{conv}} \times \cot(\alpha), \tag{4.9}$$

where Z_{conv} and R_{conv} are the z and ρ positions of the conversion vertex. The second method uses the position of the supercluster and conversion vertex to calculate the z-position of the primary vertex via

$$Z_{PV} = \frac{Z_{\text{conv}} - R_{\text{conv}}}{(R_{SC} - R_{\text{conv}})(Z_{SC} - Z_{\text{conv}})}, \tag{4.10}$$

where Z_{SC} and R_{SC} are the z and ρ positions of the supercluster. A diagram of the two techniques can be seen in figure 4.13. The reason for the two different methods is that there is significant performance degradation in the TIB, TOB, and TEC, as defined in section 3.2.3.2, for method 4.9, because there are to few tracker hits for the conversion legs to provide a high-resolution measurement of the conversions direction. Hence in these regions, method 4.10 is used because the supercluster position provides better position information than the direction measurement from the conversion tracks. The z-resolution of the conversions is measured in γ+jet data and Monte Carlo simulation

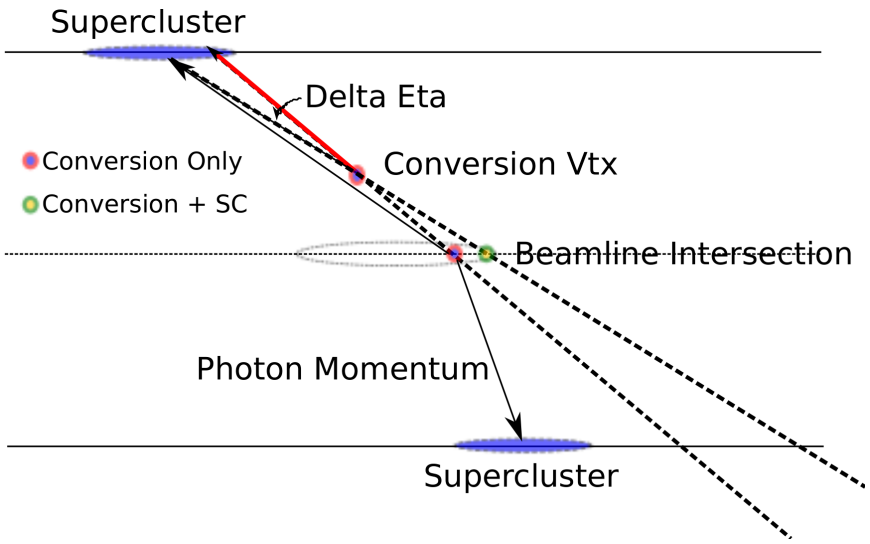

Figure 4.13. A diagram of the two conversion vertexing techniques used in the $H \to \gamma\gamma$ analysis. The conversion only method is used in the Pixel Barrel, Pixel Endcap, and TIB. The conversion + SC method is used in the TIB, TOB, and TEC.

and can be seen in figure 4.14 for all tracker regions. The γ + jet events are used because the tracks associated with the jet identify the correct vertex, which is then used to check the conversion performance. From the distributions in figure 4.14, the effective sigma is calculated and can be seen in table 4.21. The total conversion vertex efficiency in the six tracker regions can be seen in figure 4.15, where the efficiency is defined as the fraction of conversions where the z-position from the conversion is within 3, 5, or 10 mm of the vertex selected by the jet [81].

4.8.2 Vertex Selection BDT Performance

The performance of the vertex identification BDT is measured in data and Monte Carlo simulation in $Z \to \mu\mu$ events. In order to mimic a $H \to \gamma\gamma$ event, the high p_T tracks of the muon are removed when the BDT evaluates the event. The output of the vertex selection BDT and its performance in data and Monte Carlo simulation

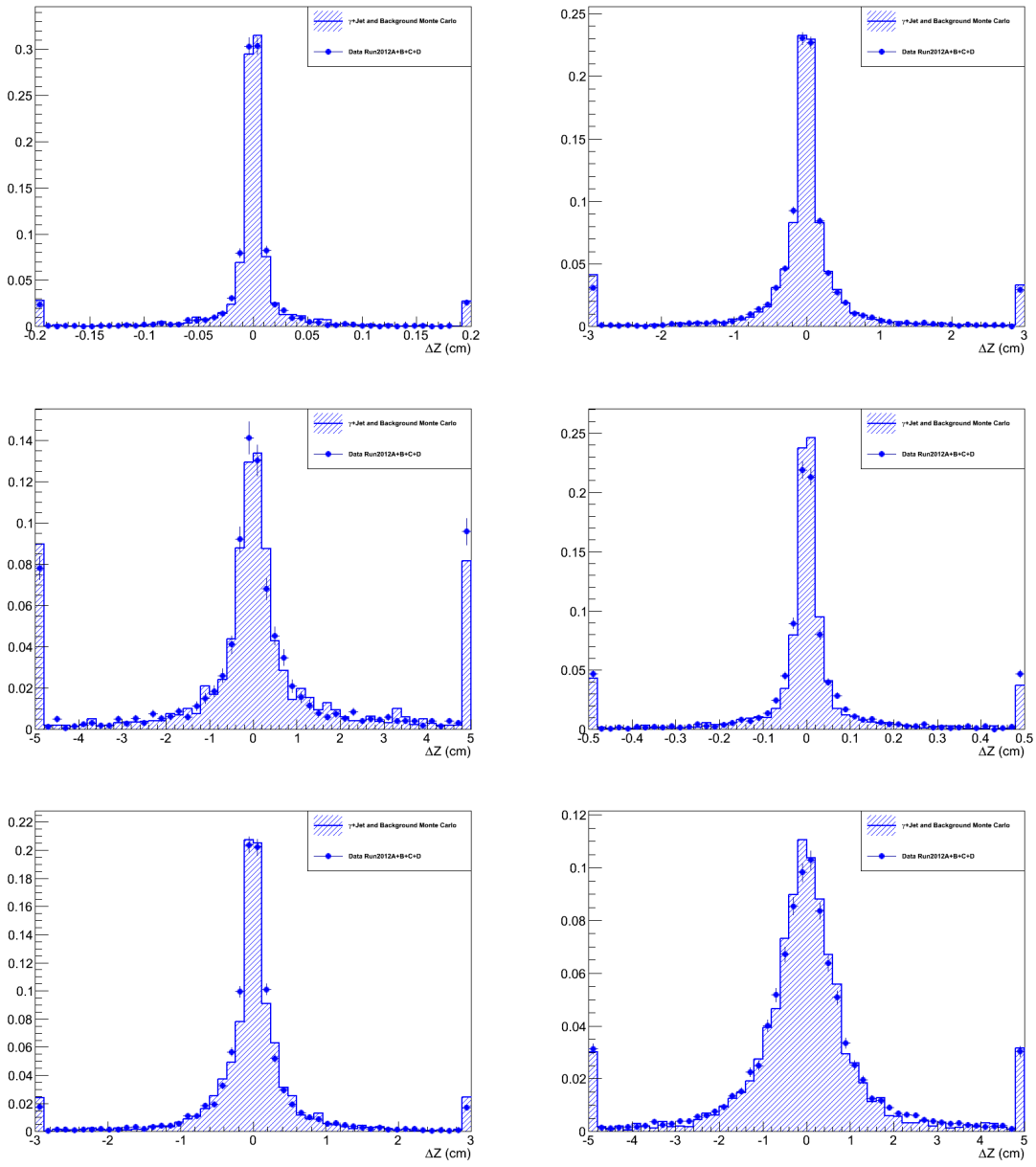

Figure 4.14. Δz distributions for the two conversions methods for the six different tracker regions. The top two histograms are for the Pixel Barrel (left) and TIB (right), followed by the TOB (left) and Pixel Forward (right). The histograms for the TID (left) and TEC (right) can be found in the last row.

TABLE 4.21

CONVERSION RESOLUTION

σ (cm)	Pix Barrel	TIB	TOB	Pix Fwd	TID	TEC
Data 2012 RunABCD	0.011	0.289	1.389	0.060	0.311	1.031
Simulated γ + jet	0.011	0.305	1.452	0.045	0.344	0.924
Ratio data/simulation	1.	0.948	0.957	1.333	0.904	1.116

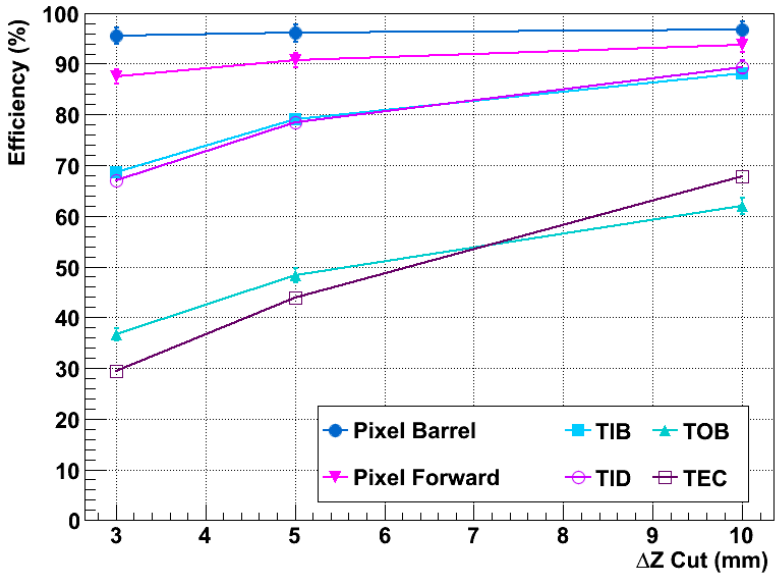

Figure 4.15. Conversions vertex efficiency in three different bins for γ + jet events in 8 TeV data.

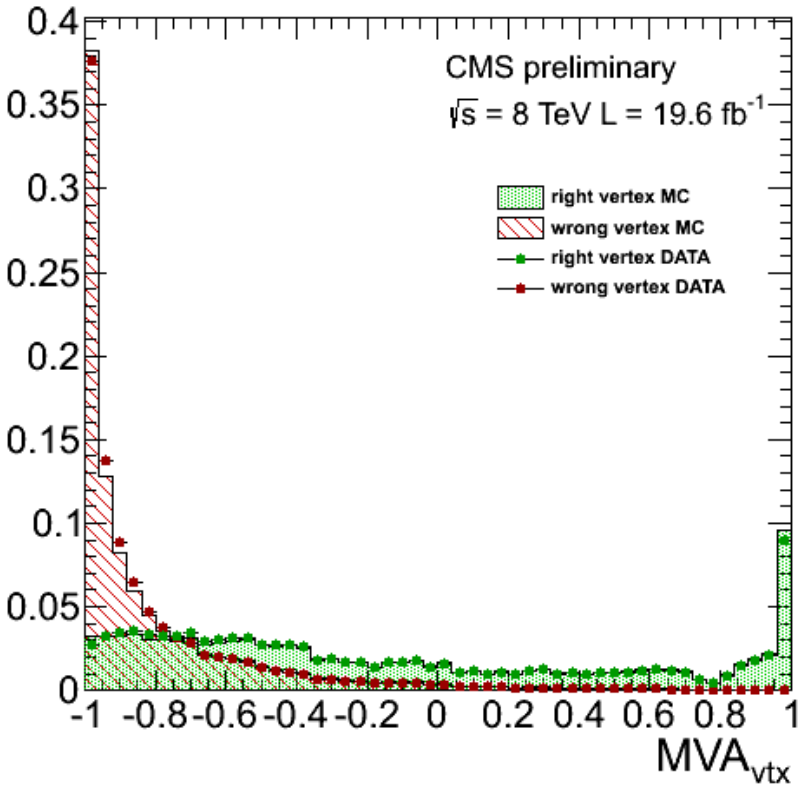

Figure 4.16. Output of the vertex selection BDT for the primary and pileup vertices in $Z \to \mu\mu$ events in data and Monte Carlo simulation.

can be seen in figures 4.16 and 4.17, respectively. The efficiency is measured by the fraction of events where the selected vertex is within 1 cm of the correct vertex. The systematic uncertainty for the vertex finding efficiency is taken from the disagreement between $Z/\gamma^* \to ee$ data and Monte Carlo simulation. In events with conversions, $\gamma+$jet events are used to evaluate the performance of the vertex selection BDT. This is done by vetoing all the tracks associated with the jet from the BDT quantities. The output of the vertex selection BDT and its performance in events with conversions can be seen in figure 4.18 and 4.19, respectively [81].

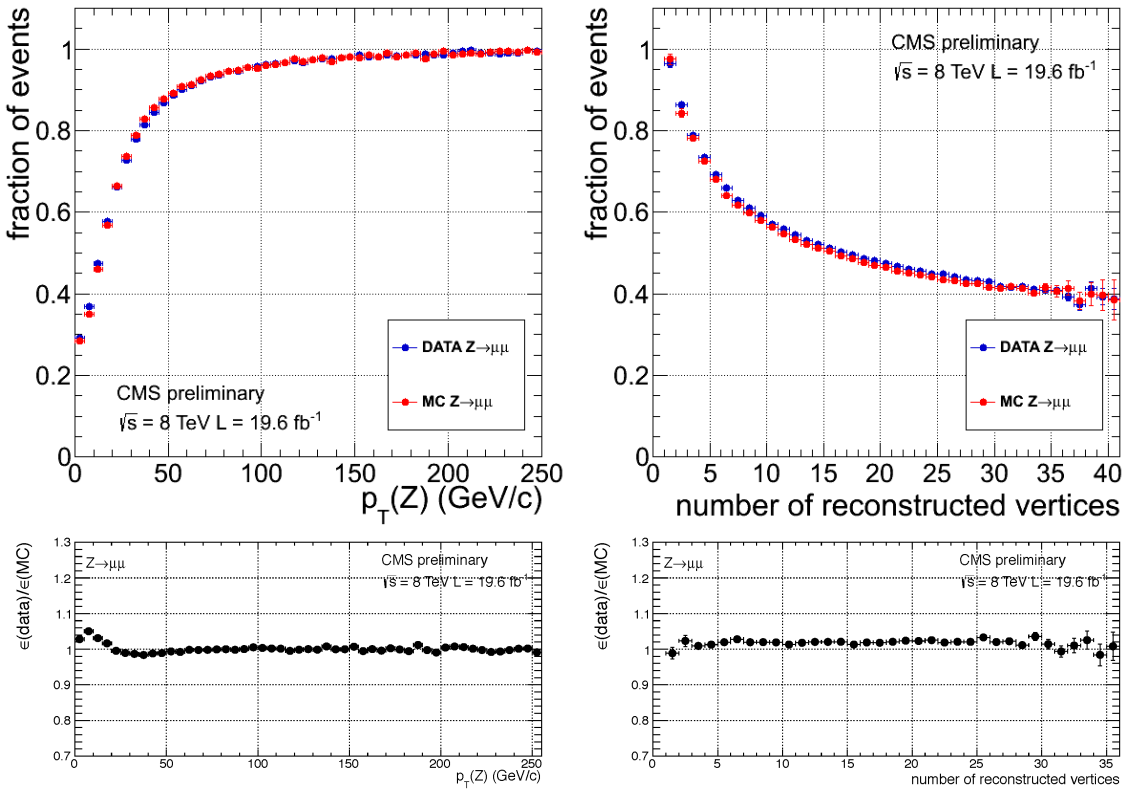

Figure 4.17. The performance of the vertex selection BDT versus p_T (left) and number of number vertices (N_{vtx}) (right) in data and Monte Carlo simulation for $Z \to \mu\mu$ events.

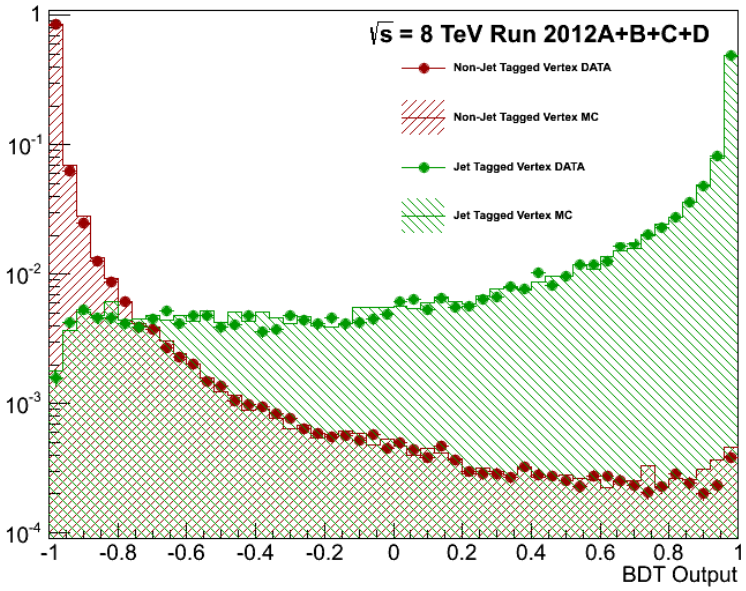

Figure 4.18. Output of the vertex selection BDT for events with conversion in γ + jet events for data and Monte Carlo simulation.

4.8.3 Per-event Vertex Probability

Since the vertex selection BDT only selects the correct vertex 75% of the time, a second BDT is used to estimate the probability that the correct vertex is selected. This is done in order to categorize the events with the absolute best resolution. The per-event vertex probability BDT is trained on 130 GeV $H \to \gamma\gamma$ Monte Carlo simulation to select events where the primary vertex is within 1 cm of the true vertex. The per-event vertex BDT has five inputs: p_T of the di-photon system, N_{vtx}, vertex BDT output for the top three vertices in the event, ΔZ between the top three vertices, and the number of photons matched to conversions. The output of the per-event vertex BDT is then fed into a linear function that returns the probability that the correct vertex has been selected. The dependence of the vertex selection probability on the per-event vertex BDT can be seen in figure 4.20. The performance

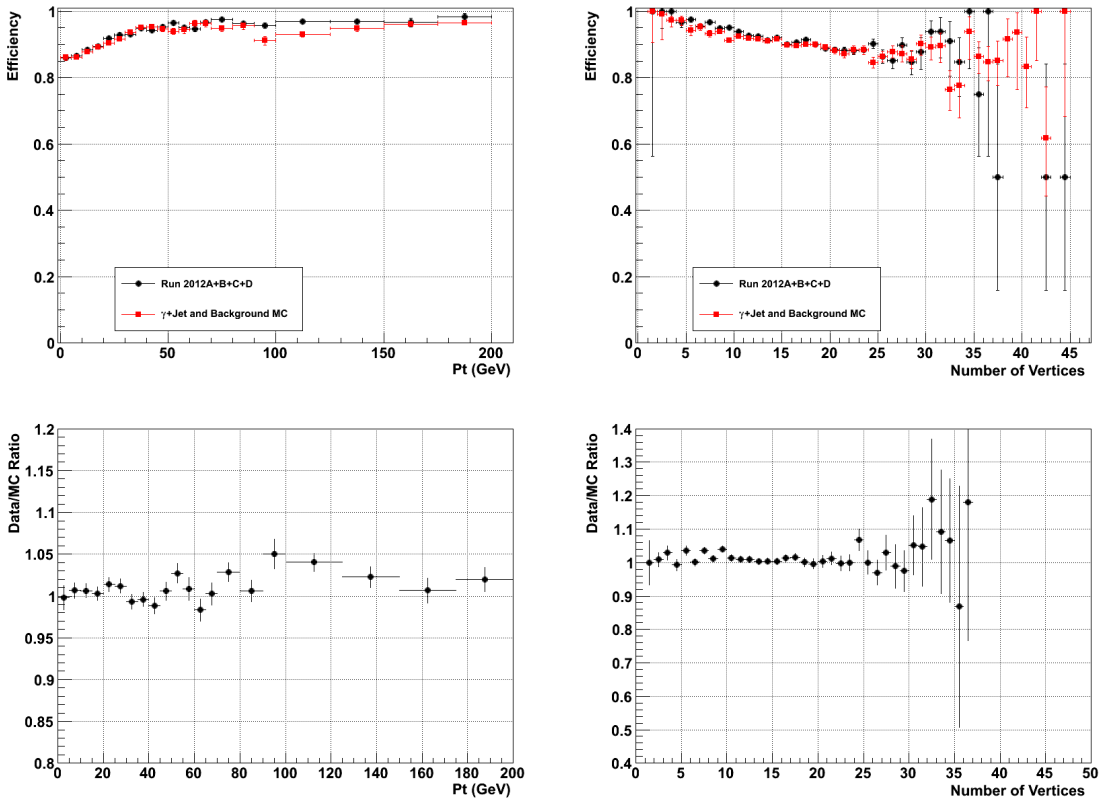

Figure 4.19. The performance of the vertex selection BDT in $\gamma + \text{jet}$ events with conversions as a function of p_T (left) and $\mathrm{N_{vtx}}$ (right) for data and Monte Carlo simulation.

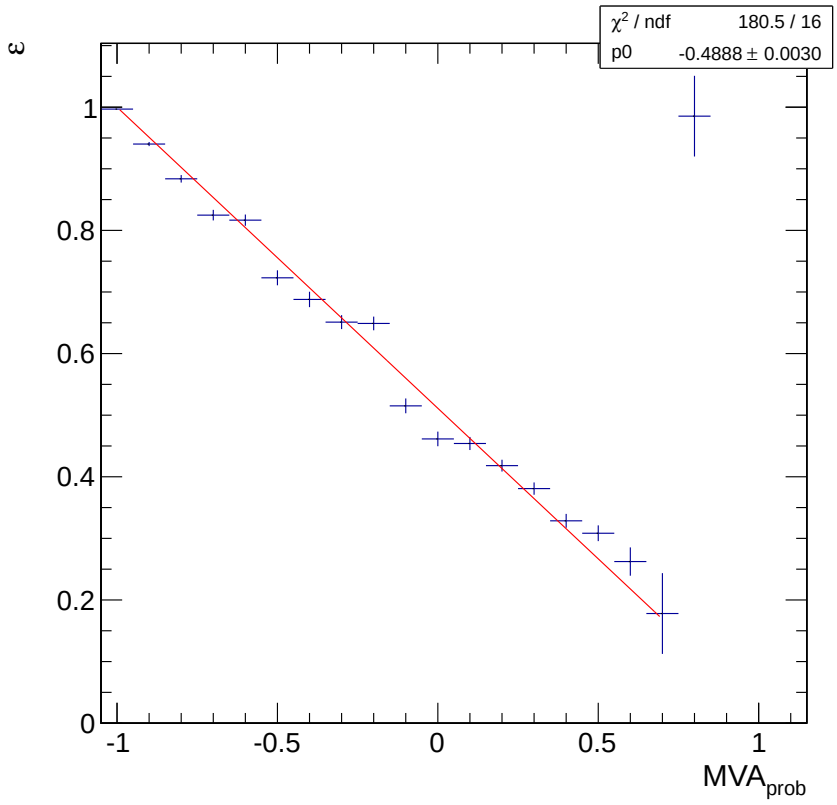

Figure 4.20. The correct vertex identification probability versus the output of the per-event vertex probability BDT.

of the per-event vertex BDT is checked in $Z \to \mu\mu$ and $\gamma +$jet events for events with conversions. The agreement between data and Monte Carlo simulation is fairly good, as can be seen in figure 4.21. The peak near -1 in red for the $\gamma +$jet events is because the correct vertex is only selected by the jet 97% of the time. The spike at -1 occurs when the conversion selects the correct vertex and the jet does not. This effect is modeled in Monte Carlo simulation and can be seen as the dark red line [81].

4.9 Photon Identification

Photon identification is important to the analysis because $H \to \gamma\gamma$ has a large background due to prompt-prompt, prompt-fake, and fake-fake processes. While

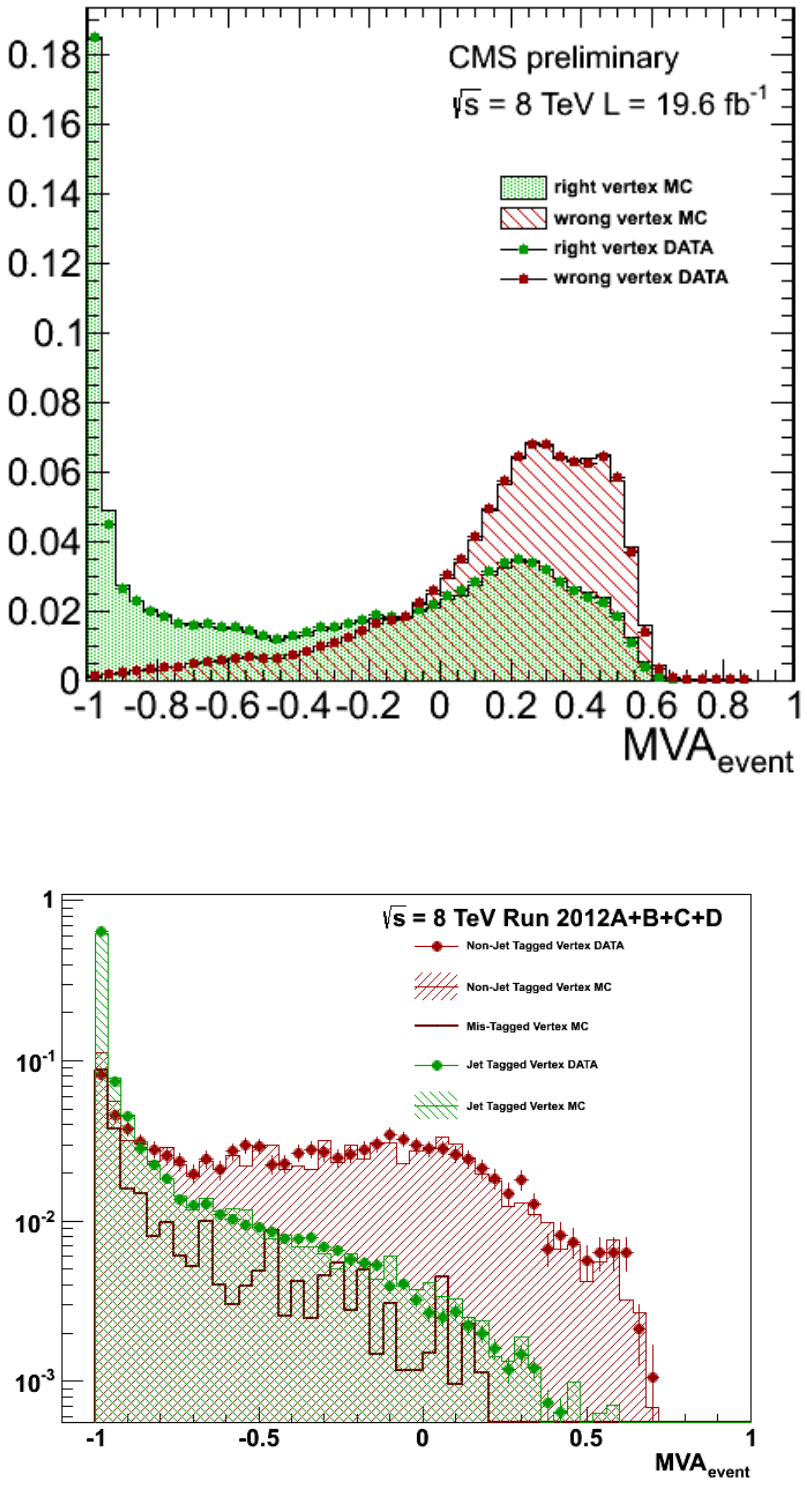

Figure 4.21. The output of the per-event BDT in events without (right) and with conversions (left) from $Z \to \mu\mu$ and $\gamma +$ jet events, respectively.

the prompt-prompt background is irreducible, the other two are reducible. Photon identification distinguishes between prompt and fake photons. Fake photons are predominately from boosted $\pi^0 \to \gamma\gamma$ decays that merge into one supercluster. Discrimination between real and fake photons is done with two methods. For the main analysis, each of the photons is evaluated by the photon identification BDT. A loose cut is applied to each photon and the photon information is passed to the di-photon BDT. In the cut-based cross-check analysis a cuts-in-categories approach is used where the photon identification cuts vary based on photon category. The BDT approach is preferable for two reasons. First, it enables photon quality as a category discriminate when combined with the di-photon BDT, and second, it uses all information to evaluate the quality photon, which is more flexible than fixed cuts for a few variables.

4.9.1 Photon Identification BDT

The Identification BDT takes information about the supercluster's position and shower-shape, isolation, and event pileup and then produces a singular output that parameterizes the quality of the photon. The photon identification BDT is trained on a simulated $\gamma +$ jet sample that is enriched as generator level for QCD objects that will fake photons. All photons are required to pass the pre-selection described in section 4.7. The prompt photons, which are photons with mothers that are quarks or anti-quarks, are marked as signal and fake photons, photons that fail the prompt requirement, are marked as background. All events are used for training the signal sample while only even events are used to train the background. For testing the prompt photons, a $H \to \gamma\gamma$ Monte Carlo simulation sample at 124 GeV is used. A complete list of photon identification BDT inputs can be found below.

1. Shower Shape Variables

    1. $\sigma_{i\eta i\eta}$: The energy weighted standard deviation for the crystal η within a 5×5

crystal array centered on the maximum energy crystal in the supercluster.

2. $\text{cov}_{i\eta i\phi}$: The covariance of the crystal η and ϕ within a 5×5 crystal array centered on the maximum energy crystal in the supercluster.
3. $E_{2\times2}/E_{5\times5}$: The ratio of energy within a 2×2 crystal array that contains the maximum energy crystal and the 5×5 crystal array.
4. R_9: The ratio of energy within the center 3×3 crystals to the supercluster energy.
5. σ_η: The energy weighted standard deviation of η for the supercluster.
6. σ_ϕ: The energy weighted standard deviation of ϕ for the supercluster.
7. σ_{RR}: The standard deviation of ES shower in x and y (EE only).

2. Isolation Variables

    1. PF Photon Isolation: The particle flow photon isolation sum in a ΔR cone of 0.3.
    2. PF Charged Isolation (Selected Vertex): The particle flow charged hadron isolation sum in a ΔR cone of 0.3 for charged particle objects associated with the selected primary vertex.
    3. PF Charged Isolation (Worst Vertex): The largest particle flow charged hadron isolation sum in a ΔR cone of 0.3 for any vertex.

3. Pileup and Supercluster Information

    1. ρ: The average energy deposited in the detector per unit of solid angle.
    2. η: The η position of the supercluster associated with the photon.

The output of the photon identification BDT can be seen in figure 4.22. There is good agreement between the training and test samples for both the barrel and endcap. The ROC curve showing the signal versus background efficiency for 7 and 8 TeV can be seen in figure 4.23. The input and output of the photon ID BDT is checked on $Z/\gamma^* \to ee$ data and Monte Carlo simulation. A comparison of the photon ID BDT's input can be seen in figures 4.24, 4.25, and 4.26 and its output can be seen in figure 4.27. There is fairly good agreement between data and the Monte Carlo simulation, and the greatest divergence can be seen in the tails of the distributions. In order to cover this effect a shift of ± 0.01 in the output value of the ID BDT is taken as a systematic. The photon ID BDT is also validated in $Z \to \mu\mu\gamma$ events

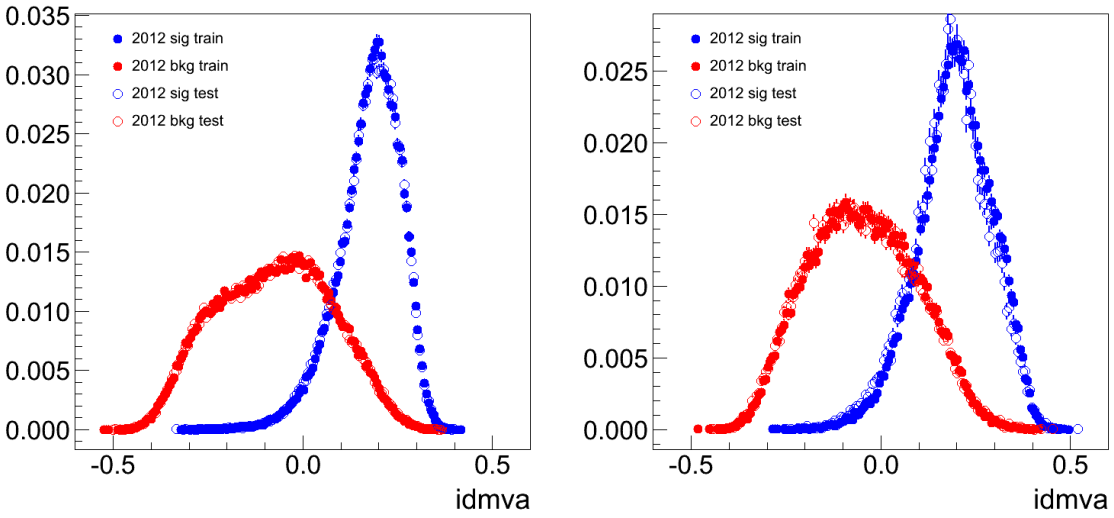

Figure 4.22. The output of the photon identification BDT for the Barrel (left) and Encap (right).

in data and Monte Carlo simulation, exploiting the very high purity of this channel. The presence of the two muons significantly reduces background contamination from QCD di-jet processes and the invariant mass requirement on the $\mu\mu\gamma$ system ensures that the selection is nearly (99%) background free. The output of the photon ID BDT for the photons in $Z \to \mu\mu\gamma$ events can be seen in figure 4.28 [81].

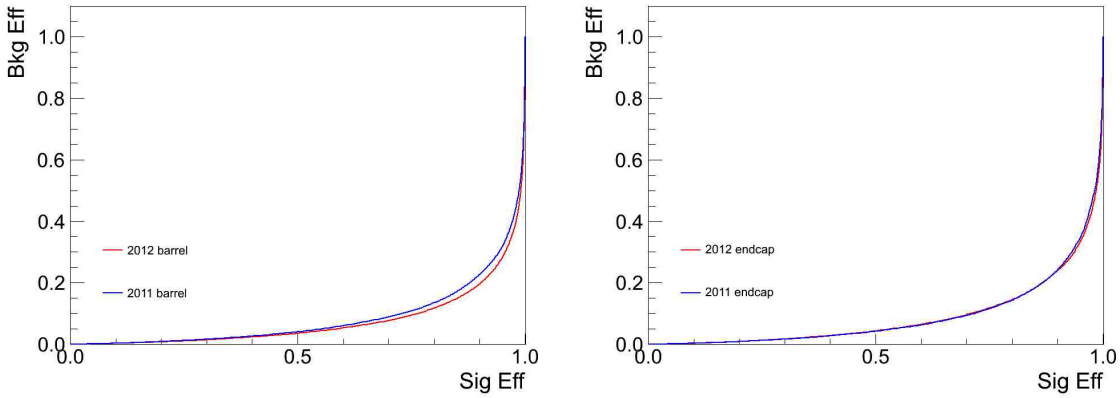

Figure 4.23. Background versus signal efficiency for the photon identification BDT for 7 and 8 TeV for the barrel (left) and endcap (right).

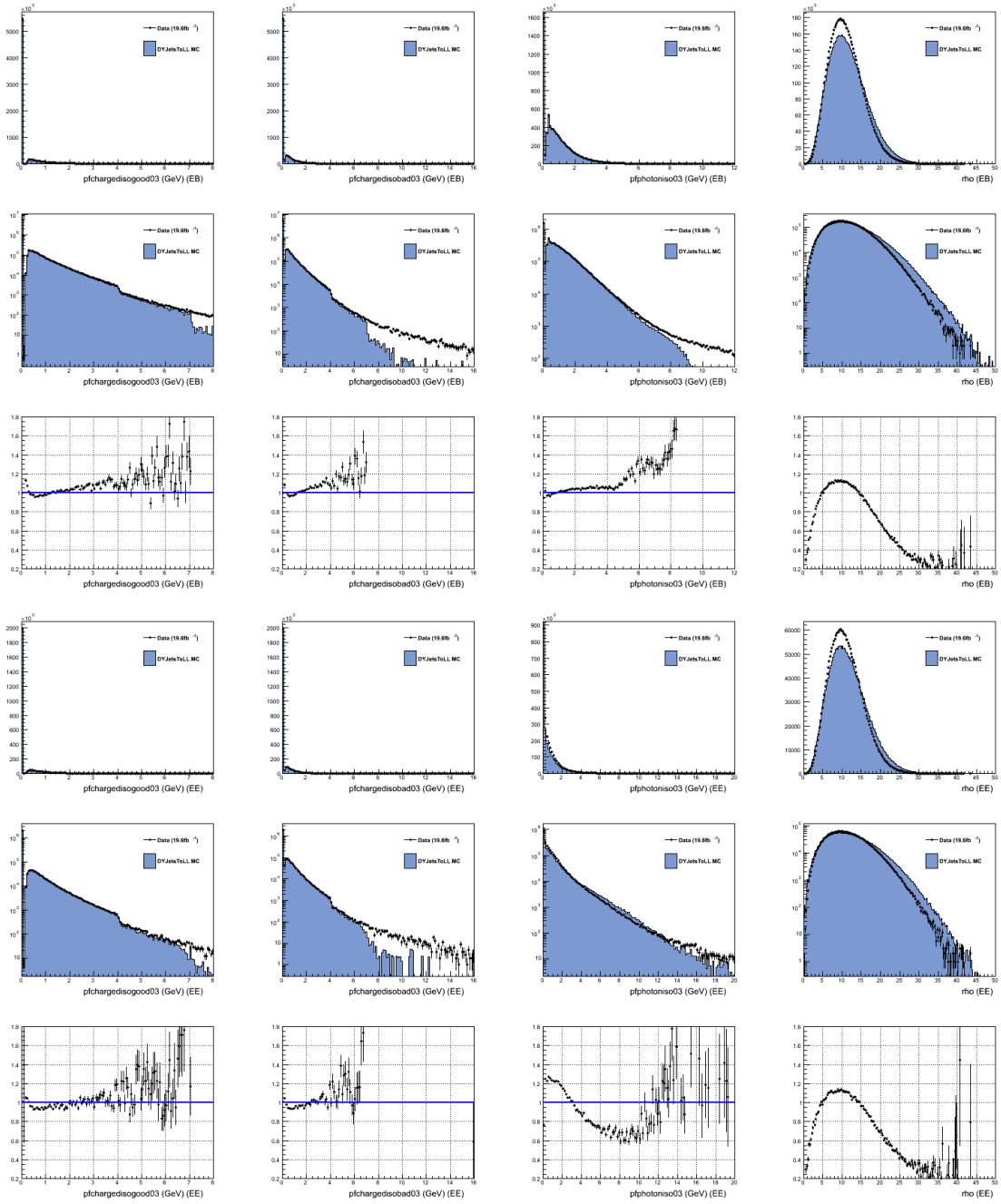

Figure 4.24. The distributions of the Photon ID BDT inputs for $Z/\gamma^* \to ee$ events in data and Monte Carlo simulation for barrel (top) and endcap (bottom) electrons with an inverted electron veto. For each variable the linear scale, log scale, and data/MC ratio are presented for data and Monte Carlo simulation. The $Z/\gamma^* \to ee$ events must pass the photon pre-selection and the photon ID BDT cut at -0.2.

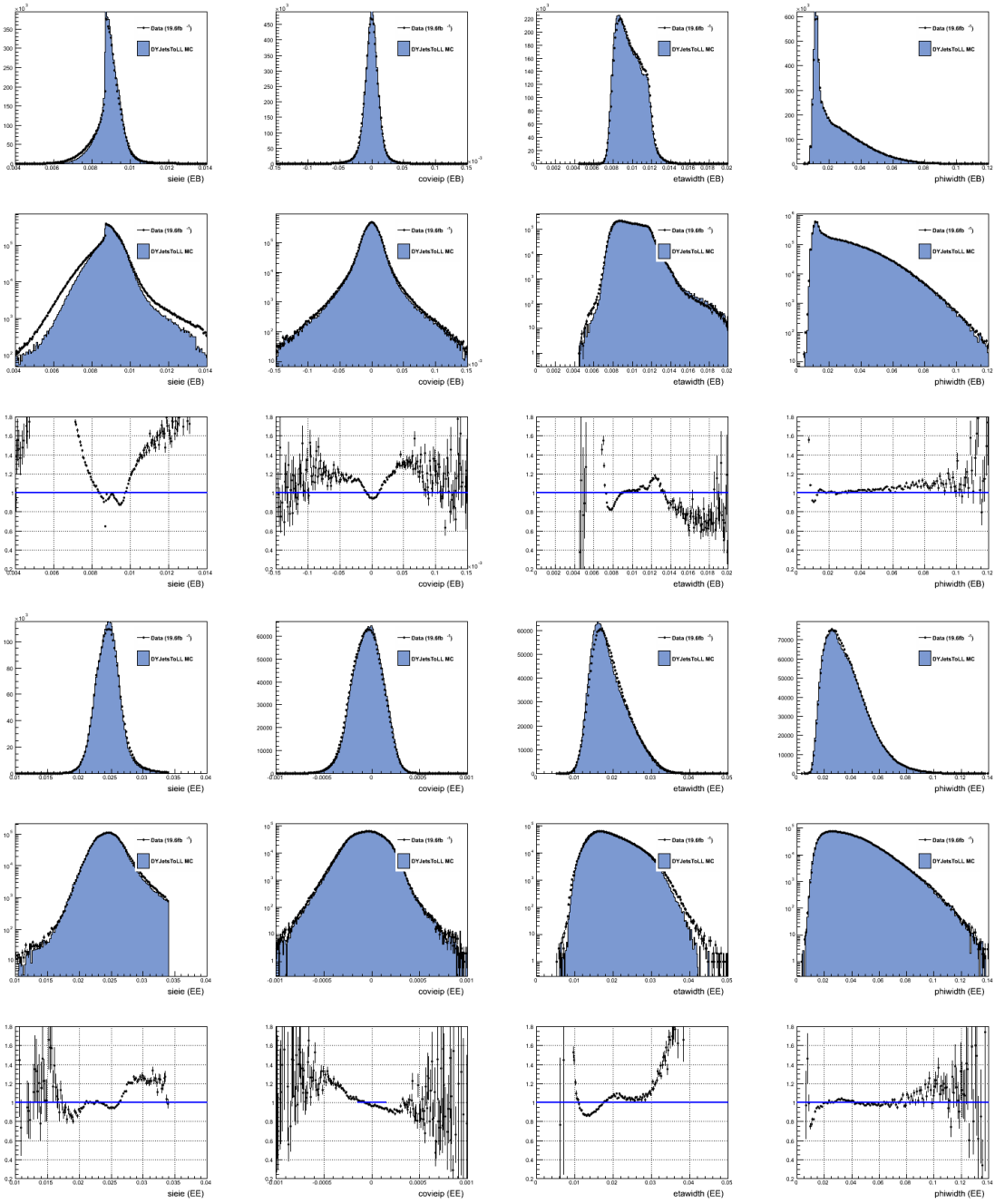

Figure 4.25. The distributions of the Photon ID BDT inputs for $Z/\gamma^* \to ee$ events in data and Monte Carlo simulation for barrel (top) and endcap (bottom) electrons with an inverted electron veto. For each variable the linear scale, log scale, and data/MC ratio are presented for data and Monte Carlo simulation. The $Z/\gamma^* \to ee$ events must pass the photon pre-selection and the photon ID BDT cut at -0.2.

4.9.2 Cut-Based Photon Identification

In the cut-based cross-check a cuts-in-categories (CiC) method is used for photon identification. The cuts in categories separates photons into two bins of η and two bins of R_9 for a total of four categories. The cuts are then machine optimized to maximize the acceptance of photons for a selected S/B ratio. Cuts in the low R_9 categories are tighter than those in high R_9 categories. This is done for two reasons. First, photons with high R_9 values have better resolution, so they increase the sensitivity of the analysis. Having a looser isolation selection for high R_9 photons ensures more high-resolution photons are available for the final measurement. Second, low R_9 photons are associated with background processes from QCD, so stricter isolation requirements are used to limit the background contamination. For the cut-optimization, the sub-leading photon in $H \to \gamma\gamma$ events at 120 GeV are used as signal and $\gamma +$ jet events are used as background. The cuts are optimized at nine different working points and the fourth working point is selected for the analysis (CiC4PF or "SuperTight"). A full list of cuts at CiC4PF can be seen in tables 4.22 and 4.23 for 7 and 8 TeV. The full set of cuts are applied to both the lead and sub-lead photon. The efficiency of the CiC selection is measured in $Z/\gamma^* \to ee$ data with a tag-and-probe methodology. The efficiency of the CiC4PF selection in each category with respect to the photon pre-selection can be seen in tables 4.24 and 4.25 for 7 and 8 TeV [81, 88].

4.9.3 Comparison of the Photon ID BDT and the CiC Method

In order to make a meaningful comparison between the photon ID BDT and the CiC selection a working point for the photon ID BDT is selected with the same signal efficiency as the cut-based working point. The signal and background efficiency can be

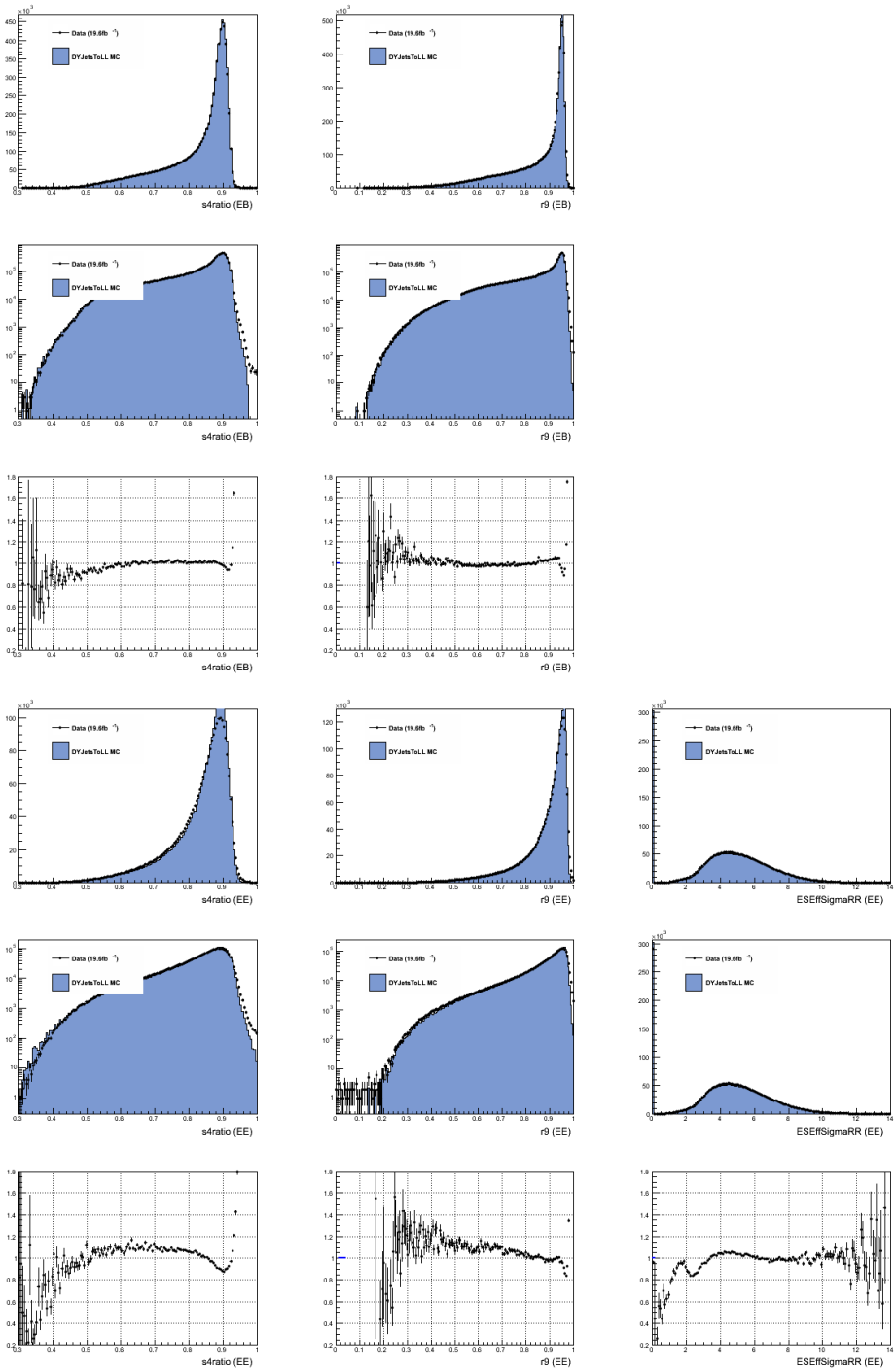

Figure 4.26. The distributions of the Photon ID BDT inputs for $Z/\gamma^* \to ee$ events in data and Monte Carlo simulation for barrel (top) and endcap (bottom) electrons with an inverted electron veto. For each variable the linear scale, log scale, and data/MC ratio are presented for data and Monte Carlo simulation. The $Z/\gamma^* \to ee$ events must pass the photon pre-selection and the photon ID BDT cut at -0.2.

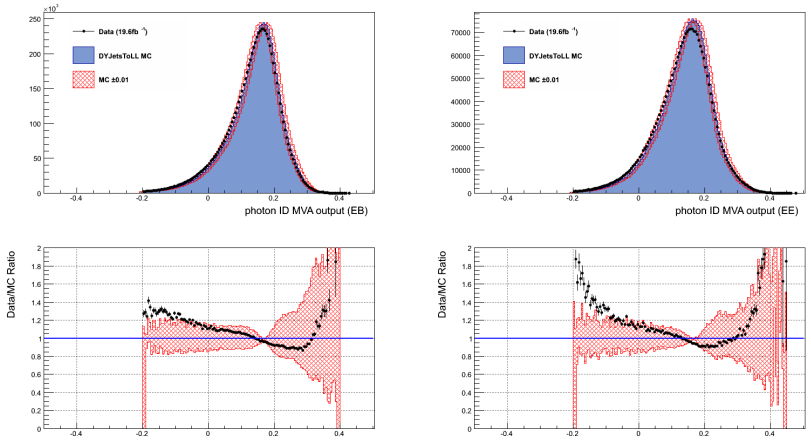

Figure 4.27. The output of the photon ID BDT for $Z/\gamma^* \to ee$ events with an inverted electron veto in data and Monte Carlo simulation for the barrel (right) and endcap (right). Only electrons that pass the ID BDT > -0.2 cut are plotted. The ± 0.01 shift in the photon ID BDT is the hashed, red region.

TABLE 4.22

7 TEV CIC4 CUT VALUES

Variable	Barrel		Endcap	
	$R_9 > 0.94$	$R_9 < 0.94$	$R_9 > 0.94$	$R_9 < 0.94$
Rel. Comb. Iso. (Selected Vertex)	3.8	2.2	1.77	1.29
Rel. Comb. Iso. (Worst Vertex)	11.7	3.4	3.9	1.84
Rel. Track Iso. (Selected Vertex)	3.5	2.2	2.3	1.45
$\sigma_{i\eta i\eta}$	0.0106	0.0097	0.028	0.027
H/E	0.082	0.062	0.065	0.048
R_9	0.94	0.36	0.94	0.32
ΔR to GSF Electron track	-	0.062	-	-

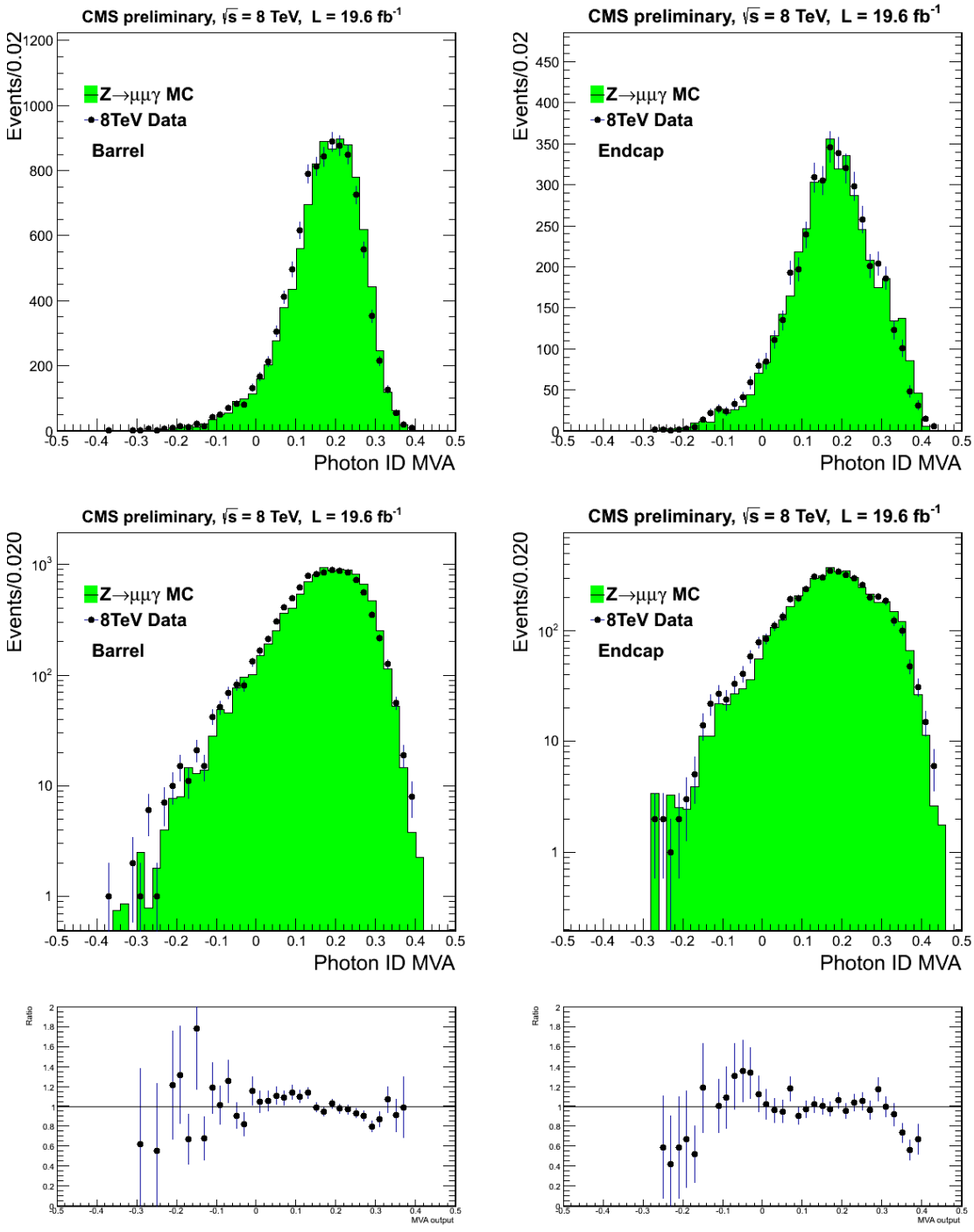

Figure 4.28. Photon ID BDT output of photons in $Z \to \mu\mu\gamma$ events for data and Monte Carlo simulation for the barrel (left) and endcap (right).

TABLE 4.23

8 TEV CIC4PF CUT VALUES

Variable	Barrel		Endcap	
	$R_9 > 0.94$	$R_9 < 0.94$	$R_9 > 0.94$	$R_9 < 0.94$
PF Isolation (Selected Vertex)	6	4.7	5.6	3.6
PF Isolation (Worst Vertex)	10	6.5	5.6	4.4
Charged PF Isolation	3.8	2.5	3.1	2.2
$\sigma_{i\eta i\eta}$	0.0108	0.0102	0.028	0.028
H/E	0.124	0.092	0.142	0.063
R_9	0.94	0.298	0.94	0.24

TABLE 4.24

7 TEV CIC4PF IDENTIFICATION EFFICIENCIES

Category	$\epsilon \pm \sigma_{\mathrm{STAT}} \pm \sigma_{\mathrm{SYST}}$ (DATA)	$\epsilon \pm \sigma_{\mathrm{STAT}}$ (MC)	Ratio$\pm\sigma_{\mathrm{STAT}}$
EB R_9 >0.94	0.8926±0.06±0.04	0.9079±0.05	0.983±0.001
EB R_9 <0.94	0.6831±0.06±0.55	0.6854±0.05	0.996±0.009
EE R_9 >0.94	0.7365±0.14±0.39	0.7365±0.12	0.999±0.006
EE R_9 <0.94	0.5125±0.11±1.25	0.4920±0.08	1.040±0.025

TABLE 4.25

8 TEV CIC4PF IDENTIFICATION EFFICIENCIES

Category	$\epsilon \pm \sigma_{\mathrm{STAT}} \pm \sigma_{\mathrm{SYST}}$ (DATA)	$\epsilon \pm \sigma_{\mathrm{STAT}}$ (MC)	Ratio$\pm\sigma_{\mathrm{STAT}}$
EB R_9 >0.94	0.9087±0.0008±0.0025	0.9228±0.0005	0.985±0.003
EB R_9 <0.94	0.7207±0.0011±0.0080	0.7436±0.0006	0.968±0.011
EE R_9 >0.94	0.8042±0.0013±0.0055	0.7820±0.0008	1.028±0.007
EE R_9 <0.94	0.5093±0.0019±0.0115	0.5085±0.0010	1.001±0.024

seen in table 4.26 from Monte Carlo simulation and the efficiency for data and Monte Carlo simulation in $Z/\gamma^* \rightarrow ee$ tag-and-probe can be seen in table 4.27 and 4.28 for 7 and 8 TeV. This working point is for illustrative purposes only, as the main analysis only places a loose cut of -0.2 on the photon ID BDT. The performance of the photon ID BDT versus the cut-based approach (CiC4PF) can be seen in figure 4.29. It can be seen that the performance of the photon ID BDT is less dependent on photon p_T, η, and ρ than the cut-based approach.

TABLE 4.27

7 TEV PHOTON ID BDT EFFICIENCIES

Category	$\epsilon \pm \sigma_{\mathrm{STAT}}$ (DATA)	$\epsilon \pm \sigma_{\mathrm{STAT}}$ (MC)	Ratio$\pm\sigma_{\mathrm{STAT}}$
EB R9>0.9	0.9267±0.0012	0.9275±0.0006	0.999±0.0013
EB R9<0.9	0.8882±0.0023	0.9025±0.0010	0.984±0.0025
EE R9>0.9	0.9442±0.0010	0.9387±0.0009	1.006±0.0014
EE R9<0.9	0.8639±0.0010	0.8517±0.0011	1.014±0.0015

TABLE 4.26

PHOTON ID BDT AND CIC SELECTION EFFICIENCIES AT 8 TEV

Region	2012 BDT	2011 BDT	2012 CiC
	Prompt Photon Efficiency		
Barrel	91.2 ±0.1%	91.2 ±0.1%	91.2 ±0.1%
Endcap	77.4 ±0.3%	77.5 ±0.3%	77.3 ±0.3%
	Fake Photon Efficiency		
Barrel	21.2 ±0.2%	24.2 ±0.2%	21.9 ±0.2%
Endcap	13.1 ±0.2%	13.0 ±0.2%	15.8 ±0.2%

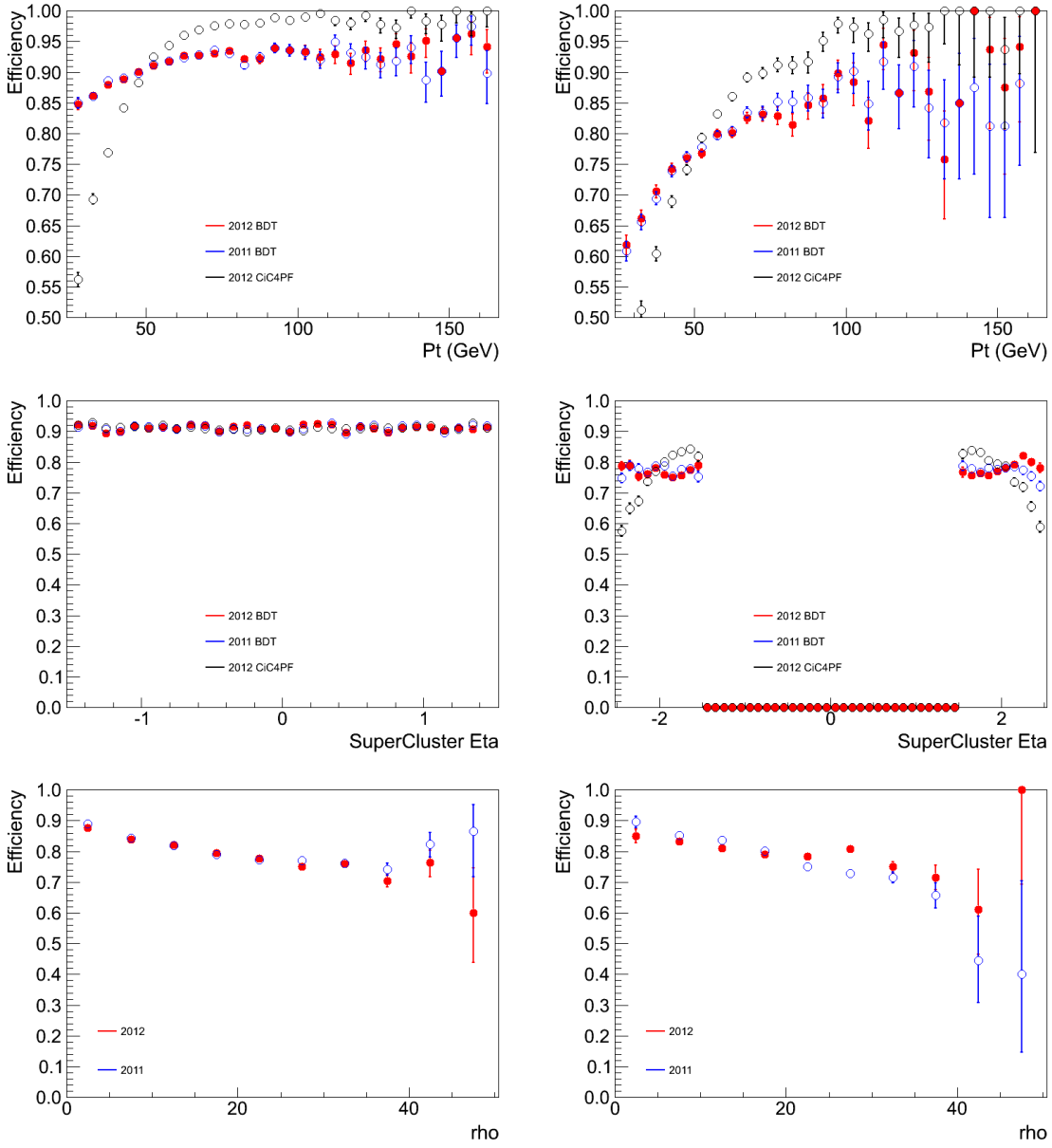

Figure 4.29. Signal efficiency versus p_T, η, and ρ for the barrel (left) and endcap (right).

TABLE 4.28

8 TEV PHOTON ID BDT EFFICIENCIES

Category	$\epsilon \pm \sigma_{\mathrm{STAT}}$ (DATA)	$\epsilon \pm \sigma_{\mathrm{STAT}}$ (MC)	Ratio$\pm\sigma_{\mathrm{STAT}}$
EB R_9 >0.94	0.99958±0.00004	0.99941±0.00003	1.0002±0.0001
EB R_9 <0.94	0.99494±0.00017	0.99469±0.00007	1.0003±0.0002
EE R_9 >0.94	0.99958±0.00005	0.99966±0.00003	0.9999±0.0001
EE R_9 <0.94	0.99577±0.00022	0.99774±0.00009	0.9980±0.0003

4.10 Inclusive Categorization

The $H \to \gamma\gamma$ search is highly dependent on the resolution of the detector and the signal to background ratio. By separating the events into multiple categories the overall sensitivity of the analysis can be increased. This is done by separating events with good resolution and high S/B ratio from those events with worse resolution and lower S/B ratios [92]. In each of the analyses there are a total of nine categories, four inclusive and five exclusive, at 8 TeV and five categories, four inclusive and one exclusive, at 7 TeV. The inclusive categories only require a di-photon final state that passes the photon identification and categorization cuts. The exclusive categories are events with additional objects in the final state: muon, electron, VBF di-jet, or $\not\!\!E_T$. For the main analysis the inclusive categories are separated with a di-photon categorization BDT. In the cut-based cross-cut analysis, the inclusive categorization is done with a simple cut in η and R_9.

4.10.1 Multivariate Categorization

For the main analysis both photons are required to pass the pre-selection in section 4.7. In addition to the pre-selection, a loose cut is placed on the photon identification BDT. The output of the photon identification BDT for each photon is required to be greater than -0.2. This cut retains 99% of $H \to \gamma\gamma$ signal events and removes 23.5% of the events in data between $100 < m_{\gamma\gamma} < 180$ GeV. There is also an addition kinematic cut on the lead and sub-lead photon. The p_T of the lead photon must be greater than $\frac{1}{3}$ the invariant mass of the di-photon system, and the p_T of the sub-lead photon must be at least $\frac{1}{4}$ the invariant mass of the di-photon system:

- $p_T^{\gamma_1} > \frac{1}{3} m_{\gamma\gamma}$
- $p_T^{\gamma_2} > \frac{1}{4} m_{\gamma\gamma}$

The sliding cut corresponds to values of $p_T > 40$ GeV and $p_T > 30$ GeV at $m_{\gamma\gamma} = 125$ GeV. In order to maximize the sensitivity of the analysis, events with high S/B and excellent resolution are placed in high sensitivity categories and events with low S/B and worse resolution are placed in low sensitivity categories. The event classification algorithm uses a boosted decision tree that incorporates the kinematics of the di-photon system, the resolution information for the photons and the vertex, and the quality of the photons. A complete list of the inputs to the di-photon categorization BDT is:

- $p_T^{1,2}/m_{\gamma\gamma}$: The relative transverse momentum of the lead and sub-lead photons.
- $\eta^{1,2}$: The η of the lead and sub-lead superclusters associated for each of the photons.
- $\cos(\Delta\phi_{\gamma\gamma})$: The cosine of the opening angle between the two photons in ϕ.
- Photon identification BDT output for the lead and sub-lead photon.
- The per-event mass resolution estimate assuming the correct vertex has been selected.
- The per-event mass resolution estimate assuming the incorrect vertex has been selected.

- The per-event probability that the correct vertex has been selected.

The per-event mass resolution is calculated from the estimated photon energy resolution returned by the energy resolution BDT, from section 4.4.3, for each photon:

$$\sigma_m^{\text{right}}/m_{\gamma\gamma} = \frac{1}{2}\sqrt{(\sigma_{E_1}/E_1)^2 + (\sigma_{E_2}/E_2)^2}. \tag{4.11}$$

However, the energy resolution BDT is trained on the Monte Carlo simulation, which is known to have better energy resolution than data. The additional smearing from section 4.4.5 is added in quadrature to each photons' energy resolution estimate in order to have it accurately return the resolution in data. Also, equation 4.11 assumes that the correct vertex is selected. However, it is known that the vertex selection BDT selects the correct vertex 75% of the time. For this reason an additional quantity is evaluated that represents the energy resolution of the event in the case that the wrong vertex is selected,

$$\sigma_m^{wrong}/m_{\gamma\gamma} = \frac{1}{2}\sqrt{(\sigma_m^{\text{right}}/m_{\gamma\gamma})^2 + (\sigma_m^{\text{vtx}}/m_{\gamma\gamma})^2}, \tag{4.12}$$

where σ_m^{vtx} is the mass resolution that is computed from the position of the two photon superclusters and the distance to the true vertex, which can be modeled as a Gaussian with a width of $\sqrt{2}\sigma_{BS}$. When the BDT is trained it needs to know that the S/B ratio is inversely proportional to mass resolution. This is done by weighting the signal sample events by

$$\omega_{sig} = \frac{p_{\text{vtx}}}{\sigma_m^{\text{right}}/m_{\gamma\gamma}} + \frac{1 - p_{\text{vtx}}}{\sigma_m^{\text{wrong}}/m_{\gamma\gamma}}. \tag{4.13}$$

By weighting the training events by their resolution the BDT output naturally assigns events with better resolution a higher BDT value. The BDT is trained with simulated samples of $H \to \gamma\gamma$ with an invariant mass at 123 GeV and several simulated QCD

backgrounds that consist of prompt-prompt, prompt-fake, and fake-fake backgrounds.

Once an event receives a score from the di-photon BDT, it is separated into five different categories. The categories are based on the BDT score alone and are selected to maximize the CL_s^{95} exclusion. This is done by scanning the category boundary across all possible di-photon BDT values and placing the boundary where it maximizes the asymptotic CL_s^{95} exclusion. The process is then repeated two more times to get the four category boundaries. The optimization is stopped after four categories, because the next additional category failed to increase the analysis sensitivity by more than 1%. The lowest sensitivity category (di-photon BDT $<$ -0.05 for 8 TeV and BDT $<$ 0.05 for 7 TeV) is cut from the analysis. A histogram of the optimization process can be seen in figure 4.30, and the selected category boundaries can be seen in table 4.29 and 4.30 for 7 and 8 TeV. The output of the di-photon categorization BDT for data, background Monte Carlo simulation, and signal Monte Carlo simulation at 125 GeV can be seen in figure 4.31 along with the category boundaries [81]. Extensive validation of the di-photon BDT inputs was performed by personal at the Massachusetts Institution of Technology and can be seen in appendex A.

The majority of the systematic uncertainties for the di-photon BDT comes from the uncertainty on the photon resolution and the photon ID BDT output. Both of these BDT's have corrections applied to them due to shifts between data and the Monte Carlo simulation. However, even after the correction the modeling is still imperfect. A shift of ± 0.01 is applied to the output of the photon identification BDT. The energy resolution systematic uncertainty is estimated by varying the Monte Carlo simulation to data energy smear by ± 0.10. The effect of these systematics (red hash) on the output of the di-photon BDT can be seen in figure 4.32 for simulated signal samples and 4.32 for simulated background. The systematic uncertainty can all be seen in figure 4.34, which has the output of the di-photon BDT for $Z/\gamma^* \to ee$ events

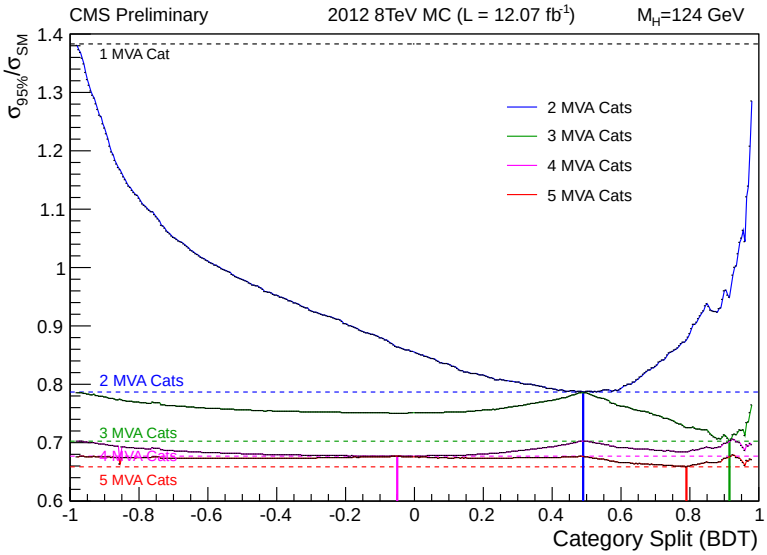

Figure 4.30. The expected exclusion ratio as a function of the di-photon BDT category boundary. The first boundary is in blue followed by green, magenta, and red. All events below the magenta line are removed from the analysis.

TABLE 4.29

7 TEV DI-PHOTON BDT CATEGORY BOUNDARIES

Category	Lower Boundary	Upper Boundary
0	0.89	N/A
1	0.74	0.89
2	0.545	0.74
3	0.05	0.545

TABLE 4.30

8 TEV DI-PHOTON BDT CATEGORY BOUNDARIES

Category	Lower Boundary	Upper Boundary
0	0.91	N/A
1	0.79	0.91
2	0.49	0.79
3	-0.05	0.50

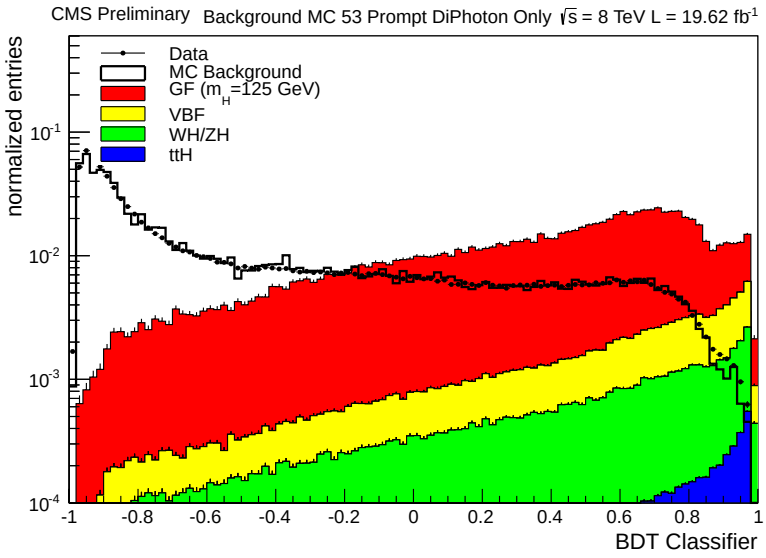

Figure 4.31. Di-photon BDT output for data, background, and signal Monte Carlo simulation at 125 GeV in the mass range of 100 GeV $< m_{\gamma\gamma} <$ 160 GeV. The four categories are marked by the black dashed line.

in data and Monte Carlo simulation. It should be noted that the $Z/\gamma^* \to ee$ events have a scale factor applied to the photon ID BDT output and to the photon energy resolution.

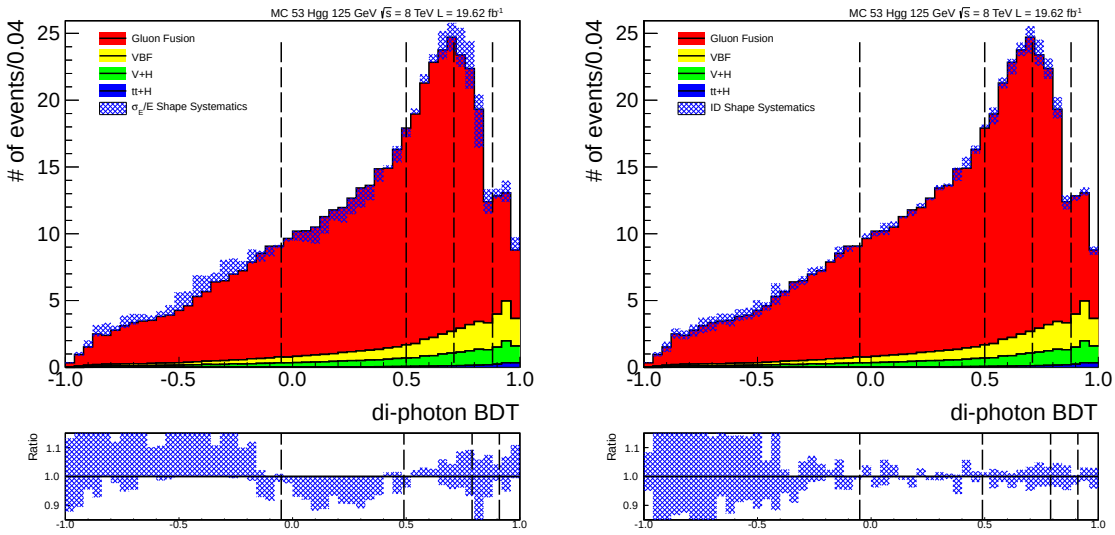

Figure 4.32. The effect of the energy resolution systematic uncertainty (left) and the photon ID systematic uncertainty (right) on simulated signal.

4.10.2 Cut-Based Categories

The categorization for the cut-based analysis is orders of magnitude simpler than that of the main analysis. Both photons are required to pass the pre-selection in section 4.7. Each photon is required to pass a kinematic requirement: $p_T/m_{\gamma\gamma} > \frac{1}{3}$ (lead) and $p_T/m_{\gamma\gamma} > \frac{1}{4}$ (sub-lead). The cut-based cross-check analysis separates events into four categories that match the cut-based photon identification. The most sensitive category is where both photons are in the barrel ($\eta < 1.4442$) and both have an $R_9 > 0.94$. This is followed by the category where one photon converts ($R_9 < 0.94$) but both photons are still in the barrel. Then there is the category where one photon resides in the endcap but both photons are unconverted. The least sensitive category is where at least one photon is located in the endcap and at least one photon is converted [92]. The division in η is a natural one because the change in crystal geometry and detector material significantly worsen the resolution at the barrel-endcap boundary. Additionally, the background from QCD is more plentiful

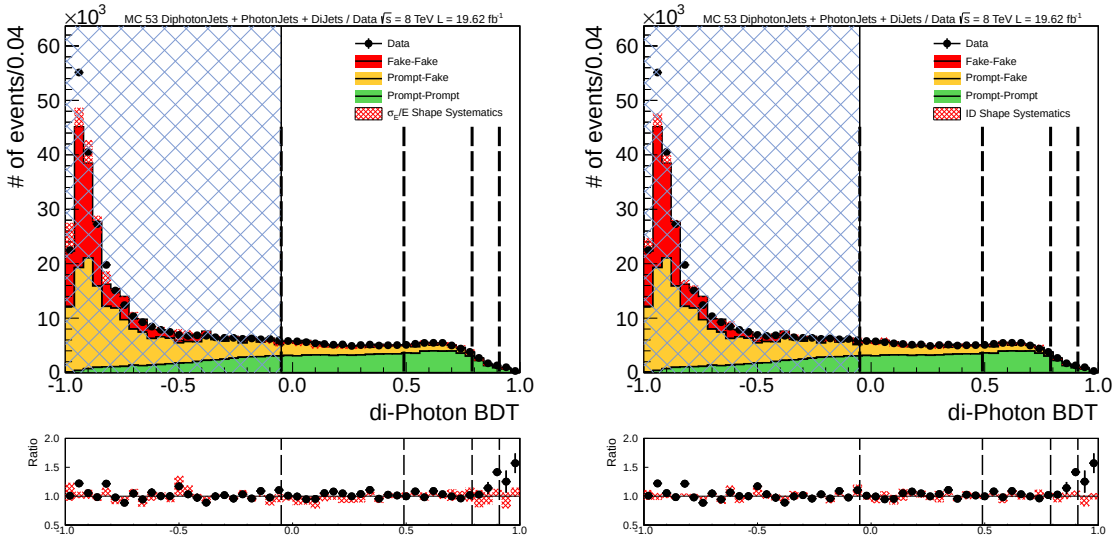

Figure 4.33. The effect of the energy resolution systematic uncertainty (left) and the photon ID systematic uncertainty (right) on simulation background. Actual data is show as black points.

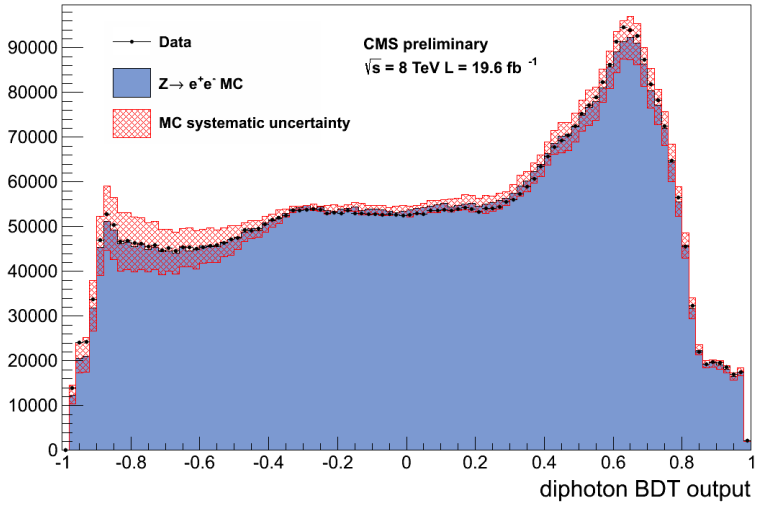

Figure 4.34. Di-photon BDT output for $Z/\gamma^* \to ee$ events in data and Monte Carlo simulation with linear scale corrections applied to σ_E and the photon ID BDT output.

at higher η. The boundary in R_9 is set because it coincides with the boundaries and scale and smear corrections.

4.11 Exclusive Categories

The $H \rightarrow \gamma\gamma$ analysis includes a set of exclusive categories in addition to the inclusive ones. While the inclusive categories search for events with di-photons that pass a pre-selection and categorization. The exclusive categories search for additional objects with the di-photon final state. These objects, presented in selection priority, are:

- Muons - From vector bosons in the higgs-strahlung and top associated production channels (figure 2.6c).
- Electrons - Also from vector bosons in the higgs-strahlung and top associated production channels (figure 2.6c).
- Di-Jets (Tight and Loose) - The two quarks in the vector boson channel form two far-forward high p_T jets (figure 2.6b).
- MET - Again, from vector bosons in the higgs-strahlung and top associated production channels (figure 2.6c).

Any event which does not fall into an exclusive channel is passed to the inclusive categories. Searching for these additional objects in the di-photon final states serves two purposes in the analysis. The primary purpose is that it increases the sensitivitiy of the coupling measurement. The secondary purpose is that it increases the overall analysis sensitivity. The next few subsections will discuss each of the exclusive categories.

4.11.1 Di-Jet Category

The exclusive di-jet category looks for an event signature that is consistent with vector boson fusion (VBF) production. The process has a cross-section that is 10 times smaller than that of gluon-gluon fusion, but also has a lower background. Two

strategies are used to identify VBF events in data. The first is a cut-based approach, which uses a set of cuts to select VBF events. The second is a VBF classification BDT that identifies events that have kinematics consistent with a VBF signature. The BDT approach is used in the 8 TeV main analysis and the cut-based approach is used in the 7 TeV main analysis and the cut-based cross-check analysis at 7 and 8 TeV.

The di-photon selection for the kinematic BDT and cut-based di-jet category is the same as that for the main analysis. The event needs two photons that pass the pre-selection, the photon ID BDT cut of -0.2, and a di-photon BDT cut of -0.05. VBF events have two far-forward jets that originate from the scattering valance quarks. Naturally, the requirement of the di-jet category is to have two jets in the event. In order to reduce the background of low energy deposits in the calorimeters from pileup events, the two jets have to pass a set of criteria for the event to be placed in the di-jet category.

The anti-k_T particle flow jet collection with a cone radius of $\Delta R = 0.5$ is used for identifying the VBF jets. The jets have their energies corrected first for contamination from pileup and then the jet energy scale corrections (JEC) are applied. Both jets are required to have an $|\eta| < 4.7$. Pileup jets are removed from the event with a cut on the compatibility of the jets' tracks with the primary vertex and the width of the jet. These two quantities are defined as:

$$\beta^* = \frac{\sum p_T^{\mathrm{tk\,vtx}}}{\sum p_T^{\mathrm{tk}}} \quad \text{and} \tag{4.14}$$

$$\mathrm{RMS} = \frac{\sum p_{T_{\mathrm{tk}}}^2 \Delta R^2}{\sum p_{T_{\mathrm{tk}}}^2}. \tag{4.15}$$

A complete listing of the cuts can be seen in table 4.31. These cuts remove the dependence of the background efficiency on the number of pileup vertices, while still maintaining a high acceptance for jets from the hard interaction. In order to eliminate

TABLE 4.31

JET-ID CUTS

Jet η	β^*	RMS
$\eta < 2.5$	$< 0.2 \log(N_{\text{vtx}} - 0.64)$	< 0.06
$2.5 < \eta < 2.75$	$< 0.3 \log(N_{\text{vtx}} - 0.64)$	< 0.05
$2.75 < \eta < 3$	-	< 0.05
$3 < \eta < 4.7$	-	< 0.055

jets reconstructed from the photons, all jets within a ΔR cone of 0.5 of the selected photons are rejected [81].

4.11.1.1 Cut-Based Di-Jet Category

The cut-base di-jet category uses a series of cuts to select events to be placed in the exclusive di-jet category. The selection cuts on the following variables:

- $p_T^{\gamma_1}/m_{\gamma\gamma}$ and $p_T^{\gamma_2}/m_{\gamma\gamma}$: The lead and sub-lead photon p_T divided by the invariant mass of the di-photon system.
- $p_T^{j_1}$ and $p_T^{j_2}$: The p_T of the lead and sub-lead jets.
- m_{jj}: The invariant mass of the di-jet system.
- $\Delta\eta_{jj}$: The $\Delta\eta$ between the two jets.
- $\eta|_{\gamma_1+\gamma_2} - (\eta_{j1} + \eta_{j2})/2$: The Zeppenfeld is the η of the Higgs candidate in the di-jet reference frame [93].
- $|\phi_{jj} - \phi_{\gamma\gamma}|$: The $\Delta\phi$ between the di-photon and di-jet system.

The cut-based selection separates the di-jet events into one category at 7 TeV and two categories, di-jet tight and di-jet loose, at 8 TeV. The difference between the

two categories at 8 TeV is that the tight category has a higher cut on the p_T on the sub-leading jet and on the invariant mass of the di-jet system. A full list of cuts for each category can be seen in tables 4.32 and 4.33 for 7 and 8 TeV [81].

TABLE 4.32

7 TEV CUT-BASED DI-JET SELECTIONS

Variable	Di-Jet
$p_T^{\gamma_1}/m_{\gamma\gamma}$	$> 55/120$
$p_T^{\gamma_2}$	> 25 GeV
$p_T^{\mathrm{j}_1}$	> 30 GeV
$p_T^{\mathrm{j}_2}$	> 20 GeV
$\lvert\Delta\eta_{jj}\rvert$	> 3.5
$\lvert Z\rvert$	< 2.5
M_{jj}	> 350 GeV
$\lvert\phi_{jj} - \phi_{\gamma\gamma}\rvert$	> 2.6

4.11.1.2 Kinematic Di-Jet BDT

The di-jet categorization BDT uses the same set of variables as the cut-based selection in section 4.11.1.1. The BDT is trained on a $H \to \gamma\gamma$ VBF Monte Carlo

TABLE 4.33

8 TEV CUT-BASED DI-JET SELECTIONS

Variable	Di-Jet Tight	Di-Jet Loose
$p_T^{\gamma_1}/m_{\gamma\gamma}$	> 0.5	> 0.5
$p_T^{\gamma_2}$	> 25 GeV	> 25 GeV
$p_T^{\mathrm{j}_1}$	> 30 GeV	> 30 GeV
$p_T^{\mathrm{j}_2}$	> 30 GeV	> 20 GeV
$\lvert\Delta\eta_{jj}\rvert$	> 3.0	> 3.0
$\lvert Z\rvert$	< 2.5	< 2.5
M_{jj}	> 500 GeV	> 250 GeV
$\lvert\phi_{jj} - \phi_{\gamma\gamma}\rvert$	> 2.6	> 2.6

simulation sample at 124 GeV as signal and a di-photon+jets sample is used as background. Before events are passed to the di-jet kinematic BDT, they have to pass a VBF pre-selection of: $p_T^{j_1} > 30$ GeV, $p_T^{j_2} > 20$ GeV, and $m_{jj} > 250$ GeV. In order to increase training statistics the leading jet p_T is reduced to 20 GeV and the invariant mass cut is reduced to 100 GeV.

The di-jet kinematic BDT is optimized by maximizing the significance of the signal to the background using a piecewise integral over the categories

$$z^2 = N \sum_{i=0}^{n_{\text{cat}}} \frac{\left(\int_{C_i}^{C_{i+1}} \epsilon_{\text{S}} \right)^2}{\int_{C_i}^{C_{i+1}} \epsilon_{\text{B}}}, \tag{4.16}$$

where C_0 to C_N are the category boundaries and N is the normalization factor that is dependent on total integrated luminosity. For the amount of data collected in 2012 (19.6 fb^{-1}), two categories are optimal. The di-jet BDT category boundaries are listed in table 4.34, and the output for data, background Monte Carlo simulation, and $H \to \gamma\gamma$ gluon fusion and $H \to \gamma\gamma$ VBF signal samples can be seen in figure 4.35 [81].

TABLE 4.34

8 TEV DI-JET BDT CATEGORY BOUNDARIES

	Lower Boundary	Upper Boundary
Di-Jet Tight	0.985	1.0
Di-Jet Loose	0.93	0.985

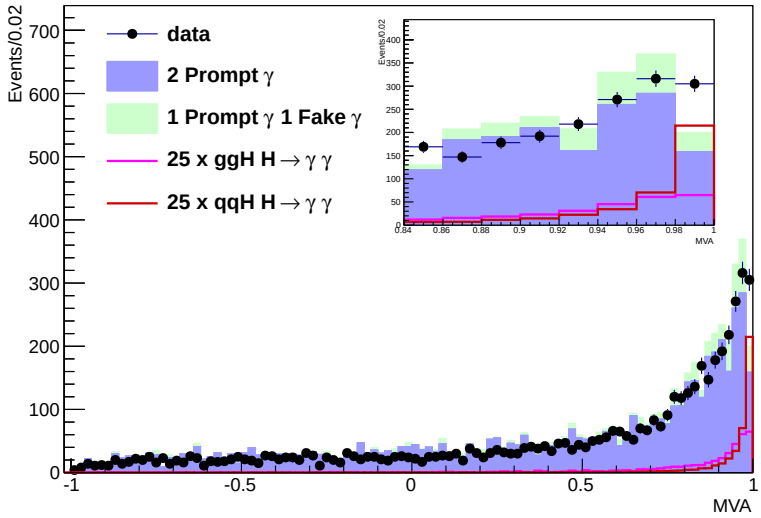

Figure 4.35. Output of the di-jet kinematic BDT for data and simulated signal and background.

4.11.1.3 Di-Jet Systematics

The systematic uncertainties associated with the di-jet channel are jet reconstruction efficiency and pileup jet identification efficiency. The uncertainty of the jet reconstruction efficiency is from the jet energy scale (JES) and jet energy resolution (JER). The JES systematics are estimated by shifting the JES by $\pm 1\sigma$, and JER uncertainty is estimated by the level of disagreement between the data and Monte Carlo simulation in QCD di-jet events. Both the JES and JER cause events to migrate in and out of the di-jet categories into the inclusive ones. The migration into the di-jet category and the migration out of the di-jet category are treated as separate systematics. The systematic uncertainty associate with the pileup jet identification efficiency is estimated from the difference in p_T and η from $Z \to \mu\mu$ +jets events in data and Monte Carlo simulation.

There are two theoretical systematic uncertainties associated with the di-jet category: systematics related to the underlying events and uncertainty on the parton

distribution of the incident protons. To evaluate the first, four different generator tunes (DT6, P0, ProPT0, and ProQ20) are compared with the default Z2 tune. Both gluon fusion and VBF $H \to \gamma\gamma$ Monte Carlo simulation samples are generated with each of the tunes. The jet selection efficiency and the category migration is measured in each of them. The jet migration between the di-jet categories is considered correlated and the jet migration to the inclusive categories is considered anti-correlated. In order to evaluate the PDF systematic uncertainty, three different PDF sets are used: CT10, MSTW2008, and NNPDF2.0. For each of the three PDF α_s is varied between 0.116 to 0.120. The systematic uncertainty is estimated by evaluating the change in efficiency between each of the PDF sets. The final systematic uncertainty is the sum in quadrature of the systematics associated with each PDF set.The systematics for the di-jet identification BDT and cut-based method can be seen in tables 4.35 and 4.36, respectively [81].

TABLE 4.35

SYSTEMATIC UNCERTAINTIES FOR THE DI-JET SELECTION BDT

Process	qqH		ggH	
Category	Tight	Loose	Tight	Loose
JEC & JER Correlated	3.5%		11%	
JEC & JER Anti-Correlated	0.5%	0.5%	7.5%	2.5%
JET ID	2%	2%	2%	2%
Tunes Correlated	8%		26%	
Tunes Anti-Correlated	1%	1%	11%	4.5%
PDFs	1.5%	1.5%	1.5%	1.5%
Total Correlated	9%		28%	
Total Anti-Correlated	1%		14%	

4.11.2 Lepton Categories

The lepton categories are a set of two exclusive categories (muon and electron) that search for an additional lepton in the di-photon final state for the 8 TeV data only. For the case of Higgs production, the lepton is from associated vector boson production or associated top production. The lepton categories are advantageous because they dramatically reduce the background from QCD causing the S/B ratio to be near one. The categories also give additional sensitivity to the boson and

TABLE 4.36

SYSTEMATIC UNCERTAINTIES FOR THE CUT-BASED DI-JET SELECTION

Process	qqH		ggH	
Category	Tight	Loose	Tight	Loose
JEC & JER Correlated	2.5%		10%	
JEC & JER Anti-Correlated	1.5%	2.5%	1.5%	0.5%
JET ID	2%	2%	2%	2%
Tunes Correlated	7%		28%	
Tunes Anti-Correlated	2.5%	3.5%	16%	6.5%
PDFs	1.5%	1.5%	1.5%	1.5%

fermion coupling of the Higgs. Since the lepton selection has a higher purity and efficiency then that of the photon selection, the lepton is identified first and then the photons are selected. So the workflow is as follows:

1. Event passed the di-photon trigger in section 4.2.
2. Event passes the lepton selection.
3. The di-photon pair is selected taking into account the selected lepton.

The photon identification for the lepton categories nearly matches that of the main analysis and the cut-based cross-check. The only difference in the main analysis is that the p_T spectrum of the Higgs in vector boson associated production is harder then that of traditional gluon fusion. The $p_T/m_{\gamma\gamma}$ cut on the lead photon is increased to 45/120 from 40/120. For the cut-based cross-check analysis the p_T threshold for the sub-leading photon is decreased to 25 GeV. It would have been ideal to lower the p_T requirement of the sub-leading photon in both analyses, but it is not possible in the main analysis because those events fall outside the di-photon BDT training and the trigger efficiency falls significantly for photons below 25 GeV. In the electron category there is additional background from Drell-Yan to two electrons, where the electron fakes a photon. Both photons have an addition selection criteria that requires the photon to have a $\Delta R > 1.0$ from the nearest GSF track.

4.11.2.1 Muon Category

The tagged muon is the highest p_T muon in the event that passes the muon selection criteria. Muons are identified through a series of cuts for global muons, where the track in the muon chamber that can be matched to a high p_T track. Each muon candidate is required to have inner tracker information and track segments in the muon chambers. It is also required to have been reconstructed by the particle flow algorithm in section 4.6.4. The muon candidate must have a $p_T > 20$ GeV and

have an $|\eta| < 2.4$. The muon identification looks at the following quantities to select candidates:

- χ^2 $/n_{dof}$: The χ^2 of the global muon fit divided by the number of degrees of freedom.
- $|d_0|$: The transverse track impact parameter with respect to the primary vertex.
- $|d_z|$: The longitudinal track impact parameter with respect to the primary vertex.
- The number of pixel hits.
- The number of total tracker hits.
- At least two muon chambers and one muon station are required to be included in the global muon fit.
- The relative combined particle flow isolation sum in a ΔR of 0.4 is less than 0.2.

Where the relative combined particle flow isolation sum is defined as

$$\frac{\sum \text{PFChIso}_{\mu} + \max(0., \text{PFPhoIso}_{\mu} + \text{PFNeuIso}_{\mu} - \Delta B)}{p_{T_{\mu}}}, \tag{4.17}$$

where PFChIso, PFPhoIso, and PFNeuIso are respectively the charged hadron, photon, and neutral hadron isolation sum in a ΔR cone of 0.4. A complete list of the muon selection criteria can be seen in 4.37. The muon selection criteria are validated on $Z \to \mu\mu$ data and Monte Carlo simulation.

TABLE 4.37

MUON SELECTION CRITERIA

Description	Criterion
Number of Pixel Hits	> 0
χ^2 /n.d.f	< 10
Number of Muon Hits	> 0
Number of Matched Muon Stations	> 1
Number of Tracker Layers	> 5
$\lvert d_0 \rvert$	< 0.2 cm
$\lvert d_z \rvert$	< 0.5 cm
Combined Relative PF Isolation	< 0.2

The systematic uncertainty for the muon category is approximated by varying the scale of the isolation and identification by $\pm\sigma$ (0.5%). The nominal signal yield is computed before the scale variation and then again after. The difference is treated as a systematic uncertainty. The MVA efficiency for data and Monte Carlo simulation can be seen in table 4.38.

4.11.2.2 Electron Category

If the event does not pass the muon selection criteria, it is then evaluated by the electron category. An electron is identified as a supercluster in the ECAL, which is narrow in η and broad in ϕ, that is matched to a GSF track. Electron candidates are

TABLE 4.38

ELECTRON IDENTIFICATION MVA EFFICIENCY IN DATA AND MONTE CARLO SIMULATION

η-range	$\epsilon \pm \sigma_{\text{STAT}} \pm \sigma_{\text{SYST}}$ (DATA)	$\epsilon \pm \sigma_{\text{STAT}}$ (MC)	Ratio$\pm\sigma_{\text{STAT}}$
$0 < \lvert\eta\rvert < 1$	$0.8557 \pm 0.0005 \pm 0.0021$	0.8692 ± 0.0003	0.984 ± 0.002
$1 < \lvert\eta\rvert < 1.44$	$0.8619 \pm 0.0007 \pm 0.0097$	0.8726 ± 0.0004	0.988 ± 0.011
$1.567 < \lvert\eta\rvert < 2.1$	$0.7858 \pm 0.0008 \pm 0.0059$	0.7738 ± 0.0005	1.016 ± 0.008
$2.1 < \lvert\eta\rvert < 2.5$	$0.7397 \pm 0.0011 \pm 0.0133$	0.7408 ± 0.0007	0.999 ± 0.018

required to have a $p_T > 20$ GeV and an $|\eta| < 1.4442$ or between $1.566 < |\eta| < 2.5$ to avoid the ECAL barrel-endcap gap. The candidate electron also must pass the relative combined isolation criteria:

$$\frac{\sum \text{PFChIso}_e + \max(0., \text{PFPhoIso}_e + \text{PFNeuIso}_e - A_{eff}\rho)}{p_{T_e}}, \tag{4.18}$$

where PFChIso, PFPhoIso, and PFNeuIso are respectively the charged hadron, photon, and neutral hadron isolation sum in a ΔR cone of 0.3. In order to reject electrons that are from photon conversions, the candidate must pass the selection criteria on the vertex probability fit and the number of missing hits. Once the electron passes the pre-selection, it is then passed to an electron identification MVA that is trained on generator matched leptons from VH, $Z/\gamma^* \rightarrow ee$, and $W \rightarrow e\nu$ events. The background training sample is provided from data that contained no real electrons. The electron candidate with the highest MVA score is chosen as the tag. If there is not an electron with an MVA score greater than 0.9 then the event fails the electron

category requirements. After the electron passes the MVA cut it has to pass the final two cuts on $|d_0|$ and $|d_z|$ in order for the event to be in the electron category. A full list of the electron selection criteria can be seen in table 4.39.

The systematic uncertainty for the electron identification MVA is estimated from $Z/\gamma^* \to ee$ tag-and-probe. The electron MVA identification efficiency is measured in multiple η-bins in $Z/\gamma^* \to ee$ events for data and Monte Carlo simulation. The disagreement is taken as a systematic uncertainty.

TABLE 4.39

ELECTRON SELECTION CRITERIA

	Barrel and Endcap
Electron ID MVA	0.9
$\|d_0\|$	< 0.02 cm
$\|d_z\|$	< 0.2 cm
Combined Relative PF Isolation	< 0.15
Vertex Fit Probability (conv. rej)	$< 10^{-6}$
Missing Hits (conv. rej.)	< 2

4.11.3 $\not{E}_T$ Category

The $\not{E}_T$ exclusive channel looks for events with a di-photon final state and large missing transverse energy ($\not{E}_T$), which is associated with a neutrino, in the 8 TeV

data. There are two production channels that can produce $\not\!\!E_T$ in the event. The WH and ZH channels produce events that are associated with the $\not\!\!E_T$ channel. In the case where the W decays leptonically, and the lepton is missed by the muon or electron categories, the event can pass to the $\not\!\!E_T$ category. This category is also populated by events where the Z decays into neutrinos. The associated top production channel can also be placed in the MET category if the event fails to be placed in the lepton channels. However, due to the small cross-section of associated top production the effect is minimal. Similarly to the rest of the exclusive categories, the $\not\!\!E_T$ category increases the sensitivity to the coupling of the Higgs to vector bosons and fermions in addition to increasing the overall sensitivity of the analysis. The $\not\!\!E_T$ category is the final exclusive category, and if an event fails the category requirements, then it is passed to the inclusive categories. The selection criteria for the $\not\!\!E_T$ channel is ordered different than that of the lepton categories:

1. Select events that passes the di-photon selection.
2. Then select events that meet the $\not\!\!E_T$ requirement.
3. Apply addition kinematic cuts to increase the S/B ratio and reduce gluon fusion contamination and $\not\!\!E_T$ mis-measure by the detector.

The di-photon selection for the $\not\!\!E_T$ category is very similar to that of the main analysis. The di-photon system has to pass the photon ID BDT cut of -0.2 and the di-photon BDT cut of -0.05. However, since the primary contribution of signal events to the $\not\!\!E_T$ category is from associated vector boson production, the p_T spectrum of the Higgs is higher than that of gluon-fusion. So the p_T threshold for the lead photon is increased to 45/120 and the sub-lead threshold is decreased to 25 GeV. Since the $\not\!\!E_T$ category is the least sensitive of the exclusive channels, only events where both photons are in the barrel are used.

The $\not\!\!E_T$ category requires that the event have large particle flow $\not\!\!E_T$ in addition to two photons that pass the selection. The majority of events that are placed in

this category have no real $\not\!\!E_T$. The measured $\not\!\!E_T$ in the event is due to detector noise, jet energy reconstruction, and misalignment of the sub-detectors. Adding to the complication is that these contributions to $\not\!\!E_T$ are often not well modeled in the Monte Carlo simulation, as seen in figures 4.36a and 4.36b. In order to have better agreement between the data and Monte Carlo simulation, a set of corrections for the $\not\!\!E_T$ have been developed. Two quantities are used when measuring the $\not\!\!E_T$ in an event: $\not\!\!E_T$ and $\not\!\!E_T^{\phi}$. The resolution in the Monte Carlo simulation needs to be smeared in order to match that in data as seen in figure 4.36a. The $\not\!\!E_T$ smearing is done by smearing the particle flow anti-k_T jets according to their resolution. The expected resolution on jet energy can vary from 3% to 15% depending on the η of the jet. The resolution uncertainty is then estimated depending on whether the PF jet can be matched to a generator jet. If the PF jet is matched to a generator jet, then the resolution is weighted by the difference in the reconstructed and generated p_T of the jet by

$$\frac{p_T^{\mathrm{RECO}} - p_T^{\mathrm{GEN}}}{p_T^{\mathrm{RECO}}}. \tag{4.19}$$

If the PF jet is not matched to a generator jet then the smearing factor is a random value pulled from a Gaussian centered at 0 with a σ that is dependent of the η and p_T of the reconstructed jet. The resolution of the PF jets in the Monte Carlo simulation is smeared according to whether they are matched to a generator jet or not. However, the standard JEC is applied to the PF jets in data. In order to correct the $\not\!\!E_T^{\phi}$ distribution, a shift is applied to the $\not\!\!E_T$ vector. The shift is different in the x and y directions and is dependent on the total magnitude of $\not\!\!E_T$ as seen in figure 4.37 and 4.38 for the Monte Carlo simulation and data respectively. In order to account for these effects, different shifts are applied to data and Monte Carlo simulation. The corrected $\not\!\!E_T$ and $\not\!\!E_T^{\phi}$ distributions can be seen in figures 4.39a and 4.39b.

After all the corrections are applied, a cut is placed on the magnitude of $\not\!\!E_T$. The value of the cut is optimized for the maximum excluding power against the standard

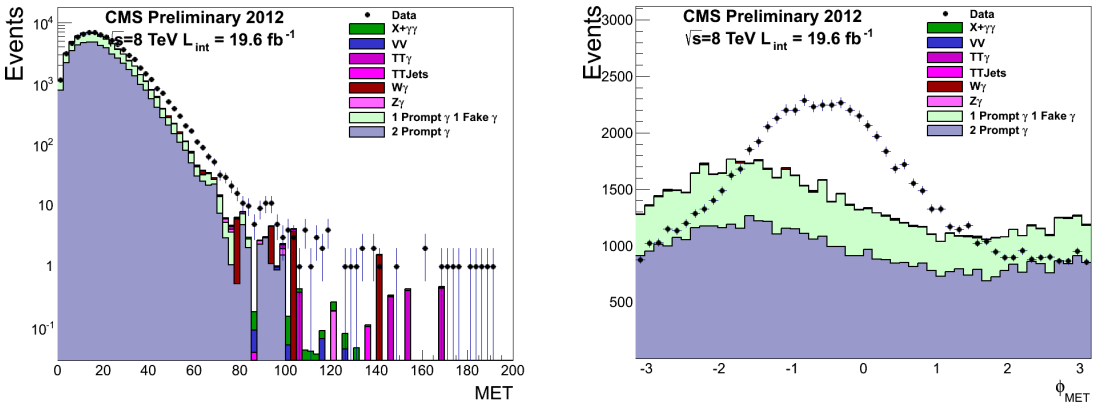

(a) $\not\!\!E_T$. (b) $\not\!\!E_T^{\phi}$.

Figure 4.36. Uncorrected Particle Flow $\not\!\!E_T$ and $\not\!\!E_T^{\phi}$.

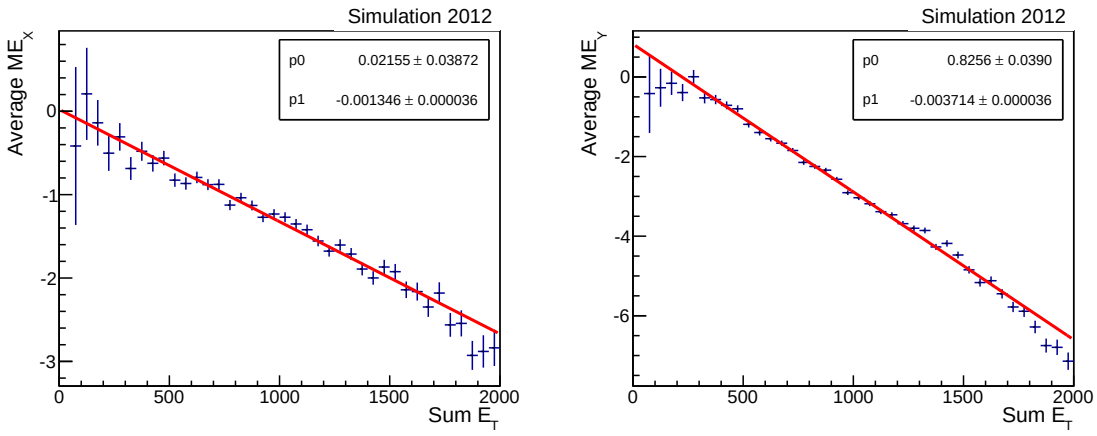

Figure 4.37. The shift in the fake $\not\!\!E_T$ in the x (left) and y (right) directions as a function of the magnitude of $\not\!\!E_T$ in the Monte Carlo simulation.

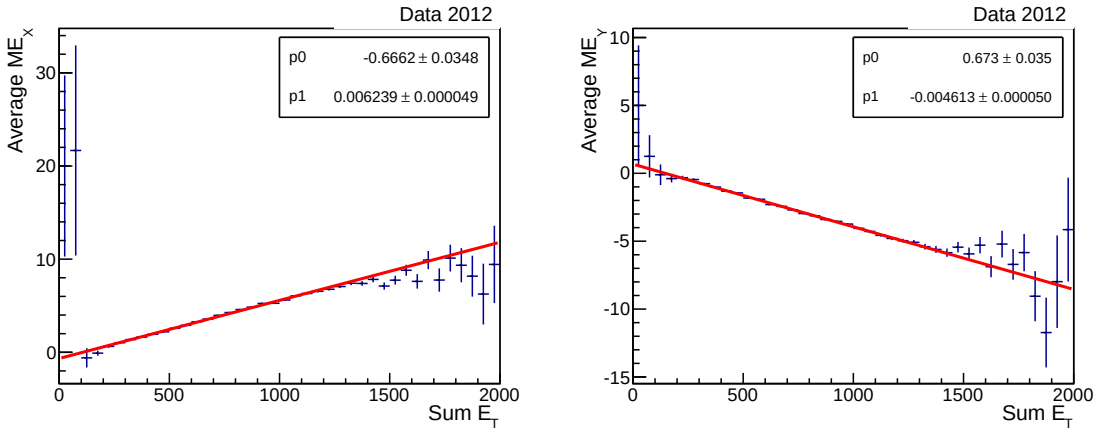

Figure 4.38. The shift in the fake $\not\!\!E_T^{\phi}$ in the x (left) and y (right) directions as a function of the magnitude of $\not\!\!E_T^{\phi}$ in Data.

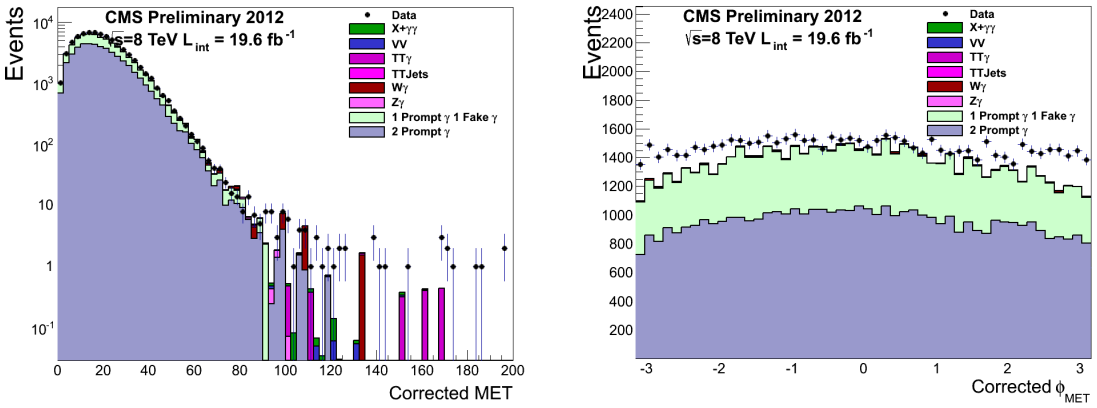

(a) $\not\!\!E_T$. (b) $\not\!\!E_T^{\phi}$.

Figure 4.39. Corrected Particle Flow $\not\!\!E_T$ and $\not\!\!E_T^{\phi}$.

model Higgs. A cut of $\not\!\!E_T > 70$ GeV is selected as can be seen in figure 4.40. In order to further reduce contamination from background, an additional kinematic requirement is on the $\not\!\!E_T$. Since the Higgs is recoiling directly off the vector boson, which is decaying to $\not\!\!E_T$, the $|\phi_{\gamma\gamma} - \phi_{\not\!\!E_T}|$ between the di-photon system and the $\not\!\!E_T$ vector must be greater than 2.1. It can be seen in figures 4.39a and 4.39b that there is still a disagreement between the $\not\!\!E_T$ in the Monte Carlo simulation and in data when $\not\!\!E_T > 100$. While this does not cause a significant problem for the analysis in general, it does decrease the S/B ratio in the $\not\!\!E_T$ category. It also adds uncertainty on the amount of gluon fusion contamination in the $\not\!\!E_T$ category. It can be seen in figure 4.41 that the excess $\not\!\!E_T$ is coming from the leading p_T jet in the event. In order to reduce this effect, the $|\phi_{\not\!\!E_T} - \phi_{\text{leadjet}}|$ between the di-photon system and the highest p_T jet in the event is required to be less than 2.7, when the leading jet has a p_T greater than 50 GeV. The final $\not\!\!E_T$ and $\not\!\!E_T^{\phi}$ distribution can be seen in figures 4.42a and 4.42b and the final di-photon and $\not\!\!E_T$ cut in table 4.40.

The $\not\!\!E_T$ uncertainty is evaluated in all of the $H \to \gamma\gamma$ channels. In the associated vector boson production channel, the systematic uncertainty is estimated by evaluating the change in efficiency when the $\not\!\!E_T^{\phi}$, jet energy resolution smearing, and jet residual correction scalings are enabled and disabled. For the non-VH $H \to \gamma\gamma$ channels, the event yields for $\gamma +$ jet events that pass the $\not\!\!E_T$ selection at 70 GeV for data and Monte Carlo simulation are compared. The statistical uncertainty of the comparison is used as the systematic uncertainty for the $\not\!\!E_T$ in these signal channels. The $\not\!\!E_T$ systematic uncertainty can been seen in table 4.41.

4.11.4 Signal and Background Yields

The total expected signal yield for each of the categories can be seen for the main analysis in table 4.42. The expected yield from data and background Monte Carlo

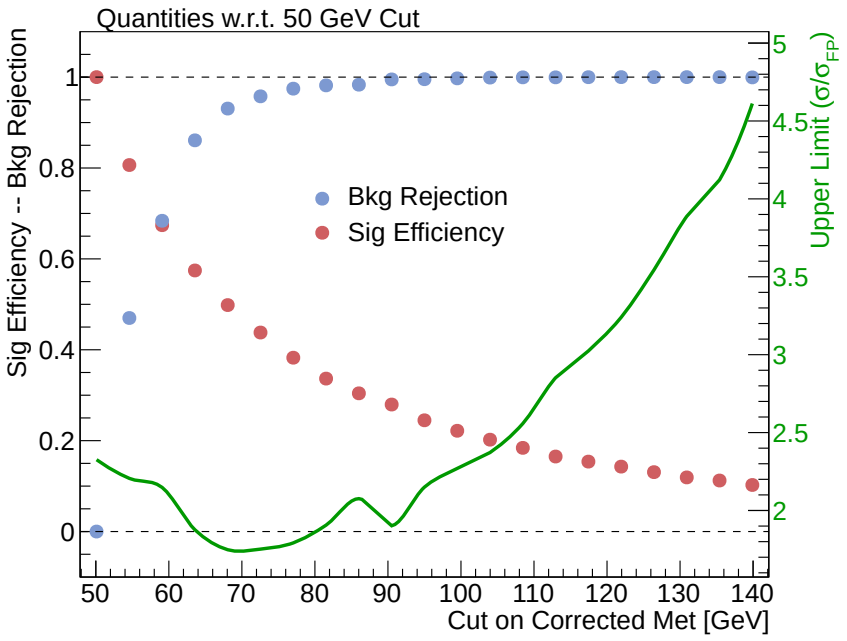

Figure 4.40. Optimization of the corrected particle flow $\not{E}_T$ with associated signal acceptance and background rejection.

TABLE 4.40

DI-PHOTON AND $\not{E}_T$ SELECTION CRITERIA

Variable	Selection
Di-Photon BDT	> -0.05
$p_T^{\gamma_1}/m_{\gamma\gamma}$	$> \frac{45}{120}$
$p_T^{\gamma_2}/m_{\gamma\gamma}$	$> \frac{30}{120}$
$\not{E}_T$	> 70 GeV
$\Delta\phi_{\not{E}_T-\text{leadjet}}$	< 2.7
$\Delta\phi_{\gamma\gamma-\not{E}_T}$	> 2.1

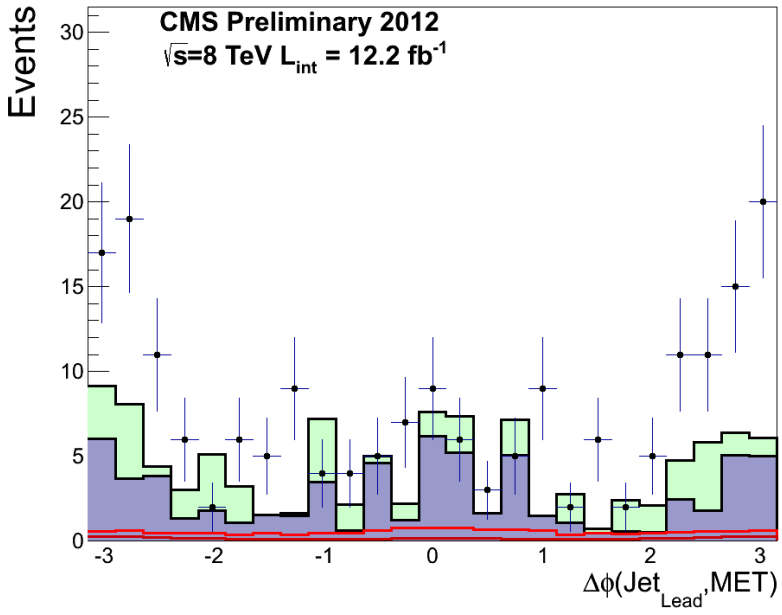

Figure 4.41. The event yield in data and Monte Carlo simulation versus the $\Delta\phi_{\not\!\!E_T-\text{leadjet}}$ between the leading jet and the $\not\!\!E_T$ vector.

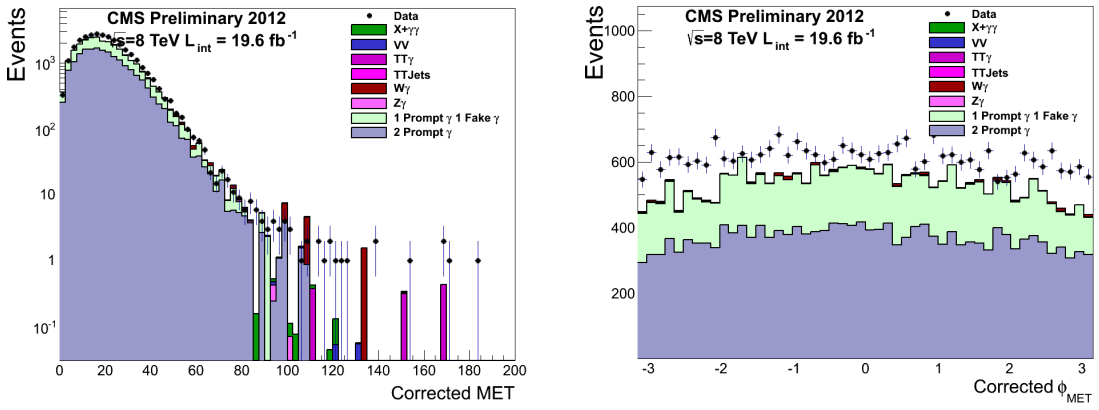

(a) $\not\!\!E_T$ (b) $\not\!\!E_T^{\phi}$

Figure 4.42. Corrected Particle Flow $\not\!\!E_T$ and $\not\!\!E_T^{\phi}$ after Topological Cleaning.

TABLE 4.41

$\not\!\!E_T$ SYSTEMATIC UNCERTAINTIES

Channel	Statistical Error with MET>70 GeV
Gluon Fusion	15%
Vector Boson Fusion	15%
Associated Vector Boson	4%
Associated Top Production	4%

simulation for each category of the main analysis can be found in table 4.43. Similarly the yields for the cut-based analysis can be found in table 4.44 and 4.45 for signal and background, respectively.

TABLE 4.42

MAIN ANALYSIS 8 TEV SIGNAL YIELD FOR $M_H = 125$ GEV

Categories	Total	ggH	VBF	VH	ttH	σ_{eff} (GeV)	FWHM/2.35 (GeV)
Inclusive 0	17.0	72.9%	11.6%	12.9%	2.6%	1.36	1.27
Inclusive 1	37.8	83.5%	8.4%	7.1%	1.0%	1.50	1.39
Inclusive 2	150.2	91.6%	4.5%	3.6%	0.4%	1.77	1.54
Inclusive 3	159.9	92.5%	3.9%	3.3%	0.3%	2.61	2.14
Di-Jet Tight	9.2	20.7%	78.9%	0.3%	0.1%	1.79	1.50
Di-Jet Loose	11.5	47.0%	50.9%	1.7%	0.5%	1.87	1.60
Muon Tag	1.4	0.0%	0.2%	79.0%	20.8%	1.85	1.52
Electron Tag	0.9	1.1%	0.4%	78.7%	19.8%	1.88	1.54
$\not{E}_T$ Tag	1.7	22.0%	2.6%	63.7%	11.7%	1.79	1.64

TABLE 4.43

MAIN ANALYSIS 8 TEV BACKGROUND YIELD

Categories	Background $m_{\gamma\gamma} = 125$ GeV (ev./GeV)	Data $100 < m_{\gamma\gamma} < 180$ GeV	Data $m_{\gamma\gamma} = 125$ GeV (ev./GeV)
Inclusive 0	22.1 ± 0.5	1449	40.0
Inclusive 1	94.3 ± 1.0	6206	101.0
Inclusive 2	570.5 ± 2.6	37939	554.0
Untagged 3	1060.9 ± 3.5	72319	1037.0
Di-Jet Tight	3.4 ± 0.2	222	2.0
Di-Jet Loose	12.4 ± 0.4	823	11.0
Muon Tag	0.7 ± 0.1	38	1.0
Electron Tag	0.7 ± 0.1	38	0.0
$\not{E}_T$ Tag	1.8 ± 0.1	124	2.0

TABLE 4.44

CUT-BASED 8 TEV SIGNAL YIELD FOR $M_H = 125$ GEV

Categories	Total	ggH	VBF	VH	ttH	σ_{eff} (GeV)	FWHM/2.35 (GeV)
Inclusive 0	109.4	91.1%	4.8%	3.6%	0.5%	1.63	1.43
Inclusive 1	144.6	91.5%	4.7%	3.4%	0.4%	2.00	1.65
Inclusive 2	55.1	89.3%	5.4%	5.0%	0.3%	3.15	2.93
Inclusive 3	71.8	90.3%	4.9%	4.6%	0.3%	3.19	2.96
Di-Jet Tight	9.4	22.1%	77.3%	0.5%	0.1%	1.93	1.56
Di-Jet Loose	10.8	52.2%	46.2%	1.6%	0.0%	1.95	1.71
Muon Tag	1.4	0.0%	0.2%	81.4%	18.5%	1.99	1.55
Electron Tag	0.9	1.1%	0.5%	80.3%	18.1%	1.92	1.58
$\not{E}_T$ Tag	1.6	22.6%	3.0%	63.8%	10.5%	1.99	1.73

TABLE 4.45

CUT-BASED 8 TEV BACKGROUND YIELD

Categories	Background $m_{\gamma\gamma} = 125$ GeV (ev./GeV)	Data $100 < m_{\gamma\gamma} < 180$ GeV	Data $m_{\gamma\gamma} = 125$ GeV (ev./GeV)
Inclusive 0	374.7 ± 2.1	24583	413.0
Inclusive 1	739.5 ± 2.9	48087	782.0
Inclusive 2	368.2 ± 2.1	24152	370.0
Inclusive 3	666.8 ± 2.8	43643	638.0
Di-Jet Tight	5.3 ± 0.2	343	4.0
Di-Jet Loose	14.9 ± 0.4	976	20.0
Muon Tag	0.7 ± 0.1	36	1.0
Electron Tag	0.8 ± 0.1	46	0.0
$\not{E}_T$ Tag	1.6 ± 0.1	114	1.0

CHAPTER 5

STATISTICAL ANALYSIS

This chapter will present the final results for the $H \rightarrow \gamma\gamma$ search in the 7 and 8 TeV datasets. The first step in measuring the signal will be the determination of the background via a likelihood fit to the data in each category. The second step is constructing a parametric signal model for each category. Once this is completed, the final limits, p-values, and cross-sections will be extracted from the data. Additional measurements of the coupling to fermions and bosons and the best-fit mass will be presented.

5.1 Multivariate Statistical Analysis

After the di-photon events pass all of the selections and categorization by the di-photon BDT, events at 7 TeV and 8 TeV are separated into five and nine categories, respectively. Events with a di-photon invariant mass between 100 and 180 GeV are fit with a Bernstein polynomial using a likelihood fit. The fit is used to determine the expected number of events for the background-only hypothesis. The signal in each of the 14 categories is modeled in order to take into account the different resolution and acceptance×efficiency of each category. Once the signal and background are properly modeled everything is in place to make the final measurements.

5.1.1 Background Modeling

For the final measurements, a fully differentiable, parametric model is needed. The background fit and its uncertainty will serve as the background-only hypothesis

for all of the final measurements. Unfortunately, the shape of the background is not known a-priori, and the addition of turn on and detector effects make using a theoretically driven background shape unfavorable. However, if the wrong background shape is used, it has the potential to introduce a bias into the analysis. Since the true background shape is unknown, multiple candidate functions are tested: exponential, power law, Bernstein polynomial, and a Laurent series. Each function and their parameters can be seen in table 5.1. Truth models are generated by fitting the data in each category with each test function, where the order (N) of the function is determined by a p-value derived from χ^2 of the fit for the 8 TeV data and an F-test for the 7 TeV data. The bias for each test function is evaluated for each of the truth models. This is done by generating a large number of Monte Carlo toys for each truth model, and then fitting the toys with the test function. In order for a test function to pass the bias test, it must have a small bias against all truth models, where a small bias requires that the median bias is less than one fifth the statistical uncertainty of the background fit.

The final selected background fit models for all the categories can be found in table 5.2. It can be seen from table 5.2 that a Bernstein polynomial is always chosen as the background fit. This is because the other functions cannot create the shape that a Bernstein polynomial can. This does not mean that the background function is actually a Bernstein polynomial, it only means that if the background is a Bernstein polynomial, then the power law, exponential fit, and Laurent series cannot model it without bias. For inclusive category 3 at 8 TeV, the measured bias is slightly beyond the 0.2 cutoff; however, a function that is less biased than a 5^{th} order Bernstein polynomial was not found [81]. A complete discussion of the truth model selection and bias test can be found in appendix B.

TABLE 5.1

TESTED TRUTH MODELS

Background Model	Function	Degrees of Freedom
Exponential	$\sum_{i=1}^{N} \beta_i e^{\alpha_i x}$	$2N$
Power Law	$\sum_{i=1}^{N} \beta_i x^{-\alpha_i}$	$2N$
Bernstein Polynomial	$\sum_{i=1}^{N} \beta_i b_{(i,N)}$ where $b_{(i,N)} = \begin{pmatrix} N \\ i \end{pmatrix} x^i (1-x)^{N-i}$	$N+1$
Laurent Series	$\sum_{i=1}^{N} \beta_i x^{\left(-4+\sum_{j=1}^{i}(-1)^j(j-1)\right)}$	N

5.1.2 Signal Modeling

The signal model for the $H \to \gamma\gamma$ analysis is built from a Monte Carlo simulation in the four production channels. The signal models take into account all the photon corrections and create a signal shape for all of the 14 categories. The signal model for each category is a continuous, analytic, parametric model that is built from a Monte Carlo simulation that is generated at fixed Higgs masses between 110-150 GeV at 5 GeV steps. The signal models for the $H \to \gamma\gamma$ analysis are built from a sum of 2 or 3

TABLE 5.2

FINAL BACKGROUND MODELS FOR THE MAIN ANALYSIS

Energy	Category	Fit Function
8 TeV	Inclusive Category 0	5^{th} Bernstein
	Inclusive Category 1	5^{th} Bernstein
	Inclusive Category 2	5^{th} Bernstein
	Inclusive Category 3	5^{th} Bernstein
	Di-Jet Tight	4^{th} Bernstein
	Di-Jet Loose	4^{th} Bernstein
	Muon Tag	3^{rd} Bernstein
	Electron Tag	3^{rd} Bernstein
	$\not\!\!E_T$ Tag	3^{rd} Bernstein
7 TeV	Inclusive Category 0	4^{th} Bernstein
	Inclusive Category 1	5^{th} Bernstein
	Inclusive Category 2	5^{th} Bernstein
	Inclusive Category 3	5^{th} Bernstein
	Di-Jet Category	3^{rd} Bernstein

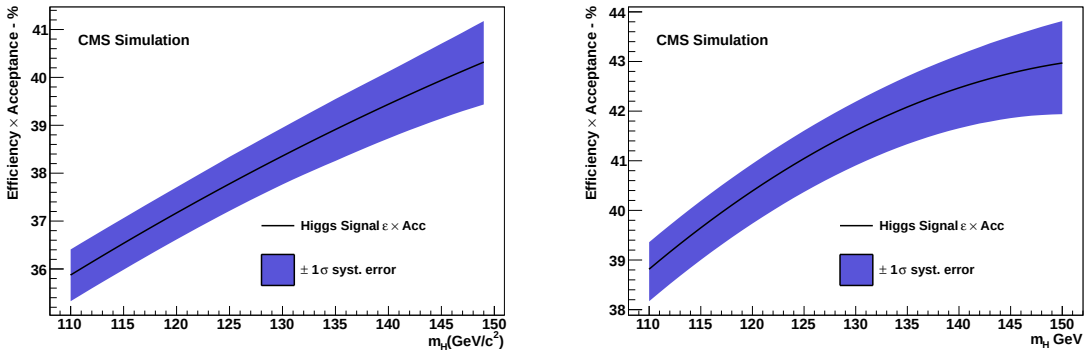

Figure 5.1. The total acceptance×efficiency for the main analysis for 7 (left) and 8 (right) TeV.

Gaussians, depending on category, where the means, widths, and relative fractions of the Gaussians are free to float. This allows the model to be extremely flexible when fitting the signal shape collected from the Monte Carlo simulation. The parameters of the fits for each production channel at the different mass points are then linearly interpolated to create a continuous signal model over the entire mass range, taking into account changing acceptance×efficiency. The interpolated parametric models for each production channel are weighted by their cross-sections and added together. Once the signal model is complete, the total acceptance×efficiency of the analysis is computed, as seen for 7 and 8 TeV in figure 5.1.

An additional signal model is made for when the wrong primary vertex in the event is selected, as this significantly impacts the resolution, as seen in figure 5.2. All other systematics are evaluated as log-normal uncertainties or as perturbations to the analytic function after it is fit from the Monte Carlo simulation. The incorrect vertex signal model is combined with the correct vertex signal model, weighted by the fraction of events where the correct vertex is selected in the Monte Carlo simulation. A closure test at 115 GeV can be seen in figure 5.3, where the interpolated signal model is compared to the non-interpolated one. The final signal models of

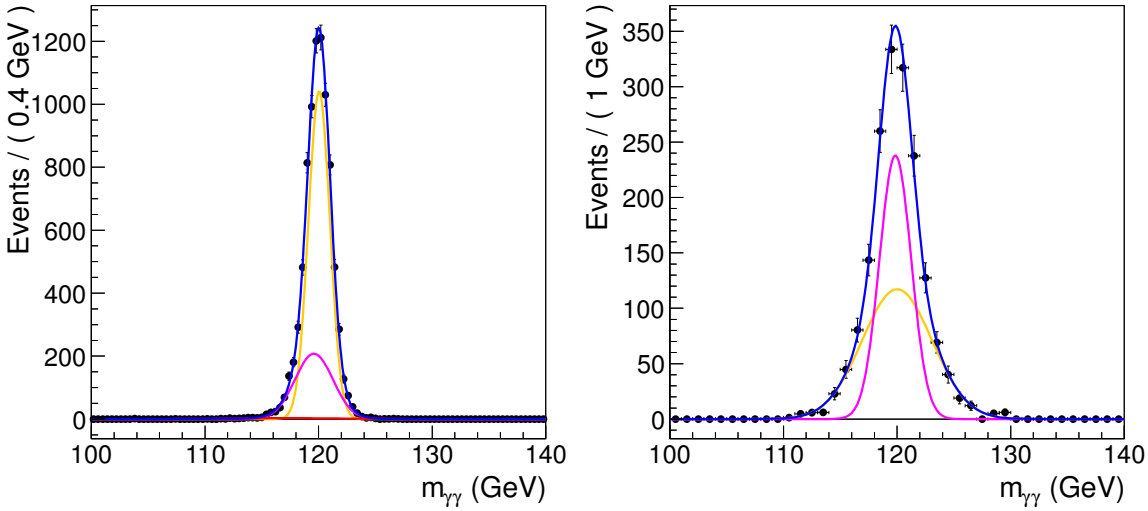

Figure 5.2. Example parametric signal model for $H \to \gamma\gamma$ in the gluon fusion production channel at 120 GeV for the correct (left) and the incorrect (right) vertex.

all the different event categories can be seen in figures 5.4 and 5.5 for 7 and 8 TeV, respectively, and figure 5.6 has the combined signal model for all the categories at 7 and 8 TeV [81].

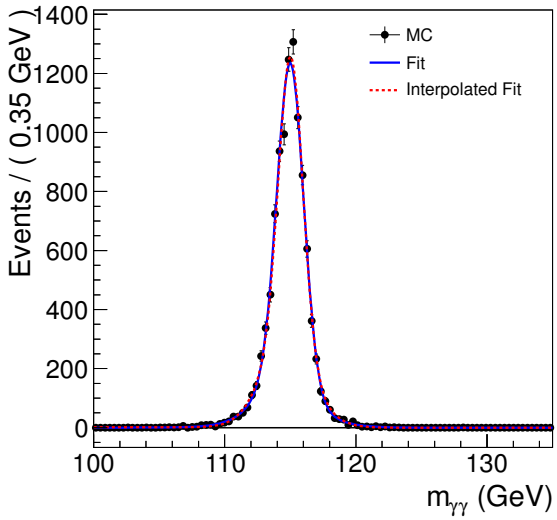

Figure 5.3. The parametric model for $H \to \gamma\gamma$ at 115 GeV with the interpolated signal model (red) and the one fit from the Monte Carlo simulation (blue).

5.1.3 Systematics

The luminosity uncertainty is estimated to be 4.5% and 4.4% for 7 and 8 TeV, respectively. The theoretical systematic uncertainties are the QCD scale uncertainty and the uncertainty associated with the proton PDF, which includes the α_s uncertainty added in quadrature [65]. Since the di-photon categorization BDT is dependent on the kinematics of the Higgs boson, the QCD scale and PDF uncertainties result in a category migration uncertainty. The luminosity, scale, and PDF uncertainties are the same for both the main and cut-based cross-check analysis. The luminosity, proton PDF, and QCD scale uncertainties and systematic uncertainties discussed earlier in the Event Selection chapter can be seen in tables 5.3 and 5.4 for 7 and 8 TeV.

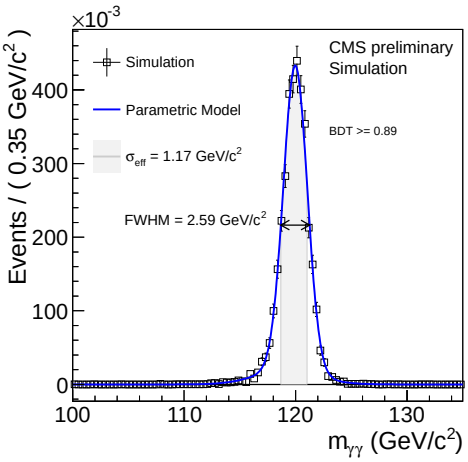

(a) BDT$>$ 0.89

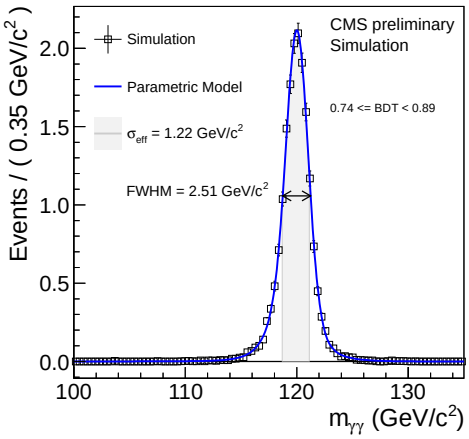

(b) 0.72 $<$BDT$<$ 0.89

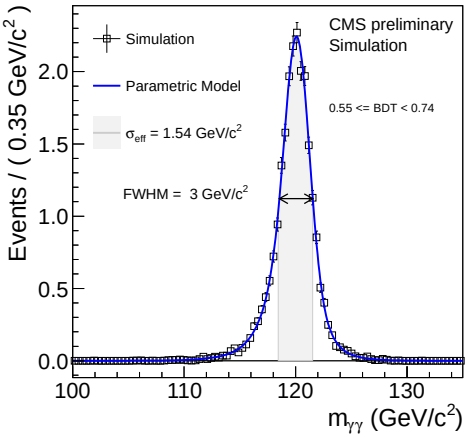

(c) 0.55 $<$BDT$<$ 0.72

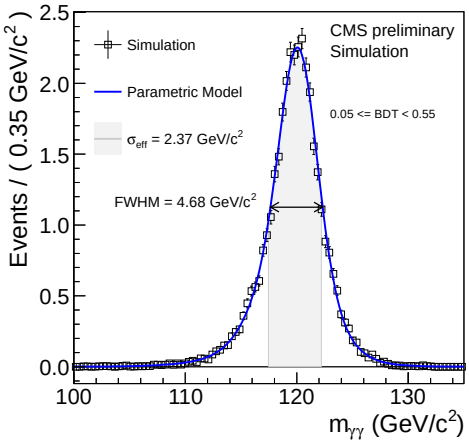

(d) -0.05 $<$BDT$<$ 0.55

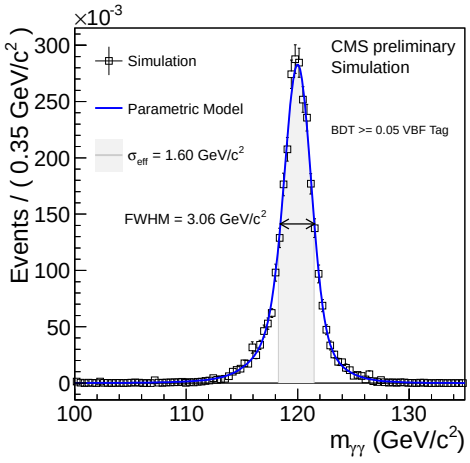

(e) BDT$>$ 0.05 Di-Jet Category

Figure 5.4. The main analysis parametric signal models for the five 7 TeV categories fit from a $H \to \gamma\gamma$ Monte Carlo simulation at 120GeV.

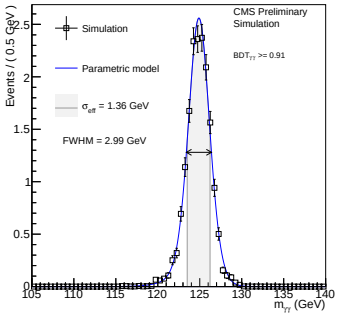

(a) BDT> 0.91

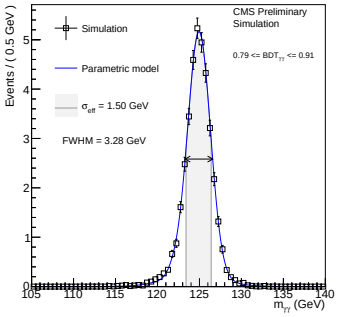

(b) 0.79 <BDT< 0.91

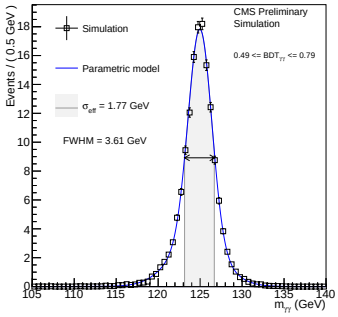

(c) 0.50 <BDT< 0.79

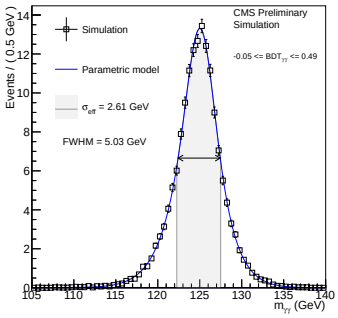

(d) −0.05 <BDT< 0.49

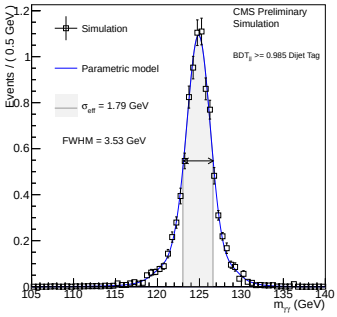

(e) BDT> −0.05 BDT_{jj} > 0.985

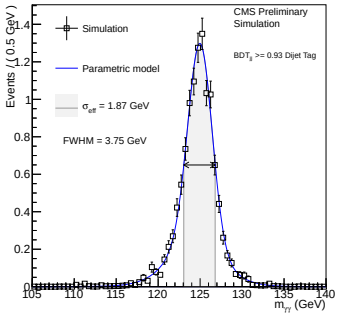

(f) BDT> −0.05 BDT_{jj} > 0.93

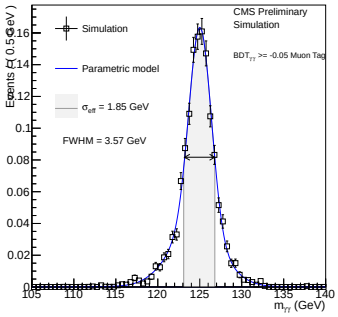

(g) BDT> −0.05 Muon tag

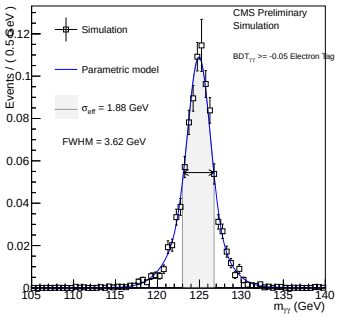

(h) BDT> −0.05 Electron tag

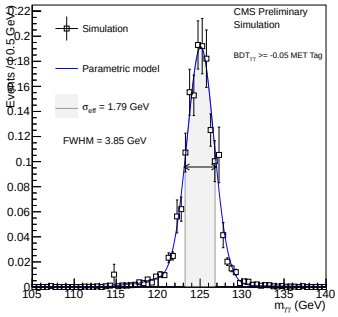

(i) BDT> −0.05 $\not\!\!E_T$ tag

Figure 5.5. The main analysis parametric signal models for the nine 8 TeV categories fit from a $H \to \gamma\gamma$ Monte Carlo simulation at 125GeV.

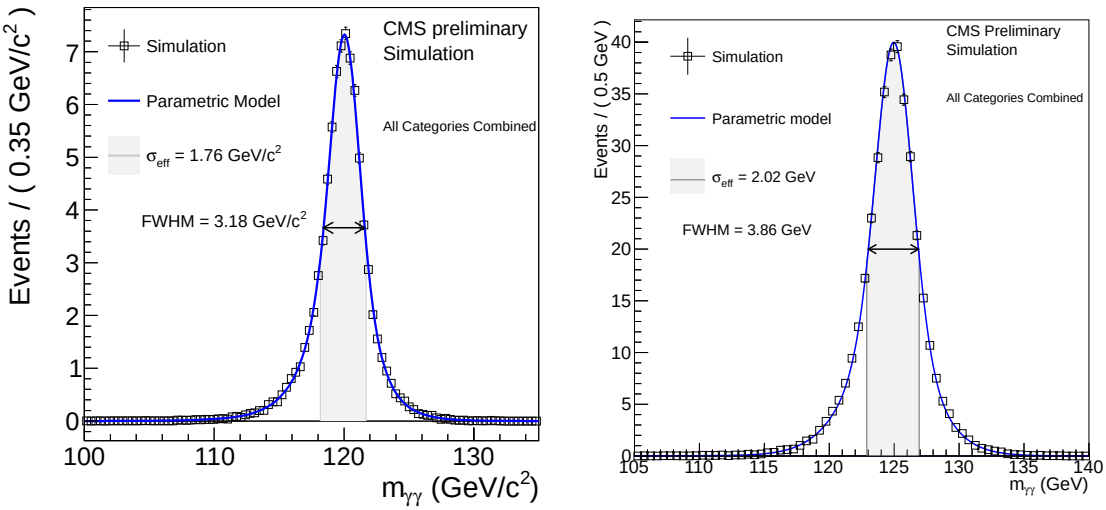

(a) Combined 7 TeV

(b) Combined 8 TeV

Figure 5.6. Combination of all the main analysis parametric signal models for 7 (left) and 8 (right) TeV.

TABLE 5.3

7 TEV SYSTEMATICS FOR THE MAIN ANALYSIS

Sources of Systematic Uncertainty		**Uncertainty**	
Per Photon		Barrel	Endcap
Photon Identification Efficiency		1.0%	2.6%
Energy Resolution ($\Delta\sigma/E_{MC}$)	$R_9 > 0.94$ (Low η, High η)	0.22%, 0.61%	0.91%, 0.34%
	$R_9 < 0.94$ (Low η, High η)	0.24%, 0.59%	0.30%, 0.53%
Energy Scale ($(E_{data} - E_{MC})/E_{MC}$)	$R_9 > 0.94$ (Low η, High η)	0.19%, 0.71%	0.88%, 0.19%
	$R_9 < 0.94$ (Low η, High η)	0.13%, 0.51%	0.18%, 0.28%
Photon Identification MVA (Effect of up to 11% event class migration.)		±0.025 (Shape Shift)	
Photon Energy Resolution MVA (Effect of up to 8% event class migration.)		±0.10 (Shape Scaling)	

TABLE 5.3

Continued

Sources of Systematic Uncertainty		**Uncertainty**
Per Event		
Integrated Luminosity		4.5%
Vertex finding Efficiency		0.4%
Trigger Efficiency	One or both photons $R_9 < 0.94$ in endcap	0.4%
	Other Events	0.1%
Di-Jet Selection		
Di-Jet Tagging Efficiency	VBF Process	10%
	Gluon-Gluon Fusion Process	70%

TABLE 5.3

Continued

Sources of Systematic Uncertainty	**Uncertainty**	
Production Cross-Sections	Scale	PDF
Gluon-Gluon Fusion	+12.5% -8.2%	+7.9% -7.7%
Vector Boson Fusion	+0.5% -0.3%	+2.7% -2.1%
Associated Production with W/Z	1.8%	4.2%
Associated Production with $t\bar{t}$	+3.6% -9.5%	8.5%
Scale and PDF Uncertainties (Effect of up to 16% event class migration.)	(η, p_T)-differential	

TABLE 5.4

8 TEV SYSTEMATICS FOR THE MAIN ANALYSIS

Sources of Systematic Uncertainty		**Uncertainty**	
Per Photon		Barrel	Endcap
Photon Selection Efficiency		0.8%	2.2%
Energy Resolution ($\Delta\sigma/E_{MC}$)	$R_9 > 0.94$ (Low η, High η)	0.23%, 0.72%	0.93%, 0.36%
	$R_9 < 0.94$ (Low η, High η)	0.25%, 0.60%	0.33%, 0.54%
Energy Scale ($(E_{data} - E_{MC})/E_{MC}$)	$R_9 > 0.94$ (Low η, High η)	0.20%, 0.71%	0.88%, 0.12%
	$R_9 < 0.94$ (Low η, High η)	0.20%, 0.51%	0.18%, 0.12%
Photon Identification MVA		$\pm$0.01 (Shape Shift)	
(Effect of up to 4.3% event class migration.)			
Photon Energy Resolution MVA		$\pm$0.10 (Shape Scaling)	
(Effect of up to 8.1% event class migration.)			

TABLE 5.4

Continued

Sources of Systematic Uncertainty	**Uncertainty**
Per event	
Integrated Luminosity	4.4%
Vertex Finding Efficiency	0.2%
Trigger Efficiency	1.0%
Global Energy Scale	0.47%
Di-Jet Selection	
Di-Jet Tagging Efficiency — VBF Process	10%
Gluon-Gluon Fusion Process	30%
(Effect of up to 15% event migration among di-jet classes.)	

TABLE 5.4

Continued

Sources of Systematic Uncertainty		**Uncertainty**
Muon Selection		
Muon Identification Efficiency		1.0%
Electron Selection		
Electron Identification Efficiency		1.0%
$\not\!\!E_T$ **Selection**		
$\not\!\!E_T$ Cut Efficiency	Gluon-Gluon Fusion	15%
	Vector Boson Fusion	15%
	Associated Production with W/Z	4%
	Associated Production with $t\bar{t}$	4%

TABLE 5.4

Continued

Sources of Systematic Uncertainty	**Uncertainty**	
Production Cross-Sections	Scale	PDF
Gluon-Gluon Fusion	+7.6% -8.2%	+7.6% -7.0%
Vector Boson Fusion	+0.3% -0.8%	+2.6% -2.8%
Associated Production with W/Z	+2.1% -1.8%	4.2%
Associated Production with $t\bar{t}$	+4.1% -9.4%	8.0%
Scale and PDF Uncertainties (Effect of up to 12.5% event class migration.)	(η, p_T)-differential	

5.2 Cut-Based Statistical Analysis

The background and signal modeling for the cut-based analysis is very similar to the main analysis. The background model for each category is subject to a truth model and bias test, and the signal models for each category are made from a sum of 2-3 Gaussians.

5.2.1 Cut-Based Background Fits

The background fits for the cut-based analysis have a lot in common with the main analysis. The only exception is the 7 TeV data is not subject to the F-test for determining the truth models, but it is still subject to the bias study. Additionally, the background fit is subject to a sensitivity loss test. The 8 TeV cut-based analysis performs the exact same procedure as the main analysis in terms of truth models and bias tests. The results of the truth model test and bias study can be seen in appendix B. The final fit functions can be seen in table 5.5.

5.2.2 Signal Modeling

The parametric signal model for the cut-based analysis is constructed identically to the main analysis as described in section 5.1.2. The acceptance×efficiency can be seen in figure 5.7. The signal models for the five 7 TeV categories and the nine 8 TeV categories can be seen in figures 5.8 and 5.9, respectively. The combined signal models for 7 and 8 TeV can be seen in figure 5.10.

5.2.3 Systematics

The cut-based cross-check systematic uncertainties are nearly identical to those of the main analysis. The primary difference in the systematics is the R_9 uncertainty associated with category migration. Since the categories in the cut-based analysis

TABLE 5.5

CUT-BASED ANALYSIS BACKGROUND MODELS

Energy	Category	Fit Function
8 TeV	Inclusive Category 0	5^{th} Bernstein
	Inclusive Category 1	5^{th} Bernstein
	Inclusive Category 2	5^{th} Bernstein
	Inclusive Category 3	5^{th} Bernstein
	Di-Jet Tight	4^{th} Bernstein
	Di-Jet Loose	4^{th} Bernstein
	Muon Tag	3^{rd} Bernstein
	Electron Tag	3^{rd} Bernstein
	$\not{E}_T$ Tag	3^{rd} Bernstein
7 TeV	Inclusive Category 0	5^{th} Bernstein
	Inclusive Category 1	5^{th} Bernstein
	Inclusive Category 2	5^{th} Bernstein
	Inclusive Category 3	5^{th} Bernstein
	Di-Jet Category	2^{nd} Bernstein

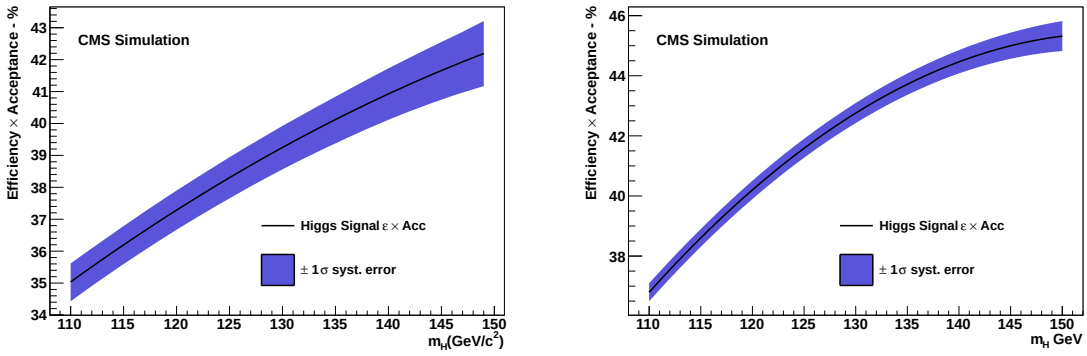

Figure 5.7. The total acceptance×efficiency for the cut-based analysis for 7 (left) and 8 (right) TeV.

directly depend on R_9, the uncertainty in the R_9 measurement causes a category migration of 4% in the barrel and 6.5% in the endcap. However, the categorization is not dependent on the kinematics of the Higgs, unlike the main analysis, so there is not an event migration associated with the QCD scale and proton PDF uncertainties. All of the systematic uncertainties associated with the 7 and 8 TeV cut-based analysis can be seen in tables 5.6 and 5.7.

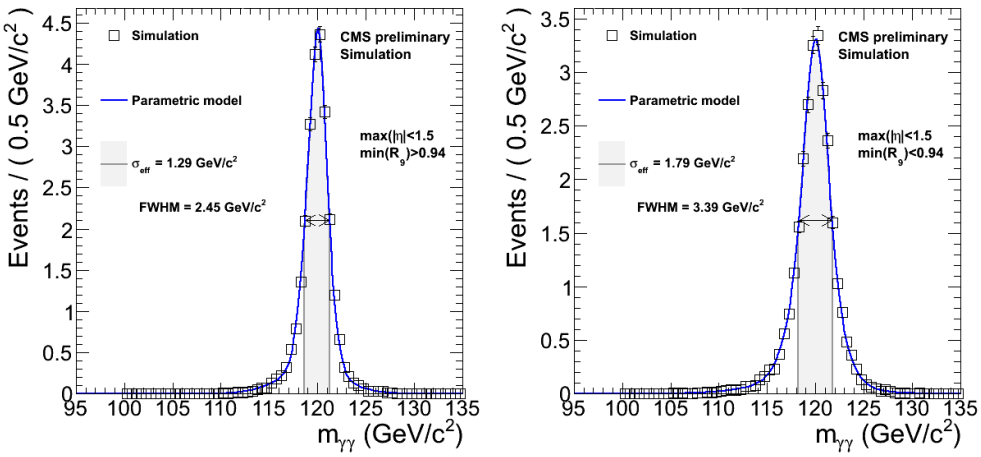

(a) Both EB, High R_9

(b) Both EB, Low R_9

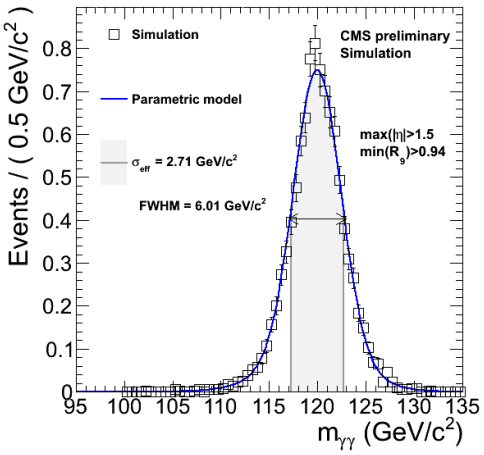

(c) One EE, High R_9

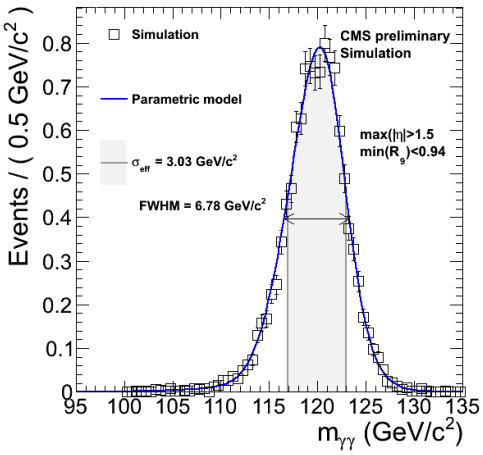

(d) One EE, Low R_9

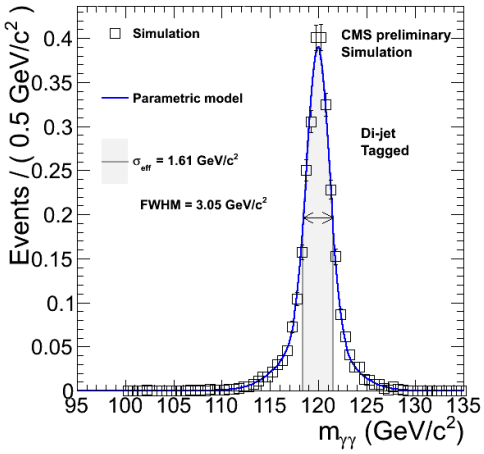

(e) Di-Jet Category

Figure 5.8. Cut-Based parametric signal models for the five 7 TeV categories created from a $H \to \gamma\gamma$ Monte Carlo simulation at 120GeV.

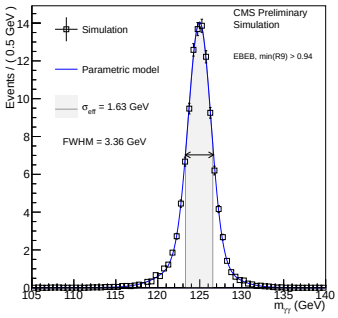

(a) Both EB, High R_9

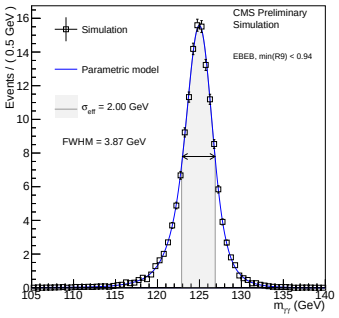

(b) Both EB, Low R_9

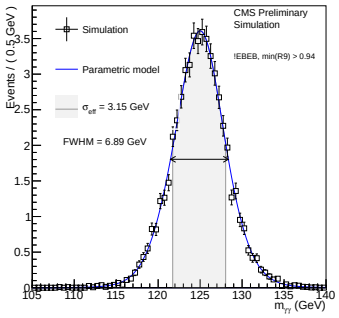

(c) One EE, High R_9

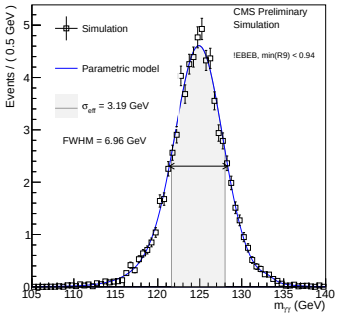

(d) One EE, Low R_9

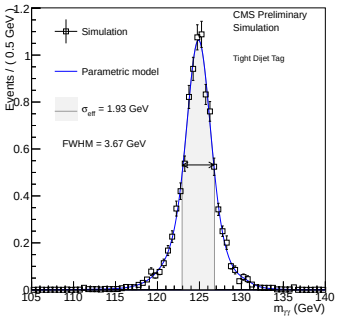

(e) Di-Jet Tight

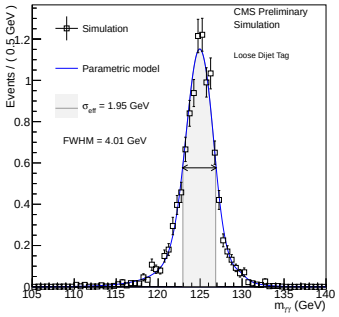

(f) Di-Jet Loose

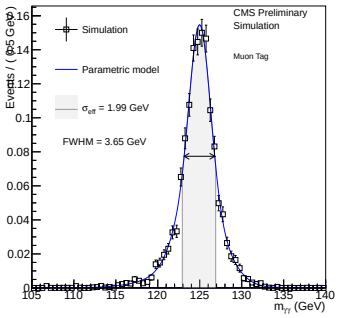

(g) Muon Category

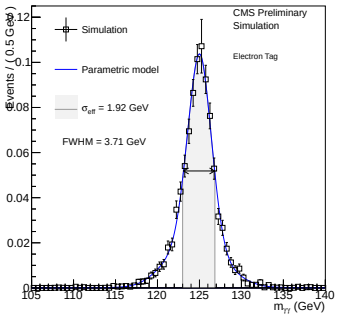

(h) Electron Category

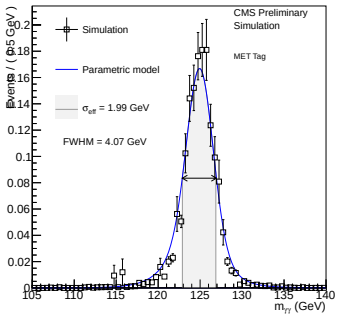

(i) $\not\!\!E_T$ Category

Figure 5.9. Cut-based parametric signal models for the nine 8 TeV categories created from a $H \to \gamma\gamma$ Monte Carlo simulation at 125GeV.

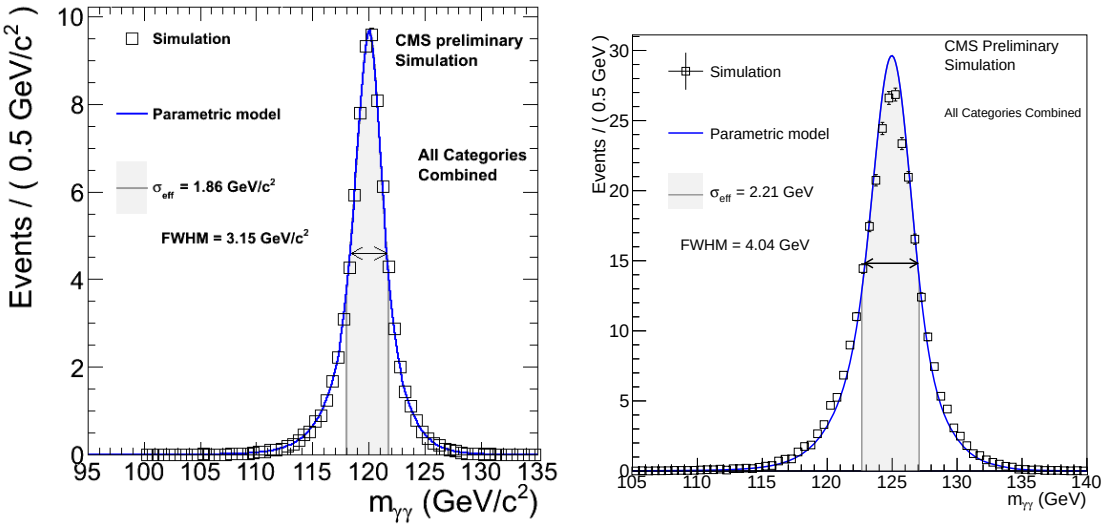

(a) Combined 7 TeV

(b) Combined 8 TeV

Figure 5.10. Combination of all the cut-based parametric signal models for 7 (left) and 8 (right) TeV.

TABLE 5.6

7 TEV SYSTEMATICS FOR THE CUT-BASED ANALYSIS

Sources of Systematic Uncertainty		**Uncertainty**	
Photon Identification Efficiency:	Barrel	1.0%	
	Endcap	2.6%	
R_9 >0.94 Efficiency	Barrel	4%	
(results in class migration)	Endcap	6.5%	
		$R_9 > 0.94$	$R_9 < 0.94$
Energy Resolution ($\Delta\sigma/E_{MC}$):	Barrel Low η, High η	0.22%, 0.61%	0.24%, 0.59%
	Endcap Low η, High η	0.91%, 0.34%	0.30%, 0.53%
Energy Scale ($(E_{data} - E_{MC})/E_{MC}$)	Barrel Low η, High η	0.19%, 0.71%	0.13%, 0.51%
	Endcap Low η, High η	0.88%, 0.19%	0.18%, 0.28%
Integrated Luminosity		4.5%	

TABLE 5.6

Continued

Sources of Systematic Uncertainty	**Uncertainty**
Trigger Efficiency: One or more photons $R_9 < 0.94$ in endcap	0.4%
Other Events	0.1%
Vertex Finding Efficiency	0.4%
Gluon fusion process cross-section (scale)	+12.5%, -8.2%
Gluon fusion process cross-section (PDF)	+7.9%, -7.7%
Vector boson fusion process cross-section (scale)	+0.5%, -0.3%
Vector boson fusion process cross-section (PDF)	+2.7%, -2.1%
Associated production with W/Z cross-section (scale)	+1.8%, -1.8%
Associated production with W/Z cross-section (PDF)	+4.2%, -4.2%
Associated production with $t\bar{t}$ cross-section (scale)	+3.6%, -9.5%
Associated production with $t\bar{t}$ cross-section (PDF)	+8.5%, -8.5%

TABLE 5.7

8 TEV SYSTEMATICS FOR THE CUT-BASED ANALYSIS

Sources of Systematic Uncertainty		**Uncertainty**	
Per Photon		Barrel	Endcap
Energy Resolution ($\Delta\sigma/E_{MC}$)	$R_9 > 0.94$ (Low η, High η)	0.23%, 0.72%	0.93%, 0.36%
	$R_9 < 0.94$ (Low η, High η)	0.25%, 0.60%	0.33%, 0.54%
Energy Scale ($(E_{data} - E_{MC})/E_{MC}$)	$R_9 > 0.94$ (Low η, High η)	0.20%, 0.71%	0.88%, 0.12%
	$R_9 < 0.94$ (Low η, High η)	0.20%, 0.51%	0.18%, 0.12%
Photon Identification Efficiency		0.8%	2.2%
$R_9 > 0.94$ Efficiency (Results in class migration)		4.0%	6.5%

TABLE 5.7

Continued

Sources of Systematic Uncertainty	**Uncertainty**
Per Event	
Integrated Luminosity	4.4%
Vertex Finding Efficiency	0.2%
Trigger Efficiency	1.0%
Global Energy Scale	0.47%
Di-Jet Selection	
Di-Jet Tagging Efficiency — VBF Process	10%
Gluon-Gluon Fusion Process	30%
(Effect of up to 15% event migration among di-jet categories.)	

TABLE 5.7

Continued

Sources of Systematic Uncertainty		**Uncertainty**
Muon Selection		
Muon identification Efficiency		1.0%
Electron Selection		
Electron Identification Efficiency		1.0%
$\not\!\!E_T$ **Selection**		
$\not\!\!E_T$ Cut Efficiency	Gluon-Gluon Fusion	15%
	Vector Boson Fusion	15%
	Associated Production with W/Z	4%
	Associated Production with $t\bar{t}$	4%

TABLE 5.7

Continued

Sources of Systematic Uncertainty	**Uncertainty**	
Production Cross-Sections	Scale	PDF
Gluon-Gluon Fusion	+7.6% -8.2%	+7.6% -7.0%
Vector Boson Fusion	+0.3% -0.8%	+2.6% -2.8%
Associated Production with W/Z	+2.1% -1.8%	4.2%
Associated Production with $t\bar{t}$	+4.1% -9.4%	8.0%

5.3 Final Results

The data, background fits, and the background plus standard model Higgs for the 7 and 8 TeV data for the main analysis can be seen in figures 5.11 and 5.12, respectively. While the signal for the Higgs boson may be hard to see in each of the individual categories, it will become apparent when a simultaneous likelihood fit is performed for each channel. The invariant mass plots for the cut-based analysis can be seen in figures 5.13 and 5.14. The combined 7 and 8 TeV invariant mass plots for the main analysis can be seen in figure 5.15. For this plot, each of the 14 categories are weighted to signal over background and the binning is expanded to 1.5 GeV bins. On the right side of the figure is the same plot minus the background fit for the data. The yellow and green bands represent the 1σ and 2σ uncertainties on the background fit. The blue line is the combined signal model scaled to the best-fit μ across all categories. The same plots for the cut-based analysis can be seen in figure 5.16 [81].

5.3.1 Limits, P-Values, and Best-Fit Cross-Section

The CL_s method is used to set limits and determine p-values. The CL_s^{95} limit is a way to determine the exclusion power of the analysis and the p-value determines the significance of any excess that is observed. The best-fit cross-section, coupling measurement, and mass measurement are extracted from a negative-log-likelihood minimization, which is equivalent to a likelihood maximization. All of the measurements start from the same assumption, in each category the number of expected events is

$$N_{\text{Exp}} = \mu S + B, \tag{5.1}$$

where N_{Exp} is the expected number of events, μ is the signal strength modifier, S is the number of expected signal events for the standard model Higgs boson (or any process), and B is the expected number of background events.[1] The likelihood can then be constructed as a product of poisson probabilities,

$$\mathcal{L}(\text{data}|\mu) = \text{Poisson}(\text{data}|\mu \cdot S + B). \tag{5.2}$$

In the case of a binned signal and background model equation 5.2 becomes,

$$\prod_i \frac{(\mu s_i + b_i)^{n_i}}{n_i!} e^{-(\mu s_i + b_i)}, \tag{5.3}$$

where n_i is the observed number of events in bin i. However, for the $H \to \gamma\gamma$ analysis, both the background and signal are constructed from a parametric model. Equation 5.2 becomes

$$\frac{1}{k} \prod_i (\mu S f_s(x_i) + B f_b(x_i)) \cdot e^{-(\mu S + B)}, \tag{5.4}$$

[1]The signal strength modifier is the ratio of the measured cross-section to the standard model cross-section ($\sigma/\sigma_{\text{SM}}$).

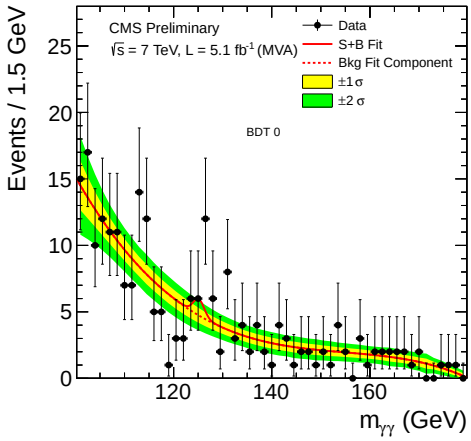

(a) BDT> 0.89

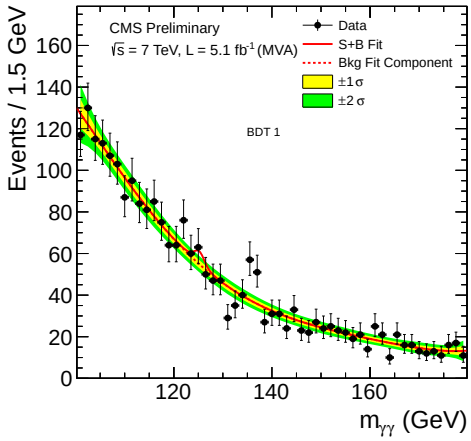

(b) 0.72 <BDT< 0.89

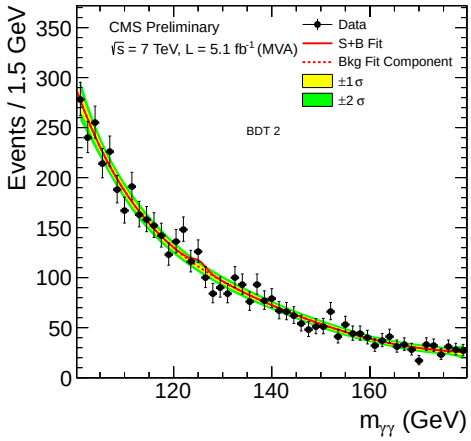

(c) 0.55 <BDT< 0.72

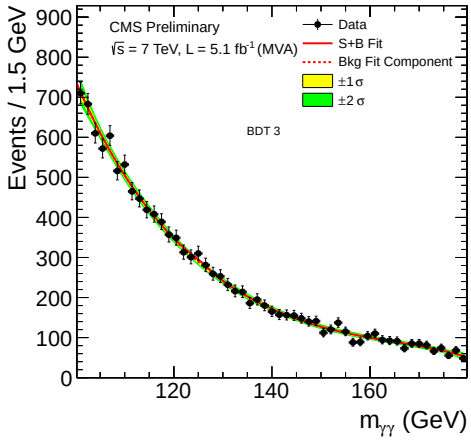

(d) −0.05 <BDT< 0.55

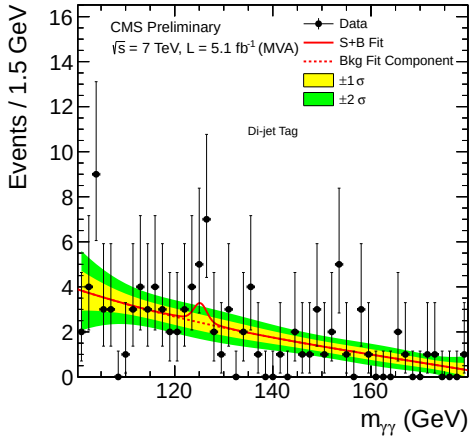

(e) BDT> 0.05 Di-Jet Category

Figure 5.11. The invariant mass distribution for all the 7 TeV categories for the main analysis with the background fit plus standard model Higgs at 125 GeV in red.

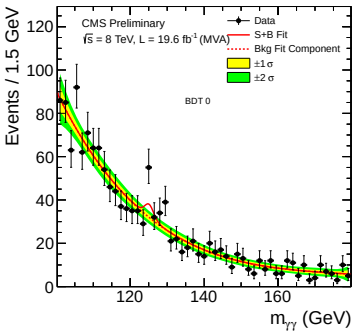

(a) BDT> 0.91

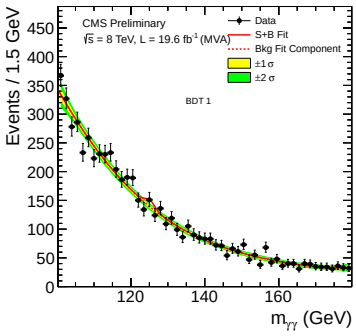

(b) 0.79 <BDT< 0.91

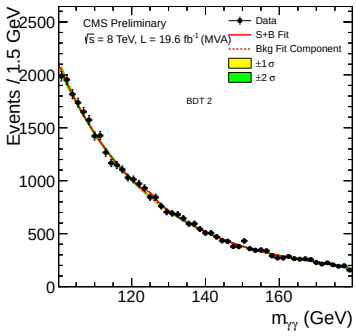

(c) 0.50 <BDT< 0.79

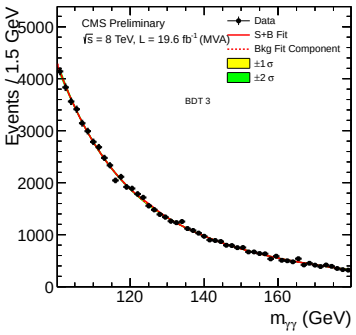

(d) −0.05 <BDT< 0.49

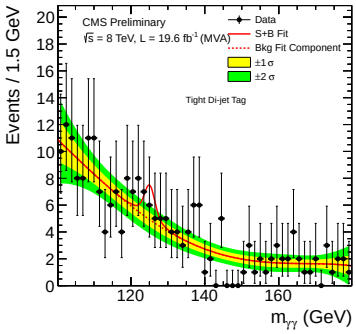

(e) BDT> −0.05 BDT_{jj} > 0.985

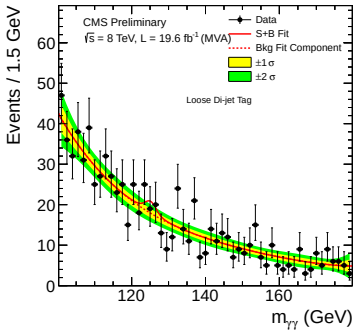

(f) BDT> −0.05 BDT_{jj} > 0.93

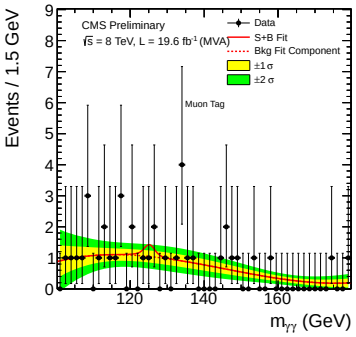

(g) BDT> −0.05 Muon tag

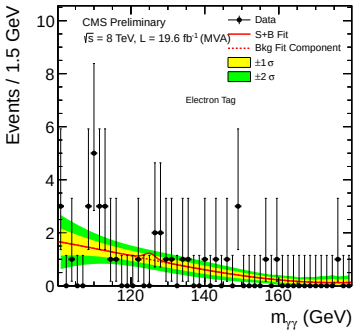

(h) BDT> −0.05 Electron tag

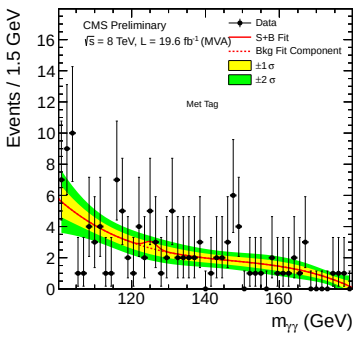

(i) BDT> −0.05 $\not\!\!E_T$ tag

Figure 5.12. The invariant mass distribution for all the 8 TeV categories for the main analysis with the background plus standard model Higgs at 125 GeV in red.

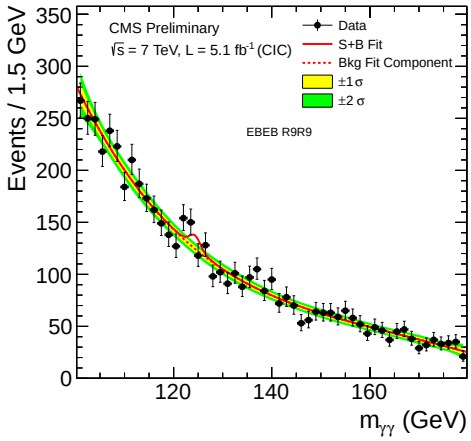

(a) Both EB, High R_9

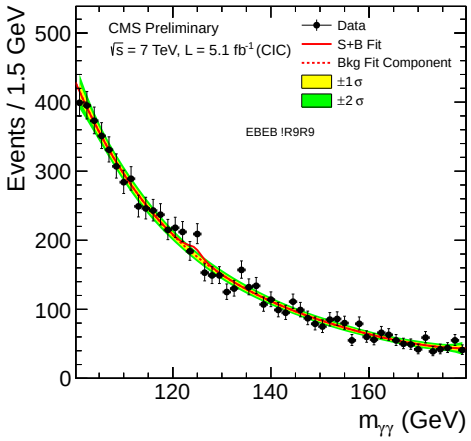

(b) Both EB, Low R_9

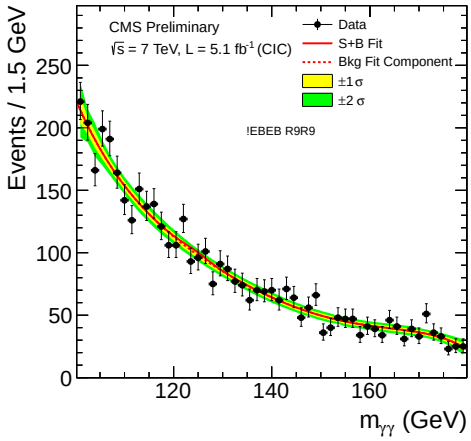

(c) One EE, High R_9

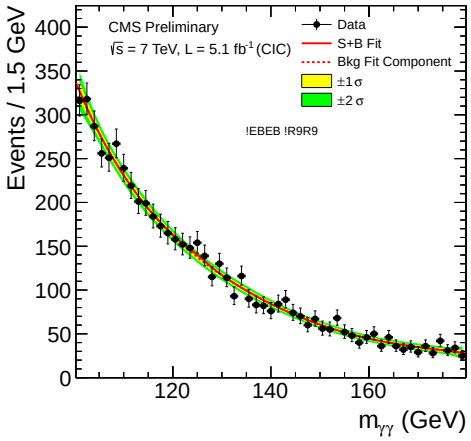

(d) One EE, Low R_9

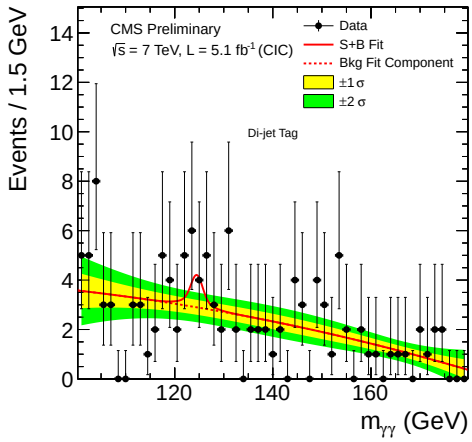

(e) Di-Jet Category

Figure 5.13. The invariant mass distribution for all the 7 TeV categories for the cut-based analysis with the background fit plus a standard model Higgs at 125 GeV.

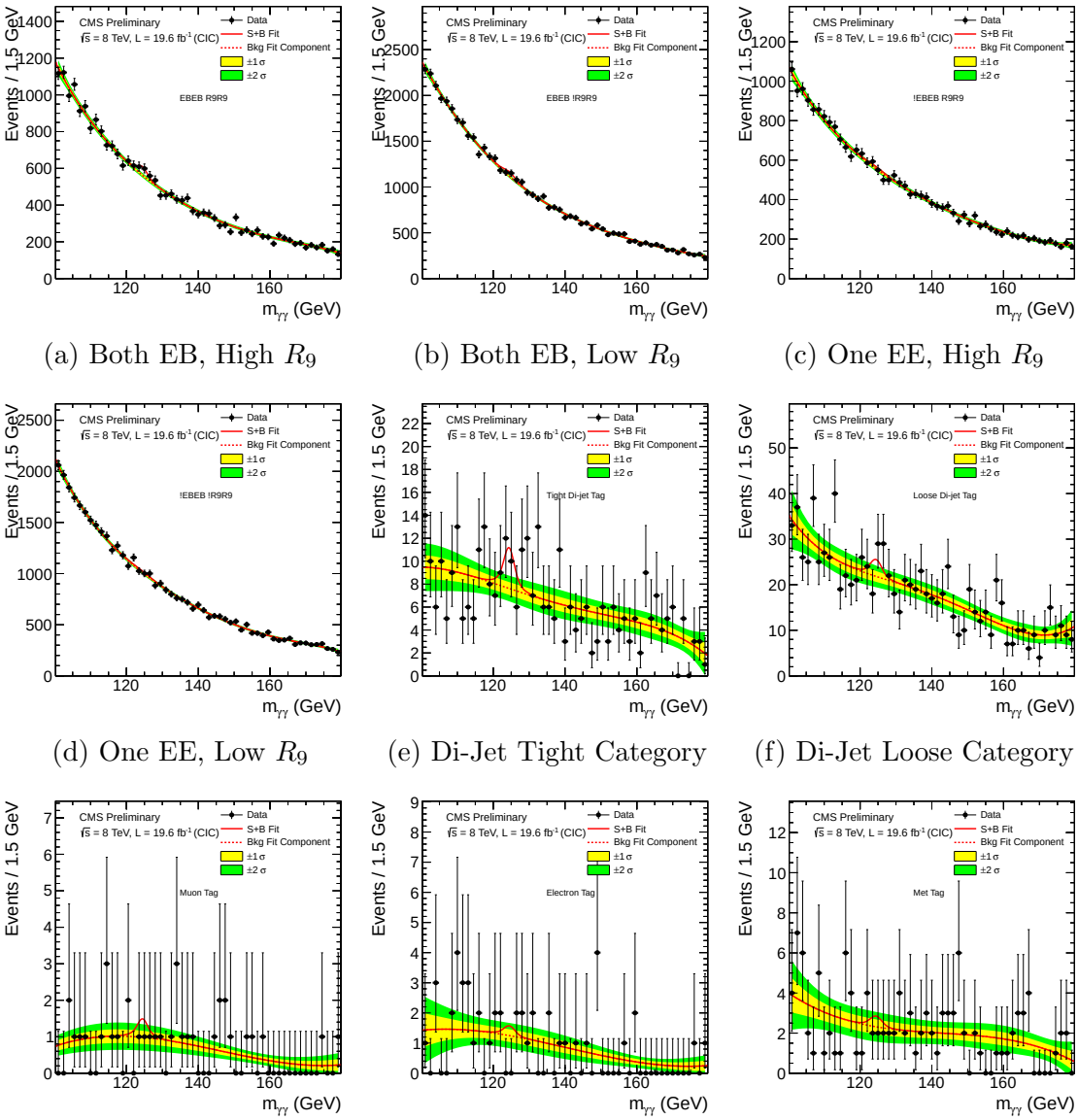

(a) Both EB, High R_9 (b) Both EB, Low R_9 (c) One EE, High R_9

(d) One EE, Low R_9 (e) Di-Jet Tight Category (f) Di-Jet Loose Category

(g) Muon Category (h) Electron Category (i) $\not\!\!E_T$ Category

Figure 5.14. The invariant mass distribution for all the 8 TeV categories for the cut-based analysis with the background plus standard model Higgs at 125 GeV in red.

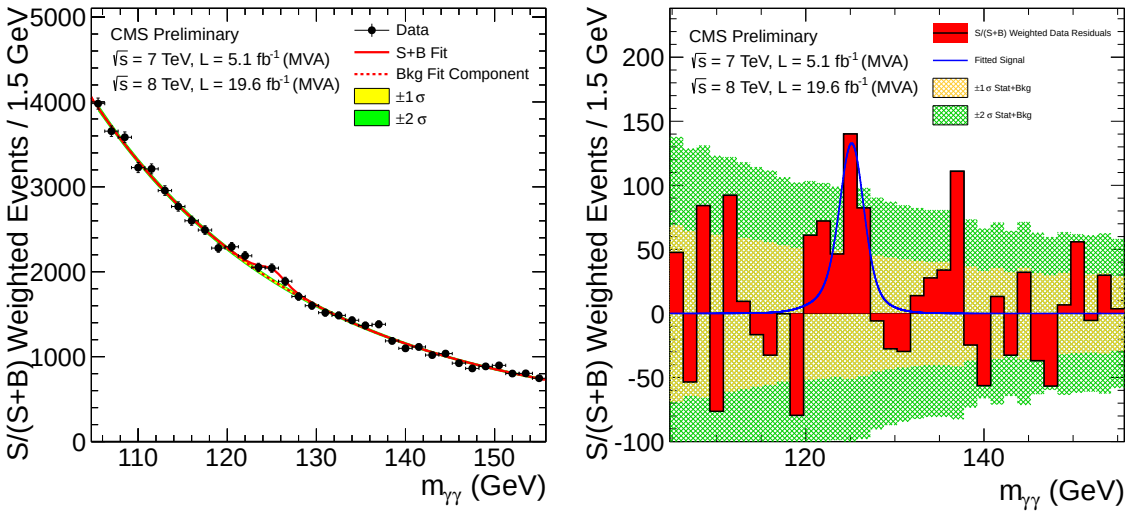

Figure 5.15. The combined 7 and 8 TeV invariant mass plot for the main analysis with each of the 14 categories weighted by S/B (left). The same plot with the dotted-red background fit subtracted from data (right). The yellow and green bands represent the 1σ and 2σ uncertainties on the background fit. The blue line is the combined signal model scaled to the best-fit μ.

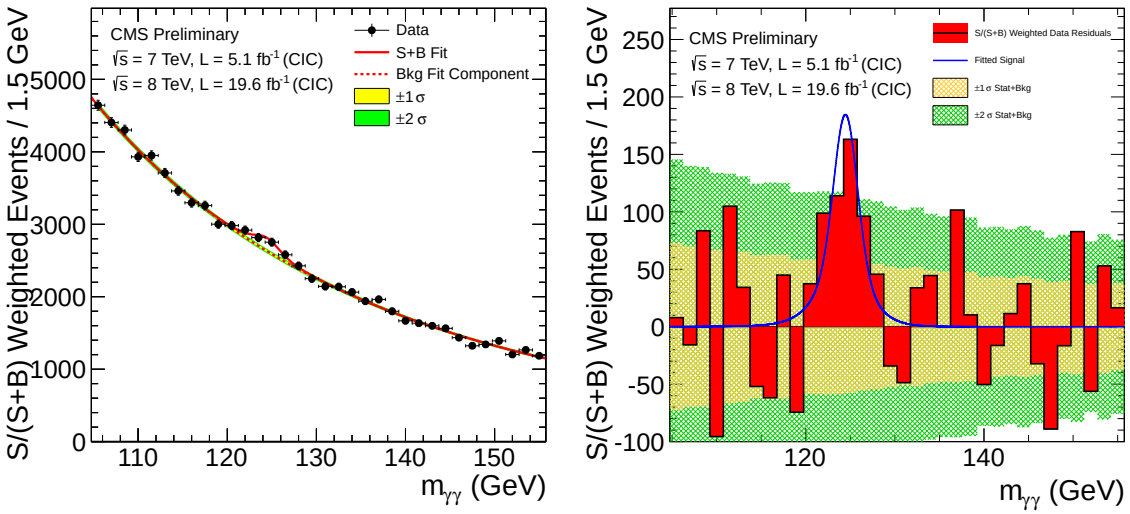

Figure 5.16. The combined 7 and 8 TeV invariant mass plot for the cut-based analysis with each of the 14 categories weighted by S/B (left). The same plot with the dotted-red background fit subtracted from data (right). The yellow and green bands represent the 1σ and 2σ uncertainties on the background fit. The blue line is the combined signal model scaled to the best-fit μ.

where k is the number of events in data, S and B are the total number of signal and background events, and $f_s(x)$ and $f_b(x)$ are the probability density functions (PDFs) of the signal and background, and $x_i = x_1, x_2, x_3, \ldots$ are the fit parameters. The $H \to \gamma\gamma$ analysis has numerous systematic uncertainties that need to be taken into account when producing the final results. The systematic uncertainties can be parameterized as a PDF: $\rho(\theta|\overline{\theta})$, where θ are the individual nuisance parameters (or systematic uncertainties) and $\overline{\theta}$ are their initial values. Using Bayes' theorem, $\rho(\theta|\overline{\theta})$ can be interpreted as

$$\rho(\theta|\overline{\theta}) \sim p(\overline{\theta}|\theta) \cdot \pi_\theta(\theta), \tag{5.5}$$

where π_θ are the hyperpriors for the measurement. So, when μ is measured the nuisance parameters float to maximize the likelihood, which serves as a measurement of the best-fit value for each individual systematic. For normal, log-normal, and gamma distributions, $\pi_\theta(\theta)$ does not vary significantly as a function of θ, and in the $H \to \gamma\gamma$ analysis most of the systematics are log-normal. Both S and B are dependent on θ, so equation 5.1 becomes

$$N_{\text{Exp}} = \mu S(\theta) + B(\theta) \tag{5.6}$$

and equation 5.2 becomes

$$\mathcal{L}(\text{data}|\mu, \theta) = \frac{1}{k} \prod_i (\mu S f_s(x_i) + B f_b(x_i)) \cdot e^{-(\mu S + B)} \cdot p(\overline{\theta}|\theta). \tag{5.7}$$

In order to compare the data with the background-only and signal-plus-background hypothesis a test statistic $\overline{q}_u$ is constructed:

$$\hat{q}_u = -2 \ln \frac{\mathcal{L}(\text{data}|\mu, \hat{\theta}_\mu)}{\mathcal{L}(\text{data}|\hat{\mu}, \hat{\theta})}, \quad \text{where } 0 \leq \hat{\mu} \leq \mu, \tag{5.8}$$

where $\mathcal{L}(\text{data}|\mu,\hat{\theta}_\mu)$ is the maximum likelihood at a fixed μ, where $\hat{\theta}_\mu$ is free to float, and $\mathcal{L}(\text{data}|\hat{\mu},\hat{\theta})$ is the global maximum likelihood, where both $\hat{\mu}$ and $\hat{\theta}$ are free to float. The constraint $0 \leq \hat{\mu}$, ensures that the signal is positive, and the second constraint $\hat{\mu} \leq \mu$, ensures that fluctuations where $\hat{\mu} > \mu$ are not evidence against the signal hypothesis [94, 95].

The test statistics is then evaluated on data for many different values of μ. This generates the value $\overline{q}_\mu^{\text{obs}}$, which is the test statistic of the observed data at any given μ. Once the test statistic is evaluated on data, the nuisance parameters for background-only, $\hat{\theta}_0^{\text{obs}}$, and signal-plus-background, $\hat{\theta}_\mu^{\text{obs}}$, hypothesis are set to the values from data. Then the test statistic distribution PDFs for the background-only, $f(\overline{q}_\mu|0,\hat{\theta}_0^{\text{obs}})$, and signal-plus-background, $f(\overline{q}_\mu|\mu,\hat{\theta}_\mu^{bos})$, hypothesis are generated from Monte Carlo simulated toys. From the distribution of test statistics, two p-values are defined for the background-only (p_b) and signal-plus-background (p_μ) hypothesis:

$$1 - p_b = P(\overline{q}_\mu \geq \overline{q}_\mu^{\text{obs}}|\text{background-only}) = \int_{\overline{q}_0^{\text{obs}}}^{\infty} f(\overline{q}_\mu|0,\hat{\theta}_0^{\text{obs}})d\overline{q}_\mu \quad \text{and} \tag{5.9}$$
$$p_\mu = P(\overline{q}_\mu \geq \overline{q}_\mu^{\text{obs}}|\text{signal+background}) = \int_{\overline{q}_\mu^{\text{obs}}}^{\infty} f(\overline{q}_\mu|\mu,\hat{\theta}_\mu^{\text{obs}})d\overline{q}_\mu.$$

These two p-values are then used to generate the CL_s value,

$$\text{CL}_s(\mu) = \frac{p_\mu}{1 - p_b} \tag{5.10}$$

The value of μ where $\text{CL}_s = 0.05$ is the lower bound of the CL_s^{95} exclusion. All μ's with a CL_s value below 0.05 are CL_s^{95} excluded. In order to evaluate the significance of an excess, a new test statistic is defined:

$$q_0 = -2\ln\frac{\mathcal{L}(\text{data}|0,\hat{\theta})}{\mathcal{L}(\text{data}|\hat{\mu},\hat{\theta})}, \quad \text{where } \hat{\mu} \geq 0. \tag{5.11}$$

Following the limit approach, the distribution of test statistics for the background-

only hypothesis, $f(q_0|0,\hat{\theta}_0^{\rm obs})$, is generated from Monte Carlo simulated toys, where the nuisance parameters are fixed from data. The p-value of the observed data can be extracted from the distribution of test statistics [94]:

$$p_0 = P(q_0 \geq q_0^{\rm obs}) = \int_{q_0^{\rm obs}}^{\infty} f(q_0|0,\hat{\theta}_0^{\rm obs}) dq_0. \tag{5.12}$$

The significance (Z) is then evaluated by integrating one side of the Gaussian tail:

$$p = \int_Z^{\infty} \frac{1}{\sqrt{2\pi}} e^{-\frac{x^2}{2}} dx. \tag{5.13}$$

For the full frequentist method, the distribution of test statistics is generated with Monte Carlo simulated toys; however, this is very CPU intensive especially for large p-values. For the results presented for $H \to \gamma\gamma$, the distribution of the test statistic is constructed analytically under the profile likelihood asymptotic approximation. This is done by removing the positive signal qualification for equation 5.8, which changes it into

$$\hat{q}_u = -2 \ln \frac{\mathcal{L}(\text{data}|\mu,\hat{\theta}_\mu)}{\mathcal{L}(\text{data}|\hat{\mu},\hat{\theta})}, \quad \text{where } \hat{\mu} \leq \mu. \tag{5.14}$$

Following from Wilks theorem [96], q_μ has half a χ^2 distribution per one degree of freedom under the signal-plus-background hypothesis. The value of μ where

$$\frac{1}{2} q_\mu = 1.92 \tag{5.15}$$

is interesting because it corresponds to a CL_{s+b} value of 0.025. This would be equivalent to the CL_s^{95} value if the data matches the background-only hypothesis ($\text{CL}_b = 0.5$). The assumption that $\hat{\mu} > 0$ causes the distribution of the test statistic for the signal-plus-background hypothesis to no longer follow χ^2. Instead it follows

this analytical formula:

$$f(\hat{q}|\mu) = \frac{1}{2}\delta\hat{q}_\mu + \begin{cases} \frac{1}{\sqrt{8\pi\hat{q}_\mu}} e^{-\hat{q}_\mu/2} & 0 < \hat{q}_\mu \leq \mu^2/\sigma^2 \\ \frac{1}{\sqrt{2\pi}(2\mu/\sigma)} e^{\frac{\hat{q}_\mu + \mu^2/\sigma^2}{2(2\mu/\sigma)^2}} & \hat{q}_\mu > \mu^2/\sigma^2 \end{cases}, \tag{5.16}$$

where $\sigma^2 = \mu^2/q_{\mu,A}$. $q_{\mu,A}$ is the Asimov dataset with all nuisance parameters set to their default values. So instead of generating hundreds of thousands of toys for the final limits and p-values, the test statistics for the background-only and signal-plus-background hypothesis is estimated from equation 5.16 [94].

5.3.2 Main Analysis Results

The final limits for the main $H \to \gamma\gamma$ analysis can be seen in figure 5.17 for 7 and 8 TeV. The final main analysis limits for the combined 7 and 8 TeV dataset can be seen in figure 5.18. The exclusion limit for both the 7 TeV, 8 TeV, and the combined dataset limit cannot exclude the standard model within the vicinity of 125 GeV. This is due to an excess of events above the background fit. The p-values for the excess at 7 and 8 TeV can be seen in figure 5.19. The combined 7 and 8 TeV p-value can be seen in figure 5.20. The minimum in figure 5.20 corresponds to a p-value of 5.8×10^{-4} or 3.2σ (4.1σ expected) at 125.0 GeV.

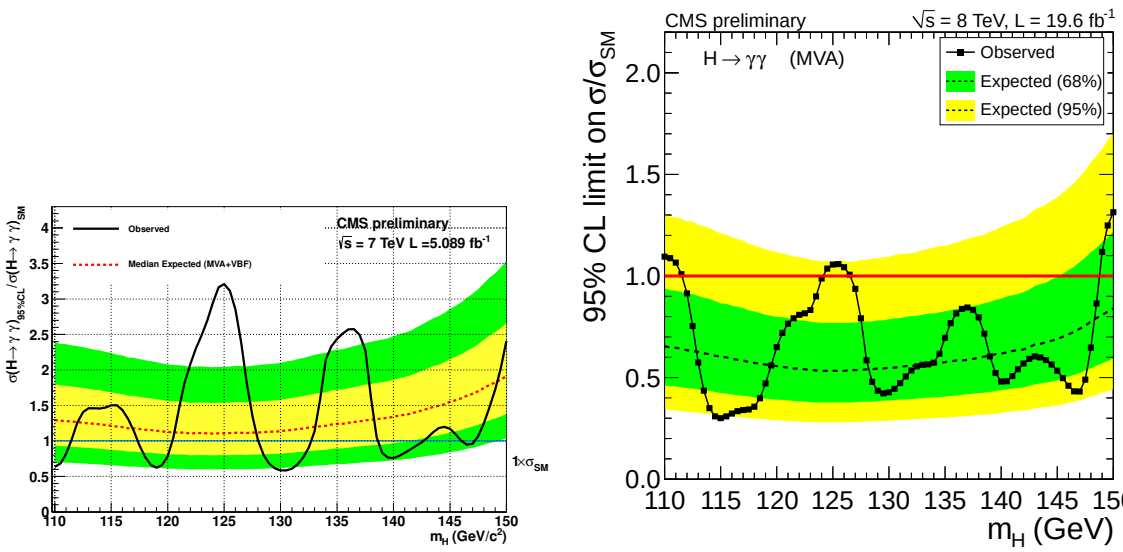

Figure 5.17. The limits for the standard model Higgs boson in the $H \to \gamma\gamma$ channel at 7 (left) and 8 (right) TeV. The black line is the observed data and the red dashed line is the expected exclusion with 1-σ and 2-σ uncertainty bands in green and yellow. An excess can be seen in both datasets near 125 GeV.

5.3.3 Cut-Based Cross-Check Results

The final limits for the cut-based $H \to \gamma\gamma$ analysis can be seen in figure 5.21 for 7 and 8 TeV in figure 5.22 for the combined 7 and 8 TeV limits. There is a general agreement between the two analysis that there is an excess near 125 GeV, but in the cut-based analysis the excess appears larger than the one in the main analysis. The p-values for the excess at 7 and 8 TeV can be seen in figure 5.23 and the 7 and 8 TeV combined p-values can be seen in figure 5.24. The minimum p-value in the cut-based analysis is 4.4×10^{-5} or 3.9σ (3.5σ) at 124.5 GeV.

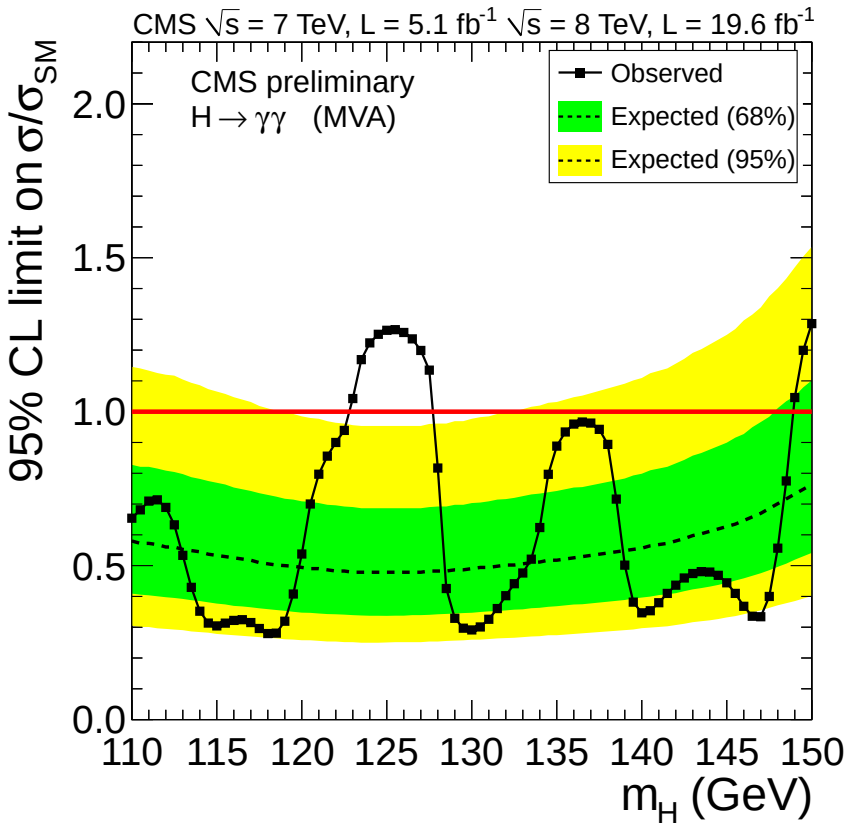

Figure 5.18. The combined limits 7 and 8 TeV limits for the $H \to \gamma\gamma$ search. A clear excess can be found near 125 GeV.

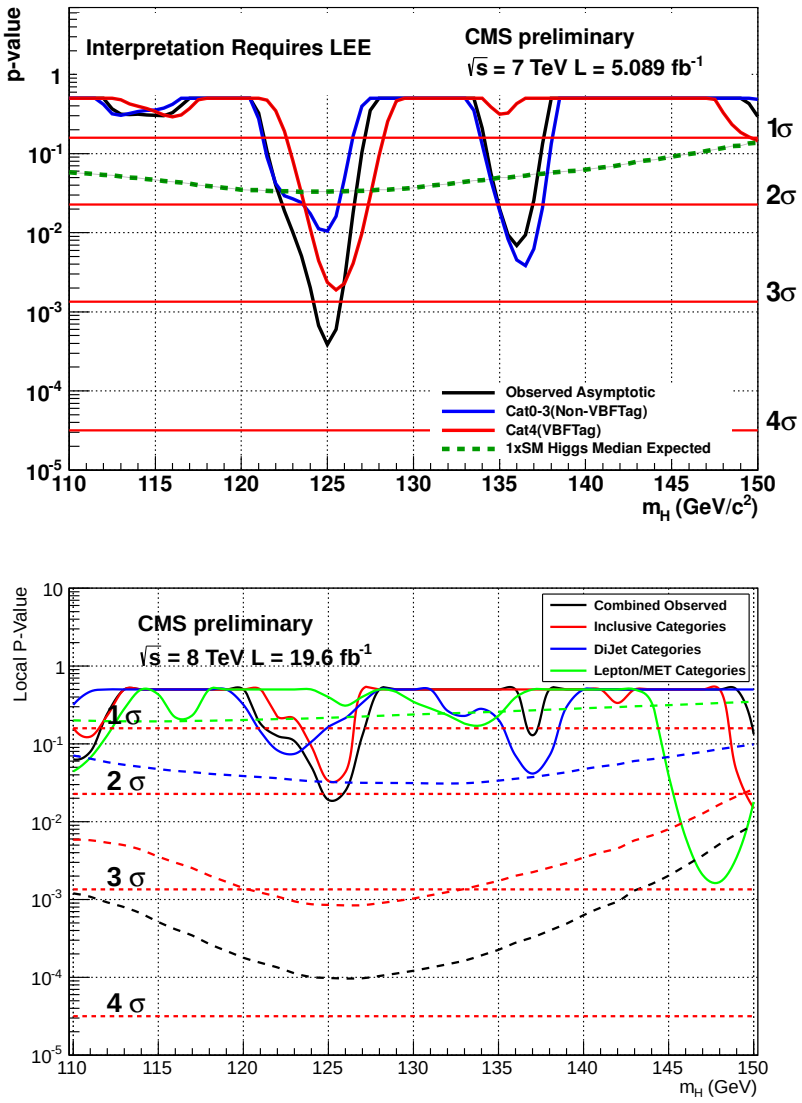

Figure 5.19. The p-values for the 7 (top) and 8 (bottom) TeV datasets. The p-values are split between inclusive and exclusive categories. The dashed line is the expected p-value from an Asimov toy with a standard model Higgs signal injected.

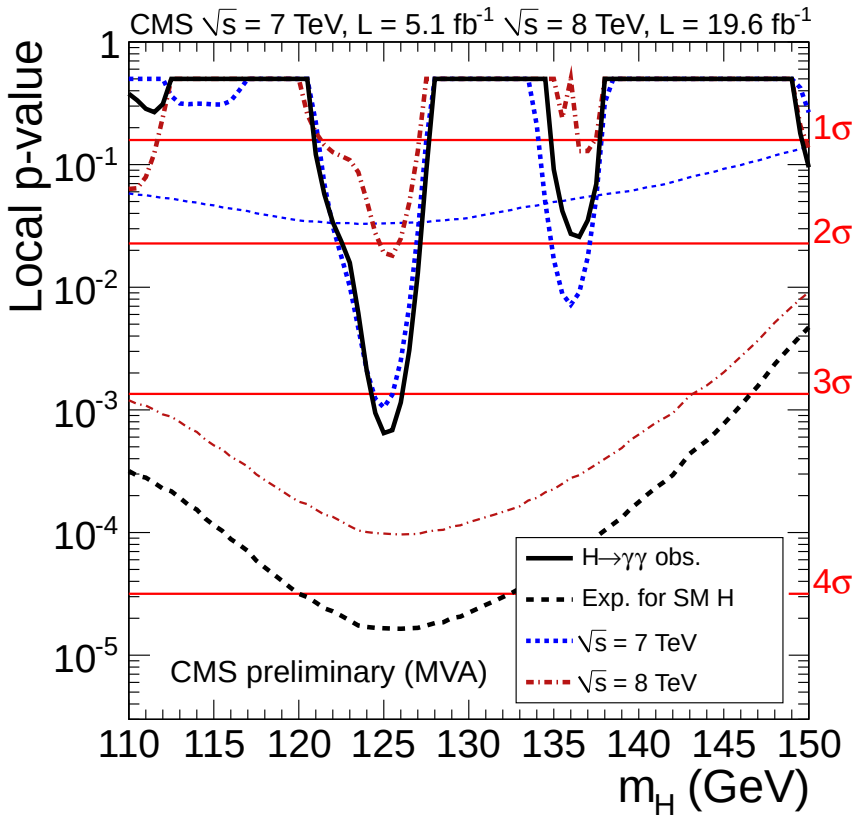

Figure 5.20. The p-value for the combined 7 and 8 TeV data. The maximum deviation from the background-only hypothises is 3.2σ at 125 GeV.

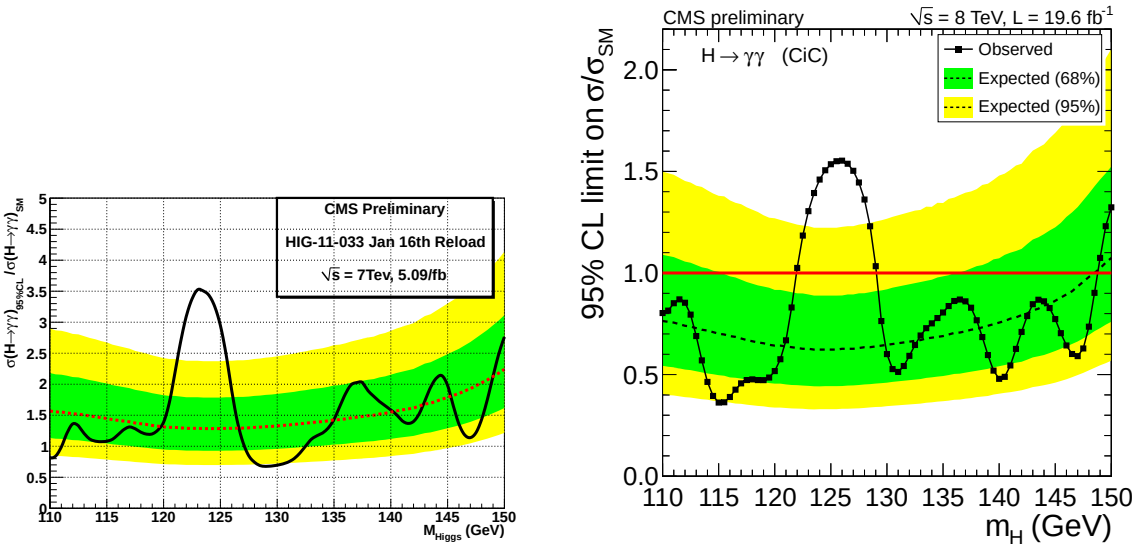

Figure 5.21. The cut-based limits for the $H \to \gamma\gamma$ analysis at 7 (left) and 8 (right) TeV.

5.3.4 Best-Fit Cross-Section

The best-fit cross-section is determined by maximizing the likelihood ratio for

$$q = -2 \ln \frac{\mathcal{L}(\text{data}|\mu_{\text{Nom}})}{\mathcal{L}(\text{data}|\mu_{\text{Alt}})}, \tag{5.17}$$

where μ_{Nom} is the case where all channels have the same signal strength μ and μ_{Alt} is where μ in each individual category is free to float. For the nominal model, the optimum μ_{Nom} is the combined best-fit cross-sections for all the categories. μ_{Nom}, as a function of mass, for the 7 and 8 TeV data can be seen in figure 5.25 for the main and cut-based analysis. Each analysis shows a rise in the best-fit cross-section near 125 GeV. For the alternative model, μ_{Alt} is the optimal cross-section for each of the individual channels. A plot of channel compatibility can be seen in figure 5.26 for the main and cut-based analysis. For the main analysis the best-fit cross-section ($\sigma/\sigma_{\text{SM}}$) is $0.78^{+0.28}_{-0.26}$ times the standard model at 125.0 GeV and for the cut-based cross-check $\sigma/\sigma_{\text{SM}}$ is $1.11^{+0.32}_{-0.30}$ at 124.5 GeV [81].

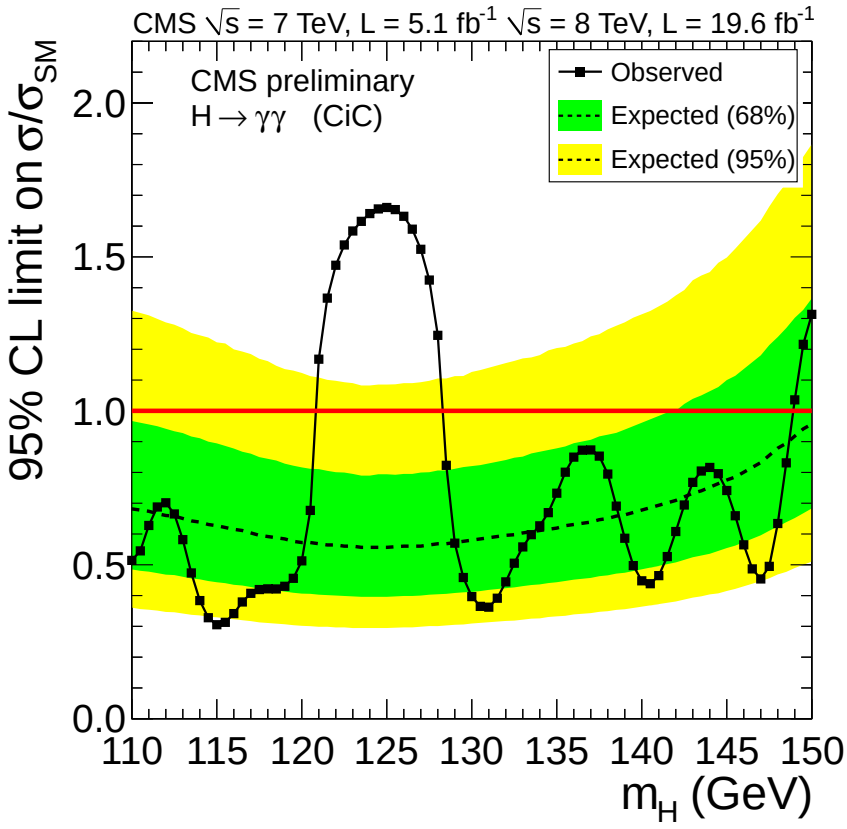

Figure 5.22. The combined cut-based limits for 7 and 8 TeV.

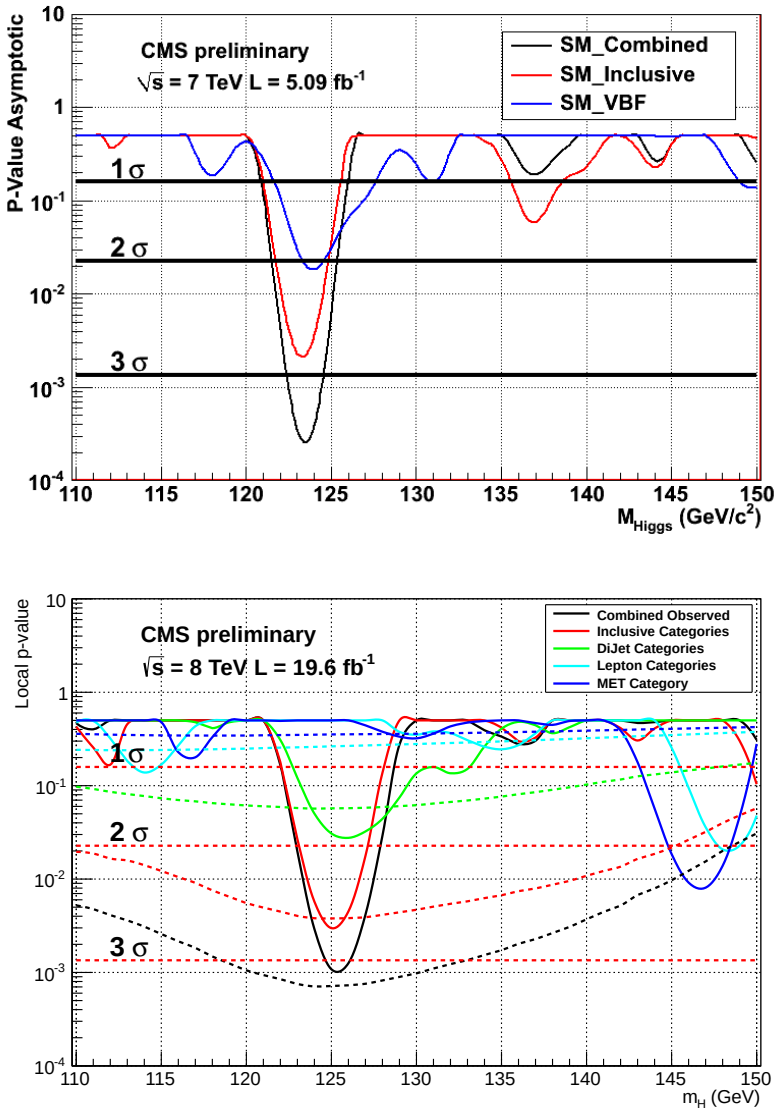

Figure 5.23. The cut-based p-values at 7 (left) and 8 (right) TeV.

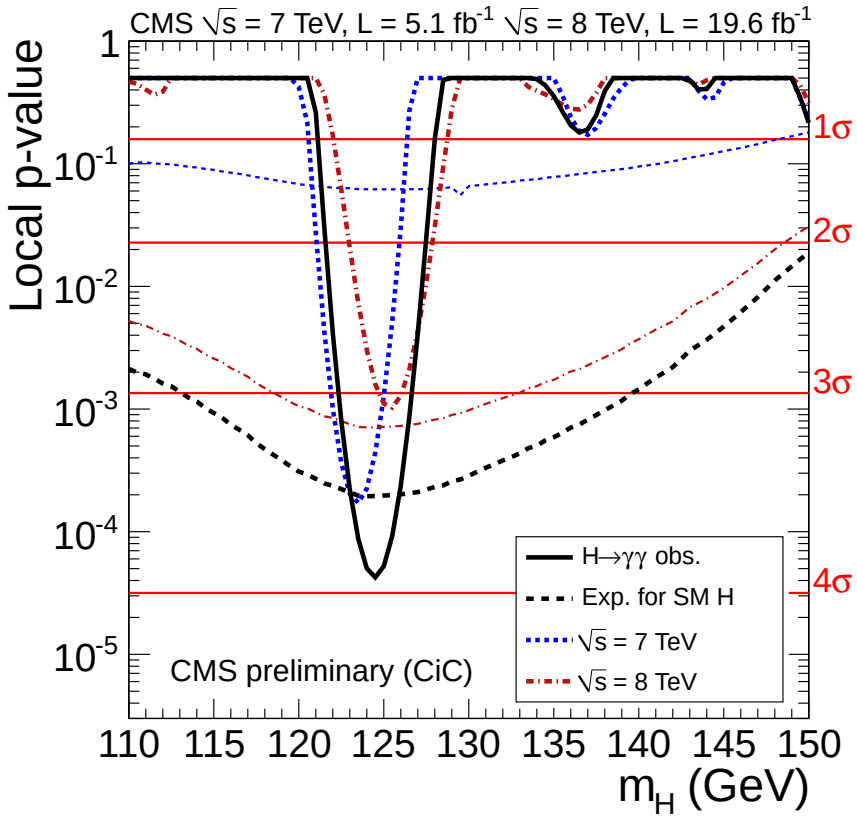

Figure 5.24. The 7 and 8 TeV combined p-values for the cut-based analysis. The minimum p-value is 4.4×10^{-5} or 3.9σ at 124.5 GeV.

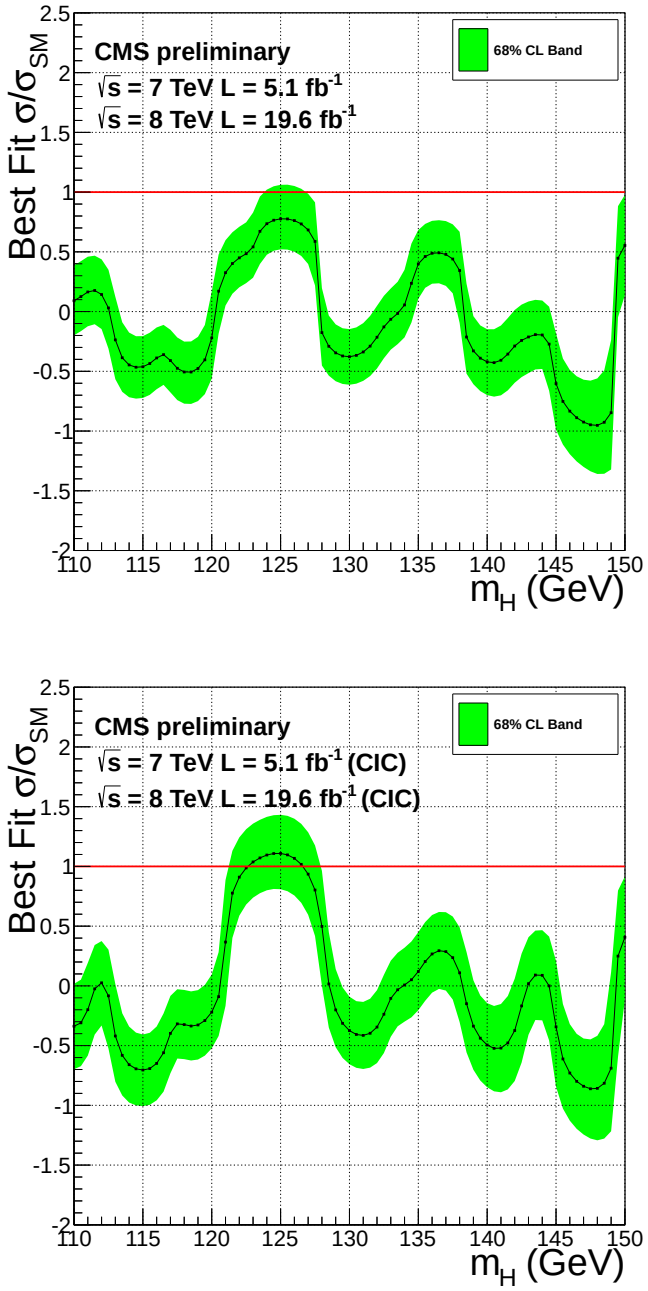

Figure 5.25. The best-fit cross-section as a function of mass for the main (top) and cut-based (bottom) $H \to \gamma\gamma$ analyses.

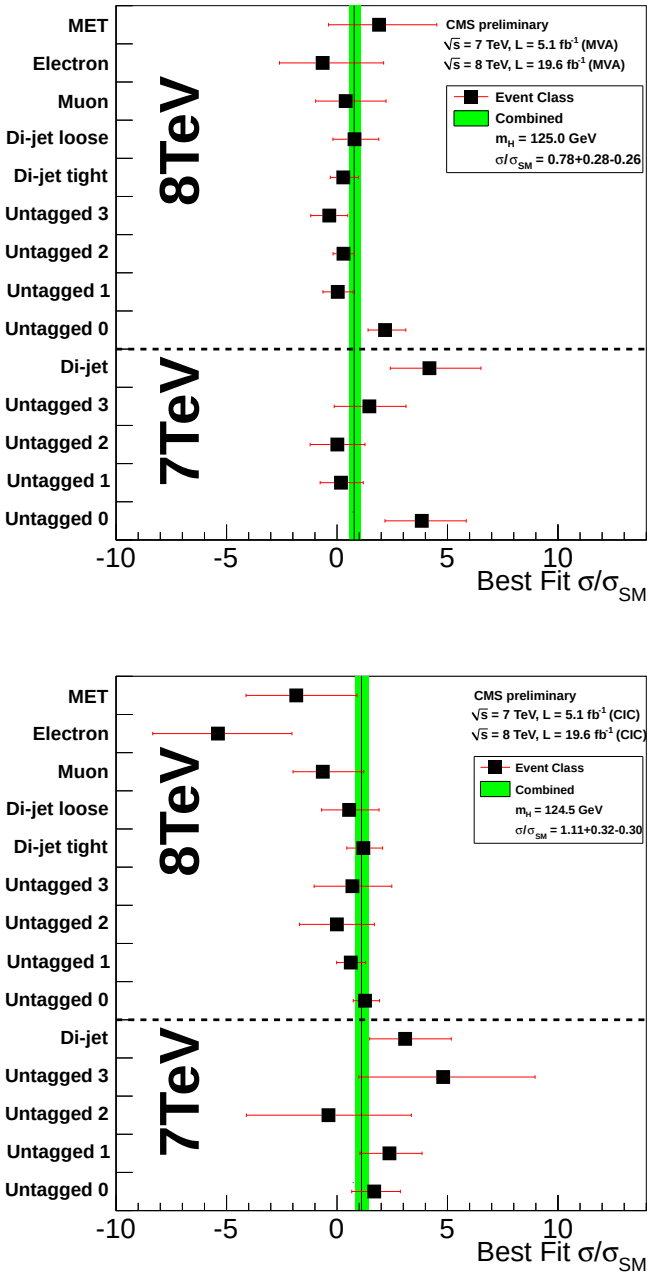

Figure 5.26. The channel compatibility test at 125.0 and 124.5 GeV for the main (top) and cut-based (bottom) analysis, respectively.

5.3.5 Coupling Measurements

The measurement of the Higgs boson's couplings to bosons and fermions is performed by scanning the likelihood in the $\mu_{\mathrm{ggH+ttH}}$ and $\mu_{\mathrm{qqH+VH}}$ plane, where $\mu_{\mathrm{ggH+ttH}}$ is the coupling of the Higgs boson to fermions and $\mu_{\mathrm{qqH+VH}}$ is the coupling of the Higgs boson in vector bosons. For the coupling measurement, the ratio between μ_{ggH} to μ_{ttH} is fixed to the standard model, and the same can be said for the ratio of μ_{qqH} of μ_{VH}. $\mu_{\mathrm{ggH+ttH}}$ and $\mu_{\mathrm{qqH+VH}}$ are allowed to float in order to minimize the negative-log-likelihood ratio. The results of the scan for the main analysis can be seen in figure 5.27 for the full 7 and 8 TeV dataset. The minimum in figure 5.27 corresponds to a $\mu_{\mathrm{ggH+ttH}} = 0.52$ and a $\mu_{\mathrm{qqH+VH}} = 1.48$, the result is within one σ of the standard model. The coupling measurement is also performed on the cut-based analysis and can be seen in figure 5.28. Its minimum is at $\mu_{\mathrm{ggH+ttH}} = 1.45$ and $\mu_{\mathrm{qqH+VH}} = 0.98$ [81].

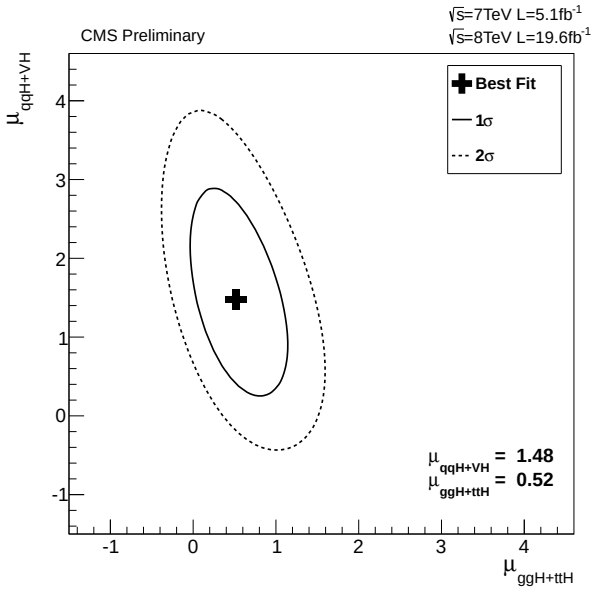

Figure 5.27. The 2D negative-log-likelihood scan of $\mu_{\mathrm{qqH+VH}}$ versus $\mu_{\mathrm{ggH+ttH}}$ for the main analysis with the combined 7 and 8 TeV dataset.

5.3.6 Mass Measurement

Since the background and signal model are completely parametric, it is possible to perform a likelihood scan while varying the signal mass. Because the energy scale is calculated from $Z/\gamma^* \to ee$ events, two additional systematics are added before measuring the mass. The first systematic uncertainty is due to the difference in simulation between electrons and photons, and the second is due to extrapolating the energy scale from m_Z to 125 GeV. The first systematic uncertainty is estimated by comparing:

- The default $Z/\gamma^* \to ee$ and $H \to \gamma\gamma$ Monte Carlo simulation.
- $Z/\gamma^* \to ee$ and $H \to \gamma\gamma$ Monte Carlo simulation samples with a different version of GEANT.

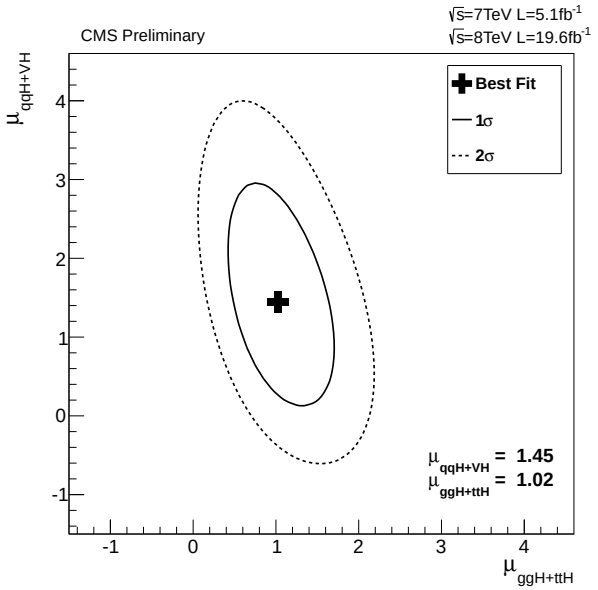

Figure 5.28. The 2D negative-log-likelihood scan of $\mu_{\mathrm{qqH+VH}}$ versus $\mu_{\mathrm{ggH+ttH}}$ for the cut-based analysis with the combined 7 and 8 TeV dataset.

- $Z/\gamma^* \rightarrow ee$ and $H \rightarrow \gamma\gamma$ Monte Carlo simulation samples with a different version of GEANT and 5% additional material in the beam pipe.

For electrons and photons with the same R_9, the energy response for electrons is 0.5% larger than photons for all three Monte Carlo simulation samples. Half of this value (0.25%) is then taken as the systematic uncertainty associated to differences in simulation between electrons and photons. The energy scale systematic uncertainty is evaluated using three different methods:

- Examining the Z mass as a function of the scalar sum of the electron p_T.
- Fitting the Z peak in different electron E_T bins.
- Looking at the E/p of electrons in p_T bins.

Each of the three methods show an energy scale uncertainty of 0.4%. The two uncertainties are then added together in quadrature, producing a total uncertainty of 0.47%. This systematic uncertainty is added for the mass measurement only and is fully correlated across all categories.

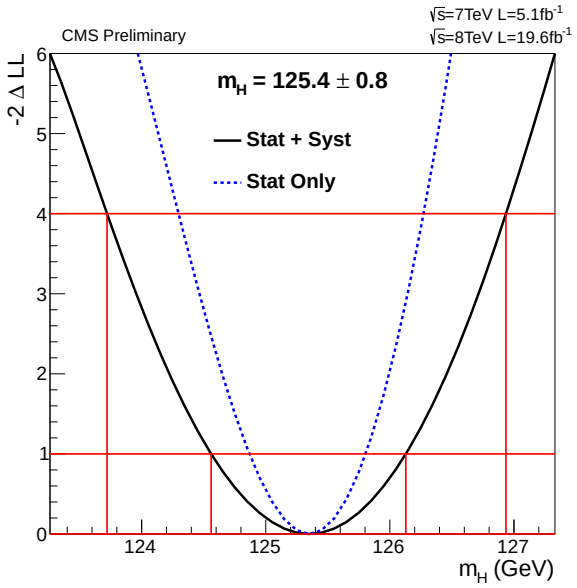

Figure 5.29. The 1D negative-log-likelihood scan of the mass for the main analysis. The minimum of the negative-log-likelihood scan is $125.4 \pm 0.5(stat.) \pm 0.6(syst.)$ GeV.

For the one dimensional likelihood mass scan, μ is fixed to its best-fit value, and the mass is varied to find the minimum negative-log-likelihood. The result of the one dimensional mass scan, for the main analysis, can be seen in figure 5.29. The best-fit mass of the new boson is $125.4 \pm 0.5(stat.) \pm 0.6(syst.)$ GeV. An additional two dimensional mass scan is also performed on the main analysis where both the mass and the μ were allowed to float. The results can be seen in figure 5.30 [81].

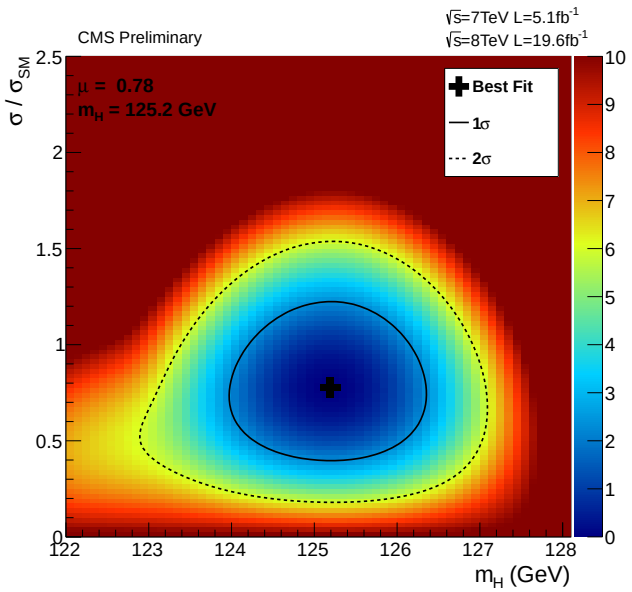

Figure 5.30. The 2D negative-log-likelihood scan of the μ versus mass for the main analysis.

CHAPTER 6

ADDITIONAL CHANNELS

The $H \to \gamma\gamma$ channel is not the only channel that measures an excess of events. In four additional channels, there have been measurements of fluctuations above the background-only hypothesis: $H \to ZZ$, $H \to W^+W^-$, $H \to \tau\overline{\tau}$, and $H \to b\overline{b}$. The excess is clearly visible in the $H \to ZZ \to 2l^+l^-$ channel, and the resonance can be seen in figure 6.1 near the same mass as the $\gamma\gamma$ channel [97]. The lower resolution channels, W^+W^- [98], $\tau\overline{\tau}$ [99], and $b\overline{b}$ [100], also see excesses in the same region as seen in figures 6.2, 6.3, and 6.4, respectively. The combined best-fit cross-section for the five channels, which observe an excess, is 0.80 ± 0.14 times the standard model as seen in figure 6.5 [101]. The results of the combined spin analysis for the ZZ and W^+W^- channels can be seen in figure 6.6, where the 2^+_{mgg} model is disfavored at $\mathrm{CL_s}$ =0.6%. The spin analyses in the ZZ channel disfavor all the non-0^+ spin hypotheses as seen in figure 6.7 and table 6.1. The fact that the excess is present in the W^+W^-, ZZ, and $\gamma\gamma$ channels and has a probable spin of 0^+ is evidence that the excess is a Higgs boson. The additional measurements of the excess in the fermion decay modes is a further indication that the excess is the standard model Higgs boson.

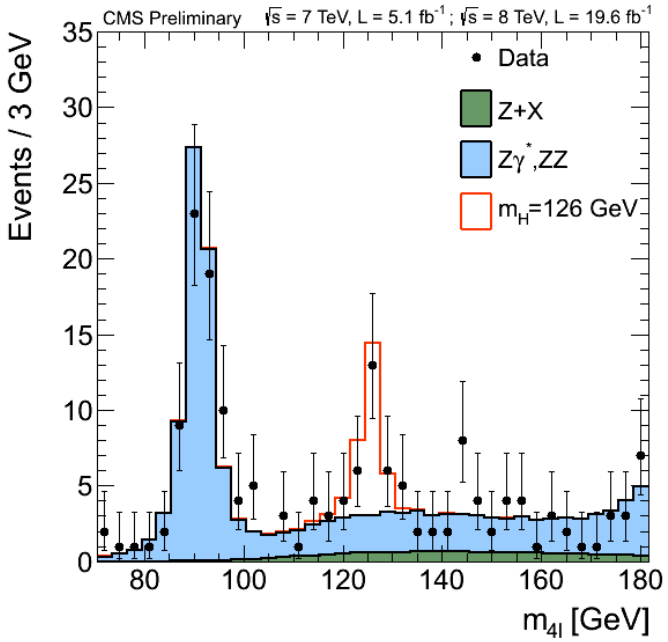

Figure 6.1. The four lepton invariant mass plot from the $H \to ZZ \to 2l^+l^-$ analysis. A large excess can be seen near 126 GeV.

TABLE 6.1

$H \to ZZ \to 2l^+l^-$ SPIN ANALYSIS

J^P	Production	Higgs Model	Expected ($\mu = 1$)	Obs. 0^+	Obs. J^P	CL_s
0^-	$gg \to X$	Pseudoscalar	2.6σ (2.8σ)	0.5σ	3.3σ	0.16%
0^+_h	$gg \to X$	Higher Dimensional Operators	1.7σ (1.8σ)	0.0σ	1.7σ	8.1%
2^+_{mgg}	$gg \to X$	Minimal Couplings	1.8σ (1.9σ)	0.8σ	2.7σ	1.5%
$2^+_{mq\bar{q}}$	$q\bar{q} \to X$	Minimal Couplings	1.7σ (1.9σ)	1.8σ	4.0σ	$< 0.1\%$
1^-	$q\bar{q} \to X$	Exotic Vector	2.8σ (3.1σ)	1.4σ	$> 4.0\sigma$	$< 0.1\%$
1^+	$q\bar{q} \to X$	Exotic Pseudovactor	2.3σ (2.6σ)	1.7σ	$> 4.0\sigma$	$< 0.1\%$

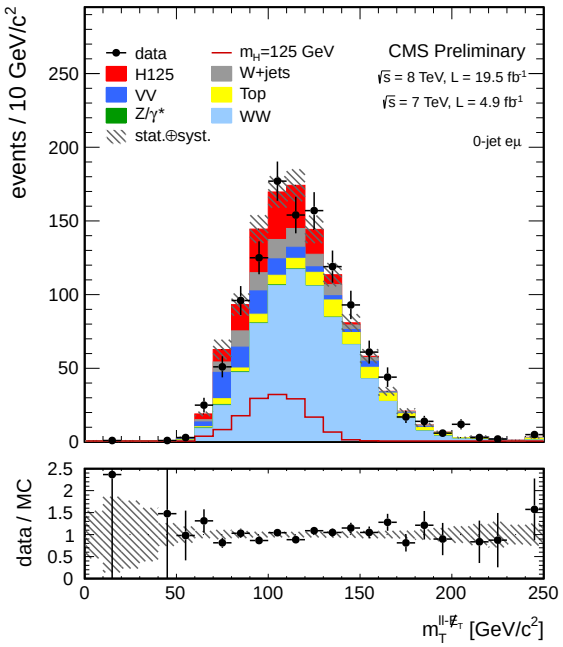

Figure 6.2. The transverse mass of the di-lepton and $\not\!\!E_T$ system from the $H \to W^+W^- \to l^+l^-\nu\overline{\nu}$ analysis. The excess of events is consistent with a standard model Higgs at 125 GeV.

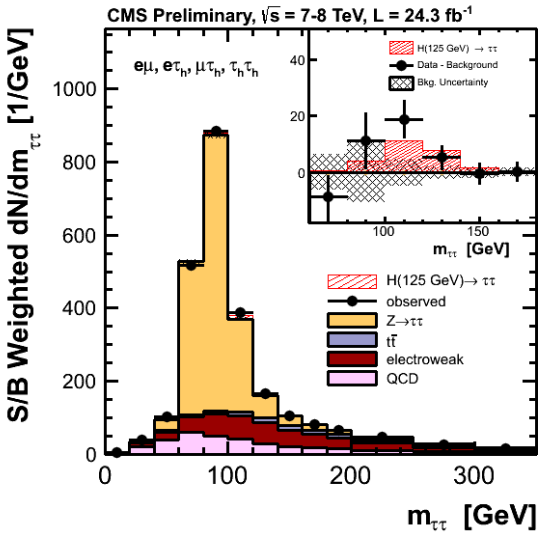

Figure 6.3. The S/B weighted combination of all the $H \to \tau\overline{\tau}$ search channels. The excess of events is consistent with a standard model Higgs at 125 GeV.

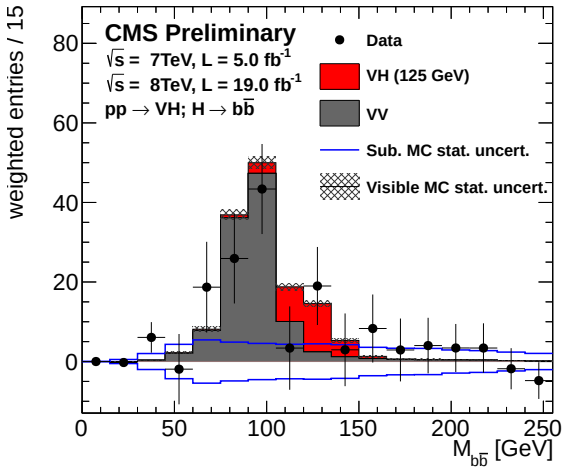

Figure 6.4. The S/B weighted invariant mass of the two selected b-jets for all channels combined in the $VH \to b\bar{b}$.

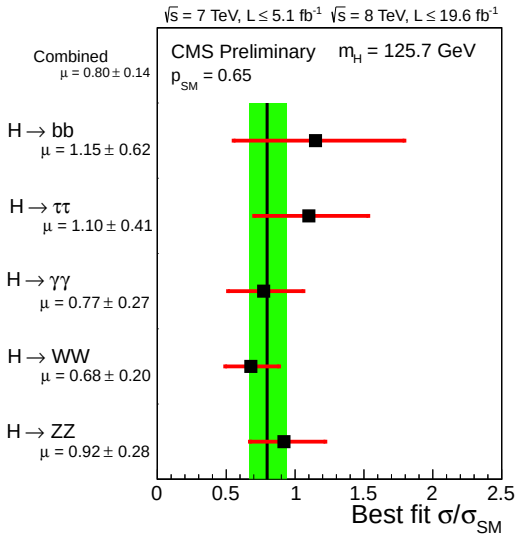

Figure 6.5. The combined channel compatibility measurement for all five channels that see an excess near 125 GeV. The combined best-fit cross-section is 0.80 ± 0.14 times the standard model.

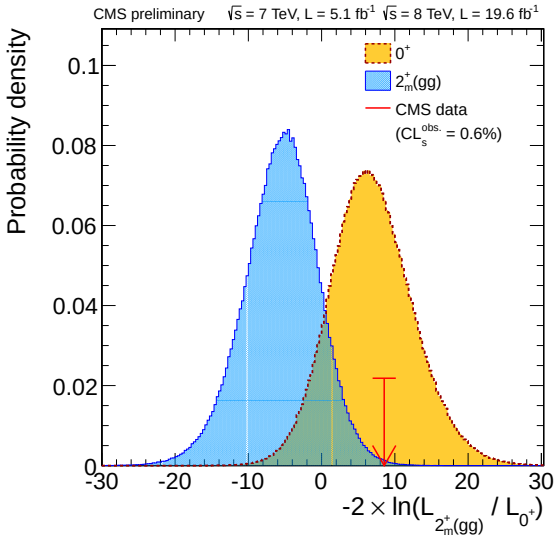

Figure 6.6. The results of the combined spin analysis for the $H \to ZZ \to 2l^+l^-$ and $H \to W^+W^- \to l^+l^-\nu\overline{\nu}$ channels. The measurement disfavors the $2^+_{\rm mgg}$ hypothesis at $\rm CL_s$ =0.6%

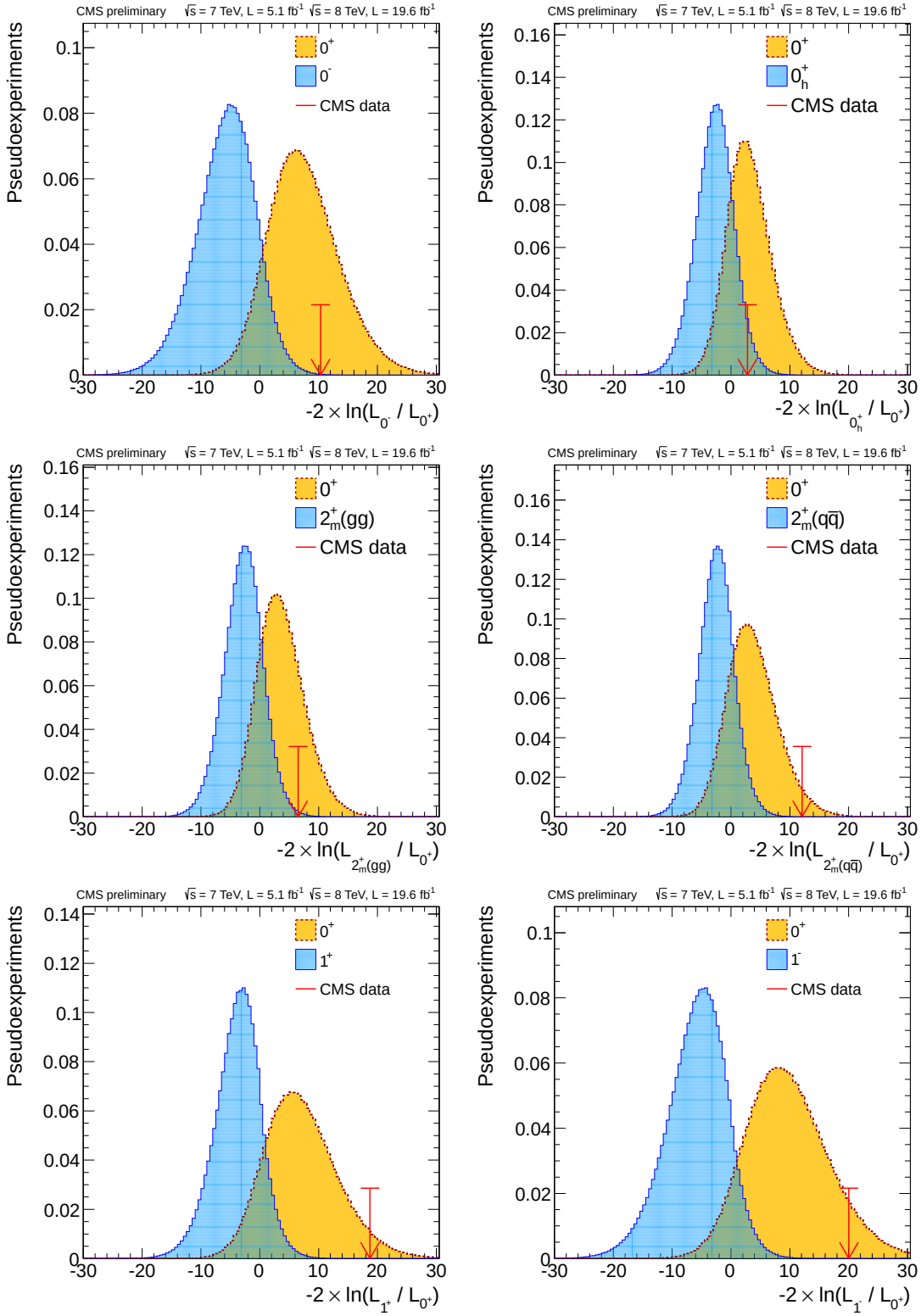

Figure 6.7. The results of all the tested spins for the $H \to ZZ \to 2l^+l^-$ analysis. All measurements disfavor a non-standard model Higgs.

CHAPTER 7

CONCLUSIONS

A search for the standard model Higgs boson decaying to two photons has been presented. The analysis covers 5.1 fb^{-1} of 7 TeV and 19.6 fb^{-1} of 8 TeV data collected by the CMS detector at the LHC. The expected limit of the search was 0.48 to 0.76 times the standard model cross-section. The search excludes at CL_s^{95} the standard model Higgs boson between 110-122.5 and 128-148.5 GeV. The un-excluded region is due to an excess of events observed near 125 GeV. The significance of the excess is 3.2σ (4.1σ expected). This result constitutes evidence of a new resonance state decaying to two photons. The measured cross-section of the resonance is $0.78^{+0.28}_{-0.26}$ times the standard model, and the best-fit mass of the resonance is $125.4 \pm 0.5(stat) \pm 0.6(syst.)$ GeV. The resonance is also observed in a cut-based cross-check analysis with a significance of 3.9σ (3.5σ expected) and a best-fit cross-section of $1.11^{+0.32}_{-0.30}$ at 124.5 GeV.

Currently at CMS, there is evidence of the Higgs boson in five channels. An excess has been measured in the $H \to \gamma\gamma$, $H \to ZZ$, $H \to W^+W^-$, $H \to \tau\overline{\tau}$, and $H \to b\bar{b}$ channels, and the spin measurements in the $H \to ZZ$ and $H \to W^+W^-$ channels disfavor the non-0^+ hypothesis. All of these measurements combine to form a convincing argument that the observed excess is the Higgs boson. However, further measurements are still needed to verify that the Higgs has the branching ratios and width predicted by the standard model.

APPENDIX A

DI-PHOTON BDT VALIDATION

The di-photon BDT was validated by The input variables for the di-photon BDT are validated in a control region in the di-photon spectrum that is signal free, $m_{\gamma\gamma} >$ 160 GeV, and in the search region, 100 GeV $< m_{\gamma\gamma} <$ 160 GeV. It can be seen in figures A.1 and A.2 that there is good agreement between data and Montre Carlo. It can also be seen that there is weak mass dependence on the input variables. The most mass dependent variables are the energy resolution estimates and the output of the photon ID BDT. This is because the ECAL energy resolution improves at higher energies and the fake rate is also lower. There is also very good agreement in the di-photon BDT output in both the control region and signal region in figure A.3. The dependence on the invariant mass is primarily due to changes in the background composition.

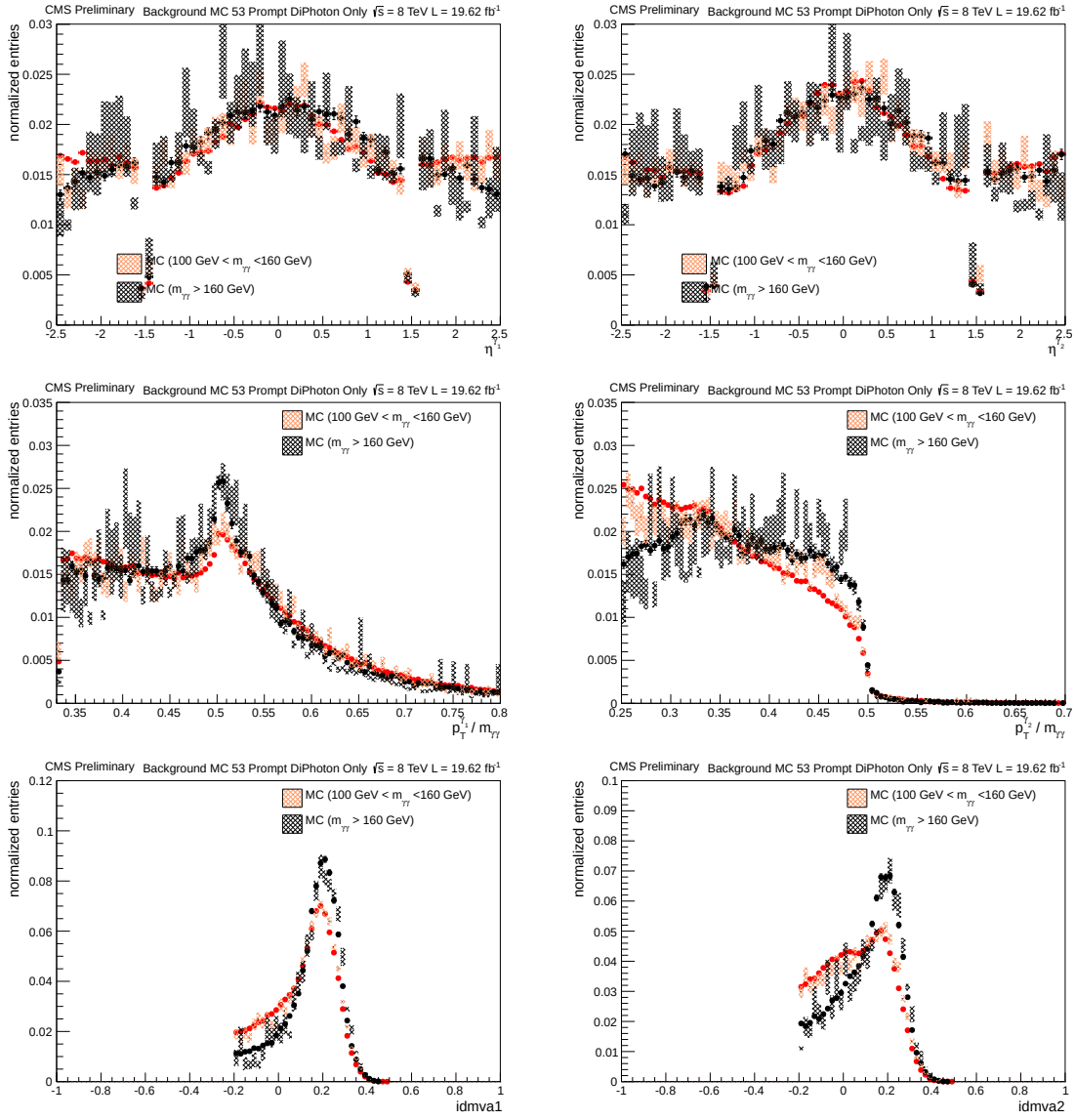

Figure A.1. Comparison of the di-photon BDT inputs between data (points) and Monte Carlo simulation (hashed) in the control region (black) and in the signal region (red).

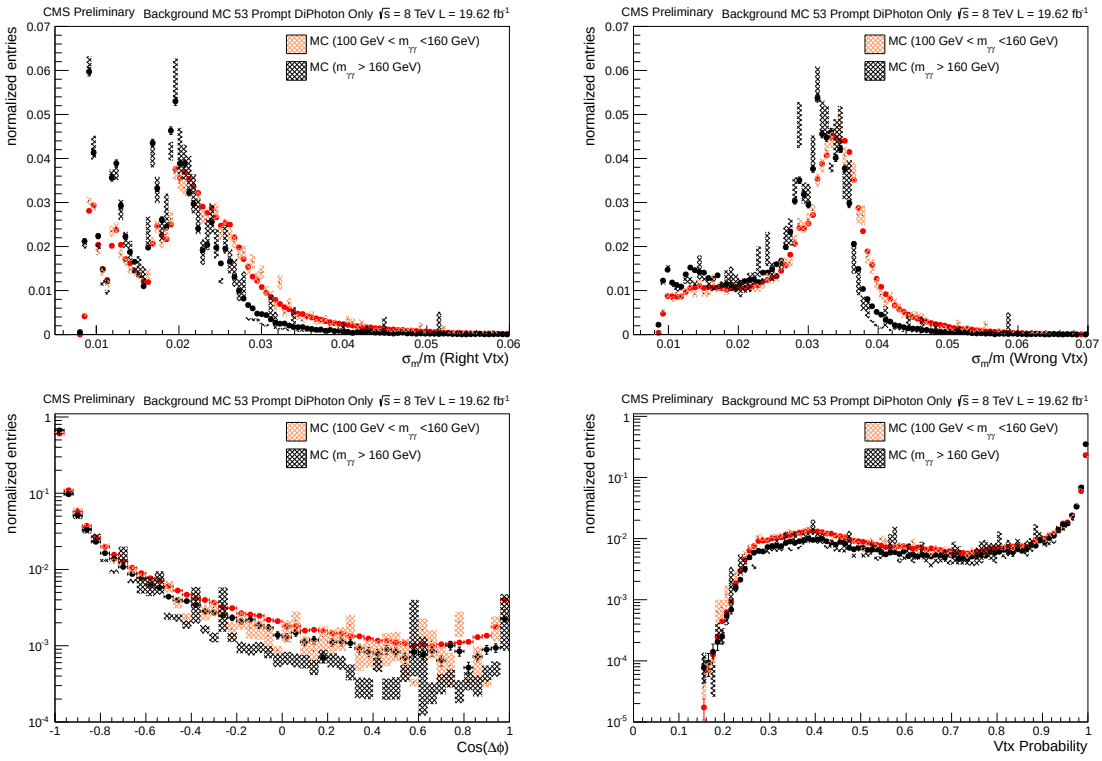

Figure A.2. Comparison of the di-photon BDT inputs between data (points) and Monte Carlo simulation (hashed) in the control region (black) and in the signal region (red).

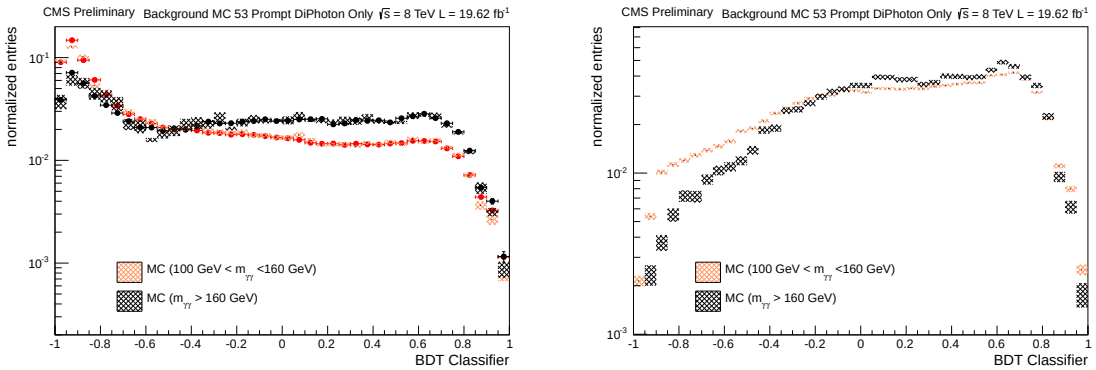

Figure A.3. Left: Di-photon BDT output for the data (points) and Monte Carlo simulation (hashed) in the control region (black) and in the signal region (red). Right: Di-photon BDT output prompt-prompt background Monte Carlo simulation only in the control region (black) and in the signal region (red).

APPENDIX B

BACKGROUND STUDIES

B.1 Multivariate Statistical Analysis

For each of the background models an initial low N value is selected (1, 2, or 3) and a maximum likelihood fit is performed to the observed data. The order (N) of the fit is increased by one and the fit is performed again to the same data. The iterative process stops if $p(\chi^2 \geq \chi^2_{N\to(N+1)}) > 0.05$. The χ^2 is derived from the minimized negative-log-likelihood (NLL) value of the fit. Twice the difference of the two NLL values, for fits of the same model type, follow a χ^2 distribution with n degrees of freedom, where n is the difference in the number of degrees of freedom in the two functions. The χ^2 value,

$$\chi^2_{N\to(N+1)} = 2(NLL_N - NLL_{N+1}), \tag{B.1}$$

is used to decide whether an increase in the number of degrees of freedom is necessary. A higher order function is not used if $p(\chi^2 \geq \chi^2_{N\to(N+1)}) > 0.05$. The benefit of this procedure is that it does not depend on the binning of the data, which is advantageous in categories where there are low event yields. In tables B.1-B.9, the truth model, its order (N), number of degrees of freedom (DoF), the NLL value, the χ^2 for going to the next order ($N+1$), and the estimated p-value associated with this transition can be seen. All of the truth models fit the data well, and there is not a clear way to decide which one is the absolute true description of the background. In order to decide which model to use, they are tested for biases against one another. For a

specific model to pass the bias test, where it must have a negligible bias over the search range 110-150 GeV. Where the bias is defined as

$$\text{Bias}(m_H) = \text{median}(N_{\text{true}}^{\text{FWHM}} - N_{\text{fit}}^{\text{FWHM}}), \tag{B.2}$$

where $N_{\text{true}}^{\text{FWHM}}$ is the number of background events from the truth model, $N_{\text{fit}}^{\text{FWHM}}$ is the number of background events from the test model, and the median is over a large set of toys thrown from the truth model fit. In order for a test model to be considered unbiased against a truth model, the ratio of the bias to the statistical uncertainty has to be less than 0.2,

$$\left|\text{median}\left(\frac{N_{\text{true}}^{\text{FWHM}} - N_{\text{fit}}^{\text{FWHM}}}{\Delta N_{\text{fit}}^{\text{FWHM}}}\right)\right| < 0.2. \tag{B.3}$$

This ratio is evaluated for all the masses in the search range. The results of the bias tests can be seen in tables B.1-B.9. Any test function that fails the bias test is highlighted in **bold**. For a model to pass the bias test it must be unbiased against all other truth models. The procedure for determining the background was developed by Fabian Stoeckli while working with the Massachusetts Institute of Technology.

B.1.1 7 TeV F-Test

For the 7 TeV data, an F-test is used in order to determine the order N of each of the truth models. The F-test is performed in a similar method to the p-value test for the 8 TeV data. For the F-test, the data is placed in 0.5 GeV bins so that the χ^2 residual values can be computed for each fit. The F-test for each function family is evaluated as

$$F = \frac{\left(\frac{\chi_1^2 - \chi_2^2}{N_2 - N_1}\right)}{\left(\frac{\chi^2}{N_{\text{bin}} - N_2}\right)}, \tag{B.4}$$

TABLE B.1

BACKGROUND STUDIES FOR INCLUSIVE CATEGORY 0

8 TeV Inclusive Category 0				
Truth Model Test				
Truth Model	DoF	NLL_N	χ^2 (ΔNLL_{N+1})	$p(\chi^2 > \chi^2$ (ΔNLL_{N+1}))
1^{st} Exponential	2	-3237.27	4.04	> 0.1
1^{st} Power Law	2	-3237.40	0.00	1.0
3^{rd} Bernstein	4	-3239.80	0.04	> 0.8
2^{nd} Laurent	2	-3237.39	0.02	> 0.9
Bias Test				
Fit Model	1^{st} Exponential	1^{st} Power Law	3^{rd} Bernstein	2^{nd} Laurent
1^{st} Exponential	0.01	**2.21**	**2.02**	**2.21**
1^{st} Power Law	**-2.23**	0.00	**2.49**	0.02
3^{rd} Bernstein	**0.49**	**1.33**	-0.02	**1.29**
4^{th} Bernstein	0.09	**0.30**	0.05	**0.29**
5^{th} Bernstein	0.03	0.11	0.03	0.11

where N_1 and N_2 are the number of degrees of freedom of the test functions and N_{bin} is the number of bins. If N_2 does not perform better than N_1, then F will follow an F-distribution. Then the quantity π, which is the quantile of an F-distribution with a value equal or larger than the observed value, is calculated. If this value is above 5% then the higher order fit is not used [102]. The results of the F-test can be seen in table B.10 and the bias studies in tables B.11-B.15.

TABLE B.2

BACKGROUND STUDIES FOR INCLUSIVE CATEGORY 1

8 TeV Inclusive Category 1				
Truth Model Test				
Truth Model	DoF	NLL_N	χ^2 (ΔNLL_{N+1})	$p(\chi^2 > \chi^2$ (ΔNLL_{N+1}))
2^{nd} Exponential	4	-22124.80	0.00	1.0
1^{st} Power Law	2	-22121.55	0.00	1.0
3^{rd} Bernstein	4	-22124.73	0.36	> 0.5
2^{nd} Laurent	2	-22121.36	0.60	> 0.3
Bias Test				
Fit Model	2^{nd} Exponential	1^{st} Power Law	3^{rd} Bernstein	2^{nd} Laurent
2^{nd} Exponential	-	-	-	-
1^{st} Power Law	**-2.18**	0.02	**-3.24**	**0.22**
3^{rd} Bernstein	**0.79**	**1.37**	0.01	**1.44**
4^{th} Bernstein	0.08	**0.35**	0.04	**0.39**
5^{th} Bernstein	-0.04	0.09	0.04	0.09

TABLE B.3

BACKGROUND STUDIES FOR INCLUSIVE CATEGORY 2

8 TeV Inclusive Category 2				
Truth Model Test				
Truth Model	DoF	NLL_N	χ^2 (ΔNLL_{N+1})	$p(\chi^2 > \chi^2$ (ΔNLL_{N+1}))
2^{nd} Exponential	4	-201753.50	0.00	1.0
1^{st} Power Law	2	-201751.46	0.00	1.0
3^{rd} Bernstein	4	-201753.11	1.78	> 0.1
2^{nd} Laurent	2	-201750.80	3.58	> 0.05
Bias Test				
Fit Model	2^{nd} Exponential	1^{st} Power Law	3^{rd} Bernstein	2^{nd} Laurent
2^{nd} Exponential	-	-	-	-
1^{st} Power Law	**-2.34**	0.04	**-4.77**	**0.39**
3^{rd} Bernstein	**2.13**	**2.94**	0.05	**3.02**
4^{th} Bernstein	**0.36**	**0.74**	0.09	**0.78**
5^{th} Bernstein	0.11	0.19	0.09	0.20

TABLE B.4

BACKGROUND STUDIES FOR INCLUSIVE CATEGORY 3

8 TeV Inclusive Category 3				
Truth Model Test				
Truth Model	DoF	NLL_N	χ^2 (ΔNLL_{N+1})	$p(\chi^2 > \chi^2$ (ΔNLL_{N+1}))
2^{nd} Exponential	4	-426348.01	0.00	1.00
1^{st} Power Law	2	-426344.12	0.04	> 0.8
5^{th} Bernstein	5	-426348.45	0.14	> 0.7
2^{nd} Laurent	2	-426345.26	0.96	> 0.3
Bias Test				
Fit Model	2^{nd} Exponential	1^{st} Power Law	5^{th} Bernstein	2^{nd} Laurent
2^{nd} Exponential	-	-	-	-
1^{st} Power Law	**3.43**	0.04	**3.91**	**0.77**
5^{th} Bernstein	**0.42**	**0.29**	0.17	**0.30**
6^{th} Bernstein	**0.37**	**0.36**	**0.33**	**0.34**
7^{th} Bernstein	-	**0.28**	-	**0.29**

TABLE B.5

BACKGROUND STUDIES FOR THE DI-JET TIGHT CATEGORY

8 TeV Di-Jet Tight Category				
Truth Model Test				
Truth Model	DoF	NLL_N	χ^2 (ΔNLL_{N+1})	$p(\chi^2 > \chi^2$ (ΔNLL_{N+1}))
1^{st} Exponential	2	-35.65	1.24	> 0.5
1^{st} Power Law	2	-35.84	0.00	1.0
2^{nd} Bernstein	3	-36.52	0.10	> 0.7
1^{st} Laurent	1	-35.62	0.48	> 0.3
Bias Test				
Fit Model	1^{st} Exponential	1^{st} Power Law	2^{nd} Bernstein	1^{st} Laurent
1^{st} Exponential	0.04	**0.71**	**1.29**	**0.76**
1^{st} Power Law	**-0.71**	0.04	**1.12**	0.03
2^{nd} Bernstein	**0.43**	**0.75**	**0.31**	**0.97**
3^{rd} Bernstein	-0.04	0.12	0.15	**0.24**
4^{th} Bernstein	0.06	0.04	0.07	0.04

TABLE B.6

BACKGROUND STUDIES FOR THE DI-JET LOOSE CATEGORY

8 TeV Di-Jet Loose Category				
Truth Model Test				
Truth Model	DoF	NLL_N	χ^2 (ΔNLL_{N+1})	$p(\chi^2 > \chi^2$ (ΔNLL_{N+1}))
1^{st} Exponential	2	-1147.66	1.60	> 0.3
1^{st} Power Law	2	-1148.37	0.00	1.0
2^{nd} Bernstein	3	-1147.62	1.56	> 0.2
1^{st} Laurent	1	-1148.12	0.50	> 0.3
Bias Test				
Fit Model	1^{st} Exponential	1^{st} Power Law	2^{nd} Bernstein	1^{st} Laurent
1^{st} Exponential	0.02	**1.39**	**1.47**	**1.43**
1^{st} Power Law	**-1.40**	0.02	**-1.73**	0.01
2^{nd} Bernstein	**0.91**	**1.48**	0.02	**1.68**
3^{rd} Bernstein	0.13	**0.33**	0.05	**0.36**
4^{th} Bernstein	0.04	0.09	0.04	0.11

TABLE B.7

BACKGROUND STUDIES FOR THE MUON CATEGORY

8 TeV Muon Category				
Truth Model Test				
Truth Model	DoF	NLL_N	χ^2 (ΔNLL_{N+1})	$p(\chi^2 > \chi^2$ (ΔNLL_{N+1}))
1st Exponential	2	58.50	0.00	1.0
1st Power Law	2	59.02	0.00	1.0
1st Bernstein	2	57.17	0.06	> 0.8
1st Laurent	1	59.33	1.20	> 0.2
Bias Test				
Fit Model	1st Exponential	1st Power Law	1st Bernstein	1st Laurent
1st Exponential	0.09	**0.27**	**-0.98**	**0.33**
1st Power Law	**-0.26**	0.10	**-1.15**	0.10
2nd Bernstein	0.18	**0.27**	-0.10	**0.49**
3rd Bernstein	0.10	-0.11	0.10	0.14

TABLE B.8

BACKGROUND STUDIES FOR THE ELECTRON CATEGORY

8 TeV Electron Category				
Truth Model Test				
Truth Model	DoF	NLL_N	χ^2 (ΔNLL_{N+1})	$p(\chi^2 > \chi^2$ (ΔNLL_{N+1}))
1st Exponential	2	55.95	0.00	1.0
1st Power Law	2	56.29	0.00	1.0
1st Bernstein	2	55.66	0.26	> 0.5
1st Laurent	1	56.35	0.48	> 0.3
Bias Test				
Fit Model	1st Exponential	1st Power Law	1st Bernstein	1st Laurent
1st Exponential	0.08	**0.27**	**-0.87**	**0.32**
1st Power Law	**-0.26**	0.10	**-1.04**	0.11
2nd Bernstein	**0.26**	**0.38**	-0.09	**0.49**
3rd Bernstein	0.11	0.10	-0.07	0.15

TABLE B.9

BACKGROUND STUDIES FOR THE $\not\!\!E_T$ CATEGORY

8 TeV $\not\!\!E_T$ Category				
Truth Model Test				
Truth Model	DoF	NLL_N	χ^2 (ΔNLL_{N+1})	$p(\chi^2 > \chi^2$ (ΔNLL_{N+1}))
1st Exponential	2	55.59	0.00	1.0
1st Power Law	2	55.82	0.00	1.0
1st Bernstein	2	55.47	0.32	> 0.5
1st Laurent	1	56.80	2.10	> 0.1
Bias Test				
Fit Model	1st Exponential	1st Power Law	1st Bernstein	1st Laurent
1st Exponential	0.04	**0.46**	**-1.37**	**0.57**
1st Power Law	**-0.47**	0.03	**-1.65**	0.05
2nd Bernstein	**0.23**	**0.38**	0.03	**0.75**
3rd Bernstein	0.04	0.08	0.02	0.20

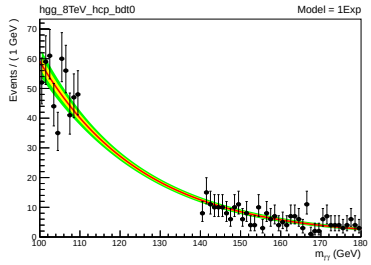

(a) 1st Exponential Truth

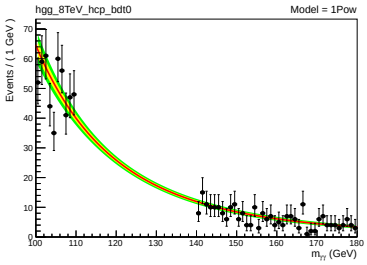

(b) 1st Power Law Truth

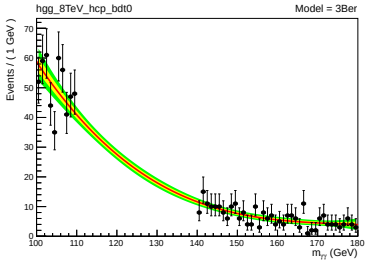

(c) 3rd Bernstein Truth

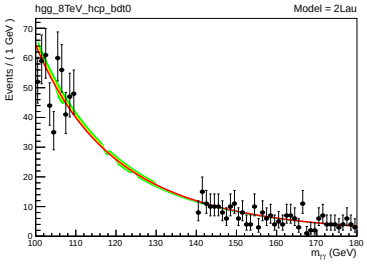

(d) 2nd Laurent Truth

Figure B.1. Fits for each truth model for inclusive category 0 at 8 TeV.

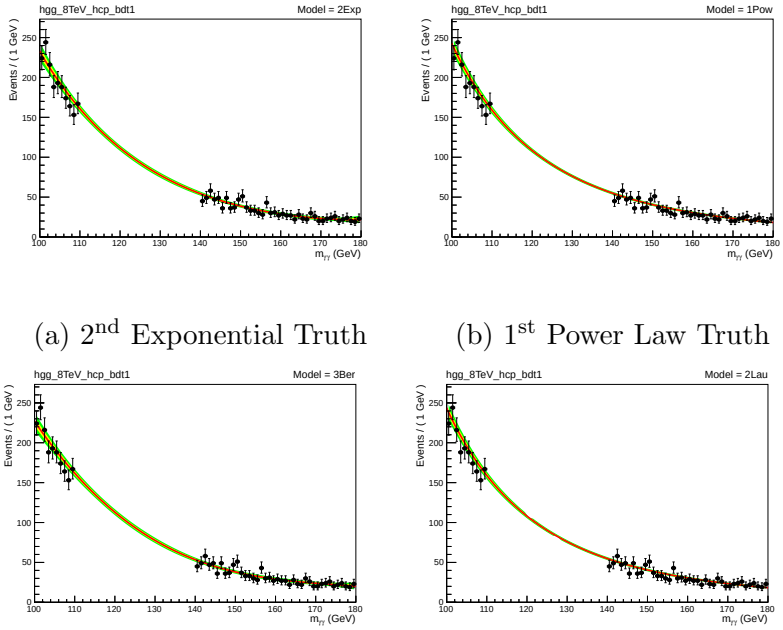

(a) 2nd Exponential Truth

(b) 1st Power Law Truth

(c) 3rd Bernstein Truth

(d) 2nd Laurent Truth

Figure B.2. Fits for each truth model for inclusive category 1 at 8 TeV.

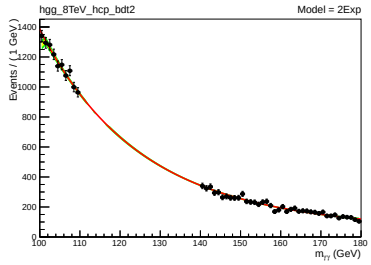

(a) 2nd Exponential Truth

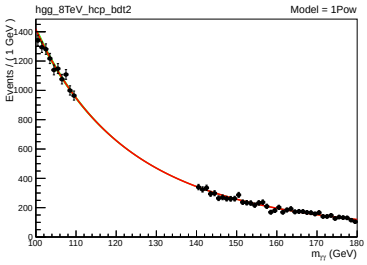

(b) 1st Power Law Truth

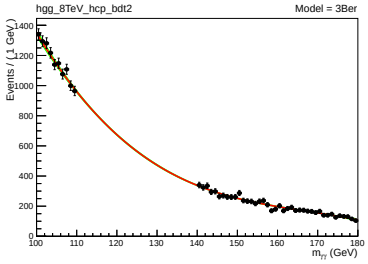

(c) 3rd Bernstein Truth

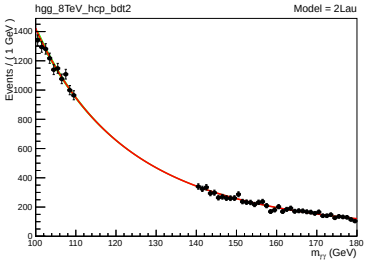

(d) 2nd Laurent Truth

Figure B.3. Fits for each truth model for inclusive category 2 at 8 TeV.

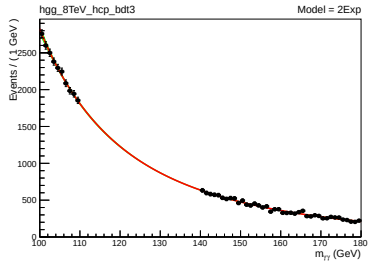

(a) 2nd Exponential Truth

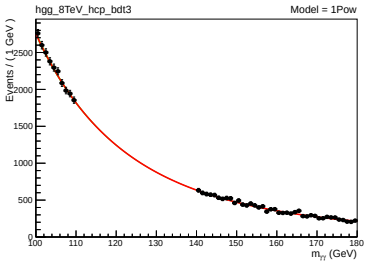

(b) 1st Power Law Truth

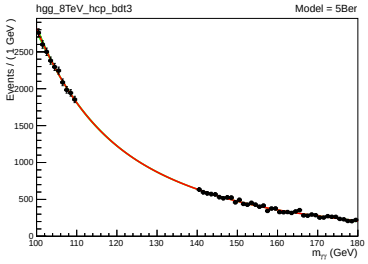

(c) 5th Bernstein Truth

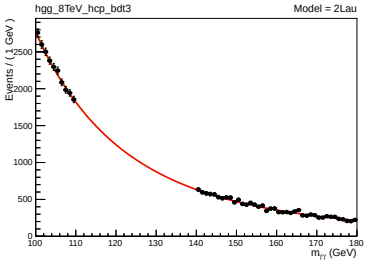

(d) 2nd Laurent Truth

Figure B.4. Fits for each truth model for inclusive category 3 at 8 TeV.

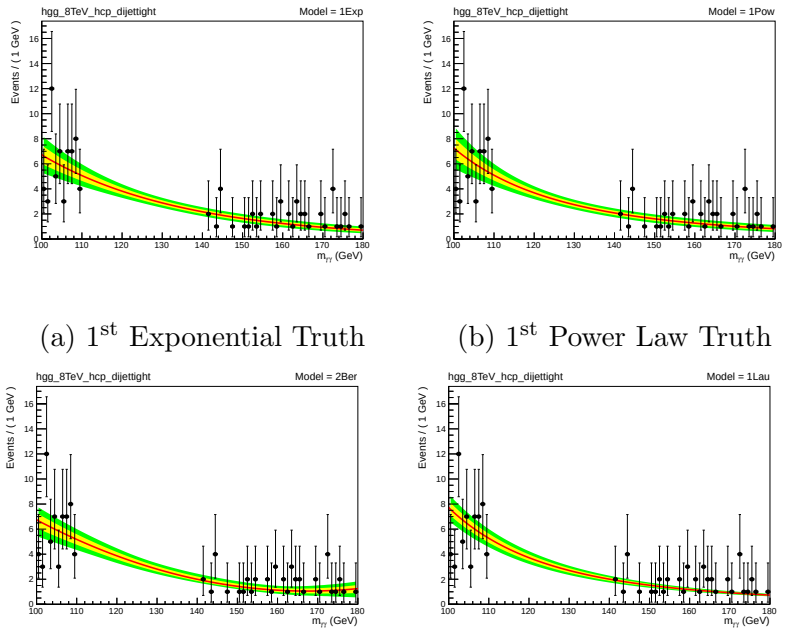

(a) 1st Exponential Truth

(b) 1st Power Law Truth

(c) 2nd Bernstein Truth

(d) 1st Laurent Truth

Figure B.5. Fits for each truth model for the di-jet tight category at 8 TeV.

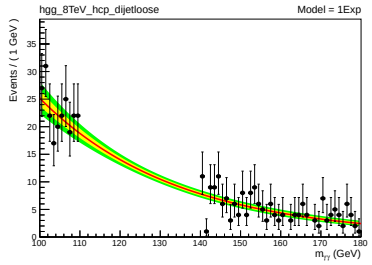

(a) 1st Exponential Truth

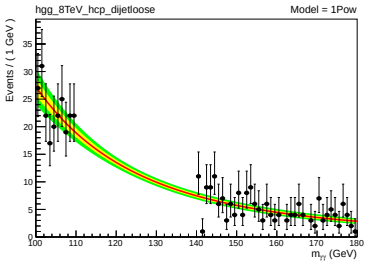

(b) 1st Power Law Truth

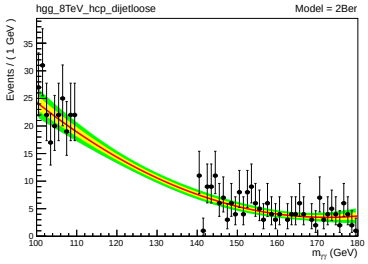

(c) 2nd Bernstein Truth

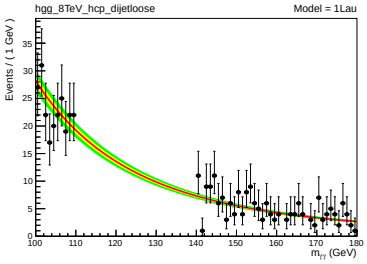

(d) 1st Laurent Truth

Figure B.6. Fits for each truth model for the di-jet loose category at 8 TeV.

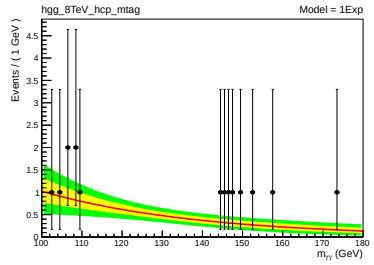

(a) 1st Exponential Truth

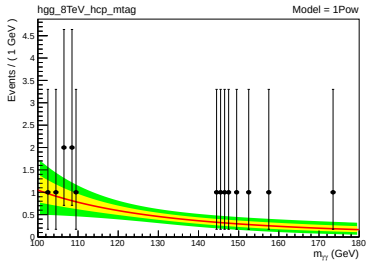

(b) 1st Power Law Truth

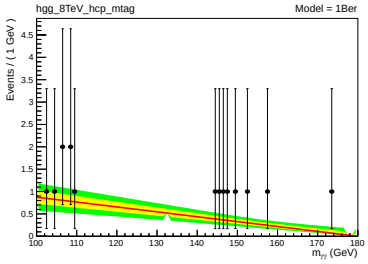

(c) 1st Bernstein Truth

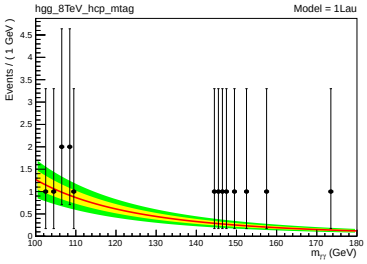

(d) 1st Laurent Truth

Figure B.7. Fits for each truth model for the muon category at 8 TeV.

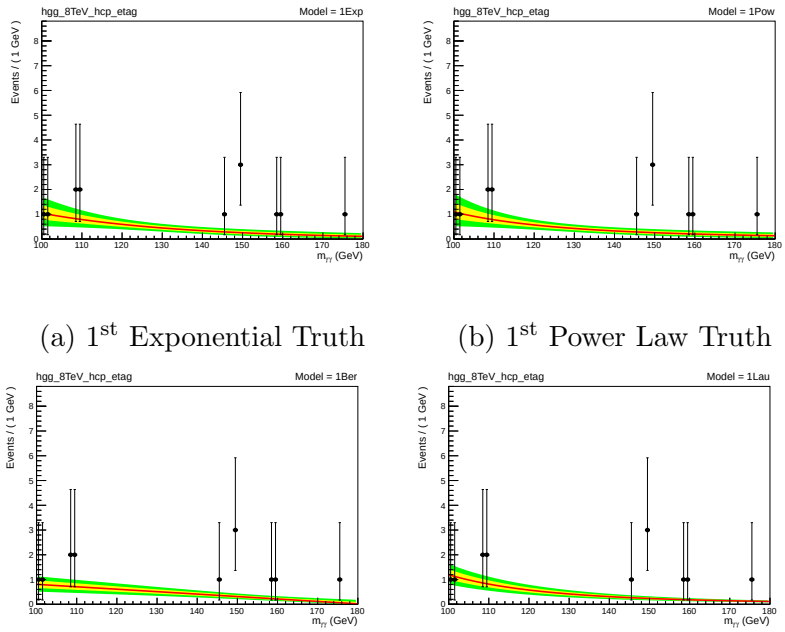

(a) 1st Exponential Truth

(b) 1st Power Law Truth

(c) 1st Bernstein Truth

(d) 1st Laurent Truth

Figure B.8. Fits for each truth model for the electron category at 8 TeV.

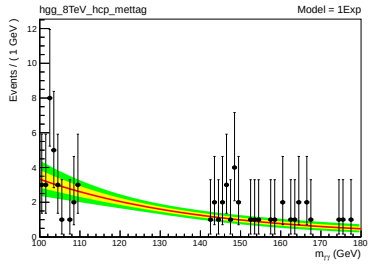

(a) 1st Exponential Truth

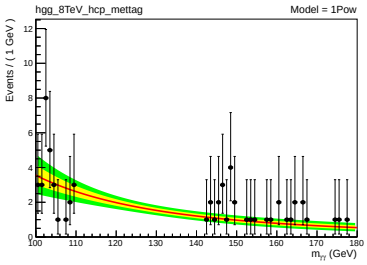

(b) 1st Power Law Truth

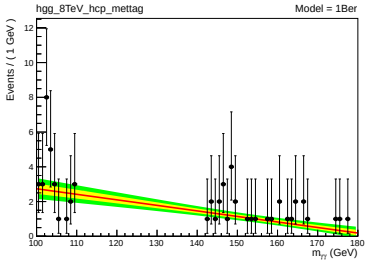

(c) 1st Bernstein Truth

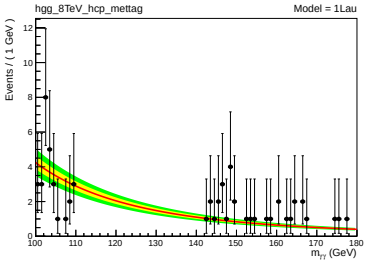

(d) 1st Laurent Truth

Figure B.9. Fits for each truth model for the $\not\!\!E_T$ category at 8 TeV.

TABLE B.10

MAIN ANALYSIS 7 TEV TRUTH MODEL STUDIES

Order (N)	χ^2	p	π	χ^2	p	π	χ^2	p	π	χ^2	p	π
	Exponential			Power Law			Berstien Polynomial			Laurent		
Inclusive Category 0												
2	150.4	69.5	-	149.5	71.3	-	162.4	43.2	-	149.6	71.1	-
3	-			-			152.9	64.3	0.2	149.5	71.3	100
4	150.0	70.3	53.5	149.5	71.3	100	146.5	77.0	1.0			
5							146.3	77.4	74.5			

TABLE B.10

Continued

Order (N)	χ^2	p	π	χ^2	p	π	χ^2	p	π	χ^2	p	π
	Exponential			Power Law			Berstien Polynomial			Laurent		
Inclusive Category 1												
2	148.6	73.1	-	145.9	78.1	-	-			146.0	77.9	-
3	-			-			152.2	65.8	-	145.1	79.5	32.5
4	144.2	81.0	9.6	145.9	78.1	100	143.9	81.4	0.3			
5	-						143.8	81.6	74.3			
6	144.0	81.3	89.9									

TABLE B.10

Continued

Order (N)	χ^2	p	π	χ^2	p	π	χ^2	p	π	χ^2	p	π
	Exponential			Power Law			Berstien Polynomial			Laurent		
Inclusive Category 2												
2	150.3	69.7	-	144.4	80.6	-	-			144.5	80.5	-
3	-			-			161.9	44.3	-	143.7	81.8	35.1
4	144.1	81.1	3.7	144.4	80.6	100	145.7	78.4	0.0			
5	-						143.8	81.6	15.4			
6	143.8	81.6	85.2									

TABLE B.10

Continued

Order (N)	χ^2	p	π	χ^2	p	π	χ^2	p	π	χ^2	p	π
	Exponential			Power Law			Berstien Polynomial			Laurent		
Inclusive Category 3												
2	223.9	0.1	-	176.4	17.8	-	-			175.9	18.5	-
3	-			-			253.6	0.0	-	175.2	19.5	43.0
4	172.0	24.5	0.0	176.4	17.8	100	169.8	28.3	0.0			
5	-						169.6	28.7	67.0			
6	172.0	24.5	100									
Di-Jet Cateogry												
2	166.6	34.4	-	167.3	33.0	-	165.7	36.2	-	167.0	33.6	-
3	-			-			165.6	36.4	75.9	167.0	33.6	100
4	165.6	36.4	33.2	167.3	33.0	100						

B.2 Cut-Based Background Fits

The results of the 8 TeV truth model test for the cut-based categories can be seen in tables B.16-B.24 and figures B.10-B.18. The results of the 7 TeV bias study and sensitivity loss test can be seen in table B.25.

TABLE B.11

BIAS STUDY OF INCLUSIVE CATEGORY 0 AT 7 TeV.

Inclusive Category 0									
mass [GeV]	110	115	120	125	130	135	140	145	150
Truth	3^{rd} Bernstein Bias [%]								
1^{st} Exponential	-1.3	-5.7	-11.3	-7.7	-5.4	-4.7	+0.7	+4.8	+4.0
1^{st} Power Law	-7.3	-19.2	-25.4	-21.3	-12.8	-5.0	+1.9	+12.1	+14.8
2^{nd} Laurent	-9.0	-20.8	-25.3	-22.7	-14.2	-4.1	+2.1	+9.7	+14.3
Truth	4^{th} Bernstein Bias [%]								
1^{st} Exponential	+0.9	-0.7	-2.7	-0.8	+1.0	-1.6	-1.8	-3.4	-7.2
1^{st} Power Law	-7.0	-8.1	-7.6	-3.8	+1.6	+3.9	+3.2	+2.8	-3.1
2^{nd} Laurent	-9.0	-7.4	-8.1	-4.7	+0.5	+5.2	+2.0	+0.5	-4.8
Truth	5^{th} Bernstein Bias [%]								
1^{st} Exponential	+3.1	+0.4	-1.9	-0.9	-0.3	-3.5	-3.5	-2.4	-5.2
1^{st} Power Law	-1.8	-1.9	-3.8	-1.8	+0.8	+0.1	-1.5	-0.5	+3.3
2^{nd} Laurent	-4.4	-2.5	-3.0	-3.1	-0.8	+1.2	-2.5	-3.1	-5.7

TABLE B.12

BIAS STUDY OF INCLUSIVE CATEGORY 1 AT 7 TeV.

Inclusive Category 1									
mass [GeV]	110	115	120	125	130	135	140	145	150
Truth	3^{rd} Bernstein Bias [%]								
1^{st} Exponential	-8.8	-13.7	-13.6	-7.6	-0.6	+6.5	+9.6	+11.9	+15.0
1^{st} Power Law	-27.3	-38.5	-30.0	-14.9	+0.9	+15.6	+27.8	+28.1	+27.1
2^{nd} Laurent	-29.0	-39.2	-30.9	-15.3	-0.1	+16.0	+28.3	+30.4	+28.5
Truth	4^{th} Bernstein Bias [%]								
1^{st} Exponential	-1.9	-1.4	-1.3	+0.1	+1.4	+3.0	+0.0	-1.7	+1.1
1^{st} Power Law	-11.0	-8.8	-1.3	+4.9	+6.5	+6.4	+3.4	-5.7	-9.5
2^{nd} Laurent	-11.9	-8.8	-1.3	+5.1	+5.8	+5.8	+4.6	-3.1	-8.0
Truth	5^{th} Bernstein Bias [%]								
1^{st} Exponential	-0.8	-0.5	-1.2	+0.3	+1.3	+1.2	-0.4	-2.7	+1.2
1^{st} Power Law	-2.9	-0.4	+1.7	+3.7	+2.4	+0.3	-0.8	-5.7	-3.9
2^{nd} Laurent	-4.8	-1.1	+1.5	+3.5	+1.2	-0.5	-0.2	-3.5	-3.4

TABLE B.13

BIAS STUDY OF INCLUSIVE CATEGORY 2 AT 7 TeV.

Inclusive Category 2									
mass [GeV]	110	115	120	125	130	135	140	145	150
Truth	3^{rd} Bernstein Bias [%]								
2^{nd} Exponential	-18.6	-26.1	-23.1	-16.3	-0.9	+8.3	+19.3	+26.4	+26.8
1^{st} Power Law	-55.0	-74.3	-61.5	-32.8	+3.3	+32.6	+52.5	+60.3	+54.8
2^{nd} Laurent	-55.8	-75.4	-62.8	-33.7	+1.9	+33.2	+53.9	+62.7	+56.1
Truth	4^{th} Bernstein Bias [%]								
2^{nd} Exponential	-5.0	-3.0	+0.6	-0.9	+2.5	+1.6	+0.8	+1.3	-0.3
1^{st} Power Law	-23.7	-16.4	-4.2	+7.5	+14.9	+12.2	+5.4	-6.0	-16.7
2^{nd} Laurent	-22.8	-16.5	-2.9	+8.5	+13.7	+13.0	+6.2	-4.4	-16.1
Truth	5^{th} Bernstein Bias [%]								
2^{nd} Exponential	-3.0	-0.8	+1.6	-1.3	+2.1	-1.1	-1.1	+0.7	+0.0
1^{st} Power Law	-7.3	-1.1	+2.3	+2.7	+3.9	+0.9	-4.2	-5.5	-4.7
2^{nd} Laurent	-6.8	-1.0	+2.6	+3.5	+3.2	+0.2	-2.9	-4.2	-4.3

TABLE B.14

BIAS STUDY OF INCLUSIVE CATEGORY 3 AT 7 TeV.

Inclusive Category 3									
mass [GeV]	110	115	120	125	130	135	140	145	150
Truth	3^{rd} Bernstein Bias [%]								
2^{nd} Exponential	-1.0	+2.2	-0.1	-1.0	-2.1	+1.8	-1.3	+0.9	-1.6
1^{st} Power Law	-161	-215	-174	-94.6	+1.9	+91.6	+159	+186	+162
2^{nd} Laurent	-160	-223	-183	-103	+2.4	+97.9	+164	+195	+167
Truth	4^{th} Bernstein Bias [%]								
2^{nd} Exponential	+0.3	+0.0	-0.8	-0.5	+3.0	+2.4	-3.1	-2.1	-4.4
1^{st} Power Law	-72.5	-54.4	-7.6	+30.7	+40.8	+35.8	+21.2	-13.3	-58.4
2^{nd} Laurent	-68.9	-55.6	-10.2	+26.2	+42.6	+39.7	+20.7	-12.9	-58.5
Truth	5^{th} Bernstein Bias [%]								
2^{nd} Exponential	-7.9	+1.7	+0.8	+0.9	+0.3	+2.1	-3.0	+1.7	-1.9
1^{st} Power Law	-23.9	-4.3	+10.1	+14.7	+5.0	-6.2	-8.2	-9.9	-8.9
2^{nd} Laurent	-14.0	-4.5	+8.0	+9.1	+7.2	-3.1	-9.2	-9.1	-9.7

TABLE B.15

BIAS STUDY OF THE DI-JET CATEGORY AT 7 TeV.

Di-Jet Category									
mass [GeV]	110	115	120	125	130	135	140	145	150
Truth	3^{rd} Bernstein Bias [%]								
1^{st} Exponential	+5.8	-6.0	-10.9	-13.1	-12.2	-10.4	-7.3	-0.0	+7.8
1^{st} Power Law	+7.0	-12.7	-19.2	-22.8	-19.7	-17.0	-10.7	-2.7	+12.3
2^{nd} Laurent	+8.0	-10.2	-16.8	-18.3	-17.9	-16.9	-8.5	-2.8	+9.2
Truth	4^{th} Bernstein Bias [%]								
1^{st} Exponential	-0.2	-2.4	-2.6	-2.6	-1.9	-1.8	-1.1	+1.3	+2.4
1^{st} Power Law	-2.5	-8.4	-7.6	-7.7	-3.6	-2.6	+0.8	+2.7	+7.6
2^{nd} Laurent	-0.9	-6.3	-6.3	-4.4	-3.4	-3.9	+1.6	+1.4	+3.2
Truth	5^{th} Bernstein Bias [%]								
1^{st} Exponential	-0.1	-1.3	-1.2	-1.5	-1.6	-1.9	-1.9	+0.2	+4.2
1^{st} Power Law	-2.0	-3.8	-2.9	-2.9	-0.6	-0.9	-0.2	+0.4	+7.2
2^{nd} Laurent	-0.1	-3.4	-3.4	-1.1	-1.2	-2.9	+0.9	+0.7	+3.4

TABLE B.16

CUT-BASED BIAS STUDY FOR INCLUSIVE CATEGORY 0

8 TeV CiC Inclusive Category 0				
Truth Model Test				
Truth Model	DoF	NLL_N	χ^2 (ΔNLL_{N+1})	$p(\chi^2>\chi^2$ (ΔNLL_{N+1}))
2^{nd} Exponential	4	-120,561.73	0.00	1.00
1^{st} Power Law	2	-120,558.93	0.00	1.00
3^{rd} Bernstein	4	-120,562.12	0.00	1.00
2^{nd} Laurent	2	-120,560.97	1.06	0.30
Bias Test				
Fit Model	2^{nd} Exponential	1^{st} Power Law	3^{rd} Bernstein	2^{nd} Laurent
2^{nd} Exponential	0.03	0.10	**0.84**	0.07
1^{st} Power Law	**-2.55**	0.02	**-3.31**	**-1.33**
3^{rd} Bernstein	**0.78**	**1.40**	0.03	**1.15**
4^{th} Bernstein	0.13	**0.37**	0.08	**0.25**
5^{th} Bernstein	0.07	0.11	0.08	0.09

TABLE B.17

CUT-BASED BIAS STUDY FOR INCLUSIVE CATEGORY 1

8 TeV CiC Inclusive Category 1				
Truth Model Test				
Truth Model	DoF	NLL_N	χ^2 (ΔNLL_{N+1})	$p(\chi^2>\chi^2$ (ΔNLL_{N+1}))
2^{nd} Exponential	4	-268,962.93	0.00	1.00
1^{st} Power Law	2	-268,939.36	0.00	1.00
3^{rd} Bernstein	4	-268,962.58	0.98	0.32
3^{rd} Laurent	3	-268,962.91	0.12	0.70
Bias Test				
Fit Model	2^{nd} Exponential	1^{st} Power Law	3^{rd} Bernstein	3^{rd} Laurent
2^{nd} Exponential	0.04	0.16	**1.13**	0.18
1^{st} Power Law	**-7.51**	0.03	**-7.47**	**-7.32**
3^{rd} Bernstein	**1.14**	**2.46**	0.03	**1.18**
4^{th} Bernstein	0.17	**0.63**	0.10	0.15
5^{th} Bernstein	0.10	0.17	0.11	0.14

TABLE B.18

CUT-BASED BIAS STUDY FOR INCLUSIVE CATEGORY 2

8 TeV CiC Inclusive Category 2				
Truth Model Test				
Truth Model	DoF	NLL_N	χ^2 (ΔNLL_{N+1})	$p(\chi^2>\chi^2$ (ΔNLL_{N+1}))
2^{nd} Exponential	4	-117,141.28	0.00	1.00
1^{st} Power Law	2	-117,134.68	0.00	1.00
3^{rd} Bernstein	4	-117,140.82	2.97	0.08
2^{nd} Laurent	2	-117,140.77	0.82	0.37
Bias Test				
Fit Model	2^{nd} Exponential	1^{st} Power Law	3^{rd} Bernstein	2^{nd} Laurent
2^{nd} Exponential	0.03	0.07	**-0.41**	0.10
1^{st} Power Law	**-4.97**	0.02	**-4.75**	**-2.93**
3^{rd} Bernstein	**0.39**	**1.01**	0.02	**0.51**
4^{th} Bernstein	0.07	**0.26**	0.07	0.09
5^{th} Bernstein	0.07	0.09	0.07	0.09

TABLE B.19

CUT-BASED BIAS STUDY FOR INCLUSIVE CATEGORY 3

8 TeV CiC Inclusive Category 3				
Truth Model Test				
Truth Model	DoF	NLL_N	χ^2 (ΔNLL_{N+1})	$p(\chi^2>\chi^2$ (ΔNLL_{N+1}))
2^{nd} Exponential	4	-238,731.55	0.07	0.97
1^{st} Power Law	2	-238,722.89	0.00	1.00
3^{rd} Bernstein	4	-238,729.80	2.68	0.10
2^{nd} Laurent	2	-238,727.81	0.00	1.00
Bias Test				
Fit Model	2^{nd} Exponential	1^{st} Power Law	3^{rd} Bernstein	2^{nd} Laurent
2^{nd} Exponential	0.06	**-1.16**	**1.00**	0.08
1^{st} Power Law	**-4.59**	0.03	**-5.27**	**-1.57**
3^{rd} Bernstein	**1.15**	**1.94**	0.02	**1.63**
4^{th} Bernstein	0.20	**0.48**	0.10	**0.35**
5^{th} Bernstein	0.09	0.13	0.11	0.11

TABLE B.20

CUT-BASED BIAS STUDY FOR THE DI-JET TIGHT CATEGORY

8 TeV CiC Di-Jet Tight Category				
Truth Model Test				
Truth Model	DoF	NLL_N	χ^2 (ΔNLL_{N+1})	$p(\chi^2 > \chi^2$ (ΔNLL_{N+1}))
1^{st} Exponential	2	-173.73	0.00	1.00
1^{st} Power Law	2	-172.83	0.00	1.00
1^{st} Bernstein	2	-174.89	0.31	0.57
2^{nd} Laurent	2	-174.66	0.00	1.00
Bias Test				
Fit Model	1^{st} Exponential	1^{st} Power Law	1^{st} Bernstein	2^{nd} Laurent
1^{st} Exponential	0.01	**0.49**	**-1.15**	**-1.06**
1^{st} Power Law	**-0.53**	0.01	**-1.59**	**-1.61**
2^{nd} Bernstein	0.09	**0.24**	0.02	**-0.67**
3^{rd} Bernstein	-0.01	0.04	0.02	**-0.30**
4^{th} Bernstein	0.02	-0.02	-0.03	-0.14

TABLE B.21

CUT-BASED BIAS STUDY FOR THE DI-JET LOOSE CATEGORY

8 TeV CiC Di-Jet Loose Category				
Truth Model Test				
Truth Model	DoF	NLL_N	χ^2 (ΔNLL_{N+1})	$p(\chi^2>\chi^2$ (ΔNLL_{N+1}))
1^{st} Exponential	2	-1,526.30	0.00	1.00
1^{st} Power Law	2	-1,525.34	0.00	1.00
2^{nd} Bernstein	3	-1,526.57	0.87	0.35
2^{nd} Laurent	2	-1,526.41	0.36	0.55
Bias Test				
Fit Model	1^{st} Exponential	1^{st} Power Law	2^{nd} Bernstein	2^{nd} Laurent
1^{st} Exponential	0.01	**0.96**	**-0.44**	**-0.92**
1^{st} Power Law	**-1.00**	0.01	**-1.45**	**-1.96**
2^{nd} Bernstein	**0.22**	**0.54**	0.02	**-0.53**
3^{rd} Bernstein	0.01	0.10	0.02	**0.26**
4^{th} Bernstein	0.02	0.02	0.01	-0.13

TABLE B.22

CUT-BASED BIAS STUDY FOR THE MUON CATEGORY

8 TeV CiC Muon Category				
Truth Model Test				
Truth Model	DoF	NLL_N	χ^2 (ΔNLL_{N+1})	$p(\chi^2 > \chi^2$ (ΔNLL_{N+1}))
1st Exponential	2	63.65	0.00	1.00
1st Power Law	2	63.89	0.00	1.00
1st Bernstein	2	63.28	0.44	0.51
2nd Laurent	2	62.73	0.82	0.37
Bias Test				
Fit Model	1st Exponential	1st Power Law	1st Bernstein	2nd Laurent
1st Exponential	0.00	0.14	**-0.39**	**-0.83**
1st Power Law	**-0.16**	-0.01	**-0.53**	**-0.96**
2nd Bernstein	0.02	0.06	0.01	**-0.52**
3rd Bernstein	0.01	0.01	0.01	-0.19

TABLE B.23

CUT-BASED BIAS STUDY FOR THE ELECTRON CATEGORY

8 TeV CiC Electron Category				
Truth Model Test				
Truth Model	DoF	NLL_N	χ^2 (ΔNLL_{N+1})	$p(\chi^2 > \chi^2$ (ΔNLL_{N+1}))
1st Exponential	2	64.33	0.00	1.00
1st Power Law	2	64.68	0.00	1.00
1st Bernstein	2	64.38	0.72	0.40
1st Laurent	1	65.01	1.09	0.30
Bias Test				
Fit Model	1st Exponential	1st Power Law	1st Bernstein	1st Laurent
1st Exponential	0.00	**0.30**	**-0.80**	**0.35**
1st Power Law	**-0.31**	-0.01	**-1.00**	0.01
2nd Bernstein	0.14	**0.24**	0.01	**0.40**
3rd Bernstein	0.02	0.04	-0.01	0.09

TABLE B.24

CUT-BASED BIAS STUDY FOR THE $\not\!\!E_T$ CATEGORY

8 TeV CiC $\not\!\!E_T$ Category				
Truth Model Test				
Truth Model	DoF	NLL_N	χ^2 (ΔNLL_{N+1})	$p(\chi^2>\chi^2$ (ΔNLL_{N+1}))
1st Exponential	2	67.33	0.00	1.00
1st Power Law	2	67.37	0.00	1.00
1st Bernstein	2	67.26	0.01	0.94
2nd Laurent	2	67.78	0.60	0.44
Bias Test				
Fit Model	1st Exponential	1st Power Law	1st Bernstein	2nd Laurent
1st Exponential	0.01	**0.29**	**-0.61**	**-0.38**
1st Power Law	**-0.30**	0.00	**-0.86**	**-0.73**
2nd Bernstein	0.05	0.14	0.00	**-0.22**
3rd Bernstein	0.01	0.02	-0.01	-0.11

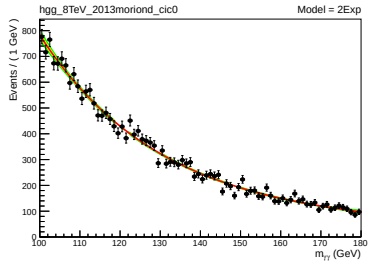

(a) 2nd Exponential Truth

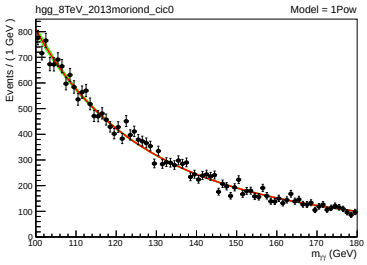

(b) 1st Power Law Truth

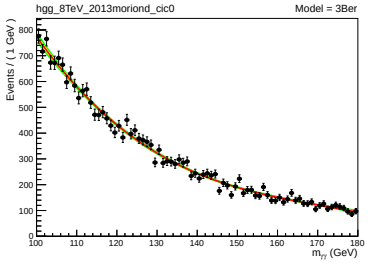

(c) 3rd Bernstein Truth

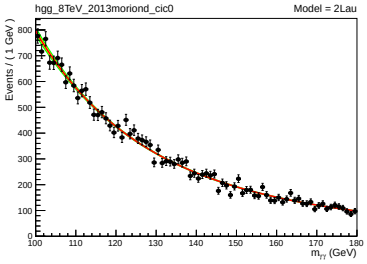

(d) 2nd Laurent Truth

Figure B.10. Fits to each of the truth models for CiC inclusive category 0.

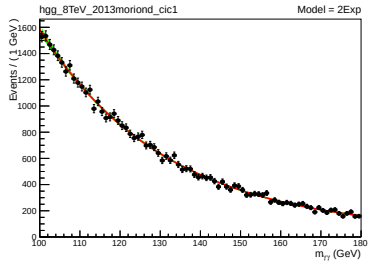

(a) 2nd Exponential Truth

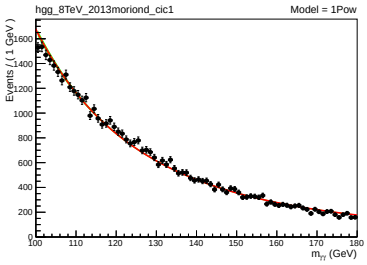

(b) 1st Power Law Truth

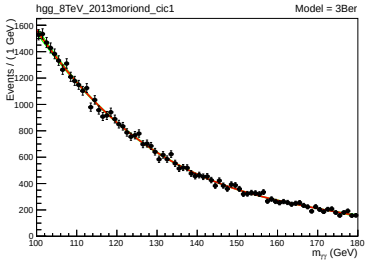

(c) 3rd Bernstein Truth

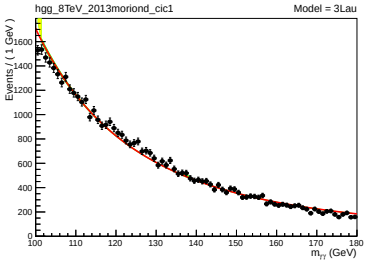

(d) 3rd Laurent Truth

Figure B.11. Fits to each of the truth models for CiC inclusive category 1.

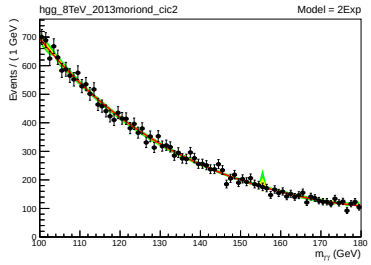

(a) 2nd Exponential Truth

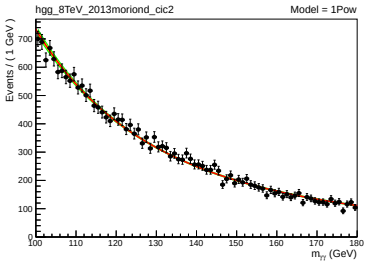

(b) 1st Power Law Truth

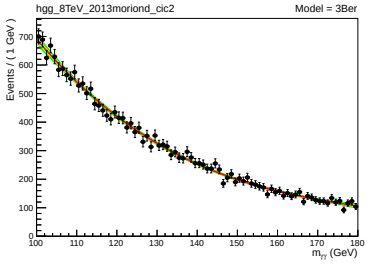

(c) 3rd Bernstein Truth

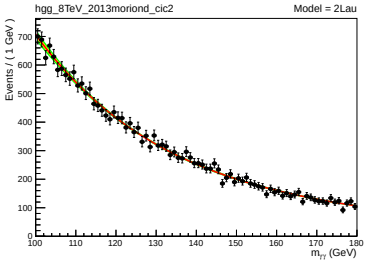

(d) 2nd Laurent Truth

Figure B.12. Fits to each of the truth models for CiC inclusive category 2.

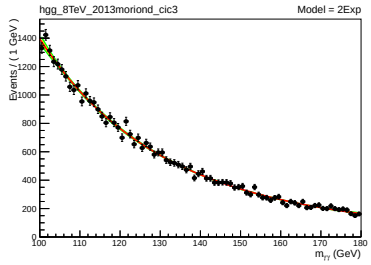

(a) 2nd Exponential Truth

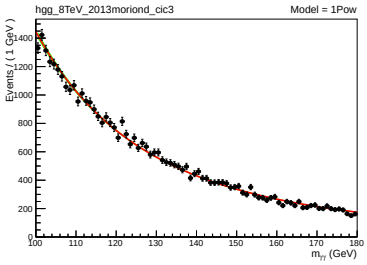

(b) 1st Power Law Truth

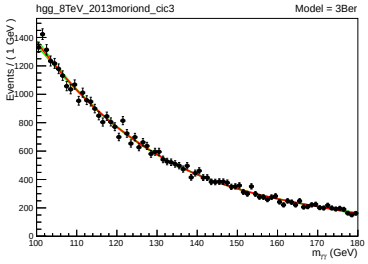

(c) 3rd Bernstein Truth

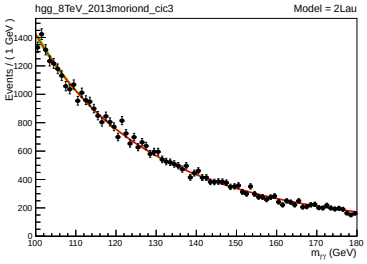

(d) 2nd Laurent Truth

Figure B.13. Fits to each of the truth models for CiC inclusive category 3.

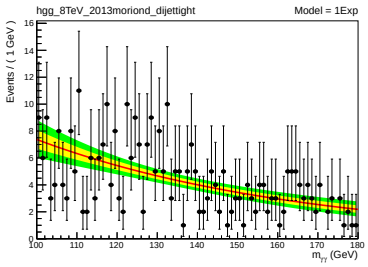

(a) 1st Exponential Truth

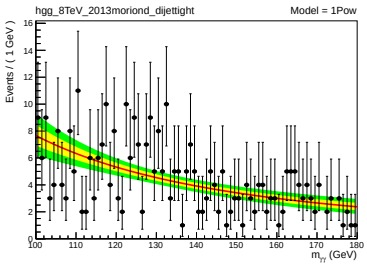

(b) 1st Power Law Truth

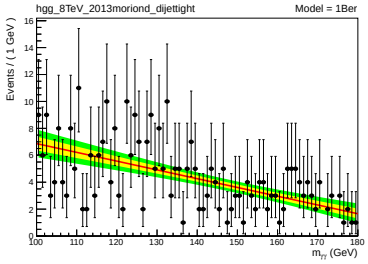

(c) 1st Bernstein Truth

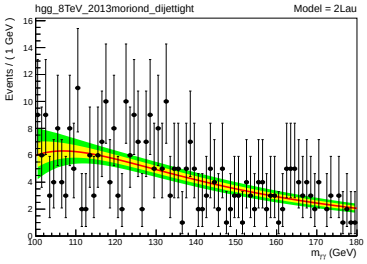

(d) 2nd Laurent Truth

Figure B.14. Fits to each of the truth models for the cut-based di-jet tight category.

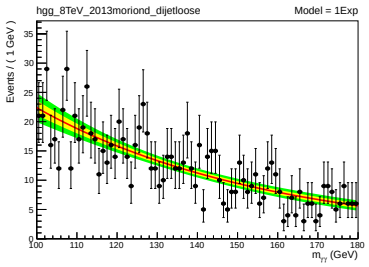

(a) 1st Exponential Truth

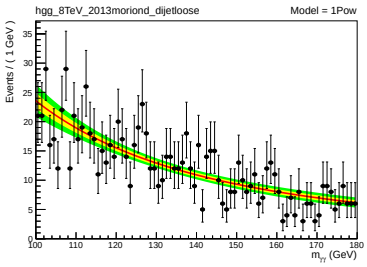

(b) 1st Power Law Truth

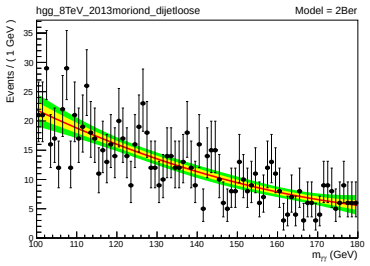

(c) 2nd Bernstein Truth

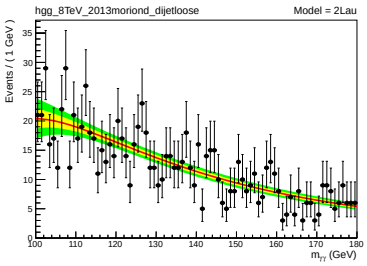

(d) 2nd Laurent Truth

Figure B.15. Fits to each of the truth models for the cut-based di-jet loose category.

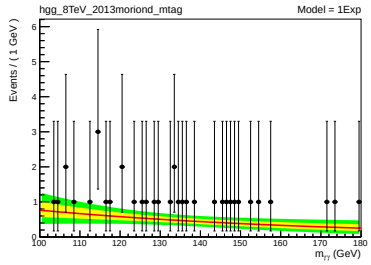

(a) 1st Exponential Truth

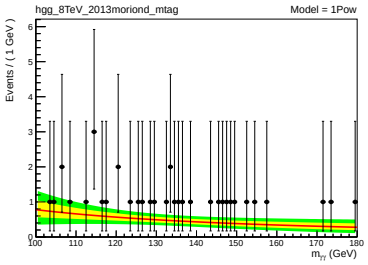

(b) 1st Power Law Truth

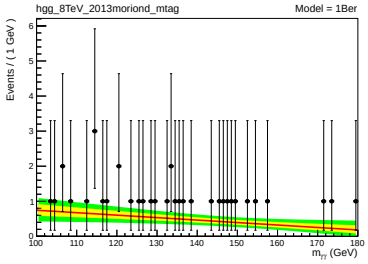

(c) 1st Bernstein Truth

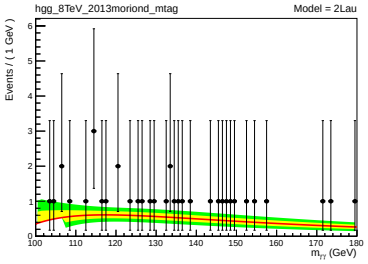

(d) 2nd Laurent Truth

Figure B.16. Fits to each of the truth models for the muon category.

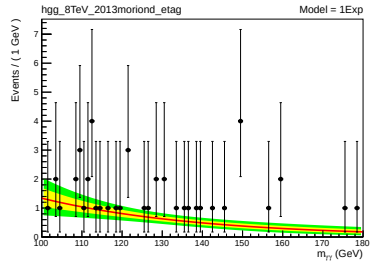

(a) 1st Exponential Truth

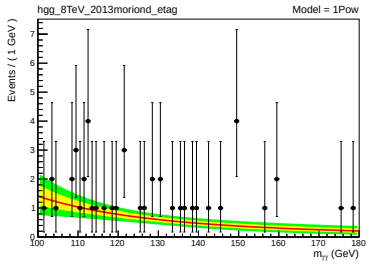

(b) 1st Power Law Truth

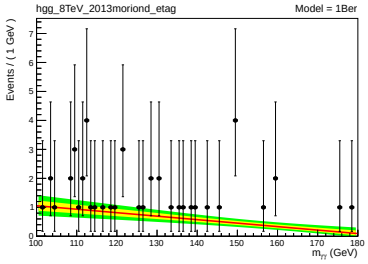

(c) 1st Bernstein Truth

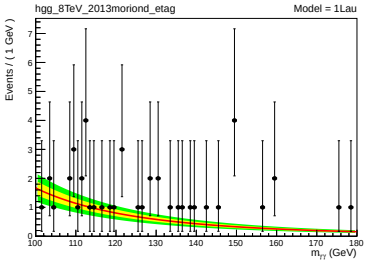

(d) 1st Laurent Truth

Figure B.17. Fits to each of the truth models for the electron category.

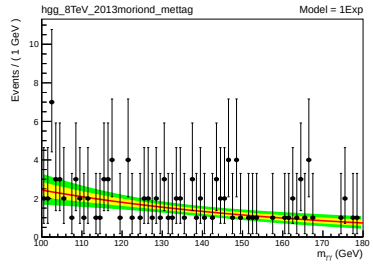

(a) 1st Exponential Truth

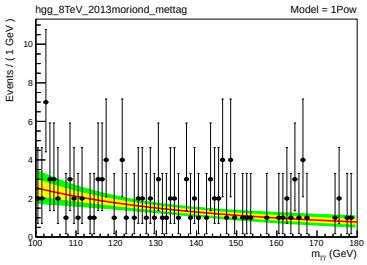

(b) 1st Power Law Truth

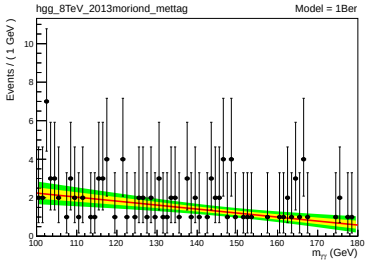

(c) 1st Bernstein Truth

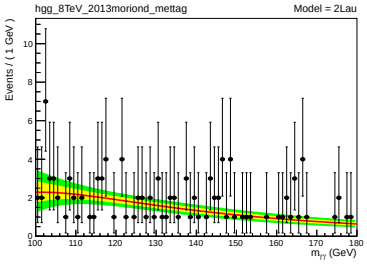

(d) 2nd Laurent Truth

Figure B.18. Fits to each of the truth models for the $\not\!\!E_T$ category.

TABLE B.25

7 TEV BIAS STUDY FOR THE CIC CATEGORIES

	Truth-model							
	2^{nd} Exponential	2^{nd} Power Law	2^{nd} Bernstein	4^{th} Laurent	2^{nd} Exponential	2^{nd} Power Law	2^{nd} Bernstein	4^{th} Laurent
Fit range: 100–160 GeV								
Fit-model	Largest Mean Bias				Mean Signal Strength (Signal+BG)			
2^{nd} Exponential	-0.04	+1.25	-1.00	+0.40	1.00	0.60	0.75	0.75
2^{nd} Power Law	-1.30	-0.05	-1.55	-0.70	1.70	1.00	1.60	1.40
3^{rd} Power Law	+0.95	-0.04	-1.70	-0.75	1.70	1.00	1.60	1.40
2^{nd} Bernstein	+0.85	+1.50	+0.05	+1.10	0.80	0.70	1.00	0.75
3^{rd} Bernstein	-0.14	-0.40	-0.05	-0.26	1.10	1.20	1.00	1.15
4^{th} Bernstein	-0.04	-0.07	-0.05	+0.09	1.00	1.00	1.00	1.00
4^{th} Laurent	+0.13	+0.11	-1.00	+0.20	0.98	0.95	0.90	0.95
6^{th} Laurent	+0.05	+0.06	-0.65	+0.06	1.00	1.00	1.30	1.00
Fit range: 100–180 GeV								
Fit-model	Largest Mean Bias				Mean Signal Strength in Signal+BG			
5^{th} Bernstein	+0.06	-0.05	-0.03	-0.03	1.00	1.00	1.00	1.00

BIBLIOGRAPHY

1. F. Zwicky. On the Masses of Nebulae and of Clusters of Nebulae. *Astrophys.J.*, 86:217–246, 1937.

2. Adam G. Riess et al. Observational evidence from supernovae for an accelerating universe and a cosmological constant. *Astron.J.*, 116:1009–1038, 1998.

3. David Galbraith and Carsten Burgard. bruvu. Website, Aug 2012. `http://bruvu.tumblr.com/post/29619095628/standard-model-standard-infographic-david`.

4. S. Tomonaga. On a relativistically invariant formulation of the quantum theory of wave fields. *Prog.Theor.Phys.*, 1:27–42, 1946.

5. Julian S. Schwinger. On Quantum electrodynamics and the magnetic moment of the electron. *Phys.Rev.*, 73:416–417, 1948.

6. Julian S. Schwinger. Quantum electrodynamics. I A covariant formulation. *Phys.Rev.*, 74:1439, 1948.

7. R.P. Feynman. Space-time approach to nonrelativistic quantum mechanics. *Rev.Mod.Phys.*, 20:367–387, 1948.

8. R.P. Feynman. Space - time approach to quantum electrodynamics. *Phys.Rev.*, 76:769–789, 1949.

9. R.P. Feynman. Mathematical formulation of the quantum theory of electromagnetic interaction. *Phys.Rev.*, 80:440–457, 1950.

10. R.P. Feynman. The Theory of positrons. *Phys.Rev.*, 76:749–759, 1949.

11. F.J. Dyson. The S matrix in quantum electrodynamics. *Phys.Rev.*, 75:1736–1755, 1949.

12. F.J. Dyson. The Radiation theories of Tomonaga, Schwinger, and Feynman. *Phys.Rev.*, 75:486–502, 1949.

13. Paul A.M. Dirac. The Quantum theory of electron. *Proc.Roy.Soc.Lond.*, A117:610–624, 1928.

14. P.A.M. Dirac. A Theory of Electrons and Protons. *Proc.Roy.Soc.Lond.*, A126:360, 1930.

15. Michael E. Peskin and Daniel V. Schroeder. An Introduction to quantum field theory. 1995.

16. Katherine Brading and Harvey R. Brown. Noether's theorems and gauge symmetries. 2000.

17. John Clive Ward. An Identity in Quantum Electrodynamics. *Phys.Rev.*, 78:182, 1950.

18. Y. Takahashi. On the generalized Ward identity. *Nuovo Cim.*, 6:371, 1957.

19. E. Fermi. An attempt of a theory of beta radiation. 1. *Z.Phys.*, 88:161–177, 1934.

20. T.D. Lee and Chen-Ning Yang. Question of Parity Conservation in Weak Interactions. *Phys.Rev.*, 104:254–258, 1956.

21. C.S. Wu, E. Ambler, R.W. Hayward, D.D. Hoppes, and R.P. Hudson. Experimental Test Of Parity Conservation In Beta Decay. *Phys.Rev.*, 105:1413–1414, 1957.

22. E.C.G. Sudarshan and R.e. Marshak. Chirality invariance and the universal Fermi interaction. *Phys.Rev.*, 109:1860–1860, 1958.

23. R.P. Feynman and Murray Gell-Mann. Theory of Fermi interaction. *Phys.Rev.*, 109:193–198, 1958.

24. David Griffiths. Introduction to elementary particles. 1987.

25. Julian S. Schwinger. A Theory of the Fundamental Interactions. *Annals Phys.*, 2:407–434, 1957.

26. S.L. Glashow. Partial Symmetries of Weak Interactions. *Nucl.Phys.*, 22:579–588, 1961.

27. Jeffrey Goldstone, Abdus Salam, and Steven Weinberg. Broken Symmetries. *Phys.Rev.*, 127:965–970, 1962.

28. J. Goldstone. Field Theories with Superconductor Solutions. *Nuovo Cim.*, 19:154–164, 1961.

29. Peter W. Higgs. Broken Symmetries and the Masses of Gauge Bosons. *Phys.Rev.Lett.*, 13:508–509, 1964.

30. F. Englert and R. Brout. Broken symmetry and the mass of gauge vector mesons. *Phys. Rev. Lett.*, 13:321–323, Aug 1964.

31. G.S. Guralnik, C.R. Hagen, and T.W.B. Kibble. Global Conservation Laws and Massless Particles. *Phys.Rev.Lett.*, 13:585–587, 1964.

32. Steven Weinberg. A Model of Leptons. *Phys.Rev.Lett.*, 19:1264–1266, 1967.

33. Abdus Salam. Weak and Electromagnetic Interactions. *Conf.Proc.*, C680519:367–377, 1968.

34. Howard Georgi and Sheldon L. Glashow. Unified weak and electromagnetic interactions without neutral currents. *Phys.Rev.Lett.*, 28:1494, 1972.

35. Christopher G. Tully. Elementary particle physics in a nutshell. 2011.

36. Hideki Yukawa. On the interaction of elementary particles. *Proc.Phys.Math.Soc.Jap.*, 17:48–57, 1935.

37. C.M.G. Lattes, G.P.S. Occhialini, and C.F. Powell. Observations On The Tracks Of Slow Mesons In Photographic Emulsions. 1. *Nature*, 160:453–456, 1947.

38. C.M.G. Lattes, G.P.S. Occhialini, and C.F. Powell. Observations On The Tracks Of Slow Mesons In Photographic Emulsions. 2. *Nature*, 160:486–492, 1947.

39. Murray Gell-Mann. Symmetries of baryons and mesons. *Phys.Rev.*, 125:1067–1084, 1962.

40. Yuval Ne'eman. Derivation of strong interactions from a gauge invariance. *Nucl.Phys.*, 26:222–229, 1961.

41. Murray Gell-Mann. A Schematic Model of Baryons and Mesons. *Phys.Lett.*, 8:214–215, 1964.

42. G. Zweig. An SU(3) model for strong interaction symmetry and its breaking. 1964.

43. M.Y. Han and Yoichiro Nambu. Three Triplet Model with Double SU(3) Symmetry. *Phys.Rev.*, 139:B1006–B1010, 1965.

44. O.W. Greenberg. Spin and Unitary Spin Independence in a Paraquark Model of Baryons and Mesons. *Phys.Rev.Lett.*, 13:598–602, 1964.

45. D.J. Gross and Frank Wilczek. Ultraviolet Behavior of Nonabelian Gauge Theories. *Phys.Rev.Lett.*, 30:1343–1346, 1973.

46. D.J. Gross and Frank Wilczek. Asymptotically Free Gauge Theories. 1. *Phys.Rev.*, D8:3633–3652, 1973.

47. D.J. Gross and Frank Wilczek. Asymptotically Free Gauge Theories. 2. *Phys.Rev.*, D9:980–993, 1974.

48. H. David Politzer. Reliable Perturbative Results for Strong Interactions? *Phys.Rev.Lett.*, 30:1346–1349, 1973.

49. Kenneth G. Wilson. Confinement of Quarks. *Phys.Rev.*, D10:2445–2459, 1974.

50. P. Petreczky. Lattice QCD at non-zero temperature. *J.Phys.*, G39:093002, 2012.

51. S. Durr, Z. Fodor, J. Frison, C. Hoelbling, R. Hoffmann, et al. Ab-Initio Determination of Light Hadron Masses. *Science*, 322:1224–1227, 2008.

52. Elliott D. Bloom, D.H. Coward, H.C. DeStaebler, J. Drees, Guthrie Miller, et al. High-Energy Inelastic e p Scattering at 6-Degrees and 10-Degrees. *Phys.Rev.Lett.*, 23:930–934, 1969.

53. Martin Breidenbach, Jerome I. Friedman, Henry W. Kendall, Elliott D. Bloom, D.H. Coward, et al. Observed Behavior of Highly Inelastic electron-Proton Scattering. *Phys.Rev.Lett.*, 23:935–939, 1969.

54. J.D. Bjorken and Emmanuel A. Paschos. Inelastic Electron Proton and gamma Proton Scattering, and the Structure of the Nucleon. *Phys.Rev.*, 185:1975–1982, 1969.

55. Richard P. Feynman. Very high-energy collisions of hadrons. *Phys.Rev.Lett.*, 23:1415–1417, 1969.

56. Jr. Callan, Curtis G. and David J. Gross. High-energy electroproduction and the constitution of the electric current. *Phys.Rev.Lett.*, 22:156–159, 1969.

57. James Stirling. Mstw pdfs. Website, Jul 2012. `http://www.hep.phy.cam.ac.uk/~wjs/plots/crosssections2012.pdf`.

58. S. Schael et al. Precision electroweak measurements on the Z resonance. *Phys.Rept.*, 427:257–454, 2006.

59. J. Alcaraz et al. A Combination of preliminary electroweak measurements and constraints on the standard model. 2006.

60. CDF Group, D0 Collaborations, the Tevatron New Physics, and Higgs Working. Updated Combination of CDF and D0 Searches for Standard Model Higgs Boson Production with up to 10.0 fb^{-1} of Data. 2012.

61. J Jackson. Tevatron Luminosity Makes an Uphill Climb. 25, 2002.

62. S.D. Holmes. Tevatron Run II Handbook. 1998.

63. Stephen Holmes, Ronald S. Moore, and Vladimir Shiltsev. Overview of the Tevatron Collider Complex: Goals, Operations and Performance. *JINST*, 6:T08001, 2011.

64. Stefano Forte and Graeme Watt. Progress in the Determination of the Partonic Structure of the Proton. 2013.

65. LHC Higgs Cross Section Working Group, S. Dittmaier, C. Mariotti, G. Passarino, and R. Tanaka (Eds.). Handbook of LHC Higgs Cross Sections: 1. Inclusive Observables. *CERN-2011-002*, CERN, Geneva, 2011.

66. A.D. Martin, W.J. Stirling, R.S. Thorne, and G. Watt. Parton Distributions for the LHC. *Eur.Phys.J.*, C63:189–285, 2009.

67. J. Beringer et al. Gauge and Higgs Bosons. *Phys. Rev. D86, 010001*, 2012.

68. G. Arduini, R. Assmann, R. Bailey, A. Butterworth, P. Collier, et al. Electron-Positron Collisions at 209 GeV in LEP. *Conf.Proc.*, C0106181:356–358, 2001.

69. F. Abe et al. Observation of top quark production in $\bar{p}p$ collisions. *Phys.Rev.Lett.*, 74:2626–2631, 1995.

70. S. Abachi et al. Search for high mass top quark production in $p\bar{p}$ collisions at $\sqrt{s} = 1.8$ TeV. *Phys.Rev.Lett.*, 74:2422–2426, 1995.

71. T. Aaltonen et al. Precise measurement of the W-boson mass with the CDF II detector. *Phys.Rev.Lett.*, 108:151803, 2012.

72. Victor Mukhamedovich Abazov et al. Measurement of the W Boson Mass with the D0 Detector. *Phys.Rev.Lett.*, 108:151804, 2012.

73. S. Chatrchyan et al. The CMS experiment at the CERN LHC. *JINST*, 3:S08004, 2008.

74. James Pinfold. MoEDAL becomes the LHC's magnificent seventh. *CERN Cour.*, 50N4:19–20, 2010.

75. The CMS Collaboration. Cms luminosity - public results. Website, Jun 2013. `https://twiki.cern.ch/twiki/bin/view/CMSPublic/LumiPublicResults`.

76. Xabier Cid Vidal and Ramon Cid. Taking a closer look at lhc. Website, May 2013. `http://www.lhc-closer.es/1/3/5/0`.

77. Cecile Noels. Cern accelerator complex. Website, Feb 2011. `https://espace.cern.ch/liu-project/LIU_images/Forms/DispForm.aspx?ID=1`.

78. A. Penzo and Y. Onel. The CMS-HF quartz fiber calorimeters. *J.Phys.Conf.Ser.*, 160:012014, 2009.

79. M. Tytgat, A. Marinov, P. Verwilligen, N. Zaganidis, A. Aleksandrov, et al. The Upgrade of the CMS RPC System during the First LHC Long Shutdown. *PoS*, RPC2012:063, 2012.

80. G. L. Bayatian et al. *CMS Physics: Technical Design Report Volume 1: Detector Performance and Software*. Technical Design Report CMS. CERN, Geneva, 2006.

81. David Futyan, Mauro Donega, Matteo Sani. Updated measurements of the new higgs-like boson at 125 gev in the two photon decay channel. *CMS Analysis Note*, CMS-AN-2013/008, 2013.

82. The $H \to \gamma\gamma$ working group. Search for a higgs boson decaying into two photons in pp collisions recorded by the cms detector at the lhc. *CMS Analysis Note*, CMS-AN-2011/426, 2011.

83. M. Anderson, A. Askew, A.F. Barfuss, D. Evans, F. Ferri, K. Kaadze, Y. Maravin, P. Meridiani, C. Seez. Review of clustering algorithms and energy corrections in ecal. IN-2010/008, 2010.

84. Pascal and Vanlaer. Electron and photon reconstruction in cms. Technical Report CMS-CR-2009-201, CERN, Geneva, Jul 2009.

85. Colin Jessop, Ted Kolberg, Nancy Marinelli. Isolated photon production cross section in pp collisions at $\sqrt{s} = 7$ tev using conversions. *CMS Analysis note*, 2011/033, 2011.

86. W Adam, R Frhwirth, A Strandlie, and T Todorov. Reconstruction of electrons with the gaussian-sum filter in the cms traker at lhc. Technical Report CMS-CR-2003-012, CERN, Geneva, Jun 2003.

87. H. Liu, N. Marinelli, G. Hanson. Conversion reconstruction with tracker-only seeded tracksin cms 900 gev data. *CMS Analysis Note*, 2010/039, 2010.

88. The $H \to \gamma\gamma$ working group. Search for a standard model higgs boson decaying into two photons. *CMS Analysis Note*, CMS-AN-2012/160, 2012.

89. P Speckmayer, A Hcker, J Stelzer, and H Voss. The toolkit for multivariate data analysis, tmva 4. *Journal of Physics: Conference Series*, 219(3):032057, 2010.

90. W. Badgeet, K. Maeshima. Putting luminosity and trigger scaler information into the event stream. IN-2007/025, 2007.

91. Particle-flow event reconstruction in cms and performance for jets, taus, and met. Technical Report CMS-PAS-PFT-09-001, CERN, 2009. Geneva, Apr 2009.

92. The CMS Collaboration. Search for a higgs boson decaying into two photons in proton-proton collisions recorded by the cms detector at the lhc. *CMS Analysis note*, 2011/129, 2011.

93. David L. Rainwater, R. Szalapski, and D. Zeppenfeld. Probing color singlet exchange in Z + two jet events at the CERN LHC. *Phys. Rev.*, D54:6680–6689, 1996.

94. A. Korytov, G. Petrucciani, M. Chen and others. Procedure for the lhc higgs boson search combination in summer 2011. *CMS Analysis Note*, 2011/298, 2011.

95. Glen Cowan, Kyle Cranmer, Eilam Gross, and Ofer Vitells. Asymptotic formulae for likelihood-based tests of new physics. *Eur.Phys.J.*, C71:1554, 2011.

96. S. S. Wilks. The Large-Sample Distribution of the Likelihood Ratio for Testing Composite Hypotheses. *Ann. Math. Statist.*, 9:60–62, 1938.

97. Properties of the higgs-like boson in the decay h to zz to 4l in pp collisions at sqrt s =7 and 8 tev. Technical Report CMS-PAS-HIG-13-002, CERN, Geneva, 2013.

98. Evidence for a particle decaying to w+w- in the fully leptonic final state in a standard model higgs boson search in pp collisions at the lhc. Technical Report CMS-PAS-HIG-13-003, CERN, Geneva, 2013.

99. Search for the standard-model higgs boson decaying to tau pairs in proton-proton collisions at sqrt(s) = 7 and 8 tev. Technical Report CMS-PAS-HIG-13-004, CERN, Geneva, 2013.

100. Search for the standard model higgs boson produced in association with w or z bosons, and decaying to bottom quarks for lhcp 2013. Technical Report CMS-PAS-HIG-13-012, CERN, Geneva, 2013.

101. Combination of standard model higgs boson searches and measurements of the properties of the new boson with a mass near 125 gev. Technical Report CMS-PAS-HIG-13-005, CERN, Geneva, 2013.

102. The $H \to \gamma\gamma$ working group. Search for a standard model higgs boson decaying into two photons employing multivariate methods. *CMS Analysis Note*, CMS-AN-2012/048, 2012.

This document was prepared & typeset with pdfLaTeX*, and formatted with* NDdiss2$_\varepsilon$ *classfile (v3.2013*β*[2013/01/31]) provided by Sameer Vijay and updated by Megan Patnott.*